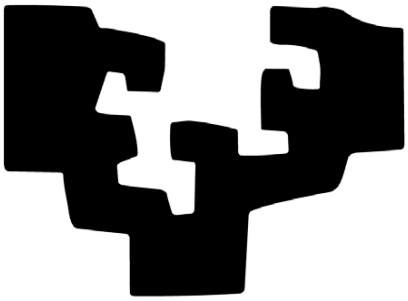

EHU

Euskal Herriko Unibertsitatea
Universidad del País Vasco

UNIVERSITY OF THE BASQUE COUNTRY

DEVELOPMENT AND CHARACTERIZATION OF NOVEL ECO–FRIENDLY ADSORBENTS BASED ON PECTIN COMPOSITES AND PVA MATS TO REMEDIATE WATER FROM EMERGING POLLUTANTS

FRANCESCO COIN

Thesis director: Dra. Silvina Cerveny

Donostia – San Sebastian 2026

“I don’t have dreams

I have goals.”

Acknowledgements

First, I would like to express my deepest gratitude to my thesis supervisor, Dr. Silvina Cerveny. Her guidance, patience, and enthusiasm have shaped my development as a researcher from the beginning. Over these years, I have learned not only techniques and methods, but also how to think critically and to work with curiosity and integrity thanks to her example. I am grateful also to Prof. Silvia Nair Goyanes, my supervisor during my short stay in Argentina at the University of Buenos Aires, for her generous mentorship, insightful discussions, and warm welcome. Those three months broadened my perspective and enriched this work in meaningful ways.

My sincere thanks go to all members of the Polymer and Soft Matter group for their help, advice, and good humor at every stage of this project and especially to the Materials Physics Center (CSIC–UPV/EHU) for supporting my contract throughout the PhD. This thesis was also made possible by financial support from national and institutional projects: Ministerio de Ciencia, Innovación y Universidades / Agencia Estatal de Investigación (projects PID2019–104650GB–C21 and PID2023–146348NB–I00), CSIC (project BILAT23076 and IMOVE2023) and Department of Education of the Basque Government under grant PIBA_2024_1_0011 and IT1566–22); which provided essential resources for consumables, instrumentation, travel, and conference participation.

I gratefully acknowledge the technical support and constant kindness of Aitor Larrañaga, Juan Carlos Raposo and Evgenii Modin. Their availability, professionalism, and patience saved me more than once and ensured that experiments ran smoothly. Thank you for always finding the time to help and for solving problems with a smile.

I am also grateful to the universities that formed me, the University of Padua, Italy (where are my origins), the University of Bordeaux (France, where I approach me to the research and academic environment for the first time), and the University of the Basque Country (where I done my PhD) for providing the foundation that allowed me to undertake and complete just a small part of my life journey.

Playing rugby for 25 years tough me the sense of life where the team counts more than the individual trusting in other people, where you learn to collaborate and manage conflicts learning not to be afraid of falling or of clashing with your opponent. Achieving your goals is a constant challenge where you receive many blows and fall many times but you always have to find the strength to get up and react in order to reach your ambitions and smile.

A special thank you to my close friends, who stood by me through both good and bad times, and to the many people I met during my PhD who shared wonderful moments and offered support along the way. Thank you, Raoni, Jorge, Andrea, Valerio, Elisa, Seb, Sebas, Eric, Pane, Ele, Caro, Phoug, Mattia,

Paula, Alexey, Miguel, Giulia, Martino, Sharon, Aurora, Victor, Juni, Samu, Javier, Pablo, and many others. Thank you as well to Alicia, Carlos, David, and Dario for making me feel at home in the lab during my stay in Argentina. And from the bottom of my heart, thank you, Ayelen, for filling my daily life with sincere love and supporting me through the hardest moments. You have scratched my heart with wonderful memories ever since I first met you in Bariloche during my stay.

Finally, my profound gratitude goes to the most important people in my life: my parents which grow me giving the opportunity to develop the person who I am. Their love, encouragement, and trust sustained me through every challenge and celebrated every small victory.

Nothing in these pages would exist without these people. Thank you for the joy and comfort that only you could bring.

Contributions

This thesis has contributed to the following publications:

1. F. Coin, C. A. Rodríguez–Ramírez, F. S. Oyarbide, D. Picón, S. Goyanes, and S. Cerveny, "Efficient antibiotic removal from water using europium–doped poly(vinyl alcohol) nanofiber mats esterified with citric acid," J. Water Process Eng., vol. 63, no. March, 2024, doi: 10.1016/j.jwpe.2024.105447.

2. C. A. Rodríguez–Ramírez, F. Coin, A. Vergara–Rubio, D. Picón, S. Cerveny, and S. Goyanes, "Enhanced tetracycline removal through 'in situ' europium incorporation in poly (vinyl alcohol) (PVA) electrospun mats: Advantages of this strategy in adsorption and reuse over doping," Chemosphere, vol. 372, no. January, 2025, doi: 10.1016/j.chemosphere.2025.144102.

3. F. Coin, A. Larrañaga, and S. Cerveny, "Structural characterization of low methoxyl pectin–based adsorbents: the role of water on pectin structure," Carbohydr. Polym. Technol. Appl., vol. 11, no. June, 2025, doi: 10.1016/j.carpta.2025.100885.

4. F. Coin, V. Di Lisio, D. Cangialosi, and S. Cerveny, "The glass transition and the dynamics of water within pectin and metal–organic framework nanochannels," J. Chem. Phys., vol. 163, no. 16, p. 164507, Oct. 2025, doi: 10.1063/5.0294531.

5. F. Coin, C. Iacovone, and S. Cerveny, "Bio-Based Pectin-Calcium Film and Foam Adsorbents with Immobilized Fe–BTC MOF for Water Contaminant Removal," Polymers, vol. 18, no. 2, 2026, doi: 10.3390/polym18020171.

In addition, Francesco Coin has contributed to the following patent and papers already published and/or submitted in topics intimately related with the topics of this thesis:

1. J. Martinez Sabando, F. Coin, G.A. Schwartz, S. Cerveny, "Composition for removing pharmaceuticals and heavy metals from polluted water". Submission number 300466912. Application number EP22383090.2, 2023. Priority countries: EU.

2. J. Martínez–Sabando, F. Coin, J. H. Melillo, S. Goyanes, and S. Cerveny, "A Review of Pectin–Based Material for Applications in Water Treatment," Materials, vol. 16, no. 6, 2023, doi: 10.3390/ma16062207.

3. J. Martínez–Sabando, F. Coin, J. C. Raposo, A. Larrañaga, J. H. Melillo, and S. Cerveny, "Dual crosslinking of low–methoxyl

pectin by calcium and europium for the simultaneous removal of pharmaceuticals and divalent heavy metals," Chem. Eng. J., vol. 475, no. June, p. 146162, 2023, doi: 10.1016/j.cej.2023.146162.

4. A. C. Santos, F. Coin, S. Cerveny, A. J. Marzocca, and S. N. Goyanes, "Beyond the surface area: The effect of electrospinning versus casting on molecular packing and its impact on the production of efficient PVA–pectin–Fe adsorbents," Int. J. Biol. Macromol., vol. 332, p. 148565, 2025, doi: 10.1016/j.ijbiomac.2025.148565.

5. C. Iacovone, F. Coin, S. Goyanes, and S. Cerveny, "Calcium Crosslinking Modulates Structure and Pharmaceutical Removal of Pectin–Based Water Treatment Adsorbents," SSRN, 2025, doi: 10.2139/ssrn.5670531.

Finally, part of this work was presented in the following conferences and workshops:

1. Authors: Francesco Coin, Javier Martinez Sabando, Jorge H. Melillo, Silvina Cerveny
   Título: **Broadband dielectric spectroscopy of pectin–based hydrogels**
   Type of participation: Talk (Oral)
   Congress: 11th Conference on Broadband Dielectric Spectroscopy and its Applications (BDS2022)
   Town: Donostia – San Sebastián
   Date: 09/09/2022

2. Authors: Francesco Coin, Javier Martinez Sabando, Jorge H. Melillo, Silvina Cerveny
   Título: **Water distribution in Calcium pectin–based hydrogels**
   Type of participation: Talk (Oral)
   Congress: Workshop Water Remediation
   Town: Donostia – San Sebastián
   Date: 11/10/2022

3. Authors: Francesco Coin, Facundo Oyarbide, Carlos Rodríguez, David Picón, Silvina Cerveny, Silvia Goyanes
   Título: **Poly(vinyl alcohol) for antibiotic removal**
   Type of participation: Talk (Oral)
   Congress: 1st Faculty of chemistry (UPV/EHU) PhD day
   Town: Donostia – San Sebastián
   Date: 14/08/2024

4. Authors: Francesco Coin, Alejandro Miccio, Aitor Larrañaga, Silvina Cerveny
   Título: **Water dynamics on calcium pectin–based hydrogels for application in water remediation**

Type of participation: Talk (Oral)
Congress: 12th Conference on Broadband Dielectric Spectroscopy and its Applications (BDS2024)
Town: Lisboa
Date: 01/09/2024

5. Authors: Francesco Coin
Título: **Una cucharada de azúcar para agua dulce más limpia**
Type of participation: Talk (Oral)
Congress: 10th Pint of Science 2025
Town: Donostia – San Sebastián
Date: 20/05/2025

6. Authors: Francesco Coin
Título: **Water remediation and water dynamics on pectin–MOF composite**
Type of participation: Talk (Oral)
Congress: DiPC – CFM PhD Student Seminar Series
Town: Donostia – San Sebastián
Date: 11/06/2025

7. Authors: Francesco Coin, Valerio Di Lisio, Daniele Cangialosi, Silvina Cerveny
Título: **The glass transition of confined water on calcium pectin–based adsorbents**
Type of participation: Invited talk (Oral)
Congress: 10th International Discussion Meeting on Relaxations in Complex Systems (10thIDMRCS)
Town: Barcelona
Date: 25/07/2025

Resumen

La contaminación del agua por contaminantes emergentes, como metales pesados, productos farmacéuticos y pesticidas, se ha convertido en uno de los desafíos medioambientales más críticos del siglo XXI. Estos contaminantes, a menudo presentes en concentraciones de trazas, son altamente persistentes y tóxicos y son apenas eliminados por las plantas de tratamiento de aguas residuales convencionales. Por ello, resulta esencial desarrollar estrategias de remediación sostenibles y eficientes. Entre las tecnologías disponibles, la adsorción destaca por su simplicidad, versatilidad y bajo coste, aunque su éxito depende en gran medida del diseño del material adsorbente.

Esta tesis aborda dicho reto mediante el diseño, la fabricación y la caracterización de adsorbentes bio–basados e híbridos para la remediación de agua, con especial atención a tres plataformas de materiales: la pectina, el metal organic framework Basolite F300® (MOF, Fe–BTC) y el alcohol polivinílico (PVA). La pectina, un polisacárido de origen vegetal, fue estudiada en detalle para dilucidar cómo su grado de esterificación, el tipo de entrecruzamiento iónico y el estado de hidratación influyen en su comportamiento adsorbente.

Se prepararon matrices de pectina entrecruzadas con calcio, capaces de adsorber zinc mediante mecanismos de intercambio iónico de coordinación. Asimismo, se desarrolló la inmovilización de Fe–BTC en matrices de pectina entrecruzadas con calcio, superando las limitaciones de manipulación del MOF en forma de polvo. Las películas y espumas obtenidas mediante solvent casting y liofilización mostraron una porosidad mejorada, una integración estructural estable y un rendimiento superior en la adsorción de zinc, paraquat y tetraciclina.

En paralelo, se investigaron las dinámicas fundamentales del agua confinada. La calorimetría diferencial de barrido (DSC) y la espectroscopía dieléctrica de amplio rango demostraron que el agua confinada en nano–canales de pectina y en poros de Fe–BTC presenta transiciones vítreas entre 170 y 200 K. Estos resultados contribuyen al prolongado debate sobre la transición vítrea del agua y aportan una visión mecanística sobre cómo la hidratación regula el rendimiento de los adsorbentes.

De forma complementaria a los sistemas de pectina, se fabricaron membranas nanofibrosas de PVA mediante electroestirado y posteriormente estabilizado mediante entrecruzamiento con ácido cítrico. El europio se incorporó tanto por dopado posterior como de forma in situ durante el proceso de electroestirado. Ambas estrategias produjeron adsorbentes estables en agua, con elevada afinidad por antibióticos. Los materiales demostraron ser reutilizables en de varios ciclos y mantuvieron su eficacia incluso en presencia de cocontaminantes como colorantes y pesticidas. En particular, la vía de incorporación in situ mejoró la distribución del europio y alcanzó una eficiencia de adsorción superior. En conjunto, los resultados de esta tesis confirman las hipótesis iniciales y demuestran que los adsorbentes híbridos bio–basados,

construidos a partir de polímeros renovables y componentes inorgánicos funcionales, constituyen soluciones eficientes, reutilizables y respetuosas con el medio ambiente para la remediación del agua. Al mismo tiempo, la integración de estudios aplicados de adsorción con investigaciones fundamentales sobre la dinámica del agua confinada proporciona un vínculo único entre los mecanismos moleculares y el rendimiento macroscópico. Esta doble perspectiva impulsa tanto el conocimiento científico como la aplicación tecnológica de adsorbentes sostenibles, reforzando su potencial como herramienta clave para afrontar el problema urgente de los contaminantes emergentes en el agua.

Abstract

Water pollution by emerging contaminants such as heavy metals, pharmaceuticals, and pesticides has become one of the most critical environmental challenges of the 21st century. These pollutants, often present at trace concentrations, are highly persistent, toxic, and poorly removed by conventional wastewater treatment plants. Developing sustainable and efficient remediation strategies is therefore essential. Among the available technologies, adsorption stands out for its simplicity, versatility, and cost–effectiveness, although its success depends strongly on the design of the adsorbent material.

This thesis addresses this challenge by designing, fabricating, and characterizing bio–based and hybrid adsorbents for water remediation, with a focus on three material platforms: pectin, the metal organic framework Basolite F300® (MOF, Fe–BTC), and poly(vinyl alcohol) (PVA). Pectin, a plant–derived polysaccharide, was studied in detail to elucidate how its degree of esterification, crosslinking, and hydration state influence its adsorption behavior.

Calcium–crosslinked pectin matrices were prepared, enabling zinc adsorption through a combination of ion exchange and coordination. The immobilization of Fe–BTC within calcium–crosslinked pectin matrices was further developed to overcome the handling limitations of MOF powders. Films and foams produced by solvent casting and freeze–drying exhibited enhanced porosity, stable structural integration, and improved adsorption performance for zinc, paraquat, and tetracycline.

In parallel, the fundamental dynamics of confined water were investigated. Differential scanning calorimetry and broadband dielectric spectroscopy demonstrated that water confined in pectin nanochannels and Fe–BTC pores undergoes glass transitions between 170 and 200 K. These results contribute to the long–standing debate on the glass transition of water and provide mechanistic insights into how hydration governs the adsorbent performance. Complementary to pectin systems, PVA nanofibrous mats were fabricated by electrospinning and stabilized through citric acid crosslinking. Europium was introduced either by post–doping or through in situ incorporation during electrospinning. Both strategies produced water–stable adsorbents with high affinity for antibiotics. The materials demonstrated reusability over several cycles and maintained performance even in the presence of cocontaminants such as dyes and pesticides. The in–situ incorporation route, in particular, provided enhanced europium distribution and superior adsorption efficiency.

Overall, the results of this thesis confirm the initial hypotheses and demonstrate that hybrid bio–based adsorbents built from renewable polymers and functional inorganic components are efficient, reusable, and environmentally friendly solutions for water remediation. At the same time, integrating of applied adsorption studies with fundamental investigations of confined water dynamics provides a unique link between molecular–level

mechanisms and macroscopic performance. This dual perspective advance both scientific understanding and technological applications of sustainable adsorbents, reinforcing their potential as a key tool for tackling the urgent problem of emerging contaminants in water.

Thesis Outline

The thesis is structured into three main sections:

- **Section 1** introduces the scientific context of the work. It addresses the problem of water pollution by emerging contaminants, reviews existing remediation technologies, and explains the rationale for focusing on adsorption as the most promising solution. This section also describes the structural and functional properties of the selected materials, such as pectin, Basolite F300®, and poly(vinyl alcohol), and provides the theoretical background on glass transition and relaxation dynamics of confined water, which underpin part of the research. In addition, it details the experimental methods and instrumentation employed, including the preparation and processing of pectin and PVA–based adsorbents and the incorporation of metal–organic frameworks and europium ions. The analytical techniques used for structural, thermal, spectroscopic, dielectric, and chemical characterization, as well as the protocols applied to evaluate adsorption performance and reusability, are also presented.

- **Section 2** contains the overall conclusions of the thesis, synthesizing the main findings and their scientific and technological implications.

- **Section 3** presents the research results, organized around the publications that comprise this compendium. Together, these works demonstrate the design, characterization, and application of novel bio–based and hybrid adsorbents for the efficient removal of heavy metals, pharmaceuticals, and pesticides from water.

Contents

List of Figures

List of Tables

Acronyms

AA – Acetic Acid

ATR – Attenuated Total Reflectance

AOPs – Advanced Oxidation Processes

BDS – Broadband Dielectric Spectroscopy

BET – Brunauer–Emmett–Teller (surface area analysis)

BTC – Benzene–1,3,5–tricarboxylate

CA – Citric Acid

Ca^{2+}– Calcium ion

CIP – Ciprofloxacin

DLS – Dynamic Light Scattering

DM – Degree of Methoxylation

DSC – Differential Scanning Calorimetry

EDX – Energy Dispersive X–ray Spectroscopy

ECs – Emerging Contaminants

Eu^{3+} – Europium ion

FT–IR – Fourier Transform Infrared Spectroscopy

GalA – Galacturonic acid

HMP – High–Methoxyl Pectin

ICP–AES – Inductively Coupled Plasma–Atomic Emission Spectroscopy

LMP – Low–Methoxyl Pectin

MB – Methylene Blue

MOF – Metal–Organic Framework

NPs – Nanoparticles

PE – Pectin

PE–Ca – Pectin crosslinked with calcium ions

PFO – Pseudo–First–Order (kinetic model)

PQ – Paraquat

PSO – Pseudo–Second–Order (kinetic model)

PVA – Poly(vinyl alcohol)

PVP – Polyvinylpyrrolidone

RH – Rhodamine

SEM – Scanning Electron Microscopy

SI – Supplementary Information

TC – Tetracycline

TGA – Thermogravimetric Analysis

Tg – Glass Transition Temperature

UV–Vis – Ultraviolet–Visible Spectroscopy

WWTPs – Wastewater Treatment Plants

XRD – X–ray Diffraction

Zn^{2+} – Zinc ion

SECTION 1

1 Water Pollution

Water is an indispensable natural resource that sustains human life, ecosystems, and industrial activities [1],[2]. Despite being a renewable resource, its availability is increasingly threatened by overexploitation, pollution, and the effects of climate change [3]. According to the United Nations Sustainable Development Goal 6, ensuring access to clean water and sanitation is one of the most urgent global priorities [4]. However, rising levels of water contamination from industrial discharges, intensive agriculture, and uncontrolled urban expansion have intensified the global water crisis. Figure 1 schematically shows the updated global water risk atlas for 2025.

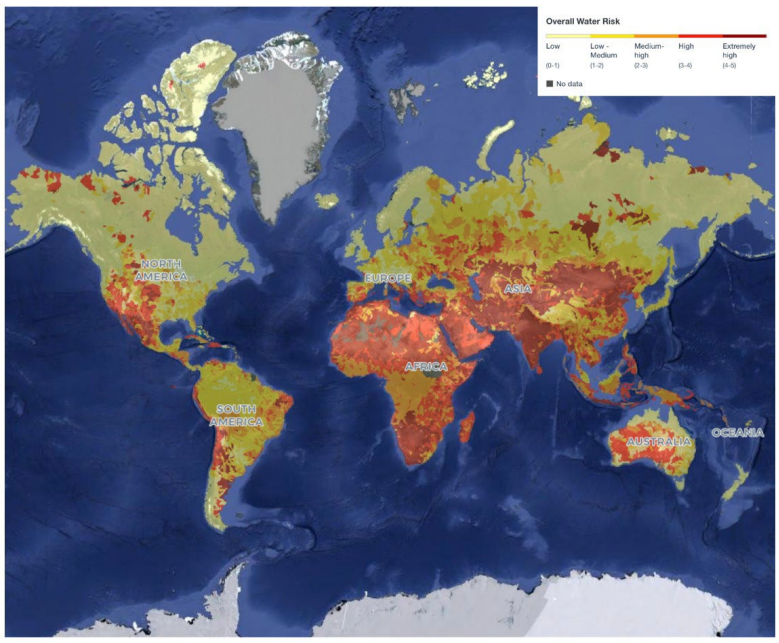

Figure 1: *Overall global water risk atlas updated to 2025. Picture taken from Aqueduct Water Risk Atlas.*

To address this challenge, new remediation technologies are being developed to limit the production of common adsorbents and filters made from common plastics, derived from fossil fuels.

The present thesis focuses on developing and characterizing new adsorbent materials based on alternative bio–polymers such as pectin (PE) and poly(vinyl alcohol) (PVA), as well as porous semi–crystalline solids such as metal–organic frameworks (MOFs). These materials, either individually or in

combination, can provide a sustainable alternative for removing heavy metals, pharmaceuticals, and pesticides from polluted water [5–7].

This introductory section (Section 1) provides the general context for the work. First, contaminants will be classified by size and chemical nature (Subsection 1). Then, the focus will be on three representative groups of emerging contaminants, like heavy metals, pharmaceuticals, pesticides, and dyes. Moreover, it presents an overview of the main water remediation technologies, highlighting adsorption as the most suitable method. Subsection 2 introduces the three main classes of novel materials studied in this thesis: pectin, Basolite F300® (Fe–BTC), and PVA. Subsection 3 summarizes the experimental techniques and method used in this thesis work. Subsection 4 presents the hypothesis and the objectives of the thesis, and Paragraph 5 shows the overview and the results discussion. Next, Section 2 synthesizes the general conclusions derived from the work. Finally, Section 3 contains the compendium of publications that constitute the core of this thesis.

1.1 Classification of Contaminants

Both organic and inorganic contaminants are classified by size [8]. Smaller contaminants are generally more difficult to remove due to their reduced size and increased mobility. According to their dimensions, contaminants can be classified into five categories summarized in Fig. 2 [9]. Macroresidues are the largest, with sizes greater than 5 mm. Microresidues range from 5 mm to 1 mm and include materials such as plastic pellets. Particulate matter, such as sediments, sand, and insoluble salts, typically falls within the range of 1 mm to 1 µm. Microorganisms, including bacteria and viruses, are smaller still, measuring between 1 µm and 1 nm. The smallest category consists of dissolved contaminants, which are less than 1 nm in size and include individual molecules in solution. Notably, the last two categories (microorganisms and dissolved contaminants) are often referred to as emerging contaminants due to their increasing relevance in environmental and health–related contexts [10].

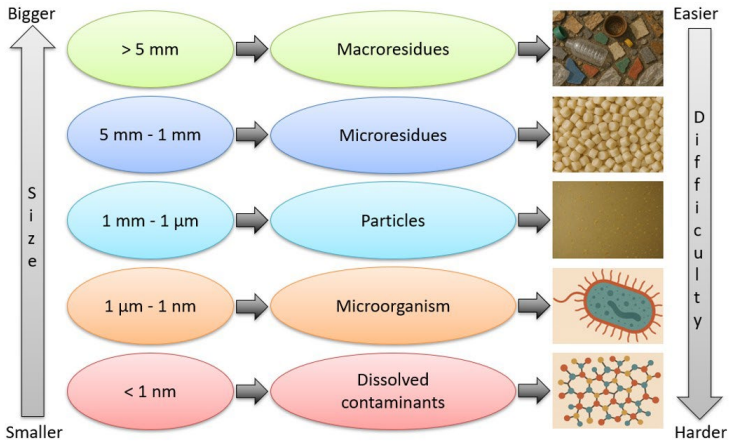

Figure 2: *Classification of water contaminants based on their size and difficulty of removal.*

1.2 Emerging Contaminants

Among the different categories of pollutants, such as suspended solids or nutrients, emerging contaminants (ECs) are often found at low concentrations (in the µg/L to ng/L range) but have strong biological activity, high persistence, and potential for bioaccumulation [11]. ECs are chemical substances of anthropogenic origin that are not yet fully regulated but are increasingly recognized as threats to environmental and human health [1]. These substances are summarized in Fig. 3 and include microplastic, heavy metals, pesticides, bacteria, pharmaceutical products, dyes, and chemicals that, although often present at trace concentrations, are highly persistent and toxicity [1].

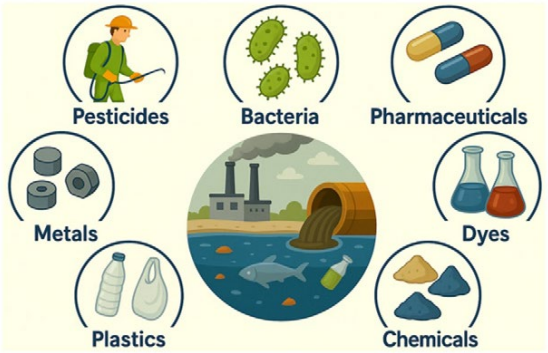

Figure 3: *Schematic representation of emerging water contaminants.*

ECs are not efficiently removed by conventional wastewater treatment plants (WWTPs) and therefore accumulate in rivers, lakes (surface water), and groundwater, contaminating the global water cycle [12]. Their presence not only affects aquatic life but also represents a global concern and a potential risk to human health, since many of these substances are bioaccumulative and can enter the food chain (Fig. 4) [3]. Their continuous release into aquatic environments originates from diverse sources, including agriculture, industry, and urban wastewater [13,14].

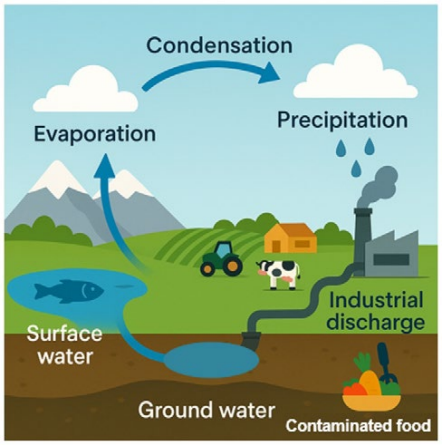

Figure 4: *Schematically representation of the world contaminated water cycle.*

1.2.1 Heavy Metals

Heavy metals are elements with high atomic mass and density that can be toxic at low concentrations. They are environmentally persistent because, unlike most organic contaminants, they do not mineralize; instead, they change speciation (oxidation state, complexation, and solid–solution partitioning) with pH, redox potential, and ligands [15]. Typical examples in aquatic systems include lead (Pb), cadmium (Cd), mercury (Hg), chromium (Cr), nickel (Ni), copper (Cu), zinc (Zn), arsenic (As), and antimony (Sb). Once released, metals are transported as dissolved ions, hydroxo/carbonato complexes, or bound to colloids and natural organic matter, leading to bioaccumulation in food. Aquatic organisms exhibit sensitive endpoints, including impaired ion regulation in fish gills, reduced photosynthetic efficiency in algae, enzyme inhibition in invertebrates, and shifts in benthic microbial communities.

Given all the facts out lined above, the United States Environmental Protection Agency (US EPA) [16], the World Health Organization (WHO) [17] and the European Union (EU) have established guidelines setting maximum contaminant levels for drinking water (see Table 1). These guidelines are created based on a review of available scientific evidence, considering the health effects of exposure, the feasibility of treatment and monitoring, and the economic and social impacts of implementing the guidelines.

***Table 1**: Maximum Contaminant Level (MCL) established by United States Environmental Protection Agency (US EPA), World Health Organization (WHO), and European Union (EU) Guideline 2020/2184, metal symbol and most common oxidation states.*

Heavy Metal	Symbol	Oxidation state	MCL US EPA [mg/L]	MCL WHO [mg/L]	MCL EU [mg/L]
Aluminum	Al	+3	0.05 – 0.2	/	0.2
Antimony	Sb	+3, +5	0.006	0.02	0.01
Arsenic	As	3, +3, +5	0.010	0.01	0.01
Barium	Ba	+2	2.0	0.7	/
Beryllium	Be	+2	0.004	/	/
Cadmium	Cd	+2	0.005	0.003	0.005
Chromium	Cr	+3, +6	0.1	0.05	0.05
Cobalt	Co	+2, +3	0.05	0.05	0.025
Copper	Cu	+1, +2	1.3	2.0	/
Iron	Fe	+2, +3, +6	0.3	0.3	2.0
Lead	Pb	+2	0.015	0.01	0.2
Manganese	Mn	+3, +4, +7	0.05	0.4	0.01
Mercury	Hg	+1, +2	0.002	0.006	0.05
Nickel	Ni	+2	0.1	0.07	0.001
Selenium	Se	–2, +4, +6	0.05	0.04	0.02
Thallium	Tl	+1, +3	0.002	/	0.02
Zinc	Zn	0, +2	5.0	3.0	/

1.2.2 Pharmaceuticals

Pharmaceutical residues, particularly antibiotics, are among the most problematic emerging contaminants [18]. Their presence in aquatic systems originates from human and veterinary use, hospital waste, the pharmaceutical industry, and especially excretion, since many antibiotics are only partially

metabolized and are released into sewage systems [19]. Conventional WWTPs are unable to remove these compounds, which persist in the environment completely. As use continues to expand and populations age, the combination of persistence, mixture effects, and selection pressures for resistance positions pharmaceuticals as a critical class of emerging contaminants. Many compounds are only partially metabolized and occur at ng–µg/L level as a complex mixture, with "pseudo–persistence" maintained by continuous inputs. They can disrupt endocrine and neurological function in aquatic organisms, alter behavior and reproduction, and, in the case of antibiotics, select for antimicrobial resistance, an emerging public–health concern even at sub–inhibitory concentrations. Monitoring is challenging because concentrations vary seasonally and episodically (e.g., after rain events), metabolites and conjugates are under characterized, and non–target screening still misses many transformation products.

1.2.3 Pesticides

Agricultural activities are one of the primary contributors to water contamination worldwide [20]. Pesticides such as insecticides, herbicides, fungicides, and seed treatments are applied to crops leaching into soil and running into rivers and groundwater, where they persist for long periods [21]. Depending on their chemical composition, pesticides may be highly toxic to non–target organisms, accumulate in sediments, and pose risks to human health [21]. Once in aquatic systems, many compounds persist or transform into metabolites that can be as mobile or toxic as the parent molecules, even at low (ng–µg)/L level. Conventional WWTPs and drinking–water facilities are not optimized for complete removal, and partial treatments can generate byproducts with residual toxicity [22]. Combined with expanding use patterns, climate–driven transport, and the rise of "next–generation" formulations, these factors position pesticides as a class of emerging contaminants that warrant improved surveillance, risk assessment focused on chronic and mixture toxicity.

1.2.4 Dyes

Industries such as textile, leather, and paper are significant sources of dye pollution, discharging large volumes of dye–laden wastewater into aquatic environments [20]. Once released, these dyes impart intense coloration to water bodies, reducing sunlight penetration, inhibiting photosynthesis, and raising biochemical oxygen demand, disrupting aquatic ecosystems. These synthetic dyes are chemically stable and resist natural degradation, allowing them to persist in the environment and even bioaccumulate in aquatic organisms; many dyes also exhibit toxic, mutagenic, or carcinogenic properties that threaten aquatic life and human health [23]. Detecting and removing dye contaminants is challenging: water monitoring often measures only overall color rather than

specific dye chemicals [24], and conventional treatment methods often fail to fully degrade these stable compounds, leaving residual dye pollution and hazardous sludge byproducts. Because of their persistence and harmful effects, synthetic dyes are now considered as emerging contaminants that require greater attention in environmental management.

1.3 Water Remediation Technologies

The purification of contaminated water requires a combination of physical, chemical, and biological processes, depending on the type and concentration of pollutants present. Traditional wastewater treatment plants (WWTPs) are highly effective for removing suspended solids, organic matter, and pathogens [2]. However, they were not originally designed to remove emerging contaminants (ECs) such as heavy metals, pharmaceuticals, and pesticides [2]. As a result, these substances often bypass conventional treatments and accumulate in natural water bodies.

Several advanced treatment technologies have been developed to address this limitation [25]. Each has particular strengths but also practical drawbacks that limit its extensive–scale application:

- **Filtration and phase separation:** Effective for suspended solids and large particles, but ineffective for dissolved contaminants such as pharmaceuticals or pesticides (Fig. 5a and 5b).
- **Membrane Processes (reverse osmosis):** Provide high rejection rates for salts, metals, and small organic molecules. Nevertheless, they are energy–intensive, prone to fouling, and expensive to operate, which limits their long–term sustainability (Fig. 5c).
- **Advanced Oxidation Processes (AOPs):** Techniques such as ozonation and photocatalysis reactions can degrade organic pollutants into smaller molecules or mineralize them into CO_2 and water. Despite their effectiveness, they require significant energy input and often generate intermediate by–products whose toxicity must be carefully assessed (Fig. 5d).
- **Electrochemical Methods:** Emerging technologies that couple pollutant removal with energy recovery. Although conceptually attractive, these methods are still in early stages of development and remain limited by high costs and low scalability (Fig. 5e).
- **Biological Treatments:** Rely on microorganisms to metabolize organic pollutants. They are cost–effective and environmentally friendly but generally inefficient for non–biodegradable or toxic contaminants such as antibiotics and pesticides.

In this landscape, adsorption (Fig. 5f) has emerged as a particularly promising approach. It combines high efficiency with operational simplicity

and relatively low costs, making it adaptable to diverse settings, from large industrial WWTPs to small–scale portable filters [25].

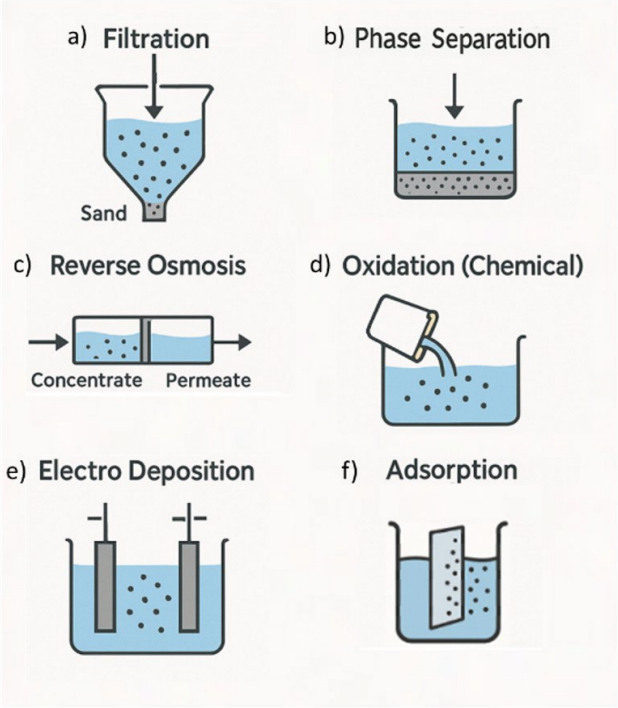

***Figure 5**: Water remediation technologies: filtration (a), phase separation (b), reverse osmosis (c), chemical oxidation (d), electro deposition (e) and adsorption (f)*

1.3.1 Adsorption

Adsorption is a process in which molecules present in a liquid phase (the adsorbates) adhere to the surface of a solid material (the adsorbent) (Fig. 6) [10].

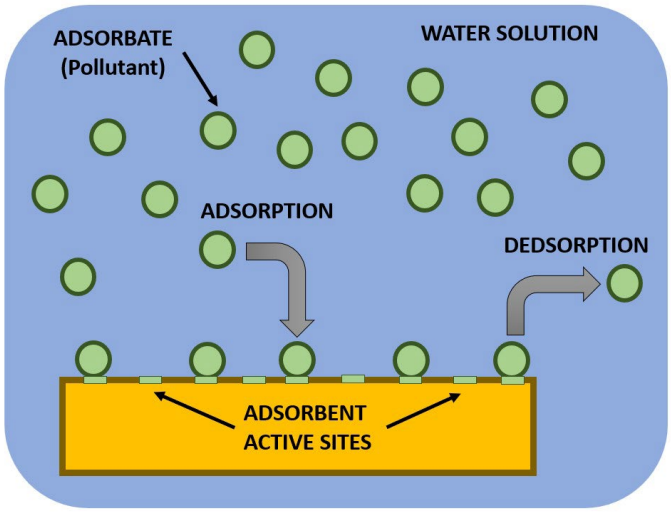

***Figure 6**: Adsorption and desorption mechanism*

During adsorption, the driving forces include electrostatic interactions, ion exchange, hydrogen bonding, Van der Waals forces, and hydrophobic effects [26].

The advantages of adsorption for water treatment are numerous [26]:

- **Cost–effectiveness:** Adsorbent materials can often be derived from natural or waste sources, reducing production costs.
- **Versatility:** A single adsorbent can capture different types of contaminants, including metals, pharmaceuticals, and pesticides.
- **Scalability:** Adsorption units can be implemented in household devices or industrial–scale reactors.
- **Reusability:** Adsorbents can frequently be regenerated by desorption of the pollutants, contributing to a circular economy.
- **Low energy demand:** Unlike reverse osmosis or oxidation, adsorption typically requires no external energy source beyond mixing.

For these reasons, adsorption has been recognized as one of the most promising technologies for tackling emerging contaminants. Its performance, however, depends critically on the choice of material, as the surface chemistry, porosity, and functional groups determine the adsorption efficiency.

1.3.2 Common Adsorbents

Over the years, a wide range of adsorbents has been developed for water remediation, and some of these are listed in Table 2. Traditional options like activated carbon have been used since the early 1900s, alongside carbon–based materials such as graphene oxide and biochar, silica–based adsorbents, inorganic materials such as zeolites and clays, and organic substances such as polymers and polysaccharides. Although the exact mechanisms by which some organic materials remove pollutants are still under investigation, they likely involve ion exchange and other surface interactions.

__Table 2__: Adsorbents used for different pollutants (list restricted to papers from 2010)

Adsorbent Type	Contaminant	Ref
Activated carbon	Dyes, heavy metals	[27][28][29]
Graphene oxide	Pharmaceuticals, Organic compounds, metal ions	[30][31]
Silica–based materials	inorganic and organic pollutants	[32][33][34]
Zeolites	Petroleum, fluoride, nitrate, dyes, heavy metals, cesium	[35][36][37]
Biochar	Heavy metals	[38][39][40]
GO–biochar	Persulfate, metal ions, dyes, pharmaceuticals	[41]

Mineral Clays (Montmorillonite, Bentonite, Kaolinite, clinoptilolite, etc.)	Nuclear waste, pharmaceuticals	[42][43]
Sugar beet pulp	Nitrites and nitrates	[44]
Organic polymer resin	Cationic and anionic surfactants, perfluoroalkyl acids	[45]
Poly(saccharide)–based materials	heavy metals (arsenic)	[46][47]
Poly (vinyl alcohol) nanofibers + Iron NPs	Arsenic	[48][49]
Poly (vinyl alcohol) nanofibers + L–cysteine	Arsenic	[50]
Polybutylene adipate terephthalate (PBAT) nanofibrous	Dyes, pharmaceuticals	[51]
Biohybrid membrane of polymeric nanofibers and free–living bacteria	Chromium (Cr–VI)	[52]

2 New Materials as Advanced Adsorbents

Several new classes of adsorbent materials have been explored and are under development for water remediation:

- **Biopolymers (pectin, alginate, chitosan, cellulose):** Renewable, biodegradable, and non–toxic polymers that can be chemically modified to improve adsorption [53]. Their main advantages are sustainability and the presence of reactive functional groups (–OH, –COOH, $–NH_2$) that can bind contaminants [54]. However, many biopolymers are water–soluble and must be crosslinked to achieve structural stability in aqueous environments [55].
- **Metal–organic frameworks (MOFs):** Crystalline porous materials formed by metal ions and organic linkers [56]. MOFs offer extremely high surface areas and adjustable functionality, making them excellent candidates for capturing pharmaceuticals and pesticides [56]. However, their practical use is limited by issues such as water stability and the handling of fine powders [56].
- **Poly(vinyl alcohol) (PVA):** A synthetic polymer that is water–soluble, non–toxic, and biocompatible, with excellent mechanical and chemical stability [57]. PVA is easily processed into membranes or nanofibers by electrospinning, offering high surface to volume ratios that are advantageous for adsorption. Since PVA dissolves in water, it must be crosslinked to ensure long–term stability; citric acid provides a green and effective crosslinker, forming ester bonds with PVA hydroxyl groups and introducing

additional carboxylate sites that enhance adsorption capacity [58][59].

The growing relevance and interest of these materials is evident from the increasing number of publications indexed in Clarivate Analytics Web of Science under the keywords “pectin and removal”, “MOF and removal and “PVA and removal” (Fig. 7)

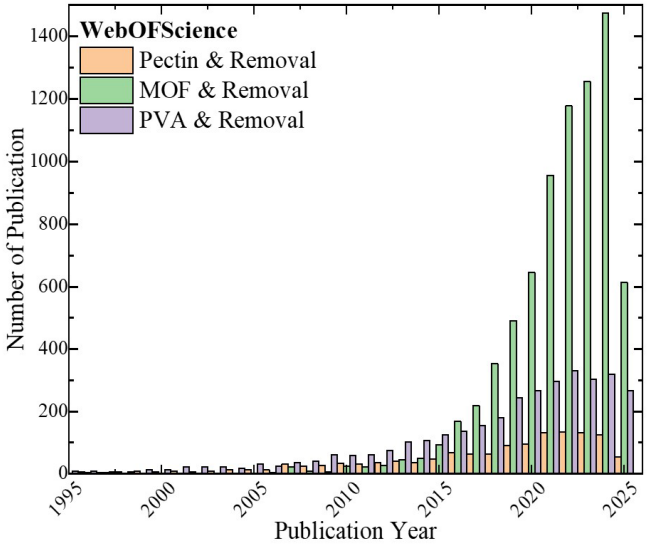

***Figure 7**: Publications in pectin, MOF and PVA water remediation for 1995–2025. Data are the number of hits of a search for publication titles containing the keywords “pectin” or “MOF” or “PVA”and “removal” using the Web of Science.*

In this thesis, three material platforms were selected to address the challenges of adsorption:

1. **Pectin (PE):** a plant–derived polysaccharide rich in carboxyl and hydroxyl groups, which can be crosslinked with calcium or europium to form stable gels and films.
2. **Basolite F300® (Fe–BTC):** a commercially available MOF with high surface area and open metal sites, suitable for pesticide and antibiotic adsorption.
3. **Poly(vinyl alcohol) (PVA):** a synthetic, non–toxic polymer that can be processed by electrospinning into nanofibers and crosslinked with citric acid to form water–stable mats.

Given the urgent need for effective water purification strategies, this thesis aims to create hybrid adsorbents that are efficient, reusable, and environmentally friendly combining the sustainability of biopolymers with the porosity and reactivity of MOFs.

2.1 Pectin

Naturally occurring polysaccharides are biopolymers that have recently attracted significant attention as sustainable alternatives to synthetic polymers derived from petroleum. Pectin is a complex hetero–polysaccharide naturally present in the primary cell walls and middle lamella of higher plants (Fig. 8) [54]. It plays a structural role by providing rigidity and facilitating cell adhesion.

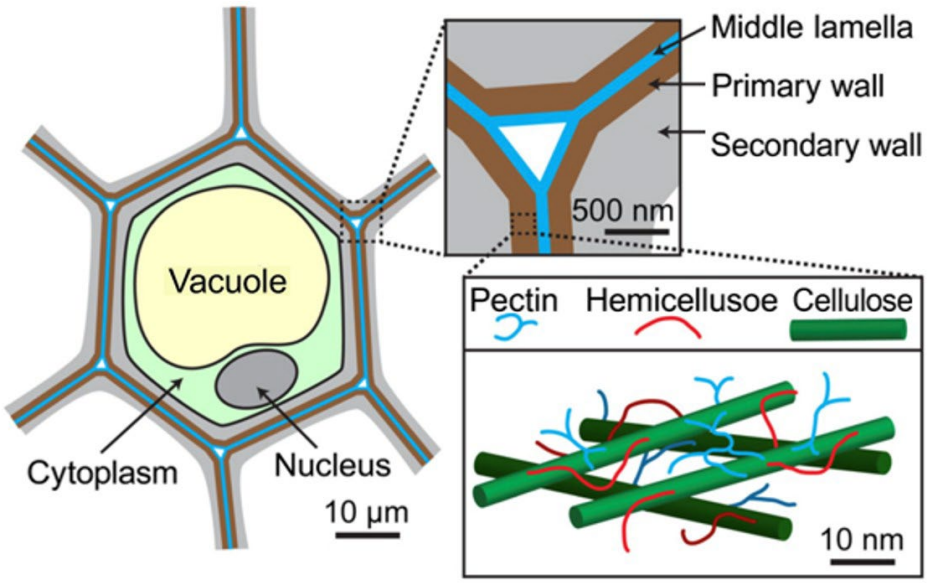

***Figure 8**: Schematic of plant cell showing arrangement of cell walls; pectin is abundant in the primary walls synthesized by growing cells (brown) and the middle lamella that adheres adjacent cells (blue), but is also present in lower amounts in secondary walls produced after the cessation of growth (gray). Inset at lower right is a simplified model of the primary cell wall showing one possible arrangement of cellulose microfibrils (green), hemicellulose (red), and pectin (blue). Picture readapted from [60].*

The source of pectin, meaning the plant from which it is extracted, significantly influences its galacturonic acid content and degree of methyl–esterification (DM), which in turn affects its gelling properties [61]. Common sources include apple pomace, oranges, and citrus peels, with citrus peels typically yielding a higher galacturonic acid content [61].

From a technological perspective, pectin is a renewable, biodegradable, and biocompatible polymer, widely used in the food, pharmaceutical, and biomedical industries [61]. Its abundance, low cost, and functional versatility also make it an attractive candidate for water remediation applications [54], [62].

2.1.1 Structure

Pectin properties and characteristics depend on its botanical origin and extraction process [61]. Pectin is mainly composed of a linear chain of galacturonic acid also, it contains other saccharides such as rhamnose, arabinose, and galactose, as well as other neutral sugars, which contribute to its branched and heterogeneous structure (Fig. 9) [61].

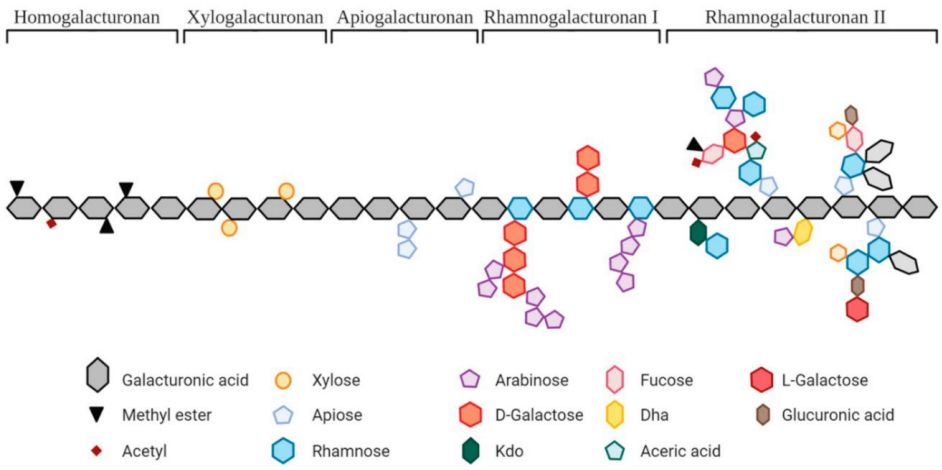

***Figure 9**: Schematic and general representation of pectin structure. Pectin molecule can contain different structural characteristics, including homogalacturonan, xylogalacturonan, apiogalacturonan, rhamnogalacturonan I, and rhamnogalacturonan II. Picture taken from [63].*

Chemically, the pectin backbone is primarily composed of α(1,4) linked D–galacturonic acid (GalA) residues partially esterified [64], which are arranged in three main regions: homogalacturonan (HG), rhamnogalacturonan I (RG–I), and rhamnogalacturonan II (RG–II).

The GalA residues at the C6 (carbon 6) position can be either methyl–esterified ($–COOCH_3$) or deprotonated carboxyl groups ($–COO^-$). Although acetylation at the O–2 and/or O–3 positions of GalA residues can also occur, it is less common. Carboxyl groups ($–COO^-$) are hydrophilic and capable of coordinating with metal ions, whereas methyl–esterified groups ($–COOCH_3$) are hydrophobic. Consequently, pectin with a lower DM (containing more $–COO^-$ groups) exhibits a higher adsorption efficiency for metal ions compared to its highly esterified counterpart.

2.1.2 Degree of methyl–esterification

The degree of methyl–esterification (DM), defined as the ratio of methyl–esterified residues, plays a crucial role in determining pectin's properties and its gelling mechanism [61]. Pectins are classified into two groups based on DM (Fig. 10): high methoxyl pectins (HMP), in which more than 50% of GalA

residues are esterified, and low methoxyl pectins (LMP), with less than 50% esterification [61].

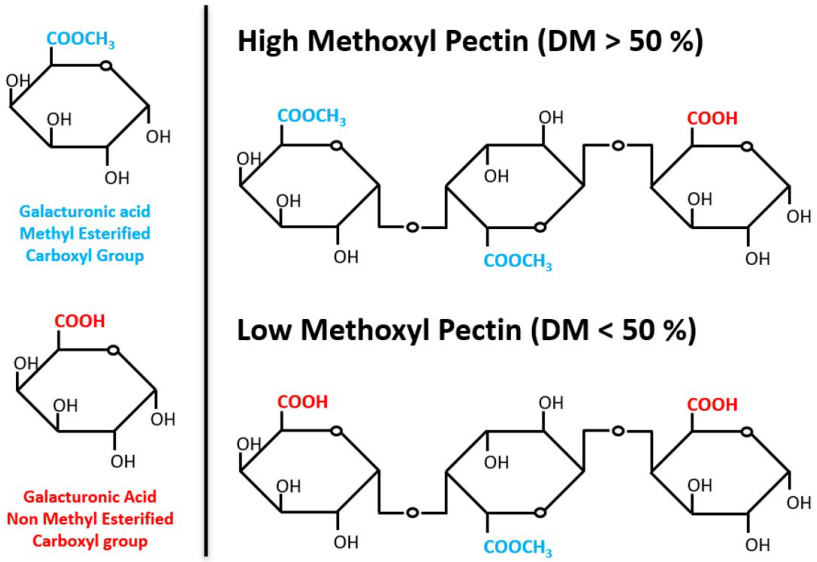

***Figure 10**: High and ow methoxyl pectin backbones.*

LMP has many free carboxyl groups, which serve as active sites for binding pollutants, such as small organic molecules and heavy metals, from contaminated water. Despite their differences in DM, pectin is inherently water–soluble, which limits its effectiveness as an adsorbent in aqueous environments. To overcome this limitation, pectin can be rendered insoluble through crosslinking with various agents, as discussed in the following sections [62,64].

In this thesis project, LMP was employed to fabricate thin films used as membranes for water purification, whose operating principle is adsorption.

2.1.3 Crosslinking

Since pectin is water–soluble, it must be to insolubilized to function effectively as an adsorbent for pollutant removal. Crosslinking LMP with cations can be achieved using various methods, each influencing the final properties of the material [65]. Two primary approaches (external and internal crosslinking) are commonly used [61]. Ionic crosslinking is the most widely employed method, as it not only stabilizes pectin but also offers the advantage of reversible adsorption, thereby enabling contaminant release (and sometimes recovery) along with adsorbent regeneration [64]. Both strategies can be adapted to incorporate other metal cations beyond calcium. For example, europium (Eu^{3+}) has been successfully employed to crosslink LMP, enhancing the material's adsorption capacity for pharmaceuticals by promoting strong metal–antibiotic complexation trough β–diketone interactions [62].

2.1.3.1 Internal Crosslinking

This method involves preparing a pectin solution and mixing it with a calcium solution under controlled pH conditions. The gradual release of Ca^{2+} ions into the pectin solution results in more uniform ion diffusion throughout the material. Although this process is more time–dependent compared to external crosslinking, it ensures a homogeneous distribution of Ca^{2+} within the pectin matrix [66].

2.1.3.2 External Crosslinking

In the external crosslinking method, a pectin film is first prepared and then immersed in a calcium (Ca^{2+}) solution. The Ca^{2+} ions diffuse into the pectin, initiating crosslinking primarily at the film's surface. This approach is relatively rapid and results in a higher surface Ca^{2+} concentration at the surface; however, the limited diffusion of Ca^{2+} into the bulk material may produce a gradient in crosslinking density [67].

2.1.3.3 "Egg–box" Model

The ion–induced gelation of pectin is described by the "egg–box" model, initially proposed for alginates but widely applied to pectin [68]. Table 3 summarizes the milestones in developing the structural models of pectin when cross–linked with metal cations.

Table 3: *Historical development of the binding mechanisms between divalent cations and both poly(galacturonic) chains or pectin*

Year	Event	Ref
1973	First postulation of egg–box model for pectin	[69]
1978	Dimers formation	[70]
1981	Junction zones model	[71]
1982	Junction zone distribution	[72]
1987	Divalent cations coordination	[73]
1991	First book on pectin chemistry and technology	[74]
2001	Shifted egg box model for pectin gels	[75]
2007	Multi–step binding ions behavior	[76] [77]
2008	Alginate and pectin comparison	[78]
2010	Structural reorganization of pectin and alginate after calcium binding	[68]
2013	Egg–box model with semi–flexible chains	[67]
2015 2016 2018	Cross–link differences between different multivalent cations	[65] [79] [80]
2020	Different ways of pectin dimers aggregation	[81]
2025	Interaction with water	[64]

In this model, divalent or trivalent cations fit into cavities formed by the alignment of galacturonic acid chains, bridging two adjacent pectin molecules through coulombic interaction between two free carboxyl groups (Fig. 11). The carboxyl groups act as “active sites” that coordinate the cation, stabilizing the polymer network [64].

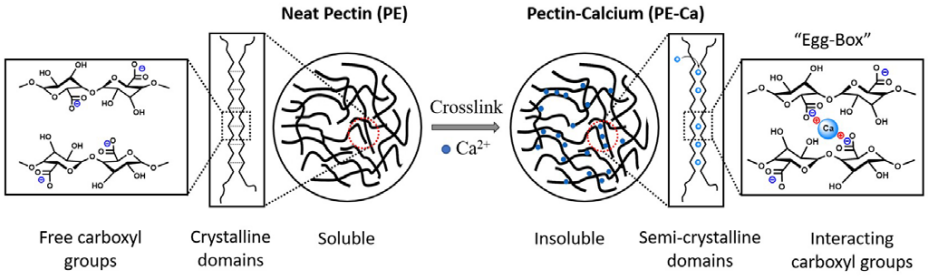

***Figure 11**: Schematic representation of calcium cross–linking in pectin.*

The stochiometric ratio R, defined as R = $[Ca^{2+}]/[GalA]$, which represents the concentration of Ca^{2+} ions relative to the galacturonic acid (GalA) content in pectin, plays a critical role in determining the resulting structure of the crosslinked material (Fig. 12) [67]:

- For R < 0.20, pectin tends to form monocomplex and point–like crosslinking.
- For $0.20 \leq R \leq 0.50$, crosslinked pectin forms "egg–box" dimers. In this structure, parallel chains of GalA align around a central Ca^{2+} ions, forming stable, ordered arrangement.
- For R > 0.50, pectin tends to form multimers, characterized by lateral aggregation of the chains. This results in a more complex and less ordered structure.

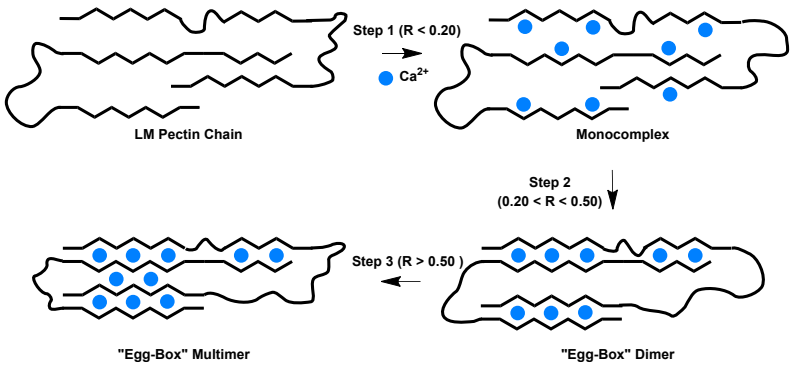

***Figure 12**: “Egg–box” model of Ca^{2+} binding to pectin in monocomplex, dimers, and multimers is shown schematically. R stands for the Ca^{2+} to the guluronate residue feeding ratio.*

In both external and internal approaches, crosslinking disrupts the periodicity of hydrogen bonds between pectin chains, leading to the amorphization of neat pectin [62,64,68]. This structural change enhances the

material's mechanical strength and thermal stability, making it more suitable for a broader range of applications.

Overall, the choice of crosslinking method and the Ca^{2+}/GalA ratio significantly influence the structural and functional properties of pectin, enabling it to be tailored for specific applications in water remediation, food packaging, and biomedical applications.

In this thesis project, the external crosslinking method was employed to insolubilize the LMP, its structural and adsorption properties as well as its interaction with water, were studied.

2.2 Basolite F300®

Metal–organic frameworks (MOFs) are a class of crystalline or semi–crystalline porous materials composed of metal centers coordinated to organic ligands. Their modular architecture, extremely high surface areas, and tuneable pore chemistry make them attractive for applications in gas storage, catalysis, sensing, and environmental remediation [82]. Basolite F300®, also known as Fe–BTC (iron(III)–benzene–1,3,5–tricarboxylate), is a commercially available MOF that has been widely studied due to its relatively low cost, high porosity, and water stability compared to many other MOFs [83]. Unlike highly crystalline analogues such as MIL–100(Fe) or MIL–101(Fe), Fe–BTC is poorly crystalline or amorphous. Still, it retains a porous framework composed of interconnected cages and channels exhibiting higher water stability [84].

2.2.1 Structure

The Fe–BTC framework is built from Fe^{3+} ions coordinated to benzene–1,3,5–tricarboxylate (BTC) ligands, forming iron–oxo clusters connected by carboxylate bridges [85]. These clusters form a three–dimensional network of mesopores and micropores, providing a large internal surface area (typically above 1300 m^2/g) and pore diameters around of 2–3 nm (Fig. 13) [85].

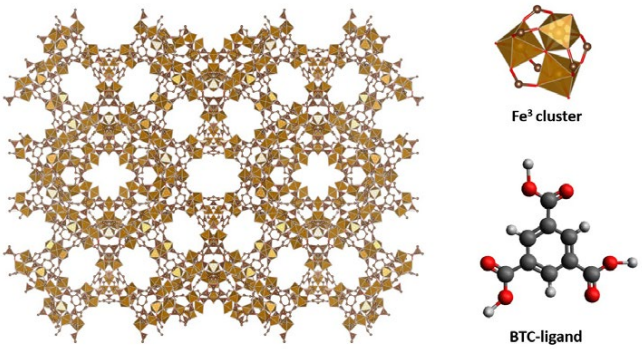

***Figure 13**: Schematic representation of Basolite F300® (Fe–BTC) structure.*

Key structural features of Fe–BTC include:

- **High porosity:** Nitrogen adsorption measurements report Brunauer–Emmett–Teller (BET) surface areas above 1000 m^2/g.
- **Mesoporous character:** Pore diameters in the 2.0–3.0 nm range, suitable for the diffusion of small organic molecules such as tetracycline [86], and paraquat [87].
- **Low crystallinity:** Broad X–ray diffraction peaks indicate a disordered structure, yet the MOF maintains functional porosity [85].
- **Open Fe^{3+} sites:** The presence of coordinatively unsaturated Fe^{3+} centres enhances adsorption capacity through electrostatic interactions and coordination with electron–donating functional groups in pollutants [85].

One of the critical challenges for MOFs in aqueous environments is framework stability. Many MOFs degrade upon exposure to water, releasing metal ions and ligands. Fe–BTC, however, demonstrates relatively high water stability due to strong coordination between Fe^{3+} and BTC linkers [88]. This stability, combined with its porous network, makes Fe–BTC a promising material for water remediation. However, using Fe–BTC in powder form poses several practical limitations, including particle aggregation, difficulties in recovery, and risks of secondary contamination by fine particles. To overcome these drawbacks, immobilization strategies have been developed.

In this thesis, Fe–BTC was incorporated into calcium–crosslinked low–methoxyl pectin (PE–Ca) matrices in the form of films and foams [89]. This approach improves material handling, prevents particle release, and enhances adsorption performance by combining the porosity of Fe–BTC with the sustainability of pectin.

2.3 Poly(vinyl alcohol)

Poly(vinyl alcohol) (PVA) is a synthetic, water–soluble polymer widely used in food packaging, biomedical devices, membranes, and water treatment applications [7], [90], [57]. It is obtained by the hydrolysis of poly(vinyl acetate), which replaces acetate groups with hydroxyl groups, yielding to a hydrophilic polymer chain (Fig. 14) [57].

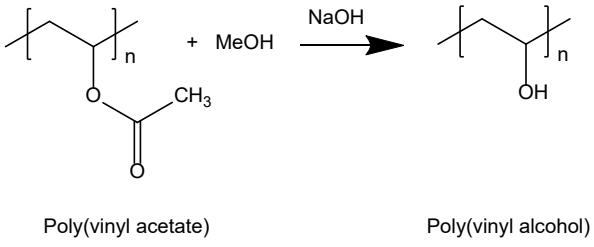

***Figure 14**: Poly(vinyl acetate) hydrolysis.*

PVA is considered environmentally friendly because it is non–toxic, biodegradable under certain conditions, and inexpensive to produce [57].

Its abundance of hydroxyl groups provides excellent chemical versatility, allowing modifications such as crosslinking, blending, and doping with inorganic or organic additives [57]. These features make PVA an excellent platform for the fabrication of functional nanofibers and hybrid adsorbents [91], [92].

2.3.1 Structure and Properties

The repeating unit of PVA consists of a vinyl backbone bearing hydroxyl (–OH) groups, which can engage in hydrogen bonding and chemical reactions [92]. The degree of hydrolysis determines the number of hydroxyl groups present:

- **Partially hydrolyzed PVA:** contains residual acetate groups, leading to higher solubility and flexibility [57].
- **Fully hydrolyzed PVA:** has almost all acetate groups removed, resulting in higher crystallinity, lower solubility, and increased hydrogen bonding capacity [57].

Key properties of PVA relevant to water remediation include:

- **Hydrophilicity and water solubility:** Facilitate swelling and diffusion of aqueous pollutants into the polymer matrix.
- **Biocompatibility:** Safe for applications where environmental or biological contact occurs.
- **Mechanical stability:** Can be processed into membranes and fibers with robust structures.
- **Processability:** Easily electrospun into nanofibers with large surface areas and interconnected porosity.

Electrospun PVA nanofibers are particularly attractive for adsorption, as their high surface–to–volume ratio ensures good contact between the polymer and contaminated water.

In this thesis, fully hydrolyzed PVA was used to fabricate nanofibers via electrospinning technique.

2.3.2 Electrospinning

Electrospinning turns a liquid polymer solution into solid nano–fibers by using a strong electric field [93]. At the tip of a metal needle the liquid forms a small droplet. Surface tension tries to keep this droplet round, while the applied voltage pulls on the liquid because charges in the solution are attracted to the

grounded collector. As the voltage is increased, the electric pull grows until it overcomes surface tension in a very small region at the droplet's tip [93]. The droplet then sharpens into a characteristic Taylor cone and a very fine liquid jet is ejected from its apex. Meanwhile, solvent evaporates rapidly along the flight, the polymer concentration rises, the jet solidifies, and a continuous fiber is deposited on the collector (Fig. 15).

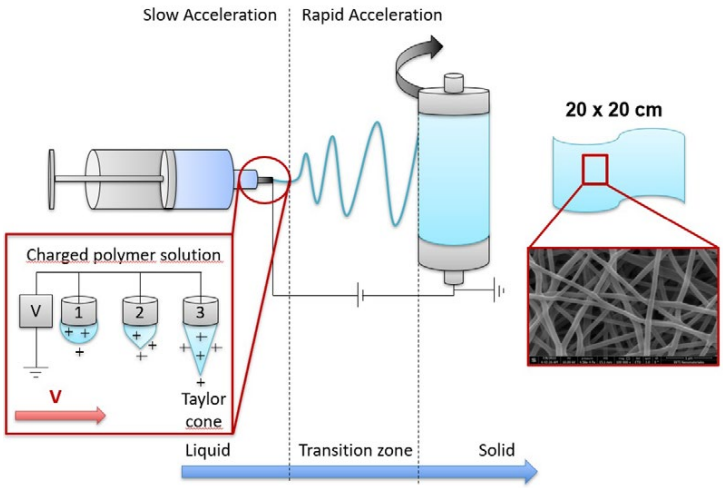

***Figure 15**: Schematic representation of the electrospinning mats fabrication.*

The tip–collector distance determines the time available for stretching and solvent evaporation. Solution properties, such as viscosity/viscoelasticity, conductivity, surface tension, and, solvent volatility govern jet stability and the final fiber diameter. Finally, environmental conditions, especially relative humidity and temperature, influence evaporation and charge leakage to air, which explains why nominally identical settings can give different fiber morphologies on humid vs. dry days.

In summary, electrospinning works because a strong electric field organizes the meniscus into a Taylor cone and pulls a charged jet that is stretched, thinned, and solidified into nanofibers.

2.3.3 Insolubilization

A significant limitation of PVA is its water solubility, which restricts its long–term application in aqueous environments. To overcome this, PVA must be rendered insoluble through crosslinking. The most common methods for insolubilizing PVA are chemical methods [94], physical methods [95], or blending with other insoluble polymers [57]. Physical methods promote chemical bonding between the hydroxyl groups of PVA molecules [96], which is typically activated by heating, leading to PVA dehydration [97]. Among all

the possible chemical agents [98], citric acid (CA) has gained attention as a green, non–toxic, and low–cost approach [99].

Crosslinking occurs via poly–esterification reactions between the hydroxyl groups of PVA and the carboxyl groups of citric acid under heating (typically 140–200 °C) (Fig. 14) [100].

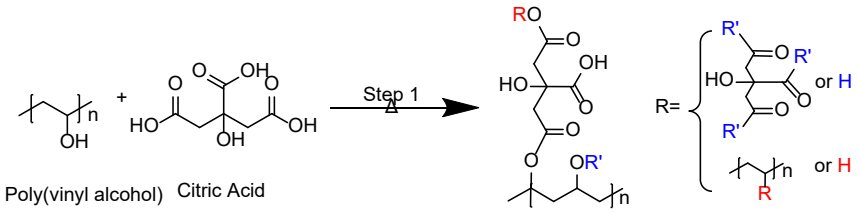

Figure 16: Reaction scheme of PVA poly–esterification with citric acid.

This process produces ester bonds that link PVA chains, reducing their solubility while increasing their mechanical stability and resistance to swelling [100]. In addition, citric acid introduces residual free carboxyl groups (–COOH/–COO^-) into the material, which act as additional active sites for adsorption of cationic spaces.

The combination of PVA electrospinning and citric acid crosslinking produces nanofibrous mats that are:

- Water–insoluble and mechanically stable.
- Rich in reactive functional groups for pollutant binding.
- Capable of incorporating additional active sites, such as europium ions (Eu^{3+}) to enhance the adsorption performance.

In this thesis, PVA was used as a versatile polymeric matrix for the fabrication of Eu–doped and Eu–incorporated nanofiber mats. Europium plays a dual role by contributing additional adsorption sites and forming stable complexes with antibiotics containing β–diketone groups, such as tetracycline and ciprofloxacin. The synergy among PVA, citric acid, and europium yields to highly efficient, reusable adsorbents for pharmaceutical removal.

3 Experimental techniques and methods

The experimental work in this thesis combined structural, thermal, spectroscopic, and adsorption analyses with material processing and chemical characterization to develop and evaluate new bio–based and hybrid adsorbents. The methodology was designed to provide both a fundamental understanding

of polymer and hybrid structures, and a functional evaluation of their adsorption performance toward representative emerging contaminants. By integrating these methodologies, this thesis combined material processing techniques (sonication, electrospinning, freeze–drying, crosslinking) with advanced analytical and characterization methods (DSC, BDS, ICP–AES, BET, DLS, SEM–EDX, FTIR, UV–Vis, gas chromatography) to achieve a multiscale characterization of bio–based and hybrid adsorbents. This comprehensive approach enabled not only the evaluation of adsorption performance but also a mechanistic understanding of how polymer structure, porosity, hydration, and crosslinking influence pollutant removal.

3.1 Sample Preparation and Conditioning

Sample preparation and conditioning were a critical first steps to ensure reproducibility. Pectin solutions were carefully dissolved and homogenized under controlled conditions, often requiring temperature control and prolonged stirring. To disperse MOF powders, a tip sonicator was used to break aggregates, and polyvinylpyrrolidone (PVP) was used employed as a stabilizer when necessary. For the production of porous foams, pectin–MOF solutions were frozen and lyophilized, ensuring high porosity and structural integrity after crosslinking. Electrospinning was employed to fabricate PVA nanofiber mats, enabling precise control over fiber diameter and morphology. Samples were dried under vacuum for one week and carefully weighed before hydration. Sample hydration was performed in humidity–controlled environments inside desiccators, with the specific relative humidity level (RH) controlled using different saturated aqueous salt solutions. Pectin and MOF samples were conditioned at 25 ºC until equilibrium.

3.2 Structural Characterization

To determine the composition of pectin, gas chromatography (GC) was employed for the analysis of residual sugars, while viscosimetry and densimetry provided information to extrapolate pectin's molecular weight. Structural characterization was primarily performed using X–ray diffraction (XRD), scanning electron microscopy (SEM), and energy dispersive X–ray spectroscopy (EDX).

XRD provided information on crystallinity and interchain distances in hydrated pectin, as well as confirmation of the structural integrity of Basolite F300® (Fe–BTC) within composite matrices. The interchain distances (d, nm) was calculated applying the Braggs law:

$$n\lambda = 2d \sin\theta \quad (1)$$

where n is the diffraction order, λ [Å] is the X–ray wavelength, and θ is the Bragg angle.

SEM revealed the morphology of pectin films, foams, and PVA nanofibers, while EDX enabled elemental mapping to verify the homogeneous dispersion of calcium, europium, and iron in the composites.

Dynamic light scattering (DLS) was also employed to evaluate the dispersion of MOF particles in aqueous suspensions, quantifying particle size distributions and aggregation states. Textural analysis of porous materials was achieved through nitrogen adsorption isotherms at 77 K.

The Brunauer–Emmett–Teller (BET) method was used to calculate specific surface areas, while pore size distributions were determined using density functional theory (DFT) models. These measurements were crucial for assessing the porosity of Fe–BTC.

3.3 Spectroscopic Analyses

Spectroscopic analyses included Fourier–transform infrared spectroscopy (FT–IR), and ultraviolet–visible spectroscopy (UV–Vis). FT–IR enabled the identification of functional groups and bonding interactions, such as esterification in PVA–citric acid crosslinking and europium coordination PVA systems.

UV–Vis spectroscopy was used to monitor concentration of the organic pollutants (such as tetracycline, ciprofloxacin, and paraquat) in solution during adsorption experiments.

3.4 Adsorption Experiments

Elemental and chemical analysis was complemented with inductively coupled plasma–atomic emission spectrometry (ICP–AES), which allowed precise quantification of metal ions (Zn^{2+}, Ca^{2+}, Eu^{3+}) before and after adsorption. This technique was essential for evaluating adsorption efficiency and ion–exchange processes in pectin–MOF and PVA–based composites.

Adsorption experiments were performed in batch mode with model contaminants: zinc, tetracycline, ciprofloxacin, and paraquat. Experimental variables including pH, initial concentration, contact time, and adsorbent dose, were systematically varied.

Adsorption kinetics were analyzed with pseudo–first–order (PFO) and pseudo–second–order models (PSO). PFO kinetics assumes that the rate of adsorption depends linearly on how many free sites are still available on the adsorbent surface and it usually describes systems where physical adsorption

(weak interactions) is more important. PSO kinetics assumes that the rate of adsorption depends on the square of the number of free sites, so it is more sensitive to how many sites are still empty and it is often associated with chemisorption, where stronger interactions (e.g., bond formation) control the process.

Equilibrium data were fitted to Langmuir, Redlich–Peterson, and Sip isotherms. Langmuir isotherm assumes a uniform surface with a fixed number of identical sites and only one molecule can occupy each site (monolayer adsorption). There are no interactions between adsorbed molecules, and once a site is filled, no further adsorption occurs there. Redlich–Peterson isotherm is a three–parameter hybrid model between Langmuir and Freundlich. It is empirical and very flexible, often used when experimental data do not fit well to simpler isotherms, especially over a wide concentration range. Sips isotherm combines model that mixes Langmuir and Freundlich behaviors. It is used for heterogeneous surfaces and can describe both low and high concentration regions more flexibly than Langmuir alone.

Finally, reusability was tested through multiple adsorption–desorption cycles, typically using acetic acid as a mild eluent.

3.5 Thermal Characterizations

Thermal characterization was carried out using differential scanning calorimetry (DSC) and thermogravimetric analysis (TGA). These experiments clarified the thermal stability and structural evolution of both pectin and MOF–based materials.

TGA was used to monitor water loss, decomposition stages, and overall thermal stability, providing complementary insights into material composition.

DSC was used not only to identify glass transitions but also to apply physical aging and step–response protocols to investigate water dynamics and relaxation processes under confinement.

3.5.1 Physical Aging

Aging experiments were performed to confirm the presence of T_g in the studied samples. Physical aging in amorphous materials is the slow structural relaxation that occurs when a glass is stored below its glass transition temperature (T_g).

Crystalline and amorphous solids differ in structure and mechanical behavior. In an ideal crystal, atomic positions are periodically arranged, giving long–range order. Solids lacking this periodicity are amorphous. Almost any liquid can be vitrified into an amorphous solid if cooled fast enough to avoid

nucleation. Under such supercooling, the liquid is brought below its freezing point without crystallizing; viscosity rises sharply and the supercooled liquid transforms into a non–equilibrium glass [101]. As illustrated in Fig. 17, for a given cooling rate the metastable supercooled state cannot be maintained and the system falls into a glassy, non–equilibrium state–a "frozen" liquid on experimental timescales.

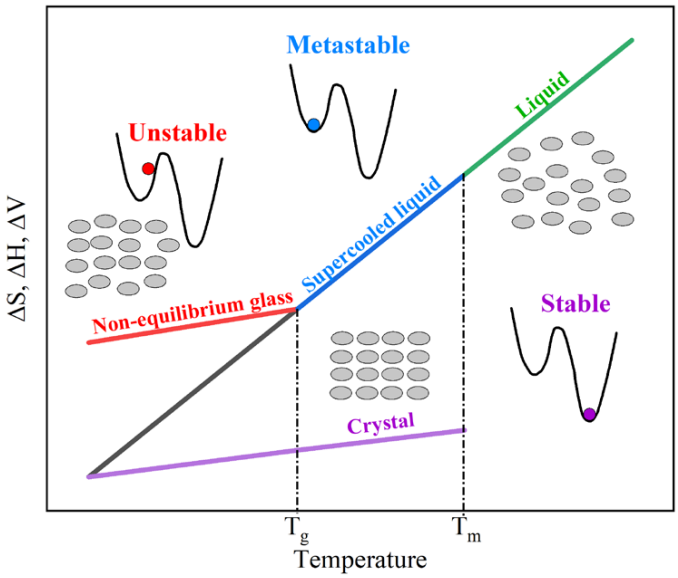

***Figure 17**: Schematic representation of the temperature dependence of thermodynamic proper–ties (entropy, enthalpy, volume) in glass–forming systems at constant pressure. The indicated temperatures are defined as: the melting temperature (T_m) and the glass transition temperature (T_g). The stability plots of the thermodynamic potential are shown for the cyrstal (stable), supercooled liquid (metastable) and the glass state (unstable).*

The temperature protocols used in these experiments are shown in Fig. 18a. The sample are rapidly cooled and then heated to a specific aging temperature (T_a), where they held for a specified time (t_a) to allow the molecules to relax toward lower energy states. Subsequently, the aged samples were cooled and reheated at a heating.

After quenching, the material is out of equilibrium; its excess free volume and configurational enthalpy decrease as the structure densifies toward the equilibrium supercooled liquid at that temperature. This leads to reductions in specific volume and enthalpy (seen as an endothermic enthalpy–recovery peak upon reheating through T_g by DSC) and to time–dependent property changes [101].

From the theory of the physical aging, a non–equilibrium glass annealed below and close to its T_g induce a reduction in the glass enthalpy trying to reach the equilibrium liquid state (Fig. 18b) [101]. As a consequence, the subsequent calorimetric heating scan exhibits a typical endothermic overshoot in proximity to the T_g step. Figure 18c show the example for xylitol which is a typical glass–former.

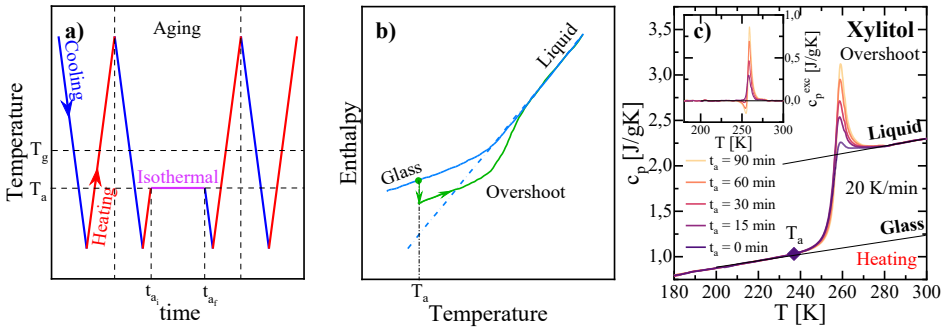

***Figure 18**: (a) Schematic of temperature protocols used for the aging experiments. (b) Enthalpy relaxation during physical aging. (c) Comparison between aged at different times and unaged samples for Xylitol, aged at 238 K for 15, 30, 60, and 90 min). Inset: Excess specific heat capacity ($c_{P\,exc}$) of the aged samples relative to the unaged reference, showing the endothermic overshoot characteristic of physical aging near the glass transition region.*

3.5.2 Step Response

A step response protocol was performed to assess the spontaneous thermal fluctuations of confined water in terms of the frequency−dependent complex specific heat. The temperature protocol comprised a repetition of temperature jumps ΔT, at a nominal heating rate β, followed by isotherms for a duration of t (Fig. 19). The step was looped, spanning all the studied temperature [102].

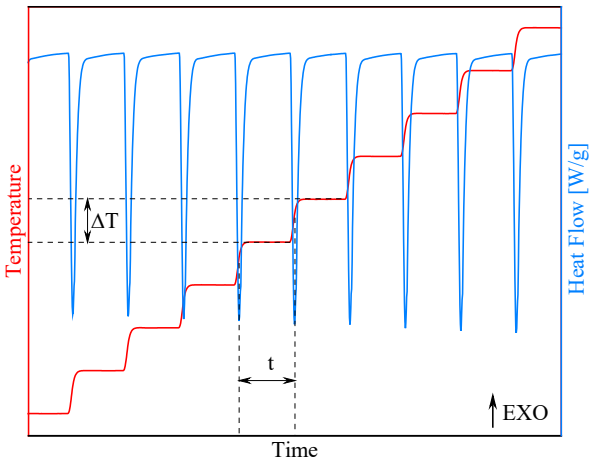

***Figure 19**: Schematic of temperature protocols used for the step response experiments.*

The period t_p required to perform a jump/isotherm step defines the base angular frequency of perturbation ω_0. The angular frequency ω_o, can be expressed as:

$$\omega_0 = \frac{2}{t_P} = \frac{2\pi}{\frac{\Delta T}{\beta} + t} \tag{2}$$

where the total period, t_P, includes the initial down–jump and the duration of the isotherm.

The frequency–dependent complex specific heat $c_p^*(\omega)$ was calculated for ω_0 and high–order harmonics ($\omega = k\omega_0$, where k = 1, 2, …) by using a discrete fast Fourier transform for each period of perturbation in the form of

$$c_p^*(\omega) = c_P'(\omega) - \mathrm{i}\, c_P''(\omega) = \frac{\sum_{t=0}^{t_P} HF(t)\, e^{-i\omega t}\Delta t}{\sum_{t=0}^{t_P} q_h(t)\, e^{-i\omega t}\Delta t} \quad (3)$$

where $HF(t)$ and q_h (t) are the instantaneous heat flow and heating rate, respectively. Finally, the frequency–dependent glass transition temperature (T_g), which is assessed in the linear perturbation regime, is calculated at the inflection point of the reversing specific heat step $c_p^{rev}(\omega)$, i.e., the modulus of c_p^* (ω).

3.6 Broadband Dielectric Spectroscopy

Broadband Dielectric Spectroscopy (BDS) measures how a material responds to an external electric field over a wide range of frequencies (from 10^{-6} to 10^{12} Hz), giving the complex permittivity $\varepsilon^*(\omega) = \varepsilon'(\omega) - i\varepsilon''(\omega)$ [103]. This complex quantity describes how much energy is stored (real part (ε')) and how much is lost as heat (imaginary part (ε'')) due to molecular motions such as dipole reorientation or ionic transport. To describe these relaxation processes, the Havriliak–Negami (HN) equation is often used:

$$\varepsilon^*(\omega) = \varepsilon_\infty + \frac{\Delta\varepsilon}{[1+(i\omega\tau)^\alpha]^\beta} \quad (4)$$

where ε_∞ is the permittivity at very high frequency, $\Delta\varepsilon$ is the dielectric strength, τ is a characteristic relaxation time, and ω is the angular frequency. The shape parameters α ($0 < \alpha \leq 1$) and β ($0 < \beta \leq 1$) control the broadening and asymmetry of the relaxation peak, respectively, and thus reflect the distribution of relaxation times in complex systems such as polymers or glass–forming liquids. When $\alpha = \beta = 1$, the HN equation reduces to the simple Debye model with a single relaxation time; intermediate cases (e.g., $\alpha = 1$ or $\beta = 1$) correspond to Cole–Davidson and Cole–Cole type behaviors respectively [103].

BDS was used to study molecular dynamics, particularly the relaxation processes of water confined in pectin nanochannels and MOF pores.

3.6.1 Arrhenius Plot

Another critical characteristic of supercooled liquids and the glass transition is the main structural relaxation process, the so–called α–relaxation, which occurs in the supercooled liquid and it is due to collective

rearrangements [103]. The configurational changes in the system that give rise to this relaxation process are directly coupled to the macroscopic viscosity, and they become dramatically slower with decreasing temperature. At T_g, the relaxation time (τ) of the α–process reaches a value of about 100 s [103]. In addition to the main relaxation, many glass–forming liquids also show weaker secondary relaxation processes, where the most common category is denoted β–relaxations. β– relaxations are faster than α–relaxation and persist below T_g (see Fig. 20).

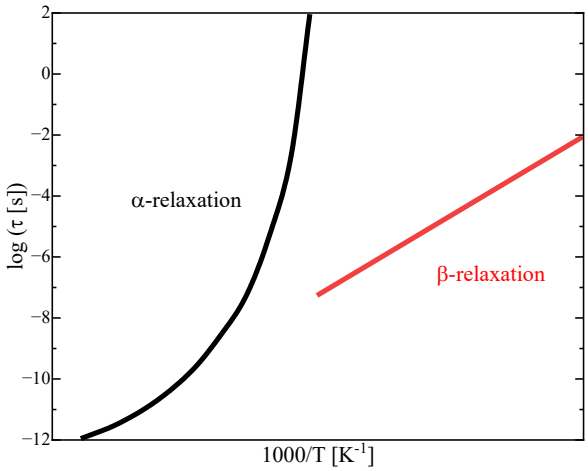

***Figure 20**: Arrhenius plot showing typical temperature dependencies of the fast β–relaxation and the slower α relaxation as well as the region where the two processes are merged to one single process.*

The α– and β–relaxation times generally show different temperature behaviors. The fast secondary β–process commonly exhibits an Arrhenius temperature dependence (Eq. 5), whereas the increase in relaxation time with decreasing temperature of the α–relaxation generally follows a Vogel–Fulcher–Tammann behavior (Eq. 6):

$$\tau = \tau_0 \cdot exp\left(\frac{E_a}{k_B T}\right) \tag{5}$$

$$\tau = \tau_0 \cdot exp\left(\frac{DT_0}{T - T_0}\right) \tag{6}$$

where τ_0 is the microscopic relaxation time extrapolated to infinite temperature, which would usually correspond to quasi–lattice and molecular vibrations of the order to 10^{-4} s, E_a is the activation energy, T_0 is the temperature where τ goes to infinity and D is a parameter that describes the deviation from Arrhenius behavior for the α–relaxation [103].

4 Hypothesis and Objectives

4.1 Hypothesis

This thesis is based on the following central hypotheses:

- Adsorption is the most suitable technique for removing emerging contaminants such as heavy metals, pharmaceuticals, and pesticides from water because it is simple, inexpensive, and scalable. Zinc, tetracycline, ciprofloxacin, and paraquat were selected as model pollutants.
- Pectin–based materials, when crosslinked with divalent (Ca^{2+}) cations, form stable, functional matrices with a high density of carboxyl groups, which can act as adsorption sites for heavy metals.
- Metal–organic frameworks (MOFs) such as Basolite F300® (Fe–BTC) have high porosity and coordinatively unsaturated Fe^{3+} sites that improve the adsorption of emerging contaminants. Their incorporation into a pectin matrix can address handling and stability issues. Poly(vinyl alcohol) (PVA) nanofibers, when crosslinked with citric acid and functionalized with europium, produce water–stable adsorbents with dual active sites (carboxyl and metal coordination) that enable efficient removal of antibiotics.
- The combination of biopolymers and inorganic porous materials can produce hybrid adsorbents that are sustainable, reusable, and highly effective for water remediation.

4.2 General Objective

To design, fabricate, and characterize sustainable bio–based and hybrid adsorbents for effective removal of emerging contaminants (heavy metals, pharmaceuticals, and pesticides) from water, focusing on the use of pectin, MOFs, and PVA as model materials.

4.3 Specific Objectives

The specific objectives are linked to the research articles that compose this compendium thesis:

- To fabricate and characterize PVA nanofibrous mats produced by electrospinning, crosslinked with citric acid, with europium ions incorporated via post–spinning doping (Paper 1) and in situ addition (Paper 2), evaluating their antibiotic adsorption performance with antibiotics.

- To study the structural role of water in calcium–crosslinked pectin adsorbents, evaluating how hydration and crosslinking time affect polymer structure, glass transition, and adsorption capacity for zinc (Paper 3).

- To investigate basic physical properties of pectin–based materials, gaining fundamental insights into confined water behavior and its implications for adsorption (Paper 4).

- To develop hybrid Pectin–MOF adsorbents by immobilizing Basolite F300® (Fe–BTC) in calcium–crosslinked pectin films and foams, and evaluate their efficiency in removing zinc, paraquat, and tetracycline (Paper 5).

5 Overview and Discussion of the Results

The results obtained throughout this thesis confirm the potential of bio–based polymers and hybrid composites as sustainable adsorbents for emerging contaminants. Each publication focused a specific aspect of this central theme, from basic structural analysis to applied adsorption research, forming a cohesive story that enhances both scientific knowledge and technological use.

5.1 Paper 1: Efficient antibiotic removal from water using europium–doped PVA nanofiber mats esterified with citric acid

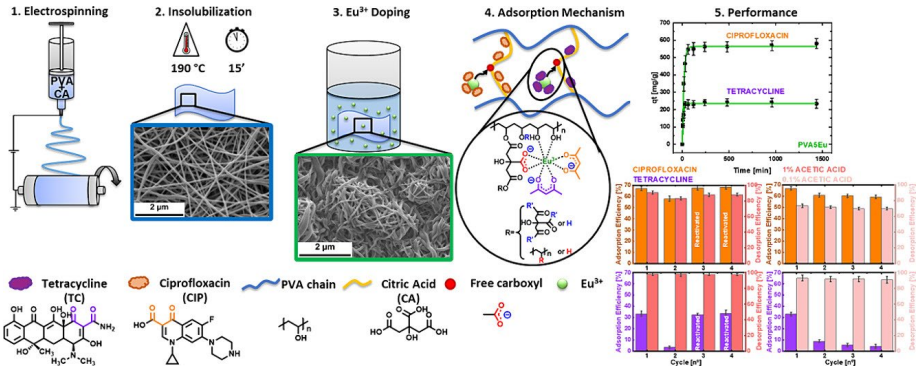

***Figure 21**: Graphical abstract Paper 1 titled "Efficient antibiotic removal from water using europium–doped PVA nanofiber mats esterified with citric acid".*

Electrospun poly(vinyl alcohol) (PVA) nanofiber mats esterified with citric acid (CA) and doped with Eu^{3+} (PVA5Eu) provide a compact, reusable platform for removing β–diketone–bearing antibiotics from water under neutral pH. The mats are produced by electrospinning aqueous PVA with or without 5 wt% of CA (PVA5 and PVA0), followed by thermal insolubilization at 190 °C for 15 min to drive polyesterification and create a CA–rich phase that stabilizes the fibers in water. Subsequent batch doping in 500 mg/L $EuCl_3$ for 60 min loads trivalent lanthanide sites throughout the swollen fibers; Eu uptake on PVA5 reaches a plateau within 25 min (PFO fit $k_1 = 0.62\ min^{-1}$, $q_e = 10.6$ mg/g). Three consecutive 2 h water washes show no detectable Eu release, indicating effective dopant immobilization.

Scanning electron microscopy confirms nanofiber integrity after processing, with diameters around 130 nm and a persistent morphology change after Eu doping; energy–dispersive X–ray analysis quantifies higher Eu content when CA is present (7.1 wt% vs 3.6 wt% without CA), consistent with carboxylate–assisted complexation. Differential scanning calorimetry (after controlled drying) reveals a low–temperature T_g near 58–65 °C that shifts upward with CA and Eu, plus a second, higher T_g (101–104 °C) that emerges only with CA, evidencing a more constrained CA–PVA phase; crystallinity decreases from ~ 60 % (PVA0) to 37–36 % (PVA5/PVA5Eu), yielding a more amorphous, adsorption–friendly network. These structural and thermodynamic signatures establish a dual–phase, water–stable mat in which CA provides fixed carboxylate groups while Eu^{3+} provides hard–acid coordination sites.

In the FT–IR results, the O–H stretching band redshifts after antibiotic exposure, and diagnostic bands for ciprofloxacin (C=O, ~1626 cm^{-1}) and tetracycline (amide I, ~1589 cm^{-1}) become evident in the spectra, demonstrating specific interactions with matrix functional groups. UV–Vis experiments on solution mixtures show a pronounced red shift of tetracycline absorbance (from 360 nm to 390 nm) upon adding Eu^{3+} (and further with CA), consistent with formation of Eu–TC and Eu–CA–TC complexes; by analogy, the β–diketone motif in fluoroquinolones (e.g., ciprofloxacin) underpins Eu–assisted binding. Together, these data indicate that CA carboxylates and Eu^{3+} centers generate complementary sites: electrostatic/acid–base interactions at COO^- and inner–sphere chelation at Eu^{3+}, both accessible within the swollen nanofiber architecture.

Under neutral conditions (pH 7; dose 1 g/L), PVA5Eu outperforms single–site controls (PVA0Eu, PVA5) for both ciprofloxacin (CIP) and tetracycline (TC), with kinetics well captured by the pseudo–first–order model. Normalized to the number of active sites (CA + Eu), the fitted capacities are $q_e = 563.7 \pm 4.1$ mg/g for CIP and 235.8 ± 3.1 mg/g for TC, with a faster approach to equilibrium for TC (50 min) than for CIP (80–85 min). On a whole–adsorbent basis, the PVA5Eu isotherm at pH 7 is Langmuir–like for CIP ($R = 0.99$; $q_M = 87.5 \pm 14.9$ mg/g), indicating near–monolayer adsorption on fairly uniform sites, whereas TC exhibits better statistics with Redlich–Peterson than with

Langmuir, consistent with site heterogeneity arising from the coexistence of CA and Eu domains. These results align with the mechanistic picture: CIP benefits strongly from Eu chelation plus electrostatic pairing at carboxylates, while TC—though also a β–diketone ligand—samples a broader distribution of environments within the CA–modified phase.

Selectivity trends in mixed–contaminant waters further validate site assignments. At pH 7, cationic dyes (methylene blue, rhodamine) compete with CIP at negatively charged carboxylates and measurably depress CIP removal. In contrast, TC adsorption remains essentially unchanged within error, reflecting it stronger reliance on Eu–centered complexation and reduced vulnerability to cationic competition. In comparison, atrazine little directly interacts with PVA5Eu under these conditions and can even coincide with enhanced CIP removal (reported increase in removal efficiency on the order of 30 %), again consistent with differential site usage by each pollutant class.

Operational stability is demonstrated over four adsorption–desorption cycles. Using acetic acid as a green regenerant, CIP performance remains high after multiple cycles. At the same time, TC shows a drop after the first cycle due to partial co–desorption of Eu together with strongly bound TC. This loss is mitigated either by Eu "reactivation" (brief re–doping) or by lowering acid strength to 0.1 %, which reduces Eu release at the cost of milder desorption. Electron microscopy after cycling confirms the nanofiber morphology is retained, albeit with expected signs of acid/swell history.

In sum, CA–esterified, Eu–doped PVA nanofibers integrate two synergistic chemistries within a robust, high–area scaffold: CA introduces fixed carboxylate sites and lowers crystallinity (enhancing accessibility), while Eu^{3+} provides strong, selective coordination for β–diketone–bearing antibiotics. The mats exhibit rapid, PFO–type uptake, high capacities when normalized to active–site mass, Langmuir–like behavior for CIP, heterogeneous adsorption for TC, resilience and regenerability, and credible performance in multi–pollutant matrices. These features make PVA5Eu a defensible, low–cost candidate for antibiotic removal at pH 7, with clear levers—CA content, Eu loading, and regeneration protocol—to balance selectivity, capacity, and longevity in realistic treatment scenarios.

5.2 Paper 2: Enhanced tetracycline removal through "in situ" europium incorporation in PVA electrospun mats

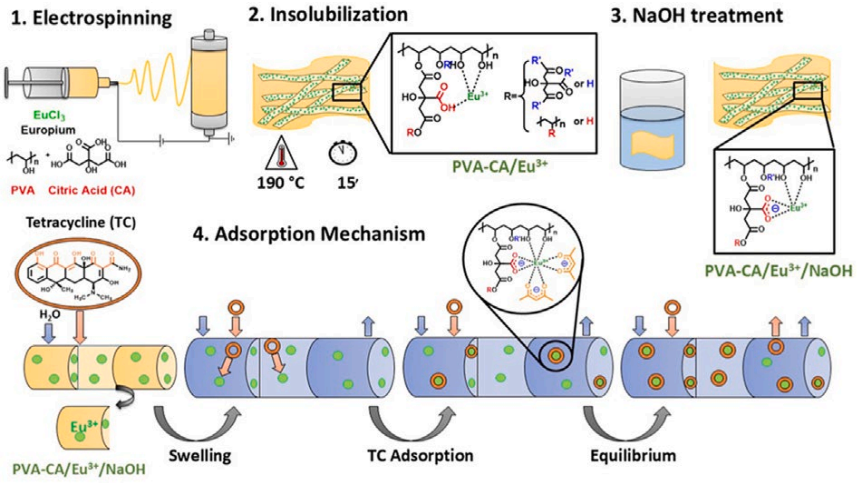

Figure 22: Graphical abstract Paper 2 titled "Enhanced tetracycline removal through "in situ" europium incorporation in PVA electrospun mats".

This paper demonstrates that incorporating Eu^{3+} directly into the spinning dope of poly(vinyl alcohol) (PVA) with citric acid (CA) produces water–stable nanofiber mats with markedly improved tetracycline (TC) removal, surpassing post–fabrication Eu "doping" despite using only ~1/3 of the europium content. The *in situ* route (12 wt% PVA, 5 wt% CA, 0.36 wt% Eu^{3+}) is followed by thermal insolubilization (190 °C, 15 min) and a mild alkaline treatment (1 M NaOH, 60 min), which together fix CA carboxylates, distribute Eu^{3+} homogeneously, and open access to coordination sites. SEM/EDS confirms uniform Eu distribution and systematic fiber thickening from ~132 ± 2 nm (PVA–CA) to 149 ± 2 nm (with Eu^{3+}) and 185 ± 3 nm after NaOH, consistent with swelling/reorganization of the polymer network upon alkalization and partial irreversible relaxation on drying.

FTIR shifts of O–H, C=O, and C–O bands to lower wavenumber corroborate Eu–carboxylate coordination; after NaOH, the emergence of COO^- signatures (1655–1550 cm^{-1}) evidences CA ionization and an increased density of hard–base ligands poised for Eu–assisted chelation. Together, morphology and spectroscopy indicate that the processing sequence creates a dual–phase, water–swellable scaffold where CA provides fixed carboxylate and Eu^{3+} provides strongly binding Lewis–acid centers.

Adsorption measurements at pH 7 establish clear advantages of *in situ* Eu incorporation and the subsequent alkaline activation. When performance is normalized to the number of active sites (Eu + CA), the alkaline–treated *in situ*

mats reach a capacity of q_e = 322.6 ± 16 mg/g for TC, exceeding both the *in situ* (no NaOH) and the doped reference despite the latter containing nearly threefold higher Eu (1 wt% vs 0.36 wt%). On a whole–adsorbent basis, equilibrium data (10–200 mg/L, 24 h) are best described by Langmuir (R^2 = 0.99) with q_m = 23.5 ± 1.3 mg/g, indicating near–monolayer uptake on a relatively uniform population of sites created by CA–Eu domains. Kinetics at pH 7 and C_0 = 50 mg/L show rapid early uptake (< 90 min), followed by diffusion–limited approach to equilibrium (920 min). Unlike the previously studied doped mats (Paper 2), where faster, surface biased–adsorption followed pseudo–first–order (PFO) behavior the *in situ* + NaOH system is better captured by pseudo–second–order (PSO; R^2 = 0.99), consistent with chemisorption at Eu–centered complexes accessed through intra–fiber diffusion in the swollen network.

Maximum removal at neutrality reflects favorable speciation of TC (zwitterionic/weakly anionic) and robust Eu–β–diketone chelation; adsorption declines at pH 5 (electrostatic penalties for cationic TC) and above pH 8 (competition from hydroxide and reduced electrostatic driving forces), mapping a practical operating window for natural/treated waters. In drug mixtures (TC with 20 mg/L co–solutes), ibuprofen and diclofenac depress TC uptake by ~25 %, plausibly via Eu sequestration by their carboxylates, whereas trimethoprim and chlorpheniramine show negligible effects, aligning with weaker competition for Eu relative to TC's β–diketone motif. Regeneration over five adsorption–desorption cycles indicates > 80 % efficiency through three cycles and ~60 % by cycle five; 1 % HCl outperforms acetic acid, likely because Eu–acetate complexation and residual TC at pH = 3 hinder full site reactivation, while chloride forms only weak Eu complexes and pH = 1 disfavors TC binding during desorption.

These results validate that homogeneous, *in situ* Eu placement plus alkaline activation yields a denser, more accessible set of Eu–carboxylate sites that improves intrinsic capacity, preserves performance across cycles, and resists interference from neutral cocontaminants. In conclusion, *in situ* Eu incorporation into PVA–CA followed by brief thermal and alkaline conditioning achieves Langmuir–type, chemisorption–driven tetracycline removal with higher site–normalized capacity than Eu–doped analogues, comparable whole–mat capacities at far lower Eu content, credible reusability, and practical robustness at neutral pH. The processing–structure–function relationships are internally consistent: alkaline treatment increases COO– density and network swellability; Eu is immobilized and uniformly dispersed; and the swollen, rubbery microenvironment facilitates diffusion to strongly binding Eu centers.

5.3 Paper 3: Structural characterization of low–methoxyl pectin–based adsorbents: the role of water on pectin structure

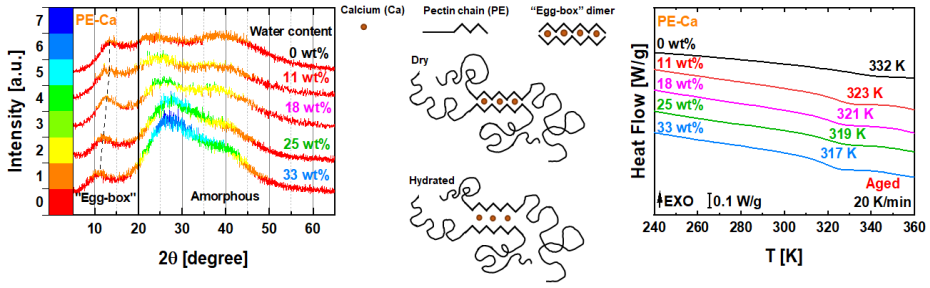

***Figure 23**: Graphical abstract Paper 3 titled "Structural characterization of low–methoxyl pectin–based adsorbents: the role of water on pectin structure".*

This study quantifies how network architecture, hydration–controlled polymer dynamics, and zinc removal are linked in externally Ca^{2+}–crosslinked low–methoxyl pectin (LMP) films. Films were prepared with increasing crosslinking times (5, 15, and 40 min; PE–Ca5/15/40), thoroughly washed to remove non–bound ions, and analyzed for structure (XRD), glass transition (DSC with physical aging), and adsorption behavior (ICP–AES kinetics/isotherms) under controlled hydration (0–33 wt% H_2O). The results show that calcium loading compacts the dry lattice and determines the dominant uptake pathway, while water acts as a plasticizer, widering interchain spacing, lowering T_g, and accelerating access to carboxylate sites. In the dry state, neat pectin displays a lateral spacing of ~0.70 nm associated with hydrogen–bonded chains. Introducing Ca^{2+} bridges broadens XRD peaks and shifts them to higher 2θ angles, shrinking the dominant spacing to 0.66, 0.65, and 0.63 nm for 5, 15, and 40 min of crosslinking, respectively, consistent with tighter packing in "egg–box" dimers. Hydration then transforms this compacted network in a threshold–like manner: up to ~11 wt% water the low–angle peak remains fixed, but above ~18 wt% it moves systematically, yielding interchain distances of 0.72, 0.78, and 0.89 nm at 18, 25, and 33 wt% water, respectively. Over the same hydration window, the glass transition of PE–Ca40 drops from 332 K (dry) to 317 K at 33 wt% water, with no ice melting detected—evidence that water remains non–freezable and bound in this regime. These coupled structural and dynamic changes indicate that water penetrates egg–box corridors, separates homogalacturonan chains, and plasticizes amorphous regions that control segmental mobility.

Adsorption data align with this picture and clarify the role of calcium. Under standard conditions (pH 7, 25 °C, dose 1 g/L, C_0 = 100 mg/L), equilibrium capacities increase with crosslinking time: q_{eq} = 54.5 ± 1.4 (PE–Ca5), 59.1 ± 0.9 (PE–Ca15), and 63.9 ± 1.2 mg/g (PE–Ca40). Kinetics follow

a pseudo–first–order model (R^2 = 0.98–0.99); PE–Ca40 ultimately reaches the highest capacity but shows slower early–time uptake, consistent with longer diffusion paths through a more swellable network. Equilibrium isotherms are captured statistically by heterogeneous Langmuir (Sips) fits. For PE–Ca40, the Sips model gives $q_M = 77.9 \pm 9.7$ mg/g with $R^2_{adj} = 0.99$; Redlich–Peterson fits are comparable, while Temkin performs worse. These outcomes are consistent with adsorption on a near–homogeneous population of carboxylate sites whose availability is modulated by Ca–bridging and hydration state, rather than multilayer growth. At trace concentrations near 1 mg/L, removal is essentially quantitative within minutes, which is suitable for polishing at environmentally relevant levels.

Insight into the mechanism is gained by tracking Ca^{2+} release during Zn^{2+} uptake. The exchange ratio (mol Zn_{ads} / mol Ca_{des}) approaches unity as crosslinking time increases: 1.24 for PE–Ca5, 1.07 for PE–Ca15, and 1.04 for PE–Ca40. Thus, lightly crosslinked networks operate via a mixed pathway: Zn–assisted additional crosslinking plus Ca and Zn exchange, whereas in highly crosslinked PE–Ca40 the process is predominantly one–for–one ion exchange. Independent corroboration appears in post–remediation DSC: T_g increases for PE–Ca5 (from 322 to 328 K) and PE–Ca15 (from 328 to 331 K), consistent with extra Zn–mediated crosslinks, but remains unchanged for PE–Ca40, matching a pure–exchange scenario with preserved structural signatures.

The pH response is practical, with capacity remaining stable between pH 6 and 8 but decreasing in acidic media (carboxylate protonation) and at high pH (partial depolymerization), which defines a robust operating window around neutrality for natural waters and secondary effluents. Hydration and temperature constitute additional handles for tuning performance. Because water depresses T_g and widens egg–box spacing, operating slightly above the hydrated T_g moves the polymer into a rubbery regime with higher chain mobility and faster ion transport. At 60 °C, PE–Ca40 reaches 71.45 % extraction after 240 min with an exchange ratio near unity, and performance increases monotonically from 40 to 60 °C, consistent with diffusion–facilitated access to sites in the plasticized network. Together, the data trace a clear causal chain from network chemistry to remediation: calcium loading compacts and stabilizes the egg–box lattice and sets the uptake mechanism from mixed Zn–crosslinking plus exchange at low Ca to nearly stoichiometric exchange at high Ca while hydration and modest heating control accessibility and rate via spacing and T_g. From a design perspective, these results support tuning crosslinking time to balance ultimate capacity (favored by higher Ca content) against early–time kinetics (penalized by longer diffusion paths), and controlling water content/temperature to operate near or just above the hydrated T_g for accelerated mass transport without compromising integrity.

The study also clarifies methodological practices that can be generalized beyond pectin. DSC with pre–aging sharpens weak glass transitions in hydrated, ion–crosslinked polysaccharides. Low–angle XRD under controlled RH resolves interchain spacing in the egg–box even when amorphous halos dominate at higher angles.

5.4 Paper 4: The glass transition and the dynamics of water within pectin and MOF nanochannels

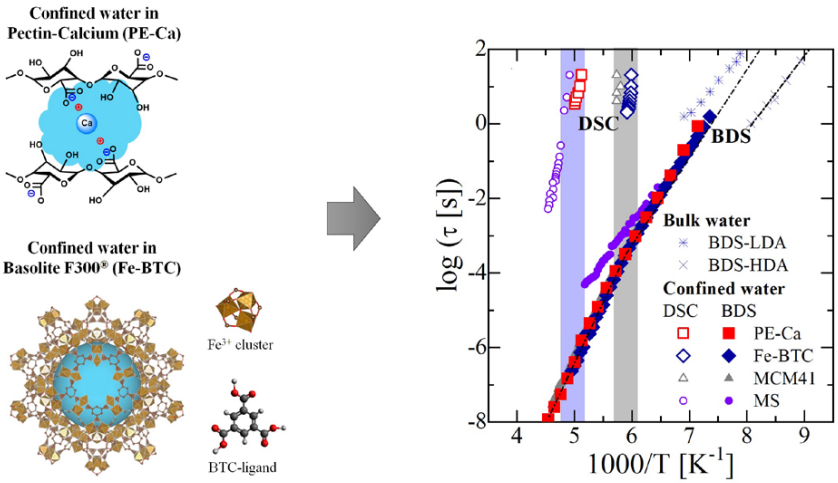

***Figure 24**: Graphical abstract Paper 4 titled "The glass transition and the dynamics of water within pectin and MOF nanochannels".*

This work shows how confinement chemistry controls the glass transition and molecular dynamics of water by comparing two confinement materials, a hydrophilic biopolymer (calcium–crosslinked pectin, PE–Ca) and a metal–organic framework (Fe–BTC). Differential scanning calorimetry (DSC) with carefully designed aging protocols, broadband dielectric spectroscopy (BDS), and ATR–FTIR were applied to controlled hydration series.

Confined water exhibits a true calorimetric glass transition at temperatures T_g = 193 K in PE–Ca and T_g = 170 K in Fe–BTC. The assignment relies on enthalpy–recovery analysis integrating the heat–capacity difference between aged and unaged states to locate the onset of non–equilibrium effects and on the coincidence between the DSC–derived T_g and a kinetic crossover in BDS. A higher–temperature step in heating scans is insensitive to aging and is attributed to adsorption/desorption at pore walls, not to vitrification. Together, these results indicate that the genuine T_g of bulk–like water is closer to 200 K. Confinements were engineered and hydrated with precision. PE–Ca films (external $CaCl_2$ crosslinking, 40 min) and Fe–BTC powders were vacuum–dried and then equilibrated for weeks in RH–controlled chambers, reaching water mass fractions up to 49 wt% (pectin) and 46 wt% (Fe–BTC).

X–ray diffraction pattern shows in pectin: beyond 18 wt% of water, the interchain expansion of the egg–box dimers increase from 0.63 nm (dry) to 0.89 nm at 33 wt%, as water opens the nanochannels. In Fe–BTC, diffraction peak

positions remain essentially invariant with hydration, consistent with a rigid pore geometry. Nitrogen sorption confirms Fe–BTC mesoporosity (BET = 1366 m^2/g; pore diameter of 2.0 nm). These structural observations frame how soft versus hard nanochannels template the hydrogen–bond network of confined water.

ATR–FTIR difference spectra and deconvolution across the OH–stretch region separate contributions from "multimer" water (~3550 cm^{-1}), tetrahedrally connected "network" water (~3400 and 3220 cm^{-1}), and a low–wavenumber strong–HB component (~3000 cm^{-1}). In PE–Ca, increasing hydration shifts the water population toward bulk–like network water. In Fe–BTC, however, a prominent strongly hydrogen–bonded fraction (0.25–0.35 of the OH–band area across all hydrations) persists, indicating water strongly coordinated to carboxylate–lined interfaces and a distorted network. This spectroscopic contrast correlates with calorimetry: the more bulk–like network in PE–Ca is associated with Tg = 193 K, whereas the interfacial strong–HB bias in Fe–BTC aligns with a lower Tg = 170 K. Substituting D_2O to resolve overlapping OH polymer bands reproduces the same trends, confirming that differences arise from water–matrix interactions.

Dielectric spectroscopy resolves two confined–water processes. A fast, universal relaxation (P2) follows Arrhenius behavior with E_a = 0.49 eV at low temperature and crosses over to super–Arrhenius behavior precisely near the DSC T_g (192 K in PE–Ca; 167 K in Fe–BTC). A slower process (P3), masked by conductivity in raw ε″ data, is recovered via derivative analysis and, more cleanly, via calorimetry by DSC step–response protocol, which yields frequency–dependent reversing heat capacity. Extrapolating the relaxation time to 100 s gives a T_g that matches the T_g obtained from enthalpy recovery measurements. Using both BDS and DSC criteria, secures the assignment of the true glass transition temperature. P2 is consistent with a Johari–Goldstein β–relaxation of confined water universal across disparate hosts; while P3 corresponds to the structural α–relaxation that defines vitrification. Low–temperature annealing clarifies the long–debated "136 K transition." Aging Fe–BTC–confined water at ~113 K produces only a weak, broad endotherm which is far smaller than the overshoot recovered after annealing near T_g. This low–temperature feature matches a sub–T_g or "shadow" transition, widely observed below T_g in many glass formers, and not a principal glass transition. Taken together, the DSC, BDS, and FT–IR data for PE–Ca, Fe–BTC, and earlier studied hard confinements converge to a consistent picture where confined water shows a single glass transition (T_g) in the 170–200 K range, and its value is controlled by how the confining material changes the hydrogen-bond network. In this view, the common 130–140 K signal is a secondary, non-structural endothermic event.

From a materials perspective, soft and hydrophilic nanochannels like PE–Ca allow water to form a hydrogen-bond network that is closer to bulk water. This raises Tg and promotes cooperative α-relaxation at higher temperatures. In contrast, carboxylate groups in rigid pores such as Fe–BTC stabilize strongly bound interfacial water, lowering Tg and shifting the kinetic crossover to lower

temperatures. These results are relevant for sustainable separation and transport technologies: by tuning pore chemistry and mechanical flexibility, one can control water mobility, ion conduction, and reaction selectivity in hydrated soft solids and MOFs. At a more fundamental level, the agreement of thermodynamic and kinetic indicators near 200 K in "bulk-like" confinements supports a higher Tg for water than the long-accepted 136 K value, and it suggests that the 136 K transition is a secondary "shadow" event rather than the main vitrification of water.

5.5 Paper 5: Bio–based pectin–calcium film and foam adsorbents with immobilized Fe–BTC MOF for water contaminant removal

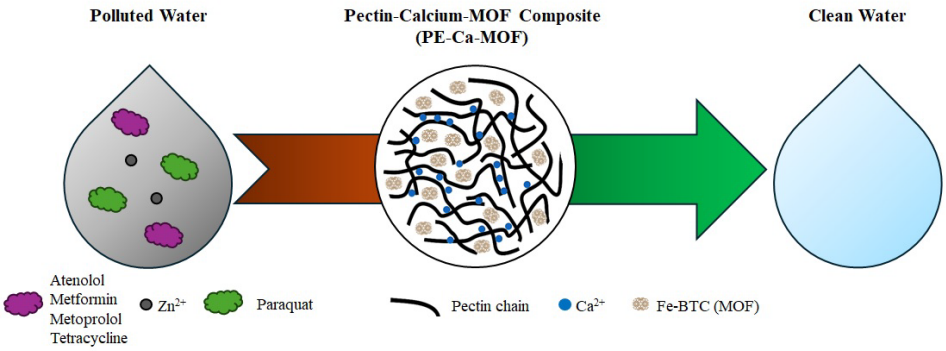

***Figure 25**: Graphical abstract Paper 5 titled "Bio–based pectin–calcium film and foam adsorbents with immobilized Fe–BTC MOF for water contaminant removal".*

This work develops bio–based adsorbents by physically immobilizing Basolite F300® (Fe–BTC) within externally Ca^{2+}–crosslinked low–methoxyl pectin (PE–Ca). The study shows how MOF dispersion strategy and composite geometry govern accessibility, mechanics, and pollutant removal. Fe–BTC is incorporated either by direct aqueous dispersion at 1–10 wt% or via a polyvinylpyrrolidone (PVP) surfactant route limited to 1 wt%. Composite are prepared as solvent–cast films or as highly porous foams obtained by freeze–drying, with all samples externally crosslinked and thoroughly washed to remove unbound ions.

Across methods, structural and thermal analyses confirm that neither the MOF framework nor the pectin network collapses during fabrication. FT–IR retains the specific vibration of BTC carboxylates and pectin COO^-/COOH bands. XRD patterns show a broad amorphous pectin halo together with Fe–BTC reflections, and TGA/DTG shows delayed MOF degradation in the composite, indicating a stabilizing matrix effect. DSC reveals that, for water–dispersed films, increasing MOF content rigidifies the matrix shifting the T_g

from 332 K to 336 K, whereas PVP acts primarily as a plasticizer (lower T_g), an effect amplified in foams where porosity further reduces effective chain constraints. SEM/EDX maps highlight the key processing variable, showing that aqueous dispersion promotes Fe–BTC aggregation and leads to brittle composites with drying cracks (10 wt%), while PVP yields smaller, uniformly distributed domains in both film and foam, improving active–site exposure without chemical side reactions.

The composites preserve the hallmark heavy–metal performance of PE–Ca while adding MOF–enabled affinity for bulky organics. After identical crosslinking and five washes, the Ca content (R = 0.28–0.29 Ca^{2+}/GalA for all formulations) is the same across samples, and pure Fe–BTC does not uptake Ca^{2+} or Zn^{2+}. Consequently, Zn^{2+} adsorption at pH 7 (C_0 = 50 mg/L; composite dose 1 g/L; 24 h) remains governed by an ion–exchange process with q_{24h} = 31–33 mg/g and removal of 62–64% across 0–10 wt% MOF. Kinetic fits are pseudo–first–order (PFO) with essentially stoichiometric Ca and Zn exchange (exchange ratio close to 1.0). However, the presence of the MOF slows the approach to equilibrium by reducing swelling and delaying adsorption. These control experiments indicate that immobilized Fe–BTC does not alter the Ca crosslink and the heavy-metal adsorption.

Fe–BTC adsorb paraquat (PQ) and tetracycline (TC), two pollutants that neat PE–Ca fails to remove under neutral conditions. In addiction at pH 7 (C_0 = 10 mg/L; composite dose 1 g/L; 24 h), MOF systematically elevates uptake across ATE/MET/MTF/PQ/TC panels, with the most pronounced gains for PQ and TC. However, the apparent optimum does not coincide with the highest MOF loading. At 10 wt% of MOF loading, films suffer from aggregation and embrittlement, whereas 5 wt% films balance capacity and integrity and are therefore used for detailed modeling. Sips isotherms describe the equilibrium well (PQ: q_M = 627 ± 64 mg/g, n = 0.92; TC: q_M = 298 ± 27 mg/g, n = 0.95), and PFO kinetics capture the time evolution at C_0 = 10 mg/L (PQ: q_e = 161 ± 5 mg/g, $k_1 = 5.9\times10^{-3}$ min^{-1}; TC: q_e = 91 ± 3 mg/g, $k_1 = 4.9\times10^{-3}$ min^{-1}).

Spectroscopy supports a mixed interaction picture: for TC, band shifts and attenuation of free C=O near ~1700 cm^{-1} signal coordination to unsaturated Fe^{3+} ions, complemented by hydrogen bonding and π–π interaction with BTC linkers. For PQ, π–donor–acceptor interactions with the aromatic framework dominate alongside weaker electrostatics. Altogether, the data highlight Fe–BTC as a stable, high–area host filler that extends the contaminant uptake in PE–Ca.

Dispersion and geometry are as important as chemistry. PVP–assisted films with only 1 wt% MOF match the paraquat removal of 5 wt% water–dispersed films, showing that homogeneous, accessible MOF domains outperform larger, occluded aggregates even at lower nominal loadings. Converting the same PVP–stabilized suspensions into foams further improves accessibility, especially for bulkier tetracycline, by combining better particle distribution with macroporosity that reduces transport limitations. This processing–structure relationship is also reflected in the thermal response. T_g

decrease in PVP films and foams indicating an increase of free volume and plasticization. These conditions promote diffusion within the matrix without compromising integrity of the components.

Finally, five adsorption–desorption cycles at pH 7 (adsorption) and 2% acetic acid (desorption) demonstrate good reusability. PQ displays stable adsorption (18–21 %) with high desorption efficiencies (87–95 %) and retention > 88% through cycle five, suggesting non–covalent interactions. TC removal is lower (9–12 %) and less regenerable (desorption 15–39 %; retention trending to 81% by cycle five), in line with stronger coordination to Fe sites that only partially release under the chosen green acid.

In summary, immobilizing Fe–BTC in PE–Ca yields a modular platform in which dispersion chemistry (PVP vs water), filler loading, and macro–architecture (film vs foam) tune the balance between mechanical integrity, transport, and site accessibility. Heavy–metal uptake remains governed by PE–Ca ion exchange, whereas MOF domains unlock high affinity routes for PQ and TC without sacrificing stability or recyclability. The clearest design rule from this study is that the distribution of the MOF is at least as important as how much is added. Homogeneous, plasticized, and porous composites make the most efficient use of Fe–BTC at low loading and enable sustainable, low-leaching adsorbents for neutral-pH water polishing.

References

1. Mekonnen, M.M.; Hoekstra, A.Y. Sustainability: Four Billion People Facing Severe Water Scarcity. *Sci Adv* 2016, *2*, 2–7, doi:10.1126/sciadv.1500323.

2. Schwarzenbach, R.P.; Egli, T.; Hofstetter, T.B.; Von Gunten, U.; Wehrli, B. Global Water Pollution and Human Health. *Annu Rev Environ Resour* 2010, *35*, 109–136, doi:10.1146/annurev-environ-100809-125342.

3. Yu, L.; Gan, J. Mitigation of Eutrophication and Hypoxia through Oyster Aquaculture: An Ecosystem Model Evaluation off the Pearl River Estuary. *Environ Sci Technol* 2021, *55*, 5506–5514, doi:10.1021/acs.est.0c06616.

4. Hugonnet, R.; McNabb, R.; Berthier, E.; Menounos, B.; Nuth, C.; Girod, L.; Farinotti, D.; Huss, M.; Dussaillant, I.; Brun, F.; et al. Accelerated Global Glacier Mass Loss in the Early Twenty-First Century. *Nature* 2021, *592*, 726–731, doi:10.1038/s41586-021-03436-z.

5. Wang, R.; Liang, R.; Dai, T.; Chen, J.; Shuai, X.; Liu, C. Pectin-Based Adsorbents for Heavy Metal Ions: A Review. *Trends Food Sci Technol* 2019, *91*, 319–329, doi:10.1016/j.tifs.2019.07.033.

6. Rojas, S.; Navarro, J.A.R.; Horcajada, P. Metal-Organic Frameworks for the Removal of the Emerging Contaminant Atenolol under Real Conditions. *Dalton Transactions* 2021, *50*, 2493–2500, doi:10.1039/d0dt03637d.

7. Choudhury, R.R.; Gohil, J.M.; Dutta, K. Poly(Vinyl Alcohol)-Based Membranes for Fuel Cell and Water Treatment Applications: A Review on Recent Advancements. *Polym Adv Technol* 2021, *32*, 4175–4203, doi:10.1002/pat.5431.

8. Kaur, G.; Aulakh, J.S. *Carbon Nanotubes for Clean Water*; 2022; ISBN 9783319956022.

9. Verhaar, H.J.M.; Vanleeuwen, C.J.; Hermens, J.L.M. Classifying Environmental-Pollutants .1. Structure-Activity-Relationships for Prediction of Aquatic Toxicity. *Chemosphere* 1992, *25*, 471–491, doi:10.1016/0045-6535(92)90280-5.

10. Kumar Reddy, D.H.; Lee, S.M. Water Pollution and Treatment Technologies. *J Environ Anal Toxicol* 2012, *02*, 2–4, doi:10.4172/2161-0525.1000e103.

11. Ojha, A. *Materials in Electrochemical Detection of Water Pollutants*; 2020; ISBN 9789811506703.

12. Rossi, L.; Chèvre, N.; Fankhauser, R.; Margot, J.; Curdy, R.; Babut, M.; Barry, D.A. Sediment Contamination Assessment in Urban Areas Based on Total Suspended Solids. *Water Res* 2013, *47*, 339–350, doi:10.1016/j.watres.2012.10.011.

13. Pal, A.; Gin, K.Y.H.; Lin, A.Y.C.; Reinhard, M. Impacts of Emerging Organic Contaminants on Freshwater Resources: Review of Recent Occurrences, Sources, Fate and Effects. *Science of the Total Environment* 2010, *408*, 6062–6069, doi:10.1016/j.scitotenv.2010.09.026.

14. Page, D.; Miotliński, K.; Dillon, P.; Taylor, R.; Wakelin, S.; Levett, K.; Barry, K.; Pavelic, P. Water Quality Requirements for Sustaining Aquifer Storage and Recovery Operations in a Low Permeability Fractured Rock Aquifer. *J Environ Manage* 2011, *92*, 2410–2418, doi:10.1016/j.jenvman.2011.04.005.

15. SenGupta, A.K. *Ion Exchange in Environmental Processes*; 2017; ISBN 9781119421283.

16. Agency, U.S.E.P.; Water, O. 2018 Edition of the Drinking Water Standards and Health Advisories Tables. 2018.

17. Encyclopedia of Lakes and Reservoirs. *Reference Reviews* 2013, *27*, 29–30, doi:10.1108/09504121311300479.

18. Patel, M.; Kumar, R.; Kishor, K.; Mlsna, T.; Pittman, C.U.; Mohan, D. Pharmaceuticals of Emerging Concern in Aquatic Systems: Chemistry, Occurrence, Effects, and Removal Methods. *Chem Rev* 2019, *119*, 3510–3673, doi:10.1021/acs.chemrev.8b00299.

19. Michael, I.; Rizzo, L.; McArdell, C.S.; Manaia, C.M.; Merlin, C.; Schwartz, T.; Dagot, C.; Fatta-Kassinos, D. Urban Wastewater Treatment Plants as Hotspots for the Release of Antibiotics in the Environment: A Review. *Water Res* 2013, *47*, 957–995, doi:10.1016/j.watres.2012.11.027.

20. Abd-Elsalam, K.; Zāḥid, M. *Aquananotechnology : Applications of Nanomaterials for Water Purification*; 2021; ISBN 9780128211427.

21. Elibariki, R.; Maguta, M.M. Status of Pesticides Pollution in Tanzania – A Review. *Chemosphere* 2017, *178*, 154–164, doi:10.1016/j.chemosphere.2017.03.036.

22. Syafrudin, M.; Kristanti, R.A.; Yuniarto, A.; Hadibarata, T.; Rhee, J.; Al-Onazi, W.A.; Algarni, T.S.; Almarri, A.H.; Al-Mohaimeed,

A.M. Pesticides in Drinking Water-a Review. *Int J Environ Res Public Health* 2021, *18*, 1–15, doi:10.3390/ijerph18020468.

23. Cherian, T.; Ragavendran, C.; Vijayan, S.; Kurien, S.; Peijnenburg, W.J.G.M. A Review on the Fate, Human Health and Environmental Impacts, as Well as Regulation of Antibiotics Used in Aquaculture. *Environmental Advances* 2023, *13*, 100411, doi:10.1016/j.envadv.2023.100411.

24. Reynel-Avila, A.B.-P.D.I.M.-C.H.E. *Adsorption Processes for Water Treatment and Purification*; 2017; ISBN 9783319581361.

25. Qadri, H.; Ahmad, R.; Mohammad, B.; Mehmood, A.; Hamid, G. *Fresh Water Pollution Dynamics and Remediation*; 2020; ISBN 9789811382765.

26. Pourhakkak, P.; Taghizadeh, A.; Taghizadeh, M.; Ghaedi, M.; Haghdoust, S. *Fundamentals of Adsorption Technology*; 1st ed.; Elsevier Ltd., 2021; Vol. 33; ISBN 9780128188057.

27. Streit, A.F.M.; Côrtes, L.N.; Druzian, S.P.; Godinho, M.; Collazzo, G.C.; Perondi, D.; Dotto, G.L. Development of High Quality Activated Carbon from Biological Sludge and Its Application for Dyes Removal from Aqueous Solutions. *Science of the Total Environment* 2019, *660*, 277–287, doi:10.1016/j.scitotenv.2019.01.027.

28. Azam, K.; Shezad, N.; Shafiq, I.; Akhter, P.; Akhtar, F.; Jamil, F.; Shafique, S.; Park, Y.K.; Hussain, M. A Review on Activated Carbon Modifications for the Treatment of Wastewater Containing Anionic Dyes. *Chemosphere* 2022, *306*, doi:10.1016/j.chemosphere.2022.135566.

29. Wang, H.; Xu, J.; Liu, X.; Sheng, L. Preparation of Straw Activated Carbon and Its Application in Wastewater Treatment: A Review. *J Clean Prod* 2021, *283*.

30. Carmalin Sophia, A.; Lima, E.C.; Allaudeen, N.; Rajan, S. Application of Graphene Based Materials for Adsorption of Pharmaceutical Traces from Water and Wastewater- a Review. *Desalination Water Treat* 2016, *57*, 27573–27586, doi:10.1080/19443994.2016.1172989.

31. Perreault, F.; Fonseca De Faria, A.; Elimelech, M. Environmental Applications of Graphene-Based Nanomaterials. *Chem Soc Rev* 2015, *44*, 5861–5896, doi:10.1039/c5cs00021a.

32. Diagboya, P.N.E.; Dikio, E.D. Silica-Based Mesoporous Materials; Emerging Designer Adsorbents for Aqueous Pollutants Removal and

Water Treatment. *Microporous and Mesoporous Materials* 2018, *266*, 252–267.

33. Fan, H.T.; Wu, J.B.; Fan, X.L.; Zhang, D.S.; Su, Z.J.; Yan, F.; Sun, T. Removal of Cadmium(II) and Lead(II) from Aqueous Solution Using Sulfur-Functionalized Silica Prepared by Hydrothermal-Assisted Grafting Method. *Chemical Engineering Journal* 2012, *198–199*, 355–363, doi:10.1016/j.cej.2012.05.109.

34. Sriram, G.; Bendre, A.; Altalhi, T.; Jung, H.Y.; Hegde, G.; Kurkuri, M. Surface Engineering of Silica Based Materials with Ni–Fe Layered Double Hydroxide for the Efficient Removal of Methyl Orange: Isotherms, Kinetics, Mechanism and High Selectivity Studies. *Chemosphere* 2022, *287*, doi:10.1016/j.chemosphere.2021.131976.

35. Mahdavi Far, R.; Van der Bruggen, B.; Verliefde, A.; Cornelissen, E. A Review of Zeolite Materials Used in Membranes for Water Purification: History, Applications, Challenges and Future Trends. *Journal of Chemical Technology and Biotechnology* 2022, *97*, 575–596.

36. Dessalegne, M.; Zewge, F.; Diaz, I. Aluminum Hydroxide Supported on Zeolites for Fluoride Removal from Drinking Water. *Journal of Chemical Technology and Biotechnology* 2017, *92*, 605–613, doi:10.1002/jctb.5041.

37. El Hanache, L.; Lebeau, B.; Nouali, H.; Toufaily, J.; Hamieh, T.; Daou, T.J. Performance of Surfactant-Modified *BEA-Type Zeolite Nanosponges for the Removal of Nitrate in Contaminated Water: Effect of the External Surface. *J Hazard Mater* 2019, *364*, 206–217, doi:10.1016/j.jhazmat.2018.10.015.

38. Tomczyk, A.; Kubaczyński, A.; Szewczuk-Karpisz, K. Assessment of Agricultural Waste Biochars for Remediation of Degraded Water-Soil Environment: Dissolved Organic Carbon Release and Immobilization of Impurities in One- or Two-Adsorbate Systems. *Waste Management* 2023, *155*, 87–98, doi:10.1016/j.wasman.2022.10.039.

39. Tareq, R.; Akter, N.; Azam, M.S. Biochars and Biochar Composites: Low-Cost Adsorbents for Environmental Remediation. In *Biochar from Biomass and Waste: Fundamentals and Applications*; Elsevier, 2018; pp. 169–209 ISBN 9780128117293.

40. Zeghioud, H.; Fryda, L.; Djelal, H.; Assadi, A.; Kane, A. A Comprehensive Review of Biochar in Removal of Organic Pollutants from Wastewater: Characterization, Toxicity, Activation/Functionalization and Influencing Treatment Factors. *Journal of Water Process Engineering* 2022, *47*.

41. Fang, Z.; Gao, Y.; Bolan, N.; Shaheen, S.M.; Xu, S.; Wu, X.; Xu, X.; Hu, H.; Lin, J.; Zhang, F.; et al. Conversion of Biological Solid Waste to Graphene-Containing Biochar for Water Remediation: A Critical Review. *Chemical Engineering Journal* 2020, *390*, doi:10.1016/j.cej.2020.124611.

42. El Bastamy, E.; Ibrahim, L.A.; Ghandour, A.; Zelenakova, M.; Vranayova, Z.; Abu-Hashim, M. Efficiency of Natural Clay Mineral Adsorbent Filtration Systems in Wastewater Treatment for Potential Irrigation Purposes. *Sustainability (Switzerland)* 2021, *13*, doi:10.3390/su13105738.

43. Chang, P.H.; Li, Z.; Jiang, W.T.; Sarkar, B. Clay Minerals for Pharmaceutical Wastewater Treatment. In *Modified Clay and Zeolite Nanocomposite Materials: Environmental and Pharmaceutical Applications*; Elsevier, 2018; pp. 167–196 ISBN 9780128146187.

44. Khakimova, N.; Maravić, N.; Davidović, P.; Blagojević, D.; Bečelić-Tomin, M.; Simeunović, J.; Pešić, V.; Šereš, Z.; Mandić, A.; Pojić, M.; et al. Sugar Beet Processing Wastewater Treatment by Microalgae through Biosorption. *Water (Switzerland)* 2022, *14*, doi:10.3390/w14060860.

45. Gönder, Z.B.; Vergili, I.; Kaya, Y.; Barlas, H. Adsorption of Cationic and Anionic Surfactants onto Organic Polymer Resin Lewatit VPOC 1064 MD PH. *Environ Geochem Health* 2010, *32*, 267–273, doi:10.1007/s10653-010-9297-7.

46. Kwok, K.C.M.; Koong, L.F.; Al Ansari, T.; McKay, G. Adsorption/Desorption of Arsenite and Arsenate on Chitosan and Nanochitosan. *Environmental Science and Pollution Research* 2018, *25*, 14734–14742, doi:10.1007/s11356-018-1501-9.

47. Nasrollahzadeh, M.; Sajjadi, M.; Iravani, S.; Varma, R.S. Starch, Cellulose, Pectin, Gum, Alginate, Chitin and Chitosan Derived (Nano)Materials for Sustainable Water Treatment: A Review. *Carbohydr Polym* 2021, *251*.

48. Torasso, N.; Vergara-Rubio, A.; Pereira, R.; Martinez-Sabando, J.; Baudrit, J.R.V.; Cerveny, S.; Goyanes, S. An in Situ Approach to Entrap Ultra-Small Iron Oxide Nanoparticles inside Hydrophilic Electrospun Nanofibers with High Arsenic Adsorption. *Chemical Engineering Journal* 2023, *454*, doi:10.1016/j.cej.2022.140168.

49. Torasso, N.; Vergara-Rubio, A.; Rivas-Rojas, P.; Huck-Iriart, C.; Larrañaga, A.; Fernández-Cirelli, A.; Cerveny, S.; Goyanes, S. Enhancing Arsenic Adsorption via Excellent Dispersion of Iron Oxide Nanoparticles inside Poly(Vinyl Alcohol) Nanofibers. *J Environ Chem Eng* 2021, *9*, doi:10.1016/j.jece.2020.104664.

50. Picón, D.; Torasso, N.; Baudrit, J.R.V.; Cerveny, S.; Goyanes, S. Bio-Inspired Membranes for Adsorption of Arsenic via Immobilized L-Cysteine in Highly Hydrophilic Electrospun Nanofibers. *Chemical Engineering Research and Design* 2022, *185*, 108–118, doi:10.1016/j.cherd.2022.06.042.

51. Picón, D.; Vergara-Rubio, A.; Estevez-Areco, S.; Cerveny, S.; Goyanes, S. Adsorption of Methylene Blue and Tetracycline by Zeolites Immobilized on a PBAT Electrospun Membrane. *Molecules* 2023, *28*, doi:10.3390/molecules28010081.

52. Pereira, P.P.; Fernandez, M.; Cimadoro, J.; González, P.S.; Morales, G.M.; Goyanes, S.; Agostini, E. Biohybrid Membranes for Effective Bacterial Vehiculation and Simultaneous Removal of Hexavalent Chromium (CrVI) and Phenol. *Appl Microbiol Biotechnol* 2021, doi:10.1007/s00253-020-11031-x.

53. Mangla, D.; Annu; Sharma, A.; Ikram, S. Critical Review on Adsorptive Removal of Antibiotics: Present Situation, Challenges and Future Perspective. *J Hazard Mater* 2022, *425*, 127946, doi:10.1016/j.jhazmat.2021.127946.

54. Martínez-Sabando, J.; Coin, F.; Melillo, J.H.; Goyanes, S.; Cerveny, S. A Review of Pectin-Based Material for Applications in Water Treatment. *Materials* 2023, *16*, doi:10.3390/ma16062207.

55. Coin, F.; Aitor, L.; Silvina, C. Structural Characterization of Low Methoxyl Pectin-Based Adsorbents: The Role of Water in Heavy Metal Adsorption (Submitted to Carbohydrate Polymers). *SSRN* 2025.

56. Liu, X.; Shan, Y.; Zhang, S.; Kong, Q.; Pang, H. Application of Metal Organic Framework in Wastewater Treatment. *Green Energy and Environment* 2023, *8*, 698–721, doi:10.1016/j.gee.2022.03.005.

57. Kumar, A.; Han, S.S. PVA-Based Hydrogels for Tissue Engineering: A Review. *International Journal of Polymeric Materials and Polymeric Biomaterials* 2017, *66*, 159–182, doi:10.1080/00914037.2016.1190930.

58. Coin, F.; Rodríguez-Ramírez, C.A.; Oyarbide, F.S.; Picón, D.; Goyanes, S.; Cerveny, S. Efficient Antibiotic Removal from Water Using Europium-Doped Poly(Vinyl Alcohol) Nanofiber Mats Esterified with Citric Acid. *Journal of Water Process Engineering* 2024, *63*, doi:10.1016/j.jwpe.2024.105447.

59. Rodríguez-Ramírez, C.A.; Coin, F.; Vergara-Rubio, A.; Picón, D.; Cerveny, S.; Goyanes, S. Enhanced Tetracycline Removal through “in Situ” Europium Incorporation in Poly (Vinyl Alcohol) (PVA) Electrospun Mats: Advantages of This Strategy in Adsorption and

Reuse over Doping. *Chemosphere* 2025, *372*, doi:10.1016/j.chemosphere.2025.144102.

60. Xiao, C.; Anderson, C.T. Roles of Pectin in Biomass Yield and Processing for Biofuels. *Front Plant Sci* 2013, *4*, 1–7, doi:10.3389/fpls.2013.00067.

61. Assifaoui, A.; Chambin, O. *Pectin: Technological and Physiological Properties*; 2020; ISBN 9783030534202.

62. Martínez-Sabando, J.; Coin, F.; Raposo, J.C.; Larrañaga, A.; Melillo, J.H.; Cerveny, S. Dual Crosslinking of Low-Methoxyl Pectin by Calcium and Europium for the Simultaneous Removal of Pharmaceuticals and Divalent Heavy Metals. *Chemical Engineering Journal* 2023, *475*, 146162, doi:10.1016/j.cej.2023.146162.

63. Pascale, N.; Gu, F.; Larsen, N.; Jespersen, L.; Respondek, F. The Potential of Pectins to Modulate the Human Gut Microbiota Evaluated by In Vitro Fermentation: A Systematic Review. *Nutrients* 2022, *14*, 1–31, doi:10.3390/nu14173629.

64. Coin, F.; Larrañaga, A.; Cerveny, S. Structural Characterization of Low Methoxyl Pectin-Based Adsorbents: The Role of Water on Pectin Structure. *Carbohydrate Polymer Technologies and Applications* 2025, *11*, doi:10.1016/j.carpta.2025.100885.

65. Assifaoui, A.; Lerbret, A.; Uyen, H.T.D.; Neiers, F.; Chambin, O.; Loupiac, C.; Cousin, F. Structural Behaviour Differences in Low Methoxy Pectin Solutions in the Presence of Divalent Cations (Ca2+and Zn2+): A Process Driven by the Binding Mechanism of the Cation with the Galacturonate Unit. *Soft Matter* 2015, *11*, 551–560, doi:10.1039/c4sm01839g.

66. Cao, L.; Lu, W.; Mata, A.; Nishinari, K.; Fang, Y. Egg-Box Model-Based Gelation of Alginate and Pectin: A Review. *Carbohydr Polym* 2020, *242*.

67. Ventura, I.; Jammal, J.; Bianco-Peled, H. Insights into the Nanostructure of Low-Methoxyl Pectin-Calcium Gels. *Carbohydr Polym* 2013, *97*, 650–658, doi:10.1016/j.carbpol.2013.05.055.

68. Gohil, R.M. Synergistic Blends of Natural Polymers, Pectin and Sodium Alginate. *J Appl Polym Sci* 2011, *120*, 2324–2336, doi:10.1002/app.33422.

69. Grant, G.T.; Morris, E.R.; Rees, D.A.; Smith, P.J.C.; Thom, D. Biological Interactions between Polysaccharides and Divalent Cations: The Egg-Box Model. *FEBS Lett* 1973, *32*, 195–198, doi:10.1016/0014-5793(73)80770-7.

70. Morris, E.R.; Rees, D.A.; Thom, D.; Boyd, J. Chiroptical and Stoichiometric Evidence of a Specific, Primary Dimerisation Process in Alginate Gelation. *Carbohydr Res* 1978, *66*, 145–154, doi:10.1016/S0008-6215(00)83247-4.

71. Walkinshaw, M.D.; Arnott, S. Conformations and Interactions of Pectins. II. Models for Junction Zones in Pectinic Acid and Calcium Pectate Gels. *J Mol Biol* 1981, *153*, 1075–1085, doi:10.1016/0022-2836(81)90468-X.

72. Powell, D.A.; Morris, E.R.; Gidley, M.J.; Rees, D.A. Conformations and Interactions of Pectins. II. Influence of Residue Sequence on Chain Association in Calcium Pectate Gels. *J Mol Biol* 1982, *155*, 517–531, doi:10.1016/0022-2836(82)90485-5.

73. Kohn, R. Binding of Divalent Cations to Oligomeric Fragments of Pectin. *Carbohydr Res* 1987, *160*, 343–353, doi:10.1016/0008-6215(87)80322-1.

74. Walter, R.H. *The Chemistry and Technology of Pectin*; Walter, R.H., Ed.; Academic press, inc., 1991; ISBN 0127338705.

75. Braccini, I.; Pérez, S. Molecular Basis of Ca2+-Induced Gelation in Alginates and Pectins: The Egg-Box Model Revisited. *Biomacromolecules* 2001, *2*, 1089–1096, doi:10.1021/bm010008g.

76. Li, L.; Fang, Y.; Vreeker, R.; Appelqvist, I.; Mendes, E. Reexamining the Egg-Box Model in Calcium - Alginate Gels with X-Ray Diffraction. *Biomacromolecules* 2007, *8*, 464–468, doi:10.1021/bm060550a.

77. Fang, Y.; Al-Assaf, S.; Phillips, G.O.; Nishinari, K. Multiple Steps and Critical Behaviors of the Binding of Calcium to Alginate - The Journal of Physical Chemistry B (ACS Publications). *Physical Chemistry B* 2007, 2456–2462.

78. Fang, Y.; Al-Assaf, S.; Phillips, G.O.; Nishinari, K.; Funami, T.; Williams, P.A. Binding Behavior of Calcium to Polyuronates: Comparison of Pectin with Alginate. *Carbohydr Polym* 2008, *72*, 334–341, doi:10.1016/j.carbpol.2007.08.021.

79. Huynh, U.T.D.; Lerbret, A.; Neiers, F.; Chambin, O.; Assifaoui, A. Binding of Divalent Cations to Polygalacturonate: A Mechanism Driven by the Hydration Water. *Journal of Physical Chemistry B* 2016, *120*, 1021–1032, doi:10.1021/acs.jpcb.5b11010.

80. Huynh, U.T.D.; Chambin, O.; du Poset, A.M.; Assifaoui, A. Insights into Gelation Kinetics and Gel Front Migration in Cation-Induced Polysaccharide Hydrogels by Viscoelastic and Turbidity

Measurements: Effect of the Nature of Divalent Cations. *Carbohydr Polym* 2018, *190*, 121–128, doi:10.1016/j.carbpol.2018.02.046.

81. Wang, H.; Fei, S.; Wang, Y.; Zan, L.; Zhu, J. Comparative Study on the Self-Assembly of Pectin and Alginate Molecules Regulated by Calcium Ions Investigated by Atomic Force Microscopy. *Carbohydr Polym* 2020, *231*, 115673, doi:10.1016/j.carbpol.2019.115673.

82. El-Sewify, I.M.; Ma, S. Recent Development of Metal-Organic Frameworks for Water Purification. *Langmuir* 2024, *40*, 5060–5076.

83. Chen, G.; Leng, X.; Luo, J.; You, L.; Qu, C.; Dong, X.; Huang, H.; Yin, X.; Ni, J. In Vitro Toxicity Study of a Porous Iron(III) Metal-Organic Framework. *Molecules* 2019, *24*, doi:10.3390/molecules24071211.

84. Zhu, R.; Cai, M.; Fu, T.; Yin, D.; Peng, H.; Liao, S.; Du, Y.; Kong, J.; Ni, J. Fe-Based Metal Organic Frameworks (Fe-MOFs) for Bio-Related Applications. 2023.

85. Fang, Y.; Yang, Z.; Li, H.; Liu, X. MIL-100(Fe) and Its Derivatives: From Synthesis to Application for Wastewater Decontamination. *Environmental Science and Pollution Research* 2020, *27*, 4703–4724, doi:10.1007/s11356-019-07318-w.

86. Shizari, P.N.; Kamran-Pirzaman, A.; Kiadehi, A.D.; Abedini, H. Paraquat Herbicide Removal from Aqueous Medium Using ZIF-8 and Fe-BTC Adsorbents: A Comparative Study. *Sep Purif Technol* 2025, *363*, 132285, doi:10.1016/j.seppur.2025.132285.

87. Khezerlou, A.; Tavassoli, M.; Abedi-Firoozjah, R.; Alizadeh Sani, M.; Ehsani, A.; Varma, R.S. MOFs-Based Adsorbents for the Removal of Tetracycline from Water and Food Samples. *Sci Rep* 2025, *15*, 1–15, doi:10.1038/s41598-024-84122-8.

88. Santos, V.P.; Wezendonk, T.A.; Jaén, J.J.D.; Dugulan, A.I.; Nasalevich, M.A.; Islam, H.U.; Chojecki, A.; Sartipi, S.; Sun, X.; Hakeem, A.A.; et al. Metal Organic Framework-Mediated Synthesis of Highly Active and Stable Fischer-Tropsch Catalysts. *Nat Commun* 2015, *6*, doi:10.1038/ncomms7451.

89. Coin, F.; Iacovone, C.; Cerveny, S. Bio-Based Pectin-Calcium Film and Foam Adsorbents with Immobilized Fe–BTC MOF for Water Contaminant Removal. *Polymers* 2026, *18*, 171, doi:10.3390/polym18020171.

90. Cui, J.; Li, F.; Wang, Y.; Zhang, Q.; Ma, W.; Huang, C. Electrospun Nanofiber Membranes for Wastewater Treatment Applications. *Sep Purif Technol* 2020, *250*, 117116, doi:10.1016/j.seppur.2020.117116.

91. Estevez-Areco, S.; Guz, L.; Candal, R.; Goyanes, S. Development of Insoluble PVA Electrospun Nanofibers Incorporating R-Limonene or β-Cyclodextrin/R-Limonene Inclusion Complexes. *J Polym Environ* 2022, *30*, 2812–2823, doi:10.1007/s10924-022-02390-9.

92. Nayl, A.A.; Abd-Elhamid, A.I.; Awwad, N.S.; Abdelgawad, M.A.; Wu, J.; Mo, X.; Gomha, S.M.; Aly, A.A.; Bräse, S. Review of the Recent Advances in Electrospun Nanofibers Applications in Water Purification. *Polymers (Basel)* 2022, *14*.

93. Ray, S.S.; Chen, S.S.; Li, C.W.; Nguyen, N.C.; Nguyen, H.T. A Comprehensive Review: Electrospinning Technique for Fabrication and Surface Modification of Membranes for Water Treatment Application. *RSC Adv* 2016, *6*, 85495–85514, doi:10.1039/c6ra14952a.

94. Bolto, B.; Tran, T.; Hoang, M.; Xie, Z. Crosslinked Poly(Vinyl Alcohol) Membranes. *Progress in Polymer Science (Oxford)* 2009, *34*, 969–981, doi:10.1016/j.progpolymsci.2009.05.003.

95. Miraftab, M.; Saifullah, A.N.; Çay, A. Physical Stabilisation of Electrospun Poly(Vinyl Alcohol) Nanofibres: Comparative Study on Methanol and Heat-Based Crosslinking. *J Mater Sci* 2015, *50*, 1943–1957, doi:10.1007/s10853-014-8759-1.

96. Zhou, X.H.; Wei, D.X.; Ye, H.M.; Zhang, X.; Meng, X.; Zhou, Q. Development of Poly(Vinyl Alcohol) Porous Scaffold with High Strength and Well Ciprofloxacin Release Efficiency. *Materials Science and Engineering C* 2016, *67*, 326–335, doi:10.1016/j.msec.2016.05.030.

97. Picón, D.; Torasso, N.; Baudrit, J.R.V.; Cerveny, S.; Goyanes, S. Bio-Inspired Membranes for Adsorption of Arsenic via Immobilized L-Cysteine in Highly Hydrophilic Electrospun Nanofibers. *Chemical Engineering Research and Design* 2022, *185*, 108–118, doi:10.1016/j.cherd.2022.06.042.

98. Rynkowska, E.; Fatyeyeva, K.; Kujawa, J. Chemically and Thermally Crosslinked PVA-Based Membranes : E Ff Ect on Swelling And. 2019, 7–9.

99. Ciriminna, R.; Meneguzzo, F.; Delisi, R.; Pagliaro, M. Citric Acid: Emerging Applications of Key Biotechnology Industrial Product. *Chem Cent J* 2017, *11*, 1–9, doi:10.1186/s13065-017-0251-y.

100. Cimadoro, J.; Goyanes, S. Reversible Swelling as a Strategy in the Development of Smart Membranes from Electrospun Polyvinyl Alcohol Nanofiber Mats. *Journal of Polymer Science* 2020, *58*, 737–746, doi:10.1002/pol.20190156.

101. Cangialosi, D. Glass Transition and Physical Aging of Confined Polymers Investigated by Calorimetric Techniques. In *Handbook of Thermal Analysis and Calorimetry*; Elsevier B.V., 2018; Vol. 6, pp. 301–337 ISBN 9780444640628.

102. Di Lisio, V.; Stavropoulou, V.M.; Cangialosi, D. Physical Aging in Molecular Glasses beyond the α Relaxation. *Journal of Chemical Physics* 2023, *159*, doi:10.1063/5.0157994.

103. *Broadband Dielectric Spectroscopy*; Kremer, F., Schönhals, A., Eds.; Sringer, 2003; ISBN 978-3-642-62809-2.

SECTION 2

Conclusions

This thesis shows that bio-based polymers and their hybrids with porous inorganic materials can be designed as efficient, reusable, and environmentally friendly adsorbents for emerging contaminants in water. Three main material types are studied: calcium–crosslinked low–methoxyl pectin (PE–Ca), the metal–organic framework Basolite F300® (Fe–BTC), and citric–acid–crosslinked poly(vinyl alcohol) (PVA) nanofibers functionalized with europium. The work links molecular structure and hydration dynamics to macroscopic adsorption performance for a metal (Zn^{2+}), antibiotics (tetracycline and ciprofloxacin), and a pesticide (paraquat). The hypotheses proposed in Section 1 are confirmed: adsorption is a scalable and cost-effective way to remove dilute, persistent contaminants; crosslinked pectin offers many active sites for metal uptake; MOF domains add strong binding sites for bulky organic molecules; and PVA–Eu materials form strong, selective interactions with β-diketone antibiotics at neutral pH. Overall, the results advance both the basic understanding and the practical use of sustainable adsorbents.

The first part of the thesis focused on PVA-based materials to target pharmaceuticals via a different chemistry. Electrospun PVA mats, crosslinked by citric acid (CA), form robust, high-surface-area materials rich in fixed carboxylates. Adding europium creates hard Lewis-acid sites that strongly chelate β-diketone groups present in tetracycline and fluoroquinolones. When Eu is introduced after CA–PVA formation, the materials exhibit rapid uptake, pseudo-first-order kinetics, and show high site-normalized capacity at neutral pH, with good selectivity in mixed systems and stable performance over several cycles, provided that regeneration conditions protect the Eu content. In a further step, Eu is added during electrospinning and then activated under mild alkaline conditions. This route yelds a more homogeneous Eu distribution, higher accessible COO^- density, and higher capacity for tetracycline at much lower Eu content. The kinetics shift towards pseudo-second-order behavior, consistent with chemisorption at Eu sites reached by diffusion in a swollen, rubbery network. These results provide a practical choice for the Eu addition method, CA content, and post-treatments to tune capacity, selectivity, and durability while keeping Eu leaching low.

The second part of the thesis establishes clear links between processing, structure, and function in PE–Ca films. External Ca^{2+} crosslinking compacts the pectin into “egg–box” structures whose interchain spacing and glass transition temperature (T_g) can be adjusted by changing the water content. When water plasticizes the matrix and widens nanochannels, access to carboxylate groups becomes faster and Zn^{2+} uptake occurs mainly through stoichiometric ion exchange at higher Ca contents. In more lightly crosslinked

networks, an additional mechanism appears, where Zn^{2+} also forms additional crosslinks beyond ion exchange. These results identify practical control variables such as crosslinking time (and therefore the amount of Ca), water content, and operating temperature near the hydrated T_g to balance fast initial uptake and total capacity in waters around neutral pH. The combined use of low-angle XRD under controlled humidity, DSC with physical aging, and ion-specific mass balances provides a solid method to separate ion exchange from new crosslink formation in hydrated ionomers.

The third part studies water under confinement to connect material design with transport behavior. By comparing soft, hydrophilic PE–Ca nanochannels with rigid Fe–BTC MOF pores, the thesis shows, with consistent calorimetric (DSC trough enthalpy recovery) and dielectric (BDS) evidence, that confined water undergoes a real glass transition between about 170 and 200 K, rather than at the commonly assumed 136 K event. The T_g depends on how the type of confining environment changes the hydrogen-bond network. In PE–Ca, water is a more bulk-like, and T_g is higher (~193 K). In Fe–BTC, water is more strongly bound at interfaces and T_g is lower (~170 K). This picture helps to clarify long-standing discussions about the glass transition of water and, more importantly, links hydration state and pore chemistry to mobility, diffusion, and adsorption rates in hydrated adsorbents.

The next part applies these ideas to develop a hybrid PE–Ca/Fe–BTC composites (PE–Ca–MOF). Immobilizing Fe–BTC within pectin films and foams solves handling issues associated with MOF powders and extends the range of contaminants that can be removed. Heavy-metal uptake is still controlled by pectin's Ca-mediated ion exchange and is mostly unchanged at moderate MOF contents. In contrast, paraquat and tetracycline, which are not removed by pure PE–Ca at pH 7, are efficiently adsorbed through π–π, electrostatic, and coordination interactions at Fe–BTC sites. The way the MOF is dispersed and the overall material structure are as important as the amount of MOF. Surfactant-assisted (PVP) dispersions and foamed structures promote homogeneous MOF distribution, reduce diffusion limitations, and limit the loss of flexibility observed at high, aggregated loadings. Reuse with green regenerants (such as acetic acid) is possible for weakly coordinated species like paraquat, but less effective for strongly coordinating antibiotics like tetracycline. This shows that a balance between strong binding and easy regeneration can be controlled through dispersion strategy, porosity, and the chemistry of the regenerant solution.

From these studies, it is possible to identify some general design principles. Hydration is central control factor because it affects chain mobility, access to active sites, and diffusion. Working close to the T_g often increases adsorption rates while the material remains mechanically stable. The way that active domains (MOF or Eu sites) are distributed is more important than their total amount. Materials with well dispersed domains and porous structures perform better than materials with a larger active phase that is clumped together. It is also important to balance strong binding with easy regeneration. Very strong interactions, such as Eu–tetracycline coordination, improve its removal but

require specific regeneration solutions that are still environmentally friendly and sometimes with extra reactivation steps. Finally, combining different interaction types (ion exchange in PE–Ca, π and coordination interactions in Fe–BTC, and hard-acid chelation in Eu-functional materials) enables the removal of a wide range of contaminants at neutral pH and gives low-leaching materials suitable for treating secondary effluents or decentralized water treatment.

The thesis also defines current limitations and future opportunities. In PE–Ca–MOF composites, very high MOF contents can make the materials brittle and limit access to active sites. These problems can be reduced by changing particle size or linker chemistry, or by using thin films and foams. For Eu-functional PVA mats, retaining Eu within the material using mild regeneration solutions (or occasional re-doping) is essential when targeting antibiotics with multiple functional groups. All the adsorption tests were done in controlled batch experiments. Studying competitive adsorption in real wastewaters should be further explored, and measuring long-term leaching and mechanical stability are important steps to move closer to practical applications.

In summary, this thesis presents a clear, experimentally supported approach for designing sustainable adsorbents that combine renewable polymers with functional inorganic components. It also shows how to operate these materials effectively by controlling hydration, dispersion, and regeneration. By connecting studies of confined water with adsorption tests, the work explains how molecular and nanoscale interactions can be used to create practical, reusable materials for emerging contaminants. These results support future work on continuous-flow systems, on life-cycle and economic evaluations, and the adaption of these ideas to other non-toxic crosslinkers, trivalent ions, and MOF structures, using the structure–dynamics–performance relationships identified in this thesis as a guide.

SECTION 3

Published Papers

In the context of this PhD thesis, the following works have been published:

1. F. Coin, C. A. Rodríguez–Ramírez, F. S. Oyarbide, D. Picón, S. Goyanes, and S. Cerveny, "Efficient antibiotic removal from water using europium–doped poly(vinyl alcohol) nanofiber mats esterified with citric acid," J. Water Process Eng., vol. 63, no. March, 2024, doi: 10.1016/j.jwpe.2024.105447. The journal was Q1 in *Water Resources* (9/131) with an impact factor of 6.7 at the time of the publication.

2. C. A. Rodríguez–Ramírez, F. Coin, A. Vergara–Rubio, D. Picón, S. Cerveny, and S. Goyanes, "Enhanced tetracycline removal through 'in situ' europium incorporation in poly (vinyl alcohol) (PVA) electrospun mats: Advantages of this strategy in adsorption and reuse over doping," Chemosphere, vol. 372, no. January, 2025, doi: 10.1016/j.chemosphere.2025.144102. The journal was Q1 in *Environmental Science* (32/358) with an impact factor of 8.1 at the time of the publication.

3. F. Coin, A. Larrañaga, and S. Cerveny, "Structural characterization of low methoxyl pectin–based adsorbents: the role of water on pectin structure," Carbohydr. Polym. Technol. Appl., vol. 11, no. June, 2025, doi: 10.1016/j.carpta.2025.100885. The journal was Q1 in *Polymer Science* (9/94) with an impact factor of 6.5 at the time of the publication.

4. F. Coin, V. Di Lisio, D. Cangialosi, and S. Cerveny, "The glass transition and the dynamics of water within pectin and metal–organic framework nanochannels," J. Chem. Phys., vol. 163, no. 16, p. 164507, Oct. 2025, doi: 10.1063/5.0294531. The journal was Q2 in *Physics, Atomic, Molecular & Chemical* (10/39) with an impact factor of 3.8 at the time of the publication.

5. F. Coin, C. Iacovone, and S. Cerveny, "Bio-Based Pectin-Calcium Film and Foam Adsorbents with Immobilized Fe–BTC MOF for Water Contaminant Removal," Polymers, vol. 18, no. 2, p. 171, Jan. 2026, doi: 10.3390/polym18020171. This journal was Q1 in *Polymer Science* (19/94) with an impact factor of 4.9 at the time of the publication.

Journal of Water Process Engineering 63 (2024) 105447

Contents lists available at ScienceDirect

Journal of Water Process Engineering

journal homepage: www.elsevier.com/locate/jwpe

Efficient antibiotic removal from water using europium-doped poly(vinyl alcohol) nanofiber mats esterified with citric acid

Francesco Coin [a,b], C.A. Rodríguez-Ramírez [c,d], Facundo Sanchez Oyarbide [c], David Picón [c,d,e], Silvia Goyanes [c,d,*], Silvina Cerveny [a,f,**]

[a] Centro de Física de Materiales (CSIC, UPV/EHU)-Materials Physics Center (MPC), Paseo Manuel de Lardizabal 5, San Sebastián 20018, Spain
[b] Departamento Polímeros y Materiales Avanzados: Física, Química y Tecnología, University of the Basque Country (UPV/EHU), P. Manuel Lardizábal 3, 20018 San Sebastián, Spain
[c] Universidad de Buenos Aires, Facultad de Ciencias Exactas y Naturales, Departamento de Física, Laboratorio de Polímeros y Materiales Compuestos (LP&MC), Ciudad Autónoma de Buenos Aires, Argentina
[d] CONICET - Universidad de Buenos Aires, Instituto de Física de Buenos Aires (IFIBA), Ciudad Universitaria (C1428EGA), Ciudad Autónoma de Buenos Aires, Argentina
[e] Instituto de Ciencias, Universidad Nacional de General Sarmiento (UNGS), J. M. Gutiérrez 1150, B1613GSX, Los Polvorines, Prov. de Buenos Aires, Argentina
[f] Donostia International Physics Center (DIPC), San Sebastián 20018, Spain

ARTICLE INFO

Editor: Ludovic F. Dumée

Keywords:
Poly(vinyl alcohol)
Adsorption
Antibiotics
Water treatment
Emerging contaminants

ABSTRACT

Increasing antibiotic pollution in water poses both environmental and health risks, contributing to an increase in antibiotic-resistant bacteria. This study proposes a novel adsorbent made of nanofibers of poly(vinyl alcohol) (PVA) created through electrospinning incorporating europium and citric acid that has exceptional adsorption capacities for ciprofloxacin (563.7 mg/g) and tetracycline (235.8 mg/g), two antibiotics of everyday use. Our findings demonstrate that this combination results in a swollen fiber structure where europium and citric acid remain immobilized even when in contact with water and promotes the creation of antibiotic chelation sites. Moreover, the adsorbent maintained its performance for four cycles and two reactivations. Finally, we studied how the adsorption of antibiotics is affected by other contaminants commonly found in water, such as dyes (methylene blue and/or rhodamine) and pesticides (atrazine). This innovative approach involving the use of esterified-doped PVA nanofiber has significant potential for enhancing remediation capacity and represents a promising solution for removing antibiotics from multipolluted water.

1. Introduction

The widespread presence of antibiotics in water systems poses a dual threat to human and environmental health. These pharmaceuticals leak into our water sources, impacting both ourselves and the ecosystems we rely on, as demonstrated in a recent study [1]. When various pollutants exist, antibiotics are highly dangerous, fueling the increase in antibiotic-resistant bacteria [2]. This resistance threatens our ability to treat common infections, potentially creating untreatable superbugs and jeopardizing medical advancements. Additionally, antibiotics disrupt the delicate balance of aquatic ecosystems, harming microorganisms and nutrient cycles and ultimately affecting the health of entire environments. Addressing this growing issue through effective antibiotic removal from water systems has become increasingly essential for safeguarding human and ecological well-being.

Adsorption [3] is a promising approach for tackling antibiotic contamination in water. This process uses solid materials (adsorbents) that attract and bind pollutants such as antibiotics through physical or weak chemical interactions. While existing adsorbents can target various pharmaceuticals, choosing the right one depends on specific water conditions, antibiotic types, and desired water quality. Despite significant advances, the number of adsorbents for the remediation of pharmaceutical products still needs to be increased and probed under multiple adsorption conditions.

* Correspondence to: S. Goyanes, Universidad de Buenos Aires, Facultad de Ciencias Exactas y Naturales, Departamento de Física, Laboratorio de Polímeros y Materiales Compuestos (LP&MC), Ciudad Autónoma de Buenos Aires, Argentina.
** Correspondence to: S. Cerveny, Centro de Física de Materiales (CSIC, UPV/EHU)-Materials Physics Center (MPC), Paseo Manuel de Lardizabal 5, San Sebastián 20018, Spain.
E-mail addresses: goyanes@df.uba.ar (S. Goyanes), silvina.cerveny@ehu.es (S. Cerveny).

https://doi.org/10.1016/j.jwpe.2024.105447
Received 25 March 2024; Received in revised form 1 May 2024; Accepted 6 May 2024
Available online 17 May 2024

Electrospinning technology enables the creation of very tiny fibers (nanofibers) with various applications [4], with poly (vinyl alcohol) (PVA) being the most commonly used polymer because it is non-toxic, water-soluble, cost-effective, and environmentally friendly with an excellent mechanical and chemical stability [5,6]. This is due to its water solubility (simplifying the production process and allowing for the easy incorporation of additives or other materials into the solution), biocompatibility (well tolerated by cells and tissues), and versatility (allowing for the creation of a wide range of fiber diameters and morphologies by adjusting the concentration, viscosity, and applied voltage during electrospinning). However, PVA is water-soluble, which limits its application effectiveness when prolonged exposure to water is needed. Insolubilizing PVA increases its stability, preventing it from dissolving or leaching into treated water. The most common methods for insolubilizing PVA are chemical methods [7], physical methods [8], or blending with other polymers that are insoluble in water [9].

Physical methods promote chemical bonding between the hydroxyl groups of PVA molecules [6], which is usually activated by heating, resulting in PVA dehydration [10]. On the other hand, chemical methods [7] involve the interaction of the hydroxyl group of PVA with reactive functional groups of the crosslinking agent, such as carboxyl, sulfonic, and phosphate groups [11]. Among all the possible chemical agents [12], citric acid (CA) can form covalent bonds with the hydroxyl groups in PVA polymer chains through poly-esterification reactions promoted by heating between 140 and 220 °C, which results in PVA reticulation [13]. CA is recognized as a green functional agent for PVA insolubilization [6,14] and has other advantages, such as low toxicity and cost [15]. It has also been shown that the incorporation of CA into graphene oxide/carboxymethyl cellulose nanocomposite films [16], Banyan aerial root-based biomaterials [17], and β-cyclodextrin/carboxymethyl cellulose hydrogel films [18] improved the performance of the material for antibiotic adsorption. The carboxylic acid groups in CA provide reactive sites on the surface of the material, improving the affinity for antibiotic adsorption.

Electrospun nanofibers based on PVA in combination with other materials (such as cellulose acetate [19], polyacrylonitrile, chitosan, or polyvinylidene fluoride [20]) and additives (citric acid or L-cysteine [10]) have been used to remediate antibiotics in water [21], being the main limitation their low removal efficiency. However, increasing the number and types of active sites on PVA mats can increase the removal efficiency. It has already been proven [22] that incorporating CA into PVA nanofiber can improve the adsorption of antibiotics. Moreover, in previous work [23], we explored the ability of lanthanides (such as europium (Eu)) to bind pharmaceutical products in a pectin matrix crosslinked with Eu with promising results. Therefore, here, the combination of CA and europium was investigated as a doping agent to enhance the performance of PVA-based adsorbents for the first time. This is because a family of widely used antibiotics (for instance, tetracycline) form stable complexes with Eu [24,25], Regarding Eu toxicity, Destefani et al. [26] recently conducted research categorizing Eu as a "category 4" material, indicating that it is not harmful at low concentrations, such as those used here.

This work presents a low-cost, ecofriendly, stable and reusable multi antibiotic adsorbent that combines citric acid and europium within nanofibrous PVA mats fabricated by electrospinning. PVA mats were heat-treated at 190 °C with or without citric acid, followed by doping with europium (500 mg/L solution). We investigated the Eu doping kinetics, structural changes using SEM and infrared spectroscopy, differential scanning calorimetry and Eu^{3+} immobilization during water swelling. Subsequently, the adsorption capacities of two antibiotics, tetracycline (TC) and ciprofloxacin (CIP), were studied at pH 7. Both antibiotics showed enhanced adsorption in the presence of both citric acid and europium. Infrared and UV–Vis spectroscopy revealed the adsorption mechanism and adsorbent reusability with fibers integrity. Finally, we explored how the presence of other pollutants, such as dyes (methylene blue (MB) and rhodamine (RH)) and a pesticide (atrazine (ATRA)), affect TC and CIP adsorption with good performance in neutral condition.

2. Experimental

2.1. Materials

Poly(vinyl alcohol) (PVA) was purchased from Sigma-Aldrich (Argentina, product number 10852), citric acid anhydrous (CA) was purchased from Stanton (Argentina, product number 202106), and europium chloride hexahydrate (product number 203254) was purchased from Merck (Spain). For all the experiments, distilled water with 18.2 MΩ cm resistivity was used.

All pharmaceuticals, colorants and pesticides were purchased from Sigma-Aldrich (Spain). Tetracycline (product number 87128) and ciprofloxacin (product number 17850) were used as antibiotics. In addition, the dyes methylene blue (product number M9140) and rhodamine B (product number R6626) and the pesticide atrazine (product number 45330) were used. Sodium hydroxide was purchased from Sigma-Aldrich (product number S5881), nitric acid (65 % *w*/w) from Scharlab (product number 7697-37-2) and acetic acid (AA) glacial (99 %) were purchased from Fischer Chemical (product number UN2789).

2.2. Nanofiber fabrication and europium-doped PVA

The mats were fabricated using a TL-Pro-BM Robotic electrospinning machine. PVA and PVA-CA mats were obtained from aqueous solution following our previous protocols [13]. 3.4 g of PVA was dissolved in 24.7 mL of distilled water by constant stirring at 80 °C (PVA0). After dissolving the PVA, 0.17 g of CA (5 % of the PVA weight) was added. The mix was stirred for 10 min to obtain a homogeneous solution (PVA5). The solution was electrospun by applying 30 kV between the collector and the needles. The injection flux was 0.4 mL/h per needle, and the distance between the collector and the injector was 12.5 cm.

The mats were fabricated at room temperature and 65 % humidity. The PVA0 solution (without citric acid) was electrospun under the same conditions. To promote the insolubilization of the obtained PVA mats, thermal treatment was used by heating at 190 °C for 15 min. PVA0 and PVA5 mats were doped in 500 mg/L Eu aqueous solution for 60 min at a dose of 2.5 g/L under batch conditions (samples PVA0Eu and PVA5Eu).

Thermal insolubilization results in high mat dehydration. Therefore, the interaction between PVA chains increases. As our previous work explained [13], thermally treated PVA mats exhibit high swelling behavior. During Eu doping under batch conditions (step 2), europium ions are carried inside the fibers by water diffusion, changing their morphology (see Section 3.1).

2.3. Characterization techniques

2.3.1. Solution characterization

To choose the best electrospinning parameters at room temperature, all electrospinning solutions were first characterized regarding viscosity, pH, and conductivity. Viscosity was measured using a Brookfield LVDV – E, and the conductivity and pH of each solution were measured using a Thermo Scientific VSTAR80 ORION instrument equipped with right electrodes. Values of viscosity, conductivity, and pH of each solution are reported in Table S1 in SI.

2.3.2. Fourier-transform infrared spectroscopy

Fourier-transform infrared (FTIR) spectra were recorded on a Jasco FT-IR-6300 spectrometer from 4000 to 600 cm^{-1} with a resolution of 4 cm^{-1} and 200 scans per spectrum in attenuated total reflectance mode at room temperature. All the samples were dried in a vacuum oven for one week and at 40 °C for two days prior to the measurements to ensure a constant water content in all the samples.

2.3.3. Differential scanning calorimetry (DSC)

Standard differential scanning calorimetry (DSC) measurements were performed using Q2000 TA equipment. Experiments were performed at 10 °C/min under a constant helium flow of 25 mL/min. Samples were prepared in non-hermetic aluminium pans. The melting of the crystalline polymer (endothermic peak) was used to estimate the degree of crystallinity, assuming a linear correlation between the peak area and the percentage of crystallinity

$$X_c(\%) = \left(\frac{\Delta H}{\Delta H_{100}}\right) \times 100 \quad (1)$$

where Xc represents the degree of crystallinity, ΔH denotes the experimental heat of fusion (in J g^{-1}), and ΔH_{100} is the heat of fusion of the 100 % crystalline material, equivalent to 138.6 J g^{-1} for the used PVA [27].

2.3.4. Scanning electron microscopy

The composition and morphology of the adsorbents were investigated by scanning electron microscopy (SEM, FEG-SEM, FEI-QUANTA Fei 250) and energy dispersive X-ray (EDX) spectroscopy (silicon drift detector, EDAX). The operation voltage was set at 10 kV using 10,000 to 50,000× magnification.

2.3.5. Inductively coupled plasma–atomic emission and ultraviolet–visible spectroscopy

Inductively coupled plasma–atomic emission spectrometry (ICP–AES; Agilent 5100) was used to measure the equilibrium concentrations of europium. The concentration of the pharmaceutical products was determined using ultraviolet-visible (UV–Vis) spectroscopy (Agilent 8453A), considering the UV–Vis maximum peak at 322 nm and 358 nm for CIP and TC, respectively.

2.3.6. Adsorption experiments

Adsorption experiments were performed in batches under agitation at 125 rpm and at room temperature at pH 7. The pH of the stock solutions was adjusted to 7 using NaOH and HNO_3 at two concentrations 0.1 M and 1 M, and the adsorption dose was 1 g/L for all the experiments. Kinetic experiments were performed at different times (from 5 to 1440 min) at an initial pollutant concentration of 50 mg/L for both pharmaceuticals. Isotherm experiments were performed at different initial concentration (from 5 to 40 mg/L) for 24 h for both pharmaceuticals. The equilibrium concentration (C_{eq}) and concentration at time t (C_t) were measured via UV–Vis spectroscopy. The amount of adsorbed pharmaceutical was determined based on the difference between the initial and final concentrations in the solution.

The equilibrium adsorption capacity (q_{eq}; mg/g) and adsorption at time t (q_t; mg/g) were calculated as follows:

$$q_{eq} = \frac{C_0 - C_{eq}}{d} \quad (2)$$

$$q_t = \frac{C_0 - C_t}{d} \quad (3)$$

where C_0 is the initial concentration of a given crosslinking agent or pollutant (mg/L) and d is the adsorbent dose. The removal efficiency (R %) was calculated as follows:

$$R\% = \left(\frac{C_0 - C_{eq}}{C_0}\right) \times 100\% \quad (4)$$

All adsorption experiments were performed in triplicate, and the data were analyzed using one-way ANOVA on ranks with a 99 % confidence level ($p < 0.01$). The results are reported as the mean values ± standard deviation.

2.3.7. Adsorption data analysis

The adsorption kinetics were fitted using the empirical pseudo-first-order (PFO; Eq. (5)) and pseudo-second-order (PSO; Eq. (6)) kinetic models.

$$\text{PFO}: q_t = q_e\left(1 - e^{-k_1 t}\right) \quad (5)$$

$$\text{PSO}: q_t = \frac{q_e^2 k_2 t}{1 + q_e k_2 t} \quad (6)$$

where k_1 (min^{-1}) and k_2 (g mg^{-1} min^{-1}) are the characteristic time-related constants of the PFO and PSO models, respectively, indicating the adsorption speed at the beginning of the adsorption process [28].

The adsorption isotherms were fitted using the Langmuir (Eq. (7)) and Redlich–Peterson (Eq. (8)) models [29].

$$\text{Langmuir}: q(C_{eq}) = \frac{q_M K_L C_{eq}}{1 + K_L C_{eq}} \quad (7)$$

$$\text{Redlich–Peterson}: q(C_{eq}) = \frac{K_{RP} C_{eq}}{1 + \alpha C_{eq}^{\beta}} \quad (8)$$

where q is the adsorption capacity; q_M (mg/g) is the maximum adsorption capacity; K_L (L/mg) is the Langmuir constant; and K_{RP} (L/mg), β, and α (mg/L) are Redlich–Peterson constants. β is a dimensionless parameter between 0 and 1, representing the heterogeneity factor. The closer the value to zero, the more heterogeneous the surface where the adsorbate interacts.

2.3.8. Reusability

For regeneration and reusability studies, adsorbents were exposed to four adsorption cycles (dose of 1 g/L), each following one desorption cycle. Solutions of 50 mg/L TC or CIP at pH 7 were used for adsorption. The final concentration was measured after 3 h. Desorption was performed for 1 h using AA at 1 % (pH 2.80) and 0.1 % (pH 3.20) for TC and CIP. We chose AA because it is a green acid that is weaker than other commonly used acids [30]. Desorption and adsorption were performed under orbital shaking at 125 rpm. A washing and drying step in water between adsorption and desorption is required to remove excess reagents. The desorption efficiency (R_{des} %) was calculated as follows:

$$R_{des}\% = \left(\frac{C_{des}}{C_0 - C_{ads}}\right) \times 100 \quad (9)$$

2.3.9. Adsorption of multiple contaminants

The adsorption of the studied contaminants (tetracycline and ciprofloxacin) was tested in the presence of other substances at pH 7. Table 1 shows the various contaminant solutions used in this work to study the adsorption of TC and CIP after 24 h of adsorption. The solutions were prepared according to the following criterion: the total concentration of each contaminant must be 50 mg/L (dose of 1 g/L).

3. Results and discussion

3.1. Preparation and characterization of electrospun nanofibers

The sample preparation began by dissolving polyvinyl alcohol (PVA) in water at 25 °C. Different concentrations of citric acid were added to the solution (0 %, 5 %, 10 %, and 15 % with respect to the weight of PVA). After 10 min of vigorous stirring, the solutions were electrospun following the electrospinning procedure outlined in Section 2.2. Subsequently, the PVA mats with varying quantities of CA were heated at 190 °C for 15 min to induce esterification and crosslinking, resulting in insoluble PVA mats (see step 1 in the schematic diagram in Fig. 1). PVA was also subjected to the same procedure to produce insoluble PVA0 (see Fig. 1a). Although solutions with different amounts of CA were electrospun and tested, we will only present the results for 5 wt/wt%

Table 1
Removal of CIP and TC in the presence of dyes (MB and RH) and a pesticide (ATRA). The pH represents the pH of the solution after mixing dyes and antibiotics. The adsorption capacity (q_e) was calculated considering the mass of the active sites (CA + Eu) and the total mass of the adsorbent (PVA5Eu). R corresponds to the removal efficiency.

	Name	Pollutant 1 [mg/L]	Pollutant 2 [mg/L]	Pollutant 3 [mg/L]	q_e active sites [mg/g]	q_e adsorbent [mg/g]	R [%]
CIP	CIP-30	CIP 30 mg/L	/	/	228.5 ± 4.1	13.8 ± 0.4	49.7 ± 0.1
	CIP-48	CIP 48 mg/L	/	/	549.7 ± 4.1	33.2 ± 0.5	69.6 ± 0.5
	CIP48-MB2	CIP 48 mg/L	MB 2 mg/L	/	448.7 ± 7.4	27.1 ± 1.4	56.7 ± 1.7
	CIP48-RH2	CIP 48 mg/L	RH 2 mg/L	/	486.8 ± 7.8	29.4 ± 0.7	63.1 ± 1.5
	CIP48-MB2-RH2	CIP 46 mg/L	MB 2 mg/L	RH 2 mg/L	460.3 ± 7.9	27.8 ± 0.5	60.4 ± 1.1
	CIP30-ATRA20	CIP 30 mg/L	ATRA 20 mg/L	/	243.6 ± 6.8	14.3 ± 0.5	50.4 ± 1.3
TC	TC-30	TC 30 mg/L	/	/	248.3 ± 5.1	15.0 ± 0.5	53.0 ± 1.2
	TC-48	TC 48 mg/L	/	/	223.5 ± 6.7	13.5 ± 1.5	31.4 ± 1.1
	TC48-MB2	TC 48 mg/L	MB 2 mg/L	/	271.5 ± 7.4	16.4 ± 0.9	33.9 ± 1.4
	TC48-RH2	TC 48 mg/L	RH 2 mg/L	/	266.6 ± 7.8	16.1 ± 0.5	34.6 ± 1.9
	TC46-MB2-RH2	TC 46 mg/L	MB 2 mg/L	RH 2 mg/L	286.4 ± 6.2	17.3 ± 0.9	37.3 ± 1.4
	TC30-ATRA20	TC 30 mg/L	ATRA 20 mg/L	/	266.6 ± 7.1	16.1 ± 0.3	54.7 ± 0.6

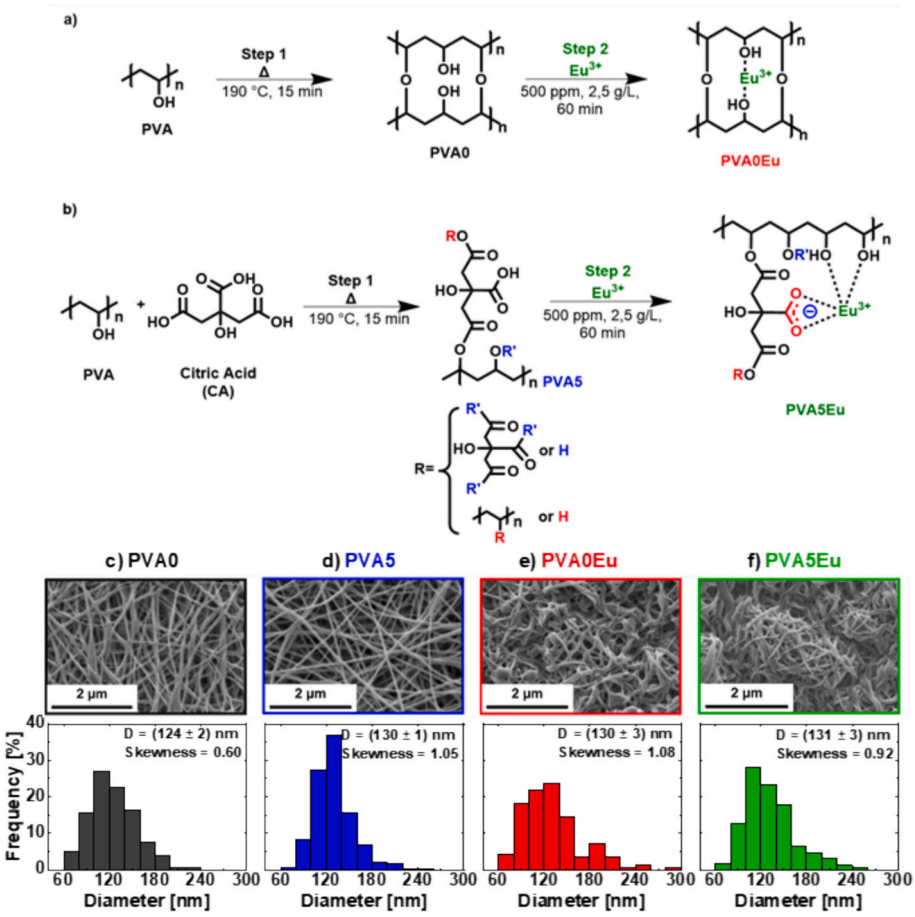

Fig. 1. Schematic diagram of the crosslinking of PVA0 (a) and the esterification and crosslinking of PVA5 with citric acid (b) represented as Step 1. Step 2 represents the doping of PVA0 and PVA5 with Eu (PVA0Eu and PVA5Eu). (c–f) SEM images of PVA mats after insolubilization (magnitude: 50,000×).

citric acid (sample PVA5). This is because there are no significant differences in the adsorption of pollutants with respect to CA content (see Fig. S1 in the SI).

SEM images of the electrospun PVA0 and PVA5 mats after thermal insolubilization are shown in Fig. 1(c–d). The typical structure of randomly oriented nanofibers produced by electrospinning can be observed in both cases. After the thermal treatment, a statistical analysis of the mean fiber diameter indicated that PVA0 exhibited thinner fibers (124 ± 2) nm than PVA5 ((130 ± 1) nm). While it is expected that the presence of CA will increase the conductivity of the electrospinning solution and produce finer fibers [13,31–33], it is also true that the presence of CA results in cross-linking and esterification of the PVA chains (as we will see later), two factors that can increase the size of the fibers in PVA5. On the other hand, with the main objective of improving the adsorption properties of pharmaceutics on PVA mats, Eu was introduced into the mats through doping, which involves immersing a PVA mat in a 500 mg/L Eu aqueous solution for some time. The duration of doping required to maximize Eu adsorption was determined by measuring the adsorption kinetics on PVA5 in a 500 mg/L Eu aqueous solution. As shown in Fig. 2a, the adsorption capacity of Eu is fast, reaching a plateau after 25 min, indicating saturation of Eu in the mat. To ensure that all possible Eu atoms are incorporated into the mat, and

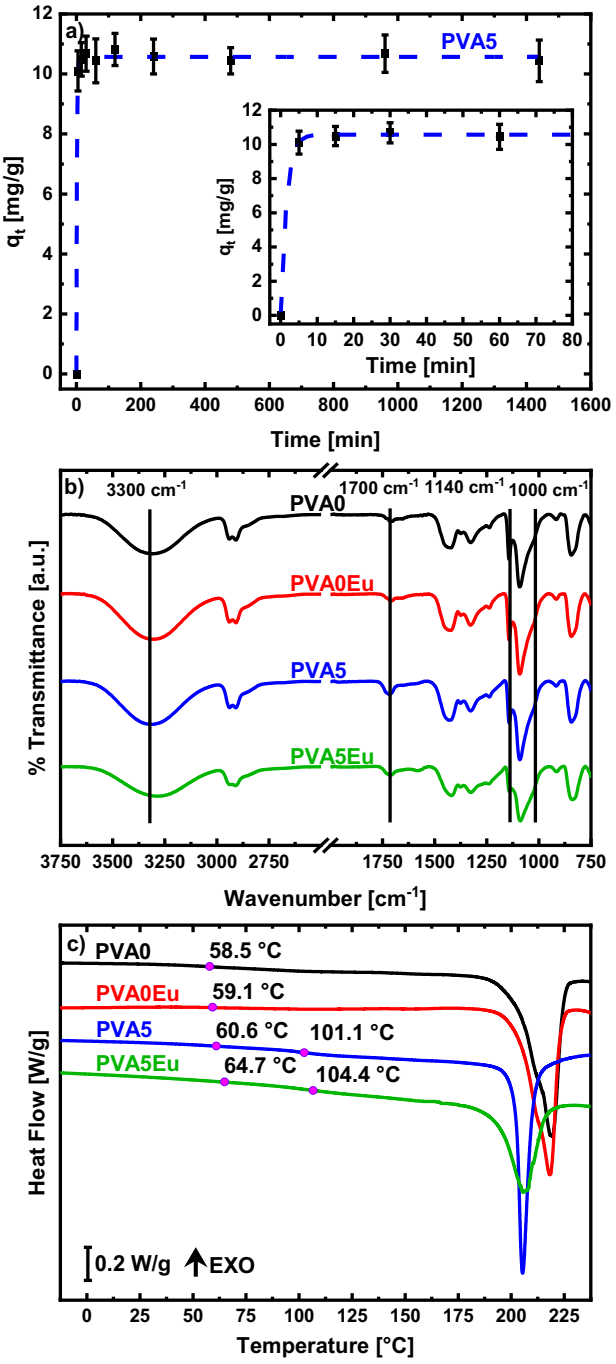

Fig. 2. (a) Adsorption kinetics of Eu (concentration of 500 mg/L) on a PVA5 mat at a dose of 2.5 g/L and pH = 7. The kinetics of doping are well fitted by a PFO model ($R^2 = 0.99$, see dashed line) using $k_1 = 0.62 \pm 0.06$ min^{-1} and $q_e = (10.57 \pm 0.05)$ mg/g. The inset shows an enlargement of the graph for the first 80 min. (b) Infrared spectra of PVA0, PVA0Eu, PVA5, and PVA5Eu. (c) Heat flow measured during heating of PVA0, PVA0Eu, PVA5, and PVA5Eu mats. The pink dots indicate the value of T_g, which was determined as the middle point. (For interpretation of the references to color in this figure legend, the reader is referred to the web version of this article.)

considering that PVA5 exhibits maximum swelling after 20 min [13], 1 h was chosen as the doping time for samples PVA0 and PVA5 in the same way. A schematic diagram of the incorporation of Eu on the PVA0 and PVA5 mats is shown in Fig. 1 as step 2.

After doping, structural changes are also detected in both the PVA0 and PVA5 mats, as shown in the SEM images (Fig. 1e and f). The mean sizes of the nanofibers were very similar, (130 ± 3) nm and (131 ± 3) nm for PVA0Eu and PVA5Eu, respectively, and comparable to those without Eu. However, there is a change in the morphology of the nanofibers that may be partly due to their contact with water during the doping process, causing additional swelling and permanently altering their structure [13]. However, even after extensively washing and drying the nanofibers, as shown in the SEM images, the morphology modification persisted, indicating the role of the Eu ions in the origin of this structural modification. In addition, the EDX results (see Table S2 in the SI) confirmed the successful adsorption of europium on the PVA mats. Moreover, the absorption of Eu is almost double when CA is on the mat (3.58 wt% for sample PVA0 and 7.12 wt% for PVA5). Therefore, CA promotes the adsorption of Eu^{3+}, as we will explain below.

The initial investigation of the developed mats focused on the immobilization of Eu in PVA5Eu after it was subjected to water swelling to ensure that no transfer of Eu to the water occurred during the adsorption process. This procedure comprised three consecutive 2-h cycles of washing in water. After each cycle, the Eu concentration was measured using ICP–AES. Notably, no traces of Eu were detected in any instance, leading to the definitive conclusion that Eu was effectively immobilized within the PVA matrix.

The infrared spectra of the PVA0, PVA5, PVA0Eu, and PVA5Eu mats are compared in Fig. 2b. In all the cases, the main bands related to the O—H (~3300 cm^{-1}), C═O (~1700 cm^{-1}), and C—O (~1140 cm^{-1} and ~1000 cm^{-1}) groups of PVA were observed, consistent with previous reports [10,34,35]. Upon doping PVA5 with Eu^{3+}, the PVA5Eu spectrum reveals that these bands are shifted to lower wavenumbers. These changes suggest that Eu^{3+} binds to the PVA chain through the hydroxyl group (OH) and that the oxygen atom in the carbonyl group of CA actively participates in the chelation of Eu^{3+} with the polymer chain [36–38], as shown in Fig. 1b.

Thus, Eu^{3+} can form complexes with certain types of molecules. Specifically, as discussed above, Eu^{3+} tens to bind with oxygen-containing substances, such as the carboxylate group (COO^-) found in citric acid or the oxygen atoms in PVA. These groups are, therefore, potential chelators for this hard metal acid (i.e., Eu^{3+}), creating exciting possibilities for absorbing pharmaceutical molecules with the availability of these groups.

In this sense, for citric acid, the formation of bidentate and tridentate complexes in which the citrate ion is coordinated with europium has been reported, as shown in Fig. 3 [39–41]. Moreover, for antibiotics of the tetracycline family, the coordination chemistry of europium is governed primarily by electrostatic interactions between the diketone moiety in the antibiotic and the europium ion. The O, O-donor ligands in the β-diketones provide strong coordination spheres for the formation of stable complexes with other trivalent lanthanide ions [42–44], as shown in Fig. 4. It is important to note that a β-diketone group is also available in other antibiotic families, such as fluoroquinolones (for instance, ciprofloxacin).

Moreover, to determine how a β-diketone group interacts with Eu^{3+} ions, we measured the UV–Vis absorption spectra of Eu^{3+} aqueous solutions (500 mg/L) mixed with CA (5 %) and/or TC (20 mg/L) under the same conditions. We examined solutions of citric acid (CA), Eu, and

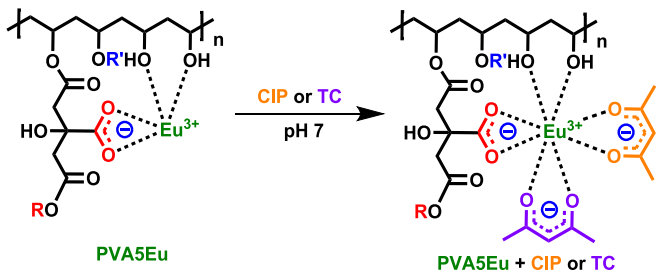

Fig. 3. (a) Proposed mechanism for the interaction between citric acid, PVA and Eu.

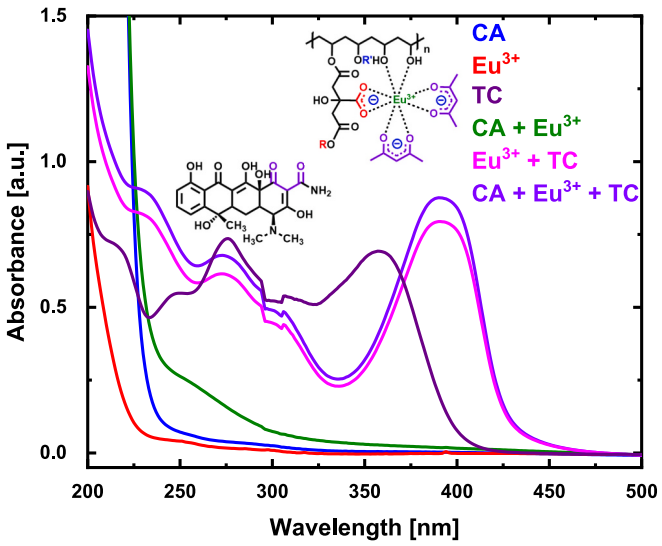

Fig. 4. UV–Vis absorption spectra of citric acid (CA), Eu, and tetracycline (TC) solutions and their combinations (Eu + TC, CA + Eu + TC and TC).

tetracycline (TC) individually, as well as their combinations (CA + Eu, Eu + TC, CA + Eu + TC). As shown in Fig. 4, the absorption peaks of the Eu^{3+} + TC and CA + Eu^{3+} + TC solutions are redshifted (from 360 nm to 390 nm) compared to that of TC alone. This shift suggests modifications in the chromophores of the TC molecule upon the addition of Eu^{3+} ions, enhancing its absorption capabilities due to coordination with β-diketone groups. Furthermore, the absorbance of the solution containing Eu^{3+} + TC was lower than that of the CA + Eu^{3+} + TC solution. Notably, solutions without TC showed negligible absorption in the studied range. These findings suggest the formation of a Eu^{3+}-CA-TC complex, with coordination favored in the presence of a citrate ligand (COO^-). Similar results have been reported for detecting TC by spectroscopic techniques [41]. These observations are also expected for fluoroquinolones such as ciprofloxacin, where a β-diketone group is also available [45].

Finally, a DSC study on the insolubilized mats was conducted to understand the impact of incorporating CA and Eu into the PVA matrix. After a drying cycle (up to 140 °C), samples were cooled and then heated up to melting of PVA. The measurements showed a change in the glass transition temperature (T_g) (58.5 °C < 59.1 °C < 60.6 °C < 64.7 °C for PVA0, PVA0Eu, PVA5, and PVA5Eu, respectively) after adding the different agents. Moreover, samples with CA develop a second glass transition at higher temperatures (104.4 and 101.1 °C for PVA5 and PVA5Eu, respectively). The presence of two Tg indicates a heterogeneous material with two immiscible and distinguishable phases, as previously observed in PVA mats with L-Cysteine and CA [10]. The low-temperature T_g is the conventional T_g associated with the dynamic arrest of pure PVA slightly modified by the additives CA and Eu, lowering the mobility of PVA chains. In contrast, the high-temperature T_g, which appears with the addition of CA, indicates a new phase mainly composed of PVA and CA that esterify and crosslink the PVA. In this phase, the mobility of PVA chains is highly restricted, as revealed by a glass transition of 40 degrees higher than PVA0. Additionally, the percentage of crystallization (determined as the area of the melting peak) changes with the addition of Eu, from 60 % for PVA0 to 55 % for PVA0Eu. Moreover, adding CA strongly decreases the crystallization percentage from 55 % to 37 and 36 % for PVA5 and PVA5Eu, respectively. Thus, CA generates a more amorphous material, probably allowing for a more efficient adsorption process.

3.2. Design of the PVA5Eu nanofibers

Based on the results discussed above, we will identify in this section what type of pharmaceutical products will show optimal compatibility with the newly developed adsorbent (PVA5Eu).

It is well known that pH plays an essential role in adsorption because it determines the ionization state of the adsorbate molecules [46] and the electrical charge on the adsorbent. Consequently, our analysis focused on evaluating the protonation state of both the adsorbent and adsorbate, aiming to elucidate potential mechanisms contributing to the adsorption process. It is crucial to emphasize that a standardized pH of 7 was maintained across all adsorption experiments. Moreover, we will consider two types of antibiotics, ciprofloxacin (CIP) and tetracycline (TC), both of which contain a β-diketone group.

For the PVA5Eu mat, free carboxyl groups are available for adsorption. These include one carboxyl group in CA that did not undergo esterification or crosslinking with PVA and one within the PVA main chain. At pH = 7, these groups are deprotonated (i.e., COO^-), resulting in negative charges on the surface of the adsorbent (see Fig. 5a). These negative charges can interact with positively charged pollutant species found at the same pH [47]. As discussed in the previous section, Eu^{3+} is also available as an adsorption site with a preference for molecules possessing a β-diketone group.

The speciation diagram of CIP (one of the pollutants proposed for adsorption) at pH 7 shows that the carbonyl group is ionized COO^- (pKa1 = 5.9), while the amine group (pKa2 = 8.9) is protonated, resulting in a positive charge [48]. Thus, zwitterionic CIP ± is the dominant species of CIP at pH 7. On the other hand, considering the second antibiotic to explore (TC), its speciation diagram (see Fig. S2 in the SI) indicates that at pH 7, the zwitterionic $TCH_2^{\pm}$ and TCH^- species predominate as the tricarbonylamide and phenolic diketone groups are deprotonated and the dimethylamine is protonated (see Fig. 5b and c) [49].

Several factors, such as the molecular size of adsorbates, the surface area of the adsorbent, and the presence of competing solutes, influence the adsorption process. First, only the effect of the pH of the solution on the ionization state of both the adsorbate and adsorbent was considered. Based on this information, batch adsorption experiments will validate our adsorption model in the next section.

3.3. Antibiotic adsorption

Based on the findings in Section 3.2, CIP and TC were evaluated as potential candidates for adsorption by PVA5Eu. Fig. 6a–c show the adsorption kinetics of CIP and TC using non-doped PVA-CA (PVA5) and Eu-doped PVA (PVA0Eu, PVA5Eu). Based on the results presented in Fig. 6 (a and b), it is evident that the combination of Eu and CA in PVA fibers provides the best adsorption of CIP and TC. In addition, the adsorption of TC for this adsorbent is very fast, reaching a plateau in the first 50 min, and it is slower for CIP, which reaches a plateau after 84 min. For both adsorbates (CIP and TC), PVA0 is not an active adsorbent (results not shown).

By analyzing the results of the adsorbents with a single active site (PVA0Eu or PVA5), it becomes evident that CIP is more significantly adsorbed by PVA5 (adsorbent with CA) than by TC. On the other hand, for PVA0Eu (adsorbent with only Eu), the adsorption efficiencies of both TC and CIP are the same. Furthermore, the results reveal that PVA5Eu has an almost additive effect on the results of PVA0Eu and PVA5 for both TC and CIP. This implies that the adsorption capacity of PVA5Eu can be represented in terms of the total number of active sites (CA + Eu) on the adsorbent that participate in the adsorption mechanism (as shown in Fig. 6c). In this representation, it is clear that TC adsorption is faster (50 min) than that of CIP (80 min).

The adsorption of CIP and TC can be fitted with the PFO model (see fitting criteria in Section S5 in the SI), indicating that both antibiotics interact via weak electrostatic interactions, as discussed in Section 3.2. The adsorption parameters of the PFO model were derived based on the number of active sites within the PVA5Eu mat for both CIP and TC. Specifically, for CIP, the parameters are: $k_1 = 0.061 \pm 0.002\ min^{-1}$ and

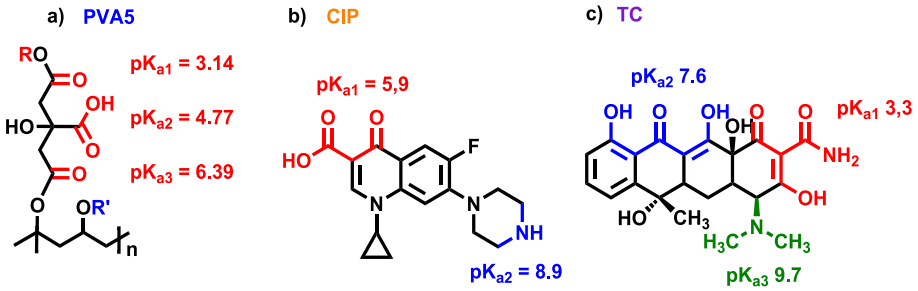

Fig. 5. Schematic representation of PVA5 mats, ciprofloxacin (CIP), and tetracycline (TC) indicating the reactive groups on each molecule with the corresponding pKa value of each group.

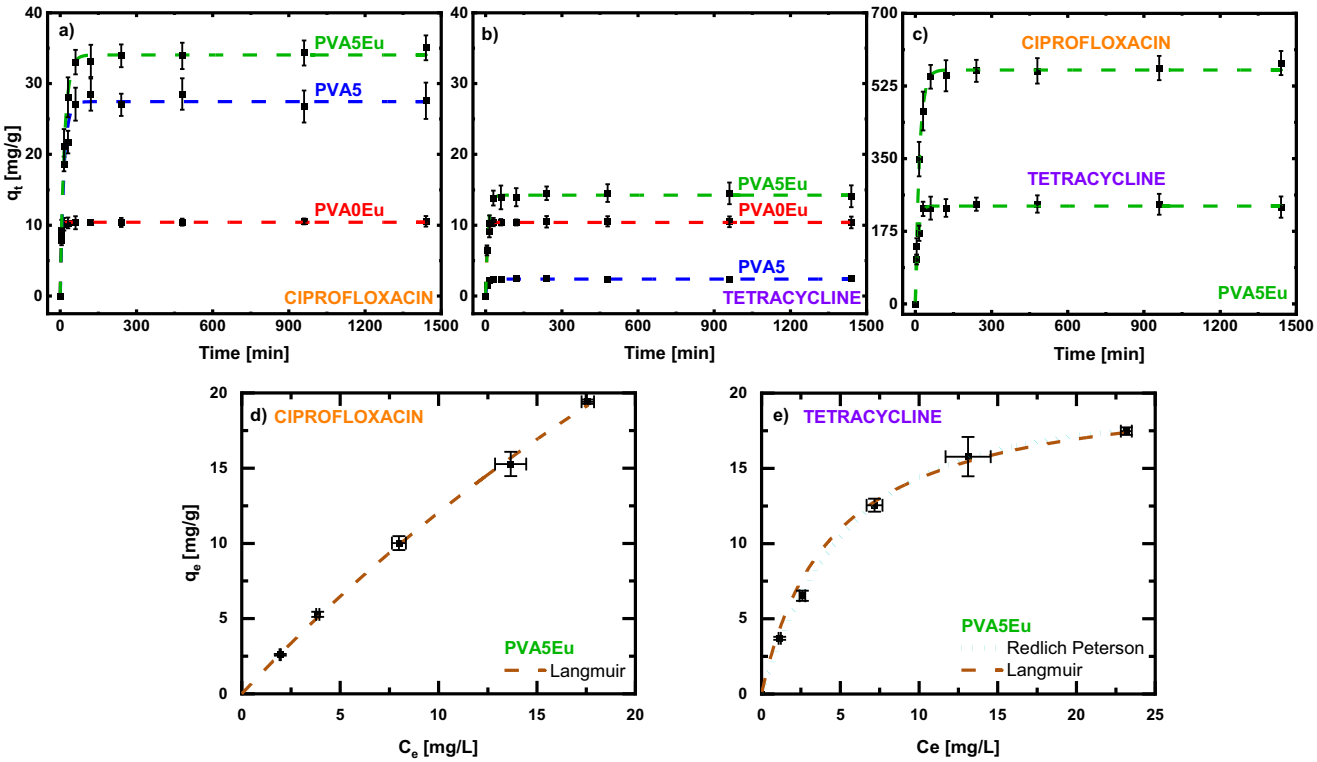

Fig. 6. Adsorption kinetics of PVA0Eu, PVA5, and PVA5Eu for CIP (a) and TC (b) at a dose of 1 g/L. The initial adsorbate concentration was 50 mg/L, and the solution pH was 7. (c) Adsorption kinetics of CIP and TC normalized to the number of active sites in the PVA5Eu mat. Dashed and filled lines represent the fitting of the PFO model (see parameters in Table S3 in the SI for (a and b) and text for data in (c)). Adsorption isotherms of PVA5Eu mat (dose of 1 g/L) at pH = 7 using (d) CIP and (e) TC. The dashed lines in (d) and (e) indicate the nonlinear fittings obtained using the Langmuir model, and the dotted line in (e) indicates the nonlinear fitting obtained using the Redlich–Peterson model.

$q_e = 563.7 \pm 4.1$ mg/g. In contrast, for TC, the parameters are: $k_1 = 0.10 \pm 0.01$ min^{-1} and $q_e = 235.8 \pm 3.1$ mg/g·TC.

Fig. 6 (d and e) shows the CIP and TC adsorption capacities of PVA5Eu after 24 h as a function of the equilibrium CIP and TC concentrations, respectively. The isotherm for CIP was fitted using the Langmuir model ($R = 0.99$, $q_M = 87.5 \pm 14.9$ mg/g). This model assumes that adsorption occurs at identical sites and that only one molecule can be adsorbed at each location [28,29]. The TC isotherm was fitted using both the Langmuir ($R = 0.97$, $q_M = 20.9 \pm 0.3$ mg/g) and Redlich–Peterson models [50] ($R = 0.99$, $\alpha = 0.09 \pm 0.02$ L/mg, $\beta = 1.14 \pm 0.05$). The Redlich–Peterson model has a better statistic, which implies that this system does not exhibit ideal monolayer adsorption behavior; the adsorption sites can be both homogeneous (in the case of Eu) or heterogeneous (in the case of CA) and not identical [51]. This indicates that the structures of the PVA5Eu mat have a better affinity for CIP than TC. Regarding the parameters obtained from the fitting, the $K_L = 0.016 \pm 0.003$ L/mg and $K_{RP} = 3.3 \pm 0.18$ L/mg values indicate that the extent of the interaction between the adsorbate and adsorbent is favorable.

Fig. 7 shows the removal rates of the different studied antibiotics for each adsorbent. For PVA0Eu (red bars in Fig. 7), the removal rate is almost independent of time and the antibiotic type; therefore, in both cases, the same number of complexes are formed (CIP-Eu or CIP-TC) independent of the antibiotic. However, for PVA5 (blue bars in Fig. 7), the removal rate depends on time, reaching a plateau after 60 min for CIP and after 30 min for TC, indicating that the interaction between citric acid and TC results faster than that for CIP.

Finally, the performance of our adsorbent is compared with that of previous adsorbents developed for antibiotics. Das et al. [19] discussed the preparation of montmorillonite-impregnated electrospun cellulose acetate nanofibers for ciprofloxacin removal, achieving a maximum adsorption capacity of 13.8 mg/g at pH 6 in a 10 mg/L solution at room temperature. Li et al. [52] developed a polyacrylonitrile carbon nanofiber membrane for the same purpose, reporting a maximum adsorption

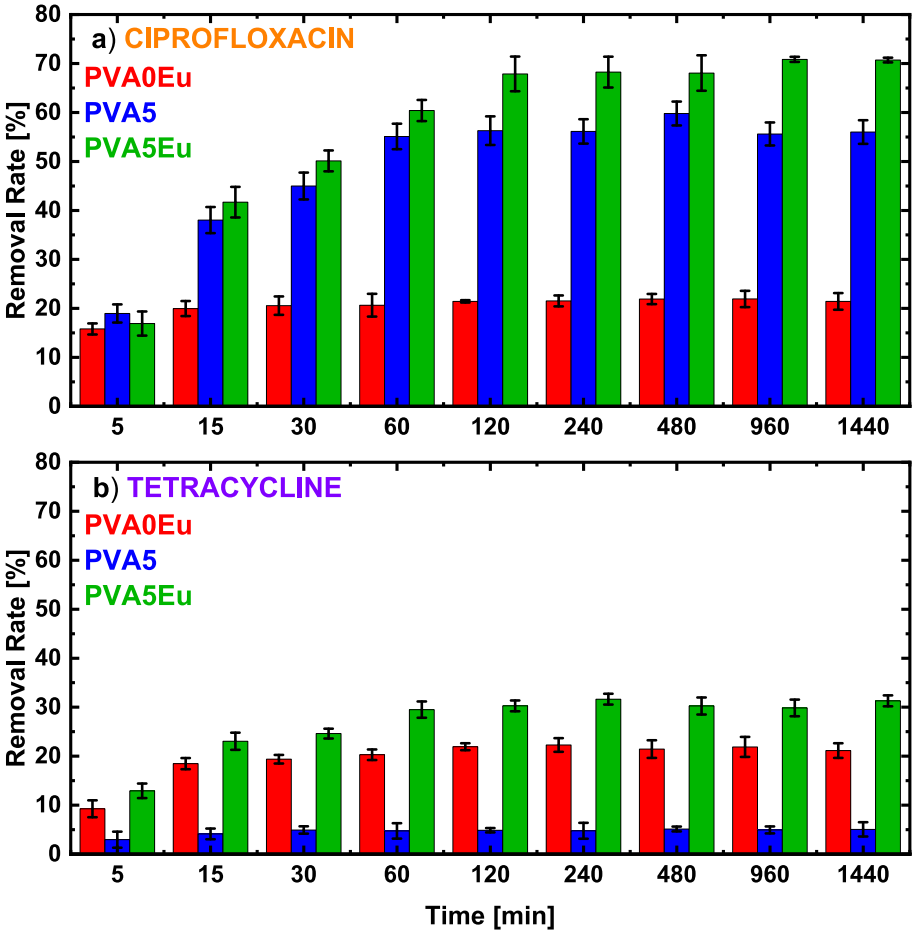

Fig. 7. Removal efficiency of the three adsorbents (PA0Eu, PVA5 and PVA5Eu) versus time.

capacity of 0.68 mmol/g at pH 6.2 in a 10 mg/L solution at room temperature after 8 h. Additionally, Abdolmaleki et al. [53] utilized glutaraldehyde-crosslinked electrospun nanofibers of chitosan/poly (vinyl alcohol) to adsorb tetracycline from water, achieving a maximum adsorption capacity of 102 mg/g at pH 6 in a 100 mg/L solution at room temperature. Park et al. [20] developed a graphene oxide-polyvinylidene fluoride nanofiber membrane, reporting a maximum adsorption capacity of 17.92 mg/g at room temperature in a pH range of 3.8–4.2 in a 200 mg/L solution. Furthermore, they are not reusable or reactivable. Thus, our PVA5Eu mat shows a superior and faster efficacy

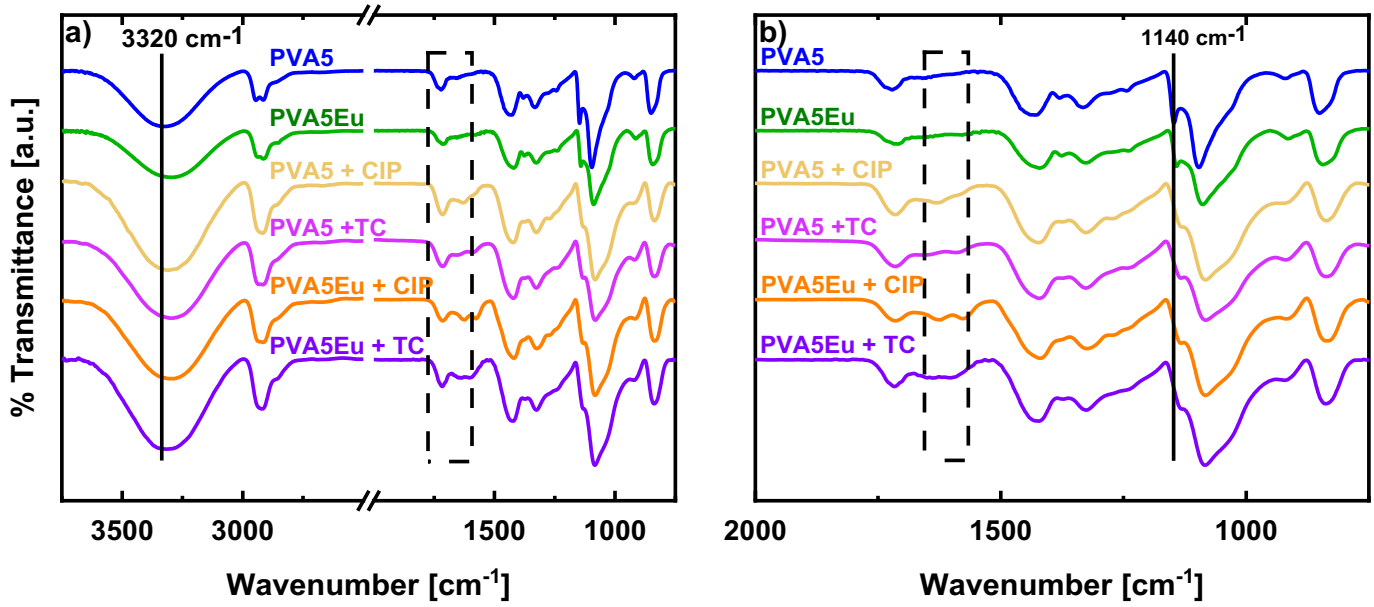

Fig. 8. (a) FTIR spectra of PVA5 and PVA5Eu before and after the adsorption of CIP and TC for 24 h; (b) magnified image of the spectra in (a) from 1600 to 800 cm^{-1}.

than numerous others recently proposed in the literature for the same purpose.

3.4. Adsorbent-adsorbate interactions – FTIR analysis

Fig. 8 compares the FT-IR spectra of the PVA5 and PVA5Eu mats before and after the adsorption of TC, CIP, and Eu^{3+} for 24 h. The typical absorption peaks for PVA were observed in all the samples and are consistent with previous reports in the literature [10,34,35,54,55].

After adsorbing the antibiotics (PVA5 + TC and PVA5 + CIP spectra), the —OH stretching band shifted to a lower wavenumber (3320 to 3300 cm^{-1}), indicating effective interactions between PVA and the antibiotic molecules. This behavior was also reported for PVA/PEG scaffolds loaded with ciprofloxacin [56]. Furthermore, in the PVA5 + CIP spectrum, a characteristic band associated with carbonyl stretching (C = O) at 1626 cm^{-1} of the CIP ketone group is observed [57]. Moreover, in the PVA5 + TC spectrum, a band at 1589 cm^{-1} corresponding to the amide I band of the TC molecule was also observed [56,57]. These results confirm the interaction of the PVA5 matrix with different pharmaceutical molecules.

The PVA5Eu + TC and PVA5Eu + CIP spectra show a similar shift in the OH stretching band to a lower energy region (from 3316 to 3276 cm^{-1}) to that observed for the PVA5Eu mat. In addition, new peaks in the 1629–1569 cm^{-1} region appear, ascribed to carboxylate ($—COO^-$) symmetric and asymmetric stretching vibrations, possibly attributed to the deprotonation of citric acid at pH 7. These results suggest that carbonyl/hydroxyl-containing molecules play an important role in the chelation reaction of trivalent Eu ions, leading to the formation of the citrate-europium complex [40,41,58]. All this information validates the previous studies in Section 3.2.

3.5. Reusability

Studying the reusability of adsorbents is crucial to understanding their possible environmental impact. The method chosen for desorption was acidic-solvent desorption because it is inexpensive, fast, and environmentally feasible. Moreover, our previous studies [23] demonstrated that 1 h was enough time for desorption, which is a relatively quick time for industrial purposes. We performed reusability studies on this adsorbent because PVA5Eu has the best performance for removing TC and CIP.

Fig. 9 shows the results after 4 cycles of desorption-adsorption for PVA5Eu and for both antibiotics, CIP and TC, indicating that PVA5Eu can be reused after adsorption.

First, we used a high acetic acid (AA) concentration (1 %) to desorb TC and CIP. We found an excellent adsorption/desorption rate for CIP even after 4 cycles (Fig. 9a). However, for TC, the adsorption efficiency decreases after the first cycle (Fig. 9b). Using ICP-AES, we determined that both TC molecules and Eu^{3+} ions are desorbing after the first desorption. This may be due to the strong complex formed between TC and Eu. This complex is favored in the presence of AA, in agreement with the above results. (Fig. 4). However, we can still reactivate the adsorbent by re-doping the material in a 500 mg/L aqueous solution of Eu. In both cases, good results were obtained for CIP and TC.

We also explored a lower concentration of AA (0.1 %) to test whether it is possible to avoid reactivation, which limits the release of Eu^{3+} during desorption, as discussed above. The adsorption efficiency decreased less after the first cycle, remained constant for subsequent cycles in the case of CIP (Fig. 9c) and gradually decreased for TC (Fig. 9d). Thus, using a more diluted AA up to 0.1 % resulted in a lower desorption activity, releasing a lower quantity of europium into the water.

Finally, we studied the structural aspect of the adsorbents after three adsorption/desorption cycles for both, the TC and CIP antibiotics. In all the cases, we can observe that the nanofibers are still present but are affected by the acid treatment and swelling (see Fig. S6 in the SI).

3.6. Removal of CIP and TC in the presence of pesticides and dyes

In natural aquatic environments, it is uncommon to encounter a single pollutant [59,60]. Research has shown that water is often contaminated with complex mixtures of chemicals. Therefore, studying how adsorption occurs in a multipollutant environment helps us understand how effective the developed adsorbent will be in actual use.

We analyzed the effectiveness of PVA5Eu in removing CIP and TC (at pH = 7) in the presence of atrazine (ATRA) and dyes (methylene blue (MB) and rhodamine (RH)), both individually and in combination. To determine any hindrance to the removal process caused by other

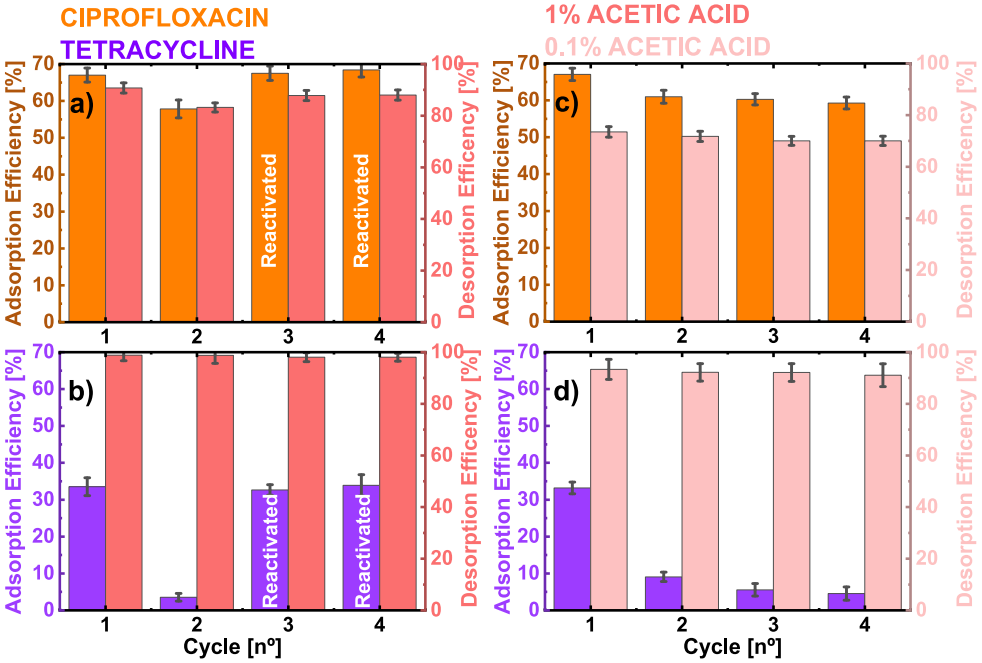

Fig. 9. CIP (a, c) and TC (b, d) adsorption–desorption cycles of PVA5Eu with 1 % acetic acid (a, b) and 0.1 % acetic acid (c, d).

molecules, we considered the protonation state of both the adsorbent and pollutant at pH = 7 (see speciation curves in Fig. S2 in the SI). All experiments were performed in triplicate at pH 7, and the results were compared with those of the reference stock solutions summarized in Table 1.

3.6.1. Removal efficiency of CIP and TC in the presence of dyes

When dyes were introduced into the solutions, noteworthy variations in pH were not observed in the aqueous solutions, indicating the maintenance of pH values at 7 following the addition of dyes. As a result, no anticipated changes in the protonation state of the active sites on the adsorbent were identified; europium remains as Eu^{3+}, and the carboxyl groups on CA remain as COO^{-}.

In terms of removal efficiency, CIP adsorption decrease as both q_e and R decreases with and without dyes (see Table 1). This implies a competitive interaction between the dyes and CIP for the active sites. At pH = 7, dyes undergo protonation, leading to their potential adsorption by PVA5Eu. This phenomenon is visually corroborated by the solutions becoming more colorless, while the film mats exhibit coloration, as evident in the accompanying photographs in the SI (see Fig. S7 in the SI). In contrast, the impact of dyes on TC adsorption is minimal, with q_e remaining virtually unchanged within the experimental error, as detailed in Table 1. Therefore, why does CIP display a more pronounced sensitivity to the presence of dyes than TC? At pH 7, MB and RH exist as cations: MB^{+} and RH^{+} [61,62]. Therefore, these cations can compete with CIP for adsorption sites in the PVA5 material. As discussed in Section 3.3, carboxylates participate in the adsorption of antibiotics, with CIP being more dependent on this type of interaction. This results in lower competition for TC than for CIP when coexisting with dyes. Consequently, the removal efficiency of CIP decreased by 13 %, while that of TC remained relatively constant within the error range in the presence of dyes.

3.6.2. Removal efficiency of CIP and TC in the presence of a pesticide

At pH = 7, ATRA is not an active compound for adsorption since the molecule is in its positive form (see Fig. S8 speciation curves in the SI). This was also confirmed by UV–Vis measurements, which did not show the adsorption of ATRA in PVA5Eu after 24 h. In the presence of ATRA, greater CIP adsorption than TC adsorption was detected (see Table 1). As discussed in Section 3.3, with increasing pH, the number of CIP-positive species increases, while the number of TC-positive species decreases. Therefore, CIP adsorption is more favorable in the presence of atrazine than in the presence of TC, increasing its removal efficiency by 32 %.

4. Conclusions

Positioned as a cost-effective and eco-friendly solution, PVA has emerged as a promising adsorbent for water remediation. In this study, we developed a novel adsorbent by esterifying PVA nanofiber with citric acid and doping them with Eu^{3+}. Our findings underline the significant structural enhancements arising from the synergistic utilization of both active sites. These factors increase the adsorption capacity of conventional PVA-based electrospun nanofibers and expose more carboxylate anions (COO^{-}), enabling the adsorption of high concentrations of pharmaceutical products, even in the presence of coexisting dyes. We also demonstrated a robust removal efficiency and adsorption capacity (70.7 ± 0.5 % and 563.7 ± 4.1 mg/g for CIP and 31.3 ± 1.1 % and 235.8 ± 3.1 mg/g for TC, respectively) at a dose of 1 g/L under neutral conditions (pH = 7). Notably, TC adsorption remains unaffected, mainly in the presence of other contaminants, whereas for CIP, there is a slight decrease in removal efficiency of approximately 10 %. Moreover, the nanofiber structure is maintained after four reusability cycles and two reactivations, positioning this adsorbent for potential industrial applications.

CRediT authorship contribution statement

Francesco Coin: Writing – review & editing, Writing – original draft, Methodology, Investigation, Formal analysis, Data curation. **Carlos Alejandro Rodríguez-Ramírez:** Investigation. **Facundo Sanchez Oyarbide:** Investigation. **David Picón:** Investigation. **Silvia Goyanes:** Writing – review & editing, Writing – original draft, Supervision, Project administration, Conceptualization. **Silvina Cerveny:** Writing – review & editing, Writing – original draft, Supervision, Resources, Project administration, Investigation.

Declaration of competing interest

The authors declare that they have no known competing financial interests or personal relationships that could have appeared to influence the work reported in this paper.

Data availability

Data will be made available on request.

Acknowledgments

Projects PID2019-104650GB-C21 and PID2023-146348NB-I00 funded by MCIN/AEI/10.13039/501100011033, IT1566-22 funded by Basque Government, BILAT23076 funded by CSIC. We kindly acknowledge the financial support of UBA (UBACYT 2023 N°20020220200117BA and PDE_2_2024), ANPCyT (PICT 2021-I-A-01218) and PIP 2022-2024 GI. Francesco Coin and Silvina Cerveny acknowledge the mobility program IMOVE CSIC.

Appendix A. Supplementary data

Supplementary data to this article can be found online at https://doi.org/10.1016/j.jwpe.2024.105447.

References

[1] J.L. Wilkinson, A.B.A. Boxall, D.W. Kolpin, C. Teta, Pharmaceutical pollution of the world's rivers, PNAS 119 (8) (2022) e2113947119, https://doi.org/10.1073/pnas.2113947119.
[2] K. Kümmerer, Resistance in the environment, J. Antimicrob. Chemother. 54 (2) (2004) 311–320, https://doi.org/10.1093/jac/dkh325.
[3] P. Pourhakkak, A. Taghizadeh, M. Taghizadeh, M. Ghaedi, S. Haghdoust, Chapter 1 - fundamentals of adsorption technology, in: M. Ghaedi (Ed.), Interface Science and Technology, Elsevier, 2021, pp. 1–70, https://doi.org/10.1016/B978-0-12-818805-7.00001-1.
[4] S.N. Goyanes, N.B. D'Accorso, Industrial Applications of Renewable Biomass Products, Springer Cham, 2017, https://doi.org/10.1007/978-3-319-61288-1.
[5] O. Duman, H. Uğurlu, C.Ö. Diker, S. Tunç, Fabrication of highly hydrophobic or superhydrophobic electrospun PVA and agar/PVA membrane materials for efficient and selective oil/water separation, J. Environ. Chem. Eng. 10 (3) (2022) 107405, https://doi.org/10.1016/j.jece.2022.107405.
[6] O. Duman, T.G. Polat, S. Tunç, Development of poly(vinyl alcohol)/β-cyclodextrin/P(MVE-MA) composite nanofibers as effective and selective adsorbent and filtration material for the removal and separation of cationic dyes from water, J. Environ. Manage. 322 (2022) 116130, https://doi.org/10.1016/j.jenvman.2022.116130.
[7] B. Bolto, T. Tran, M. Hoang, Z. Xie, Crosslinked poly(vinyl alcohol) membranes, Prog. Polym. Sci. 34 (9) (2009) 969–981, https://doi.org/10.1016/j.progpolymsci.2009.05.003.
[8] M. Miraftab, A.N. Saifullah, A. Çay, Physical stabilisation of electrospun poly(vinyl alcohol) nanofibres: comparative study on methanol and heat-based crosslinking, J. Mater. Sci. 50 (4) (2015) 1943–1957, https://doi.org/10.1007/s10853-014-8759-1.
[9] A. Kumar, S.S. Han, PVA-based hydrogels for tissue engineering: a review, international journal of polymeric materials and polymeric, Biomaterials 66 (4) (2017) 159–182, https://doi.org/10.1080/00914037.2016.1190930.
[10] D. Picón, N. Torasso, J.R.V. Baudrit, S. Cerveny, S. Goyanes, Bio-inspired membranes for adsorption of arsenic via immobilized L-cysteine in highly hydrophilic electrospun nanofibers, Chem. Eng. Res. Des. 185 (2022) 108–118, https://doi.org/10.1016/j.cherd.2022.06.042.

[11] E. Rynkowska, K. Fatyeyeva, S. Marais, J. Kujawa, W. Kujawski, Chemically and thermally crosslinked PVA-based membranes: effect on swelling and transport behavior, Polymers 11 (11) (2019) 1799.
[12] S.A. Stone, P. Gosavi, T.J. Athauda, R.R. Ozer, In situ citric acid crosslinking of alginate/polyvinyl alcohol electrospun nanofibers, Mater. Lett. 112 (2013) 32–35, https://doi.org/10.1016/j.matlet.2013.08.100.
[13] J. Cimadoro, S. Goyanes, Reversible swelling as a strategy in the development of smart membranes from electrospun polyvinyl alcohol nanofiber mats, J. Polym. Sci. 58 (5) (2020) 737–746, https://doi.org/10.1002/pol.20190156.
[14] R. Ciriminna, F. Meneguzzo, R. Delisi, M. Pagliaro, Citric acid: emerging applications of key biotechnology industrial product, Chem. Cent. J. 11 (1) (2017) 22, https://doi.org/10.1186/s13065-017-0251-y.
[15] R. Shi, J. Bi, Z. Zhang, A. Zhu, D. Chen, X. Zhou, L. Zhang, W. Tian, The effect of citric acid on the structural properties and cytotoxicity of the polyvinyl alcohol/starch films when molding at high temperature, Carbohydr. Polym. 74 (4) (2008) 763–770, https://doi.org/10.1016/j.carbpol.2008.04.045.
[16] K. Juengchareonpoon, P. Wanichpongpan, V. Boonamnuayvitaya, Graphene oxide and carboxymethylcellulose film modified by citric acid for antibiotic removal, J. Environ. Chem. Eng. 9 (1) (2021) 104637, https://doi.org/10.1016/j.jece.2020.104637.
[17] H. Fan, Y. Ma, J. Wan, Y. Wang, Z. Li, Y. Chen, Adsorption properties and mechanisms of novel biomaterials from banyan aerial roots via simple modification for ciprofloxacin removal, Sci. Total Environ. 708 (2020) 134630, https://doi.org/10.1016/j.scitotenv.2019.134630.
[18] K. Juengchareonpoon, V. Boonamnuayvitaya, P. Wanichpongpan, Kinetics and isotherms of oxytetracycline adsorption on β-cyclodextrin/carboxymethylcellulose hydrogel films, Aquacult. Res. 50 (11) (2019) 3412–3419, https://doi.org/10.1111/are.14299.
[19] S. Das, A. Barui, A. Adak, Montmorillonite impregnated electrospun cellulose acetate nanofiber sorptive membrane for ciprofloxacin removal from wastewater, J. Water Process Eng. 37 (2020) 101497, https://doi.org/10.1016/j.jwpe.2020.101497.
[20] J.-A. Park, A. Nam, J.-H. Kim, S.-T. Yun, J.-W. Choi, S.-H. Lee, Blend-electrospun graphene oxide/poly(vinylidene fluoride) nanofibrous membranes with high flux, tetracycline removal and anti-fouling properties, Chemosphere 207 (2018) 347–356, https://doi.org/10.1016/j.chemosphere.2018.05.096.
[21] K. Zhao, S.-X. Kang, Y.-Y. Yang, D.-G. Yu, Electrospun functional nanofiber membrane for antibiotic removal in water: review, Polymers 13 (2) (2021) 226.
[22] B. Nagoba, M. Davane, R. Gandhi, B. Wadher, N. Suryawanshi, S. Selkar, Treatment of skin and soft tissue infections caused by Pseudomonas aeruginosa—a review of our experiences with citric acid over the past 20 years, Wound Med. 19 (2017) 5–9, https://doi.org/10.1016/j.wndm.2017.09.005.
[23] J. Martínez-Sabando, F. Coin, J.C. Raposo, A. Larrañaga, J.H. Melillo, S. Cerveny, Dual crosslinking of low-methoxyl pectin by calcium and europium for the simultaneous removal of pharmaceuticals and divalent heavy metals, Chem. Eng. J. 475 (2023) 146162, https://doi.org/10.1016/j.cej.2023.146162.
[24] C.L. Courrol, E.R. Samad, Applications of europium tetracycline complex: a review, Curr. Pharm. Anal. 4 (4) (2008) 238–248, https://doi.org/10.2174/157341208786306216.
[25] M.E. Pacheco, C. Chimeno-Trinchet, A. Fernández-González, R. Badía-Laíño, New europium-doped carbon nanoparticles showing long-lifetime photoluminescence: synthesis, characterization and application to the determination of tetracycline in waters, Spectrochim. Acta A Mol. Biomol. Spectrosc. 284 (2023) 121756, https://doi.org/10.1016/j.saa.2022.121756.
[26] C.A. Destefani, L.C. Motta, R.A. Costa, C.J. Macrino, J.F.P. Bassane, J.F.A. Filho, E. M. Silva, S.J. Greco, M.T.W.D. Carneiro, D.C. Endringer, W. Romão, Evaluation of acute toxicity of europium–organic complex applied as a luminescent marker for the visual identification of gunshot residue, Microchem. J. 124 (2016) 195–200, https://doi.org/10.1016/j.microc.2015.08.021.
[27] C.A. Cozzolino, T.O.J. Blomfeldt, F. Nilsson, A. Piga, L. Piergiovanni, S. Farris, Dye release behavior from polyvinyl alcohol films in a hydro-alcoholic medium: influence of physicochemical heterogeneity, Colloids Surf. A Physicochem. Eng. Asp. 403 (2012) 45–53, https://doi.org/10.1016/j.colsurfa.2012.03.054.
[28] J. Wang, X. Guo, Adsorption kinetic models: physical meanings, applications, and solving methods, J. Hazard. Mater. 390 (2020) 122156, https://doi.org/10.1016/j.jhazmat.2020.122156.
[29] J. Wang, X. Guo, Adsorption isotherm models: classification, physical meaning, application and solving method, Chemosphere 258 (2020) 127279, https://doi.org/10.1016/j.chemosphere.2020.127279.
[30] G. Merli, A. Becci, A. Amato, F. Beolchini, Acetic acid bioproduction: the technological innovation change, Sci. Total Environ. 798 (2021) 149292, https://doi.org/10.1016/j.scitotenv.2021.149292.
[31] V. Jacobs, R.D. Anandjiwala, M. Maaza, The influence of electrospinning parameters on the structural morphology and diameter of electrospun nanofibers, J. Appl. Polym. Sci. 115 (5) (2010) 3130–3136, https://doi.org/10.1002/app.31396.
[32] N. Torasso, A. Vergara-Rubio, P. Rivas-Rojas, C. Huck-Iriart, A. Larrañaga, A. Fernández-Cirelli, S. Cerveny, S. Goyanes, Enhancing arsenic adsorption via excellent dispersion of iron oxide nanoparticles inside poly(vinyl alcohol) nanofibers, journal of environmental, Chem. Eng. (2021) 104664, https://doi.org/10.1016/j.jece.2020.104664.
[33] A. Vergara-Rubio, L. Ribba, D. Picón, R. Candal, S. Goyanes, A highly efficient nanostructured sorbent of sulfuric acid from ecofriendly electrospun poly(vinyl alcohol) mats, Ind. Eng. Chem. Res. 61 (5) (2022) 2091–2099, https://doi.org/10.1021/acs.iecr.1c03530.
[34] J. Lee, K. Jin Lee, J. Jang, Effect of silica nanofillers on isothermal crystallization of poly(vinyl alcohol): in-situ ATR-FTIR study, Polym. Test. 27 (3) (2008) 360–367, https://doi.org/10.1016/j.polymertesting.2007.12.005.
[35] L.V. Smirnov, N.P. Kulikova, N.V. Platonova, Infrared spectra of polyvinylalcohol, Polym. Sci. U.S.S.R. 9 (11) (1967) 2849–2856, https://doi.org/10.1016/0032-3950(67)90392-9.
[36] J. Sahoo, D.S. Lakshmi, P.S. Subramanian, T.M. George, M.L.P. Reddy, Synthesis, characterization and photo-physical properties of Eu(III) complexes and its luminescent thin films, Opt. Mater. 70 (2017) 83–91, https://doi.org/10.1016/j.optmat.2017.05.015.
[37] K.H. Mahmoud, Z.M. El-Bahy, A.I. Hanafy, Calorimetric, optical and catalytic activity studies of europium chloride–polyvinyl alcohol composite system, J. Phys. Chem. Solid 72 (9) (2011) 1057–1065, https://doi.org/10.1016/j.jpcs.2011.06.007.
[38] G. Pıhtılı, F. Biryan, Electrical investigation on Eu+3-doped copolymer composite system and conventional kinetic analysis, J. Mol. Struct. 1230 (2021) 129638, https://doi.org/10.1016/j.molstruc.2020.129638.
[39] T. Kataoka, T. Hashimoto, S. Samitsu, Z. Liu, M. Tagaya, Coordination state control of citric acid molecules on europium(III) ion-doped hydroxyapatite nanoparticles for highly efficient photoluminescence toward biomedical applications, ACS Appl. Nano Mater. 5 (2) (2022) 2305–2315, https://doi.org/10.1021/acsanm.1c03999.
[40] C. Hernández-Fuentes, R. Ruiz-Guerrero, A.D.J. Morales-Ramírez, P. Molina-Maldonado, D.Y. Medina-Velazquez, New mononuclear complex of europium(III) and benzoic acid: from synthesis and crystal structure solution to luminescence emission, Crystals 10 (8) (2020) 674.
[41] L. Han, Y.Z. Fan, M. Qing, S.G. Liu, Y.Z. Yang, N.B. Li, H.Q. Luo, Smartphones and test paper-assisted ratiometric fluorescent sensors for semi-quantitative and visual assay of tetracycline based on the target-induced synergistic effect of antenna effect and inner filter effect, ACS Appl. Mater. Interfaces 12 (41) (2020) 47099–47107, https://doi.org/10.1021/acsami.0c15482.
[42] R. Ilmi, K. Iftikhar, Synthesis, visible light absorption and luminescence of bipyrimidine bridged dinuclear lanthanide complexes of 2,4-pantanedione, Inorg. Chem. Commun. 13 (12) (2010) 1552–1557, https://doi.org/10.1016/j.inoche.2010.09.010.
[43] S. Samanta, P. Roy, P. Kar, Influence of pH of the reaction medium on the structure and property of conducting poly(o-phenylenediamine), Mater. Today: Proc. 2 (4) (2015) 1301–1308, https://doi.org/10.1016/j.matpr.2015.07.046.
[44] Q. Nie, J. Deng, T. Zhou, A facile rapid-response and on-site sensor for tetracycline detection in environmental water based on europium-doped carbonized polymer dots, J. Environ. Chem. Eng. 11 (3) (2023) 109900, https://doi.org/10.1016/j.jece.2023.109900.
[45] N. Torasso, A. Vergara-Rubio, R. Pereira, J. Martinez-Sabando, J.R.V. Baudrit, S. Cerveny, S. Goyanes, An in situ approach to entrap ultra-small iron oxide nanoparticles inside hydrophilic electrospun nanofibers with high arsenic adsorption, Chem. Eng. J. 454 (2023) 140168, https://doi.org/10.1016/j.cej.2022.140168.
[46] Y. Vieira, M.S. Netto, É.C. Lima, I. Anastopoulos, M.L.S. Oliveira, G.L. Dotto, An overview of geological originated materials as a trend for adsorption in wastewater treatment, Geosci. Front. 13 (2022) 101150, https://doi.org/10.1016/j.gsf.2021.101150.
[47] A. Heller, A. Barkleit, H. Foerstendorf, S. Tsushima, K. Heim, G. Bernhard, Curium (iii) citrate speciation in biological systems: a europium(iii) assisted spectroscopic and quantum chemical study, Dalton Trans. 41 (45) (2012) 13969–13983, https://doi.org/10.1039/C2DT31480K.
[48] C.A. Igwegbe, S.N. Oba, C.O. Aniagor, A.G. Adeniyi, J.O. Ighalo, Adsorption of ciprofloxacin from water: a comprehensive review, J. Ind. Eng. Chem. 93 (2021) 57–77, https://doi.org/10.1016/j.jiec.2020.09.023.
[49] G. Gopal, S.A. Alex, N. Chandrasekaran, A. Mukherjee, A review on tetracycline removal from aqueous systems by advanced treatment techniques, RSC Adv. 10 (45) (2020) 27081–27095, https://doi.org/10.1039/D0RA04264A.
[50] Q.-S. Liu, T. Zheng, P. Wang, J.-P. Jiang, N. Li, Adsorption isotherm, kinetic and mechanism studies of some substituted phenols on activated carbon fibers, Chem. Eng. J. 157 (2) (2010) 348–356, https://doi.org/10.1016/j.cej.2009.11.013.
[51] K.Y. Foo, B.H. Hameed, Insights into the modeling of adsorption isotherm systems, Chem. Eng. J. 156 (1) (2010) 2–10, https://doi.org/10.1016/j.cej.2009.09.013.
[52] X. Li, S. Chen, X. Fan, X. Quan, F. Tan, Y. Zhang, J. Gao, Adsorption of ciprofloxacin, bisphenol and 2-chlorophenol on electrospun carbon nanofibers: in comparison with powder activated carbon, J. Colloid Interface Sci. 447 (2015) 120–127, https://doi.org/10.1016/j.jcis.2015.01.042.
[53] A.Y. Abdolmaleki, H. Ziloueі, S.N. Khorasani, K. Zargoosh, Adsorption of tetracycline from water using glutaraldehyde-crosslinked electrospun nanofibers of chitosan/poly(vinyl alcohol), Water Sci. Technol. 77 (5) (2018) 1324–1335, https://doi.org/10.2166/wst.2018.010.
[54] S.-M. Huang, S.-M. Liu, H.-Y. Tseng, W.-C. Chen, Effect of citric acid on swelling resistance and physicochemical properties of post-crosslinked electrospun polyvinyl alcohol fibrous membrane, Polymers 15 (7) (2023) 1738.
[55] D. Yu, Y.-Y. Feng, J.-X. Xu, B.-H. Kong, Q. Liu, H. Wang, Fabrication, characterization, and antibacterial properties of citric acid crosslinked PVA electrospun microfibre mats for active food packaging, Packag. Technol. Sci. 34 (6) (2021) 361–370, https://doi.org/10.1002/pts.2566.
[56] X.-H. Zhou, D.-X. Wei, H.-M. Ye, X. Zhang, X. Meng, Q. Zhou, Development of poly (vinyl alcohol) porous scaffold with high strength and well ciprofloxacin release efficiency, Mater. Sci. Eng. C 67 (2016) 326–335, https://doi.org/10.1016/j.msec.2016.05.030.
[57] Z. Li, Z. Cui, Y. Tang, X. Liu, X. Zhang, B. Liu, X. Wang, M.S. Draz, X. Gao, Fluorometric determination of ciprofloxacin using molecularly imprinted polymer

and polystyrene microparticles doped with europium(III)(DBM)3phen, Microchim. Acta 186 (6) (2019) 334, https://doi.org/10.1007/s00604-019-3448-z.
[58] R. Yao, Z. Li, P. Huo, C. Gong, J. Li, C. Fan, S. Pu, A Eu3+-based high sensitivity ratiometric fluorescence sensor for determination of tetracycline combining bi-functional carbon dots by surface functionalization and heteroatom doping, Dyes Pigments 201 (2022) 110190, https://doi.org/10.1016/j.dyepig.2022.110190.
[59] F. Spilsbury, V. Kisielius, K. Bester, T. Backhaus, Ecotoxicological mixture risk assessment of 35 pharmaceuticals in wastewater effluents following post-treatment with ozone and/or granulated activated carbon, Sci. Total Environ. 906 (2024) 167440, https://doi.org/10.1016/j.scitotenv.2023.167440.
[60] A. Maddalon, A. Pierzchalski, J.L. Krause, M. Bauer, S. Finckh, W. Brack, A. C. Zenclussen, M. Marinovich, E. Corsini, M. Krauss, G. Herberth, Impact of chemical mixtures from wastewater treatment plant effluents on human immune cell activation: an effect-based analysis, Sci. Total Environ. 906 (2024) 167495, https://doi.org/10.1016/j.scitotenv.2023.167495.
[61] I. Khan, K. Saeed, I. Zekker, B. Zhang, A.H. Hendi, A. Ahmad, S. Ahmad, N. Zada, H. Ahmad, L.A. Shah, T. Shah, I. Khan, Review on methylene blue: its properties, uses, toxicity and photodegradation, Water 14 (2) (2022) 242.
[62] A. Steinegger, O.S. Wolfbeis, S.M. Borisov, Optical sensing and imaging of pH values: spectroscopies, materials, and applications, Chem. Rev. 120 (22) (2020) 12357–12489, https://doi.org/10.1021/acs.chemrev.0c00451.

Efficient antibiotic removal from water using Europium-doped poly(vinyl alcohol) nanofiber mats esterified with citric acid.

Francesco Coin[1,2], Carlos Rodríguez Ramírez[3,4], Facundo Sanchez Oyarbide[3,4], David Picon[3,4,5], Silvia Goyanes[3,4*], Silvina Cerveny[1,6*]

[1] Centro de Física de Materiales (CSIC, UPV/EHU)-Materials Physics Center (MPC), Paseo Manuel de Lardizabal 5, San Sebastián 20018, Spain.

[2] Departamento Polímeros y Materiales Avanzados: Física, Química y Tecnología, University of the Basque Country (UPV/EHU), P. Manuel Lardizábal 3, 20018 San Sebastián, Spain

[3] Universidad de Buenos Aires. Facultad de Ciencias Exactas y Naturales, Departamento de Física, Laboratorio de Polímeros y Materiales Compuestos (LP&MC). Ciudad Autónoma de Buenos Aires, Argentina.

[4] CONICET - Universidad de Buenos Aires. Instituto de Física de Buenos Aires (IFIBA). Ciudad Universitaria (C1428EGA), Ciudad Autónoma de Buenos Aires, Argentina.

[5] Instituto de Ciencias, Universidad Nacional de General Sarmiento (UNGS), J. M. Gutiérrez 1150, (B1613GSX), Los Polvorines, Prov. de Buenos Aires, Argentina

[6] Donostia International Physics Center (DIPC), San Sebastián 20018, Spain

*Corresponding author. Tel: +34 943 01 8808, E-mail: silvina.cerveny@ehu.es, (Silvina Cerveny). Tel: +54 11 5285-7511, E-mail: goyanes@df.uba.ar, (Silvia Goyanes)

S1. Electrospinning solution characterization

Table S1 shows the characterization values for the used electrospinning solutions.

Sample	Viscosity [cP]	Conductivity [μS/cm]	pH
PVA0	245 ± 1	610 ± 1	6.13 ± 0.01
PVA5	252 ± 1	819 ± 1	2.74 ± 0.01

Table S1. Characterization of the prepared solutions used for electrospinning.

S2. Influence of TC adsorption by PVA doped with Eu with different citric acid content

Although solutions with different amounts of CA were electrospun and tested (0, 5, 10 and 15 wt/wt% % with respect to PVA weight) and named PVA0, PVA5, PVA10 and PVA15 respectively. Samples were tested in aqueous solution of 20 ppm of TC at pH 7 for 24 hours at a dose 2.5 g/L in batch conditions. TC adsorption increase with the increase of CA content in PVA mats (Fig. S1a). However, no significant differences in TC adsorption were detected after Eu^{3+} doping by PVA esterified with different content of CA (Fig. S1b).

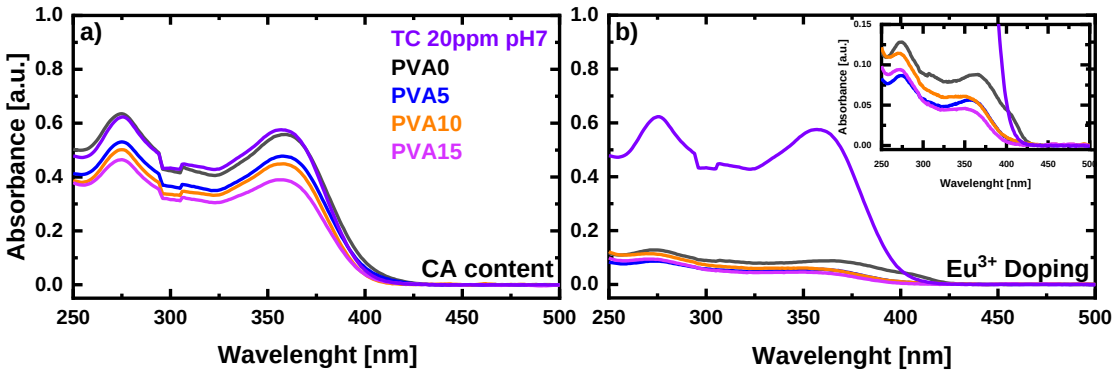

Figure S1. UV-Vis spectra of TC adsorption before (a) and after (b) doping with Eu^{3+} by PVA mats esterified with different content of CA.

S3. SEM-EDAX

Samples were sputtered with Pt and placed in aluminum substrate before SEM-EDX measurements. Before doping, PVA mats showed the existence of carbon (C) and oxygen (O). After Eu^{3+} doping, the EDX results confirmed the successful adsorption of europium on the PVA mats. EDX values were normalized considering the following criteria where η corresponds to the net counts and Mw is the molar mass.

$$\eta_{tot} = \eta_C Mw_C + \eta_O Mw_O + \eta_{Eu} Mw_{Eu}$$

$$\%C = \frac{\eta_C Mw_C}{\eta_{tot}} \times 100$$

$$\%O = \frac{\eta_O Mw_O}{\eta_{tot}} \times 100$$

$$\%Eu = \frac{\eta_{Eu} Mw_{Eu}}{\eta_{tot}} \times 100$$

EDX normalized values are summarized in table S2.

	PVA0	**PVA0Eu**	**PVA5**	**PVA5Eu**
Element	wt [%]	wt [%]	wt [%]	wt [%]
C	61.99	59.78	59.02	54.81
O	38.01	36.65	40.98	38.07
Eu	0	3.58	0	7.12

Table S2. Element content of PVA0, PVA0Eu, PVA5 and PVA5Eu obtained by EDX.

S4. Speciation diagrams of CIP an TC

Data were digitalized from literature using Origin Pro 9. Fig. S2 shows the speciation diagrams of CIP (Fig. S2a) [1] and TC (Fig. S2b) [2].

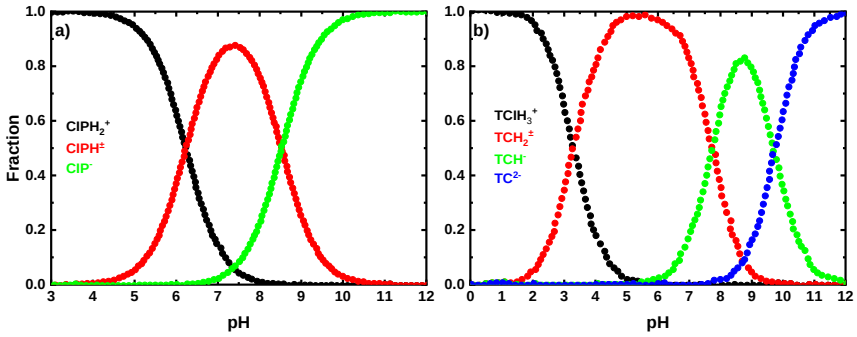

Figure S2. Speciation diagrams of CIP (a) and TC (b).

S5. Choosing criteria of kinetic adsorption model

The pseudo-first-order (PFO) and pseudo-second-order (PSO) models fitted the adsorption kinetics of antibiotics and doping. First, the R^2 and reduced χ^2 criteria were used to compare the results (Fig. S3-5).

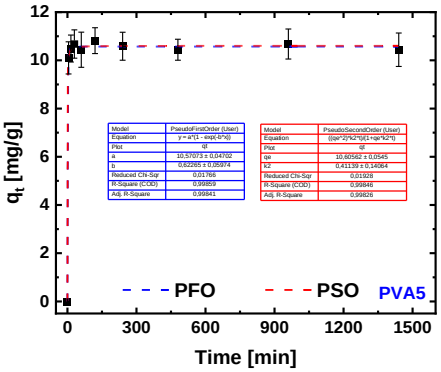

Figure S3. Europium doping kinetic experiments for the cross-linked PVA5. Each table shows the fitting parameters by the pseudo first order (PFO) and pseudo second order (PSO) kinetic models.

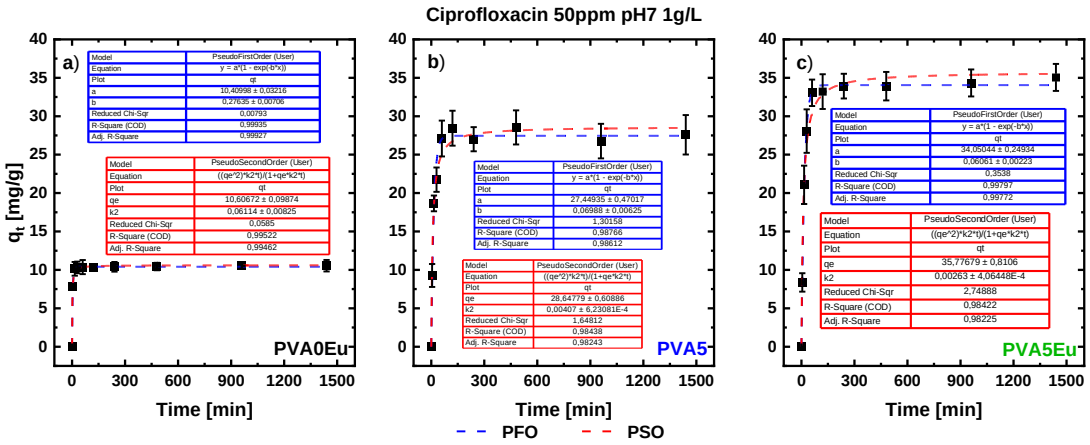

Figure S4. Ciprofloxacin adsorption kinetic experiments for the PVA0Eu (a), PVA5 (b), PVA5Eu (c). Each table shows the fitting parameters by the pseudo first order (PFO) and pseudo second order (PSO) kinetic models.

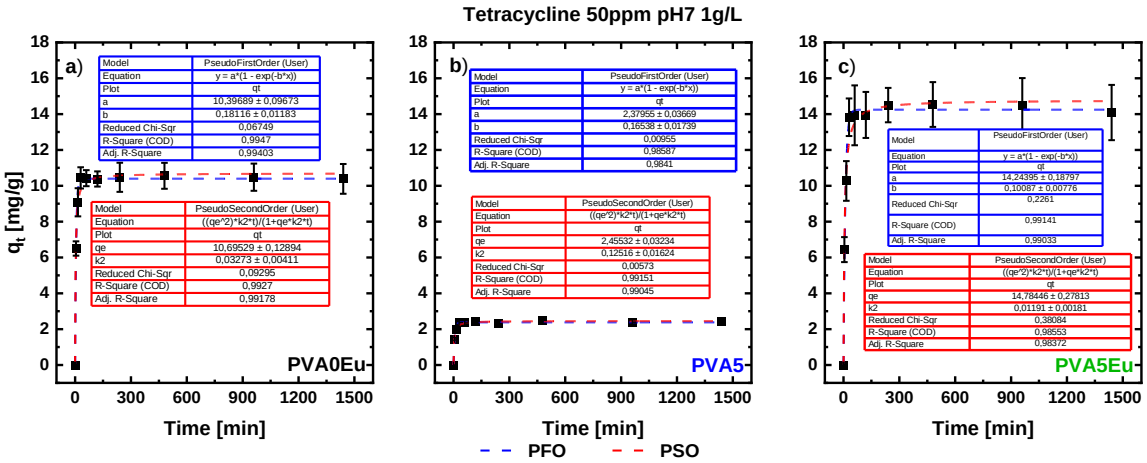

Figure S5. Tetracycline adsorption kinetic experiments for the PVA0Eu (a), PVA5 (b), PVA5Eu (c). Each table shows the fitting parameters by the pseudo first order (PFO) and pseudo second order (PSO) kinetic models.

Additionally, models were compared taking into account the following criteria [3] in order to choose the model that best explains the outcomes of the kinetic experiments:

- The coefficient R^2, which is derived from the linear fitting;

- The Akaike Information Criteria (AIC);

- The Bayesian information criteria (BIC).

$$R^2_{adj} = 1 - \left[\frac{(1-R^2)(n-1)}{n-k-1}\right] \quad (1)$$

where, R^2 is the coefficient of determination, n is the number of points in your data sample, and k is the number of variables in your model excluding constants. The value of R^2 is always between 0 and 1. The closer to 1, the better fit of the model on the data.

$$R^2 = 1 - \frac{SS_{res}}{SS_{tot}} \quad (2)$$

Equations 3 and 4, which are based on the likelihood function, are recognized as being able to measure the validity of nonlinear models. The lowest value between the two models is the one that provides the best information about the data analyzed.

$$AIC = 2p - 2\ln(L) \quad (3)$$

$$BIC = p\ln(n) - 2\ln(L) \quad (4)$$

where, n is the number of points in your data sample, p is the number of parameters estimated by the model and L is the maximized value of the likelihood function of the model.

Models comparison parameters are summarized in table S3. In our case, the three criteria coincide in choosing the model that best fits the data. The more appropriate model for doping and antibiotics adsorption by PVA mats is the PFO

Adsorbate	Sample	Model	k_1[min^{-1}] / k_2[g mg^{-1} min^{-1}]	q_{max} [mg g^{-1}]	R^2_{adj}	AIC	BIC	Prefered Model
Eu	**PVA5**	PFO	0.62 ± 0.06	10.57 ± 0.05	0.99	-32.60	-35.69	PFO
		PSO	0.4 ± 0.1	10.61 ± 0.05	0.99	-31.72	-34.81	
CIP	**PVA0Eu**	PFO	0.276 ± 0.007	10.41 ± 0.03	0.99	-40.60	-43.69	PFO
		PSO	0.061 ± 0.008	10.6 ± 0.1	0.99	-20.62	-23.71	
	PVA5	PFO	0.069 ± 0.006	27.4 ± 0.5	0.99	10.40	7.31	PFO
		PSO	0.004 ± 0.001	28.6 ± 0.6	0.98	12.76	9.67	
	PVA5Eu	PFO	34.1 ± 0.2	0.060 ± 0.002	0.99	-2.62	-5.71	PFO
		PSO	35.8 ± 0.8	0.0026 ± 0.0004	0.98	17.88	14.79	
TC	**PVA0Eu**	PFO	0.18 ± 0.01	10.4 ± 0.1	0.99	-19.19	-22.28	PFO
		PSO	0.033 ± 0.004	10.7 ± 0.1	0.99	-15.99	-19.08	
	PVA5	PFO	0.182 ± 0.006	2.40 ± 0.01	0.99	-63.85	-66.94	PFO
		PSO	0.14 ± 0.02	2.47 ± 0.03	0.99	-42.11	-45.20	
	PVA5Eu	PFO	0.101 ± 0.008	14.2 ± 0.2	0.99	-7.09	-10.19	PFO
		PSO	0.012 ± 0.002	14.8 ± 0.3	0.98	-1.89	-4.98	

Table S3. Table with model used to fit kinetic adsorption experiments and parameters q_{max}, k_1, k_2, adjusted R^2 (Adj. R^2), Akaike information criterion (AIC) and Bayesian information criterion (BIC) for the kinetic experiments for the cross-link and doped PVA. PFO: Pseudo First Order kinetic model. PSO: Pseudo Second Order kinetic model

S6. Fibers morphology after reuse and reactivation

PVA5Eu fibers integrity after reusability and reactivation were justified by SEM measurements. Fig. S6 shows the SEM images of the PVA5Eu adsorbent after three adsorption/desorption cycles with AA 1 % (a and b, reactivated) and 0,1 % (c and d, without reactivation).

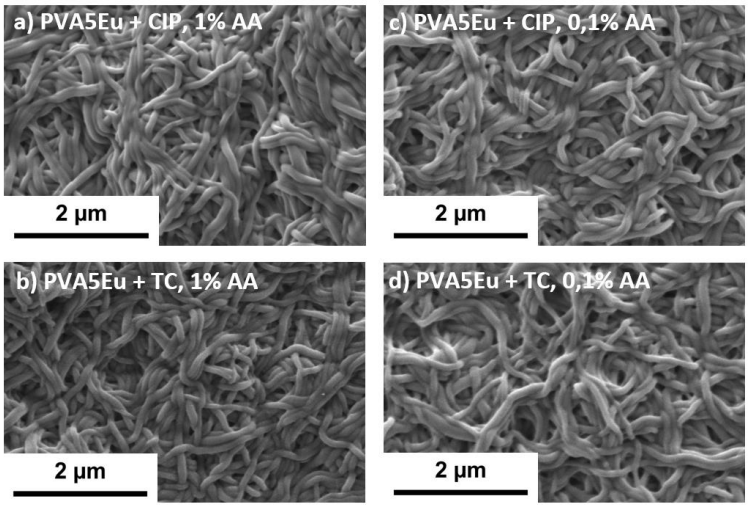

Figure S6. SEM images of PVA5Eu after three adsorption/desorption of CIP and TC. (a and b) using acetic acid 1% wt. (c and d) using acetic acid 0.1% wt.

S7. Adsorption in presence of dyes and pesticide

Fig. S7 justify the adsorption competition between antibiotics and dyes due to color changes of the PVA5Eu adsorbent and stock solutions.

Figure S7. PVA5Eu and stock solutions color changes after antibiotics adsorption in presence of dyes.

S8. Information about Atrazine

At pH = 7, ATRA is not an active compound for adsorption since the molecule is protonated (Fig. S8a) [4]. This was also confirmed by UV-Vis measurements (Fig. S8b). Fig. S8c show the adsorption of CIP and TC in presence of ATRA at pH 7 at dose 2.5 g/L after 24 h at room temperature by PVA5Eu mat.

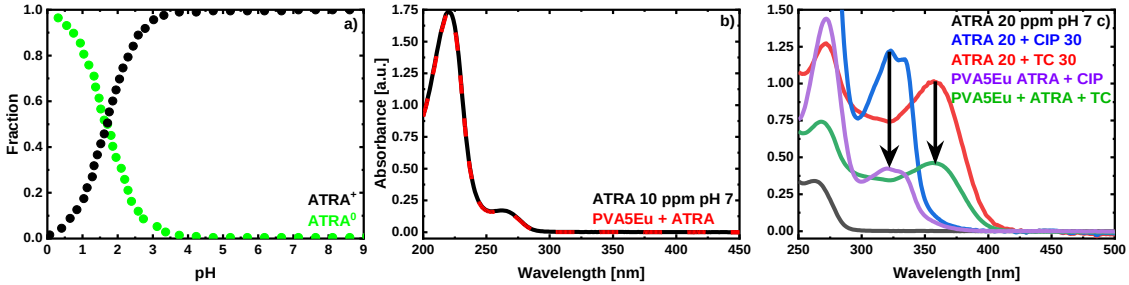

Figure S8. Speciation diagram for ATRA (a), adsorption UV-Vis spectra of 10 ppm of ATRA b) and 30 ppm of CIP and TC in presence of 20 ppm of ATRA (c) by PVA5Eu mat at pH 7 at dose 2.5 g/L after 24 h at room temperature.

References

[1] C. A. Igwegbe, S. N. Oba, C. O. Aniagor, A. G. Adeniyi, and J. O. Ighalo, "Adsorption of ciprofloxacin from water: A comprehensive review," *J. Ind. Eng. Chem.*, vol. 93, pp. 57–77, 2021, doi: 10.1016/j.jiec.2020.09.023.

[2] G. Gopal, S. A. Alex, N. Chandrasekaran, and A. Mukherjee, "A review on tetracycline removal from aqueous systems by advanced treatment techniques," *RSC Adv.*, vol. 10, no. 45, pp. 27081–27095, 2020, doi: 10.1039/d0ra04264a.

[3] J. P. Vareda, "On validity, physical meaning, mechanism insights and regression of adsorption kinetic models," *J. Mol. Liq.*, vol. 376, p. 121416, 2023, doi: 10.1016/j.molliq.2023.121416.

[4] M. S. Netto *et al.*, "Effective adsorptive removal of atrazine herbicide in river waters by a novel hydrochar derived from Prunus serrulata bark," *Environ. Sci. Pollut. Res.*, vol. 29, no. 3, pp. 3672–3685, 2022, doi: 10.1007/s11356-021-15366-4.

Chemosphere 372 (2025) 144102

Contents lists available at ScienceDirect

Chemosphere

journal homepage: www.elsevier.com/locate/chemosphere

Enhanced tetracycline removal through "*in situ*" europium incorporation in poly (vinyl alcohol) (PVA) electrospun mats: Advantages of this strategy in adsorption and reuse over doping

C.A. Rodríguez-Ramírez [a,b], Francesco Coin [c,d], Alicia Vergara-Rubio [a,b], David Picón [e], Silvina Cerveny [c,f,**], Silvia Goyanes [a,b,*]

[a] Universidad de Buenos Aires, Facultad de Ciencias Exactas y Naturales, Departamento de Física, Laboratorio de Polímeros y Materiales Compuestos, Ciudad Autónoma de Buenos Aires, Argentina
[b] CONICET - Universidad de Buenos Aires, Instituto de Física de Buenos Aires (IFIBA), Ciudad Universitaria C1428EGA, Ciudad Autónoma de Buenos Aires, Argentina
[c] Centro de Física de Materiales (CSIC, UPV/EHU)-Materials Physics Center (MPC), Paseo Manuel de Lardizabal 5, San Sebastián 20018, Spain
[d] Departamento Polímeros y Materiales Avanzados: Física, Química y Tecnología, University of the Basque Country (UPV/EHU), P. Manuel Lardizábal 3, 20018 San Sebastián, Spain
[e] Instituto de Ciencias, Universidad Nacional de General Sarmiento (UNGS), J. M. Gutierrez 1150, B1613GSX, Los Polvorines, Prov. de Buenos Aires, Argentina
[f] Donostia International Physics Center (DIPC), San Sebastian 20018, Spain

HIGHLIGHTS

- "*In situ*" Eu^{3+} incorporation followed by alkaline treatment achieved high TC adsorption capacity.
- "*In situ*" mats with 0.36% Eu^{3+} exhibit adsorption like those doped with 1% Eu^{3+}.
- The "*in situ*" mats retained over 80% efficiency in the first 3 reuse cycles, highlighting reusability.
- Ibf and Dcl reduced TC adsorption by ~25%, while Trim and Chlo showed no effect on it.

GRAPHICAL ABSTRACT

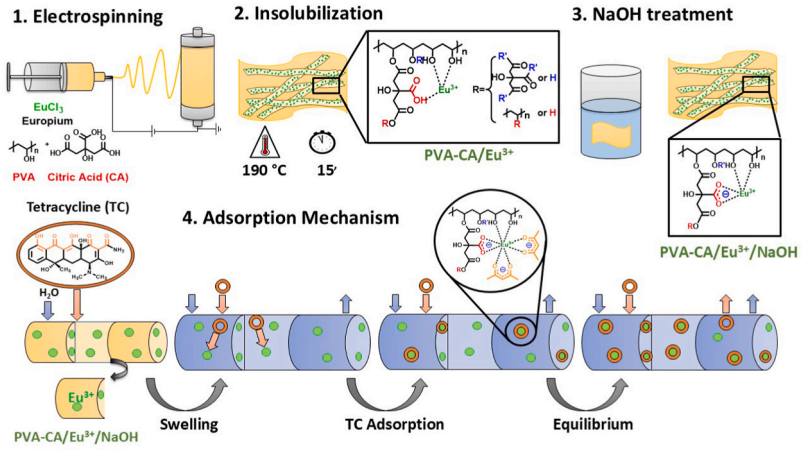

* Corresponding author. Universidad de Buenos Aires, Facultad de Ciencias Exactas y Naturales, Departamento de Física, Laboratorio de Polímeros y Materiales Compuestos, Ciudad Autónoma de Buenos Aires, Argentina.
** Corresponding author. Centro de Física de Materiales (CSIC, UPV/EHU)-Materials Physics Center (MPC), Paseo Manuel de Lardizabal 5, San Sebastián 20018, Spain.
E-mail addresses: Silvina.cerveny@ehu.es (S. Cerveny), goyanes@df.uba.ar (S. Goyanes).

https://doi.org/10.1016/j.chemosphere.2025.144102
Received 7 November 2024; Received in revised form 7 January 2025; Accepted 9 January 2025
Available online 21 January 2025

ARTICLE INFO

Handling editor: Yongmei Li

Keywords:
Electrospinning
Emerging contaminant
Poly(vinyl alcohol)
Tetracycline
Europium

ABSTRACT

Tetracycline (TC) is a widespread contaminant resulting from human, veterinary, and agricultural activities, necessitating urgent removal to protect aquatic ecosystems and the environment from persistent pollutants. We report a novel adsorbent with high efficiency for TC removal, developed by immobilizing europium ions (Eu^{3+}) in PVA nanofiber mats through a single-step electrospinning process using an aqueous solution of the polymer containing europium salt ("*in situ*" process). This approach is three times more efficient than traditional doping methods. Additionally, when "*in situ*" Eu incorporation is combined with alkaline treatment, the removal capacity significantly increases from 235.8 mg/g to 322.6 mg/g (at pH 7) with only 0.36% Eu^{3+}. This improvement results from the excellent dispersion of Eu ions in the mats and the alkaline treatment, which promotes the formation of Eu^{3+}-TC diketone complexes and thus enhances the adsorption capacity. The adsorption mechanism follows the Langmuir isotherm model, indicating that TC is adsorbed in a monolayer at specific, homogeneous sites on the adsorbent. Notably, the "*in situ*" strategy combined with alkaline treatment allows for at least five reuse cycles while maintaining high efficiency. Furthermore, the adsorbent retains its high adsorption capacity even in the presence of coexisting pharmaceuticals such as ibuprofen, diclofenac, trimethoprim, and chlorpheniramine.

1. Introduction

Tetracycline (TC) is currently one of the most commonly used antibiotics due to its efficacy against infections caused by microorganisms and the relatively low cost of production (Rusu and Buta, 2021). Generally, this antibiotic has been employed in treating human and animal diseases (Caneschi et al., 2023; Cherian et al., 2023). The indiscriminate consumption of TC has resulted in large amounts of antibiotics being continuously released into the environment due to incomplete metabolism by organisms (typically accounting for 50–80 %), resistance to degradation, high hydrophilicity, and low volatility (Cui et al., 2020; Gothwal and Shashidhar, 2015; Picon et al., 2023). TC is commonly found in wastewater and persists in aquatic environments, including drinking water sources due to inadequate treatments (Gothwal and Shashidhar, 2015; Mosharaf et al., 2024; Picon et al., 2023). These factors pose significant environmental risks, including developing antibiotic-resistant bacteria and disrupting aquatic ecosystems. In the European Union, there is currently an intention to regulate and control the release of these pollutants into the environment (Gorito et al., 2017). In Latin America, they are neither monitored nor regulated.

Recently, several technologies have been developed to remove tetracycline from water sources: coagulation-flocculation (Gorito et al., 2017), membrane technology (Torasso et al., 2023), advanced oxidation (Palacio et al., 2020), and adsorption (Picon et al., 2023). Among these, adsorption has proven simpler and less expensive, making it highly effective for antibiotic removal (Liang et al., 2021). This process uses solid materials known as adsorbents, facilitating the uptake and removal of pollutants (Liang et al., 2021). It is of utmost importance that the fabrication process of the remediation material be as environmentally friendly as possible, minimizing environmental impact by reducing the use of harmful chemicals, employing sustainable materials whenever possible, and ensuring that the adsorbent does not generate additional contamination and can be easily removed after use (Sitab et al., 2023). Consequently, recently, different eco-friendly materials such as pectin (Martínez-Sabando et al., 2023a, 2023b), biochar (Liang et al., 2021), and polyvinyl alcohol (Choudhury et al., 2021; Picón et al., 2022; Santos et al., 2024; Torasso et al., 2022; Vergara-Rubio et al., 2022) have been explored in the field of water remediation. Moreover, these materials have no tremendous efficiency alone and must be functionalized or combined with adsorbents selected based on the contaminant to be remediated. Against these challenges, some authors have focused on the multiple advantages of confining the adsorbent in a structure without losing its efficiency and environmental risk (Picón et al., 2022; Torasso et al., 2021).

Electrospinning has proven to be an effective technique for immobilizing different types of adsorbents, from metal oxides to organic molecules, on different polymers, particularly polyvinyl alcohol (PVA). PVA is a nontoxic, biocompatible in specific conditions, water-soluble, cost-effective, thermoplastic, environmentally friendly polymeric material and has good mechanical and chemical stability, making it widely used to prepare new adsorbents (Duman et al., 2022a, 2022c, 2022b). The advantage of using PVA is that its nanofibers are highly swellable with water, and therefore the adsorbent immobilized is in contact with the contaminated water and can remediate (Cimadoro et al., 2018a; Santos et al., 2024). Thus, PVA nanofiber mats containing various adsorbents have been effectively used to remove antibiotics, dyes, and heavy metals, among other contaminants (Cimadoro et al., 2018b; Estevez-Areco et al., 2022; Nayl et al., 2022). Lanthanides have emerged as a promising tool due to their ability to form stable coordination complexes with antibiotic molecules containing a β-diketone group (Coin et al., 2024; Martins et al., 2015). This chemical property allows these molecules to be selectively targeted (Martínez-Sabando et al., 2023b). Recently, our group demonstrated the high efficiency of an electrospun PVA mat doped with europium ions (Eu^{3+}) for removing antibiotics from wastewater (Coin et al., 2024). However, the material was not efficient in terms of its reusability. This inefficiency was due to the loss of (Eu^{3+}) during the antibiotic removal process, which occurred before re-evaluating its adsorption capacity. In this context, immobilizing Eu^{3+} within the nanofibers of a PVA mat could be a potential solution. Several studies have shown that when the capturing agent is embedded within the nanofibers, the material can withstand reuse while maintaining high efficiency in contaminant removal (Martins et al., 2015; Nayl et al., 2022; Torasso et al., 2023). Besides, this approach allows homogeneous and well-distributed active sites, minimizes the risk of migration of the adsorbent with the contaminant and facilitates its disposal after use (Martins et al., 2015; Picón et al., 2022; Qi et al., 2014; Torasso et al., 2023). In addition, the electrospinning technique has also been highlighted for its potential in materials development and scalability in producing nanofiber composite mats (Cimadoro et al., 2018a; Kong et al., 2022).

In this work, we present a new advanced material for removing TC from water. The strategy employed combines the advantages of immobilization and homogeneous distribution of the adsorbent (Eu^{3+}) within PVA-CA nanofibers with an alkaline treatment after mat fabrication. This strategy increases the TC adsorption capacity compared to that obtained when Eu^{3+} is incorporated by doping or when no alkaline treatment is performed. This is due to the formation of a greater number of complexes between the Eu^{3+} and the diketone groups of the TC. Both the mechanisms governing the adsorption kinetics of TC and the effect of pH were investigated. Since wastewater often contains several pharmaceuticals, the performance of the material in terms of TC removal in the presence of these compounds was also evaluated, as well as its potential for reuse.

2. Materials and methods

2.1. Materials

Citric acid (CA) supplied by Biopack (Argentina). Mowiol 10–98 polyvinyl alcohol (PVA) (98% hydrolysis and M_w = 61,000 g/mol) was used as the polymer. Europium chloride hexahydrate ($EuCl_3 \bullet 6H_2O$, 99,9%) provided by Merck (Spain) was used as a source of Eu^{3+} ions. Hydrochloric acid (HCl) (37 wt%) and sodium hydroxide (NaOH) (99 %) were used to prepare dilute solutions for pH adjustment purposes. In the adsorption studies, the following pharmaceuticals were employed: ibuprofen (Ibu), diclofenac (Dcl) provided by Sigma Aldrich (Argentina) and tetracycline hydrochloride (TC), Trimethoprim (Trim), and chlorpheniramine (Chlo), all provided by Merck (Spain). All these compounds were at least 95% pure. Deionized water was used to prepare aqueous solutions in all experiments.

2.2. Nanofibers mats preparation

PVA-CA/Eu^{3+} mat was fabricated in a single-step by electrospinning a PVA, CA and europium solution at a fixed ratio (12 wt % of PVA; 5 wt % CA and 0.36 wt % Eu^{3+} concerning the polymer mass) (Cimadoro et al., 2018b; Coin et al., 2024; Estevez-Areco et al., 2022). Firstly, 3 g of PVA and 0.15 g of CA were dissolved in 22 g of 500 mg/L of Eu^{3+} solution under magnetic stirring at 80 °C. Following the cooling of the solution to room temperature, the viscosity was determined using a Brookfield viscometer (model LV-DV-E). Additionally, the conductivity and pH of each solution were measured using a Thermo Scientific VSTAR80 ORION instrument with right electrodes. A summary of solution properties is shown in Table 1.

Electrospinning was performed in an electrospinning machine (Tong Li Tech, China) at 30 kV, flow rate of 2.0 mL/h (0.4 mL/h per needle), and a distance of 12.5 cm between the collector and the injector. Relative humidity was kept at 60 % inside the electrospinning chamber. A PVA-CA solution without europium was used to electrospun a control mat. After electrospinning, the mats were thermally treated at 190 °C for 15 min in an oven to obtain an insoluble material (PVA-CA/Eu^{3+} mat and PVA-CA mat, respectively) [21]. The PVA-CA/Eu^{3+} mats were treated with 1 M NaOH solution for 60 min, then washed with deionized water to neutral pH and finally dried in a vacuum oven at 40 °C for 24 h (PVA-CA/Eu^{3+}/NaOH).

2.3. Physicochemical characterization

Studies were performed in triplicate on random samples of three different mats.

2.3.1. Morphology

Nanofiber's morphology mats were analyzed using a scanning electron microscope Zeiss Supra 40 with a field emission gun operated at 3 kV. Scanning Electron Microscopy (FEI Helios 450S) equipped with EDS was used to evaluate the Elemental composition. Before SEM analysis, all samples were sputtered with platinum.

2.3.2. FTIR spectroscopy

Chemical characterization for all materials was performed by Attenuated Total Reflection-Fourier Transform Infrared (ATR-FTIR) spectroscopy (Jasco FTIR-4100). Spectra were collected with an average of 64 scans per sample in the 4000 cm^{-1} to 600 cm^{-1} range with a resolution of 4 cm^{-1}.

Table 1
Properties of electrospun solutions.

Electrospinning solution	Conductivity (μS/cm)	Viscosity (cP)
PVA- CA	732 ± 3	292 ± 5
PVA-CA/Eu^{3+}	963 ± 3	298 ± 7

2.4. Adsorption experiments

All batch experiments were performed with a fixed amount of PVA-CA/Eu^{3+}/NaOH (2.5 mg/L) in 10 mL of contaminant. Residual TC concentrations were determined using a UV–Vis spectrometer (Shimadzu UV-1800, Kyoto, Japan), which recorded the characteristic TC absorption band at 358 nm. A calibration curve (Absorbance = 0.0325Concentracion - 0.0037) was constructed using the absorbance values obtained in the concentration range of 0.5–200 mg/L. In addition, the experiments were performed in triplicate and at room temperature (25.0 ± 0.1) °C under orbital shaking at 120 rpm. The TC adsorption capacity (q_e) was calculated using Eq. (1).

$$q_e = V(C_0 - C_e) / W \quad (1)$$

where, C_0 (mg/L) and C_e (mg/L) are the initial and final TC concentrations, respectively. W (g) is the dosage of the adsorbents, and V (L) is the volume of the solution. To facilitate comparison with the literature, the q_e values were calculated as follows: i) considering W as the total mass of the material (mass of the PVA-CA/Eu^{3+} mat), and ii) considering W as the mass of the active adsorption sites ($Eu^{3+}$and CA) since PVA mat was not active for adsorption (Coin et al., 2024). The number of active adsorption sites was calculated based on the mass of Eu^{3+} ions and the mass of citric acid in the PVA-CA/Eu^{3+} mat. For a 2.5 g/L dose of PVA-AC/Eu^{3+} or PVA-AC/Eu^{3+}/NaOH mat, there are 0.134 g active sites, composed of 0.125 g AC and 0.009 g Eu^{3+}. This corresponds to 5% AC and 0.36% Eu^{3+} with respect to the mass of PVA. At the same time, the mass of the mats represents the total mass of the material (in this case, 2.5 g), whether it is PVA-CA/Eu^{3+} or PVA-CA/Eu^{3+}/NaOH mats.

2.4.1. Effect of pH on tetracycline removal

Additionally, to determine the pH operating range by PVA-CA/Eu^{3+}/NaOH, TC was adsorbed under the same conditions while varying the pH from 5 to 10. The pH of the TC stock solution was adjusted adding small volumes of 0.1 M NaOH and 0.1 M HCl, respectively.

2.4.2. Adsorption kinetics

Taking into account the adsorption results obtained at different pH levels and the focus of the study on the remediation of TC in drinking water, kinetic studies were carried out at pH 7. The experiments were performed at different times (from 0 to 1800 min) using an initial TC concentration of 50 mg/L. Kinetic models were used to elucidate the removal rate and equilibrium time associated with the adsorption process of TC.

The experimental data were fitted by pseudo-first-order (PFO) and pseudo-second-order (PSO) models, respectively:

The PFO model follows the equation (Duman et al., 2022a, 2022b) (Eq. (2)):

$$In(q_e - q_t) = -k_1 t + In(q_e) \quad (2)$$

The PSO model can be expressed by equation (Duman et al., 2022a, 2022b)(Eq. (3)):

$$\frac{t}{q_t} = \frac{t}{q_e} + \frac{1}{k_2 q_e^2} \quad (3)$$

where q_t (mg/g) is the amount of adsorbed TC at time t (min); while q_e (mg/g) is the amount of adsorbed TC at equilibrium; k_1 (min^{-1}) and k_2 ($g.mg^{-1}.min^{-1}$) are the rate constants of PFO equation and PSO equation, respectively.

2.4.3. Adsorption isotherm

Adsorption isotherm experiments were performed by varying the initial TC concentration (10–200 mg/L) at pH 7, maintaining stirring for 24 h. Experimental data were fitted into common isotherm models,

including the Langmuir model (Eq. (4)), the Freundlich model (Eq. (5)) and the Temkin model (Eq. (6))(Duman et al., 2022b):

$$\frac{C_e}{q_e} = \frac{1}{K_L q_m} + \frac{C_e}{q_m} \tag{4}$$

$$ln\left(q_e\right) = ln\left(K_F\right) + \frac{1}{n}\, ln\left(C_e\right) \tag{5}$$

$$q_e = B_T\, ln\,(K_T) + B_T\, ln(C_e) \tag{6}$$

The parameter in Eqs. (4)–(6), $\boldsymbol{q_e}$ (mg/g) is the equilibrium adsorption capacity, and C_e (mg/L) corresponds to the equilibrium concentration of TC in solution. For the case of the Langmuir model, $\mathbf{K_L}$ (L/mg) is the Langmuir constant, while $\boldsymbol{q_m}$ (mg/g) is the uptake capacity at equilibrium. $\mathbf{q_m}$ and K_L values were estimated through the slope obtained by plotting C_e/q_e *vs* C_e, since q_m and K_L can be determined from the slope $1/q_m$ and intercept $1/(q_m\, K_L)$, respectively.

In the Freundlich model, the Freundlich constant ($\mathbf{K_F}$) represents the adsorption capacity, expressed as $(mol.g^{-1})(L.mol^{-1})^{1/n}$, while "n" is a constant that indicates the adsorption intensity. On the other hand, in the Temkin model, $\boldsymbol{K_T}$ (J/mol), and $\boldsymbol{f}$ (L/mg) are the Temkin constant and the Temkin binding constant, respectively. These terms reflect the adsorption of heat and the maximum binding energy.

2.4.4. Reusability studies

To examine the regeneration and reusability, a series of five adsorption (50 mg/L of TC at pH 7 for 24 h) and desorption cycles on PVA-CA/Eu^{3+}/NaOH mat were conducted, at the same dose of 2.5 g/L. Desorption was carried out using 1 % in volume of hydrochloric and acetic acids for 1 h. Both desorption and adsorption were carried out under orbital shaking at 120 rpm. A washing and drying step in water between adsorption and desorption is required to remove excess reagents. The removal efficiency (RE) of each cycle is then obtained using Eq. (7):

$$RE\ (\%) = 100\frac{C_n}{C_1} \tag{7}$$

C_n (mg/L) is the final concentration after n adsorption cycles, and C_1 (mg/L) is the final concentration after the first adsorption cycle.

2.4.5. Competitive effect

The competition study was carried out at pH 7 in batches by separately preparing mixtures of TC (50 mg/L) with four different drugs (diclofenac, ibuprofen, trimethoprim and chlorpheniramine maleate) at (20 mg/L). The adsorption of TC was measured, and the amount adsorbed at 24 h (q_t) was determined using Eq. (1).

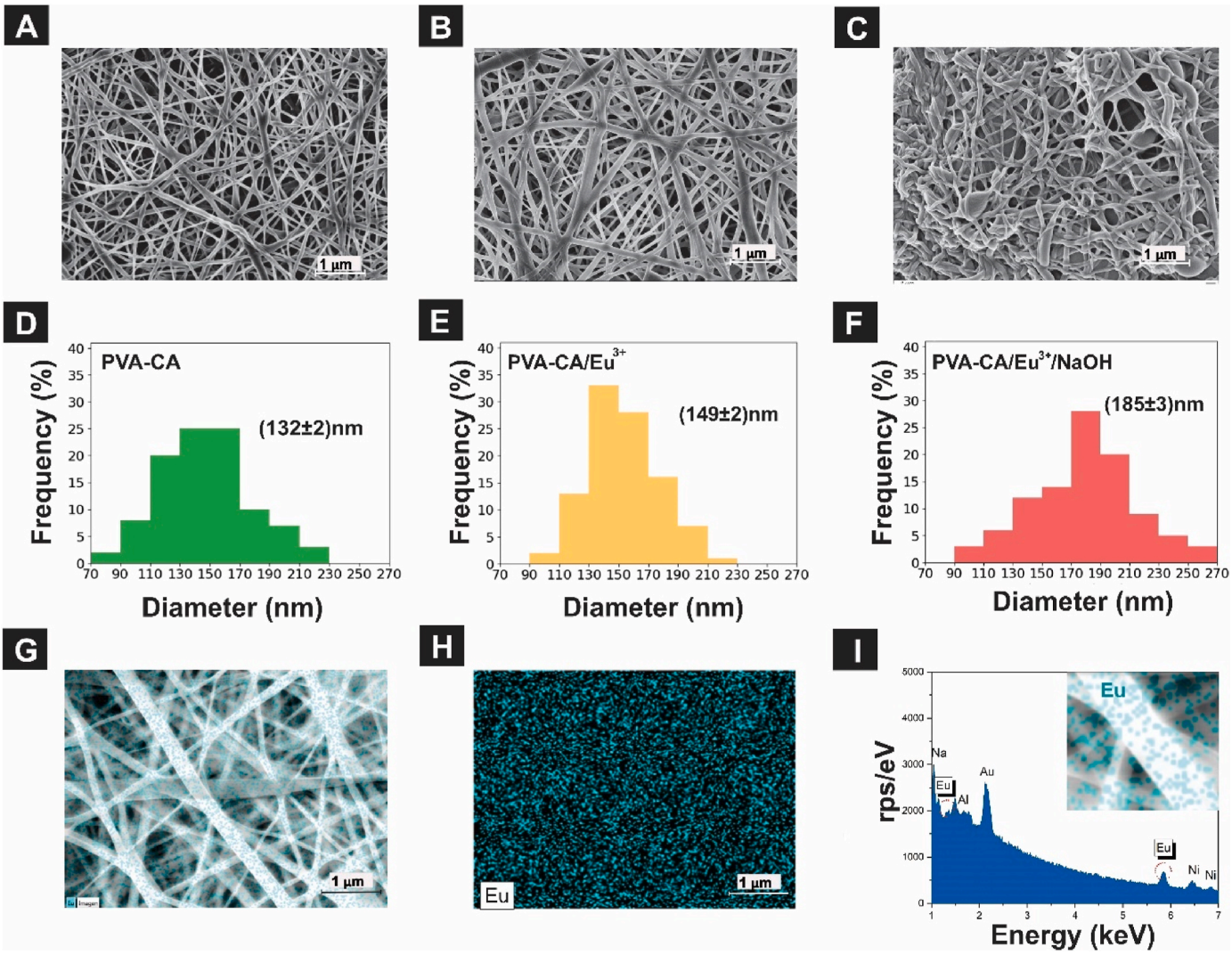

Fig. 1. SEM images of **A and D**: PVA-CA; **B and E**: PVA-CA/Eu^{3+}, **C and F**: PVA-CA/Eu^{3+}/NaOH mats and nanofiber diameter histograms for each mat. **G-I**: EDS spectrum of PVA-CA/Eu^{3+}/NaOH.

3. Results and discussion

3.1. Morphology of the electrospun mats

SEM micrographs, fiber diameter distribution, and EDS spectra of PVA-CA/Eu^{3+}/NaOH for each mat obtained are shown in Fig. 1.

PVA-CA, PVA-CA/Eu^{3+}, and PVA-CA/Eu^{3+}/NaOH mats exhibit the typical morphology for an electrospun mat characterized by randomly oriented nanofibers. The addition of Eu^{3+} increases the mean diameter of the nanofibers to (149 ± 2) nm compared to that obtained for the PVA-CA mat (132 ± 2) nm (Fig. 1A–B). However, this result is not expected as the conductivity of the solution increases (see Table 1) and, therefore, the average diameter of the nanofibers should decrease (Torasso et al., 2023). Then, our results imply that Eu^{3+} interacts with the polymer matrix chains (Coin et al., 2024), acting as a spacer between them, increasing the diameter of the nanofiber. Moreover, the PVA--CA/Eu^{3+}/NaOH mat showed a greater increase in the mean sizes of the nanofibers (185 ± 3) nm, compared with the mat without NaOH treatment, indicating a more significant change in the chemical of the material (Fig. 1B and C). The subsequent NaOH treatment, which involves immersing the PVA-CA/Eu^{3+} mat in an aqueous solution, induces water adsorption into the polymer network. This adsorption causes the fibers to swell. However, the fibers do not fully return to their original size upon drying. Previous studies on PVA-CA systems have shown that this partial irreversibility of swelling is due to residual water retention in the polymer matrix after drying (Cimadoro and Goyanes, 2020). This effect explains the observed increase in fiber diameter after the treatment. Through EDS, it was observed that the Eu/C ratio was maintained before and after the alkaline treatment (Table S1, Figs. S1 and S2). In addition, the presence and homogeneous distribution of Eu^{3+} was observed in Fig. 1G–I.

3.2. FTIR spectra analysis

The effects of the incorporation of Eu^{3+} and the alkaline treatment on the chemical structure of the polymer are presented in Fig. 2. The spectrum PVA-CA mat (Fig. 2A) exhibits the typical bands reported in previous work (Estevez-Areco et al., 2022; Vergara-Rubio et al., 2022; Zhang et al., 2019). On the other hand, the incorporation of Eu^{3+} into the PVA-CA nanofibers (PVA-CA/Eu^{3+}) can also be seen in the FTIR spectra as evidenced by the shift in the bands at 3320 cm^{-1} (O–H stretching), 1716 cm^{-1} (C═O stretching), 1145 cm^{-1} (C–*O*–C stretching) and 1096 cm^{-1} (C–O stretching) to lower wavenumbers in comparison to the as-spun PVA-CA mat spectra. These results are consistent with the observations reported by Yao et al., who attributed these changes to coordination between Eu^{3+} and carboxyl groups (Yao et al., 2022).

Previous reports (Qi et al., 2014; Shang et al., 2018; Wang et al., 2016; Zhang et al., 2019), showed strong interactions between lanthanide ions and carboxylic groups (particularly at pH levels above the pKa of carboxylic acid groups). Qi et al. (2014) studied the complexation behavior of polyacrylic acid (PAA) with lanthanide ions (Ce^{3+}, La^{3+} and Pr^{3+}) at different pH values. The ionization degree of the COOH group strongly affected the complex formation. The authors reported that the COO- group is a stronger ligand than the COOH group. The complex formation was favored between pH 6 and 8 (Qi et al., 2014). Moreover, the formation of Ce^{3+} acetate complexes in which three carboxylate groups are coordinated with one Ce^{3+} cation has been reported.

A comparative analysis of the spectra for the PVA-CA mat treated in an alkaline medium with and without Eu^{3+} reveals that the C═O stretching absorption at 1716 cm^{-1} is reduced to a minimum, and new bands in the 1655-1550 cm^{-1} range are observed (Fig. 2B). These bands are related to the symmetric and asymmetric stretching vibrations of the carboxylate group (COO-) which arise from the ionization of COOH groups of citric acid in alkaline conditions. However, the PVA-CA/Eu^{3+}/NaOH system exhibits a noticeable shifting of the O–H band to a lower energy region (from 3300 to 3285 cm^{-1}) further confirming the interaction of europium cations with oxygen-containing groups (Fig. 2A) (Qi et al., 2014).

3.3. Adsorption studies

3.3.1. Comparative study between dropping and "in situ" europium incorporation and alkali treatment in mat

Fig. 3 presents a comparative study after TC adsorption as a function of the mat mass and active sites for europium-doped mats (Coin et al., 2024), synthesized "*in situ*" and "*in situ*" with subsequent alkaline treatment.

As shown in Fig. 3, the adsorption capacity of TC, obtained as a function of the mass of the mat for the doped and "*in situ*" systems did not show significant differences. However, as a function of active sites, this capacity is slightly lower for the doped system, suggesting that many of the active sites are not available for complex formation with the diketone groups of the TC. It is important to note that, despite the doped

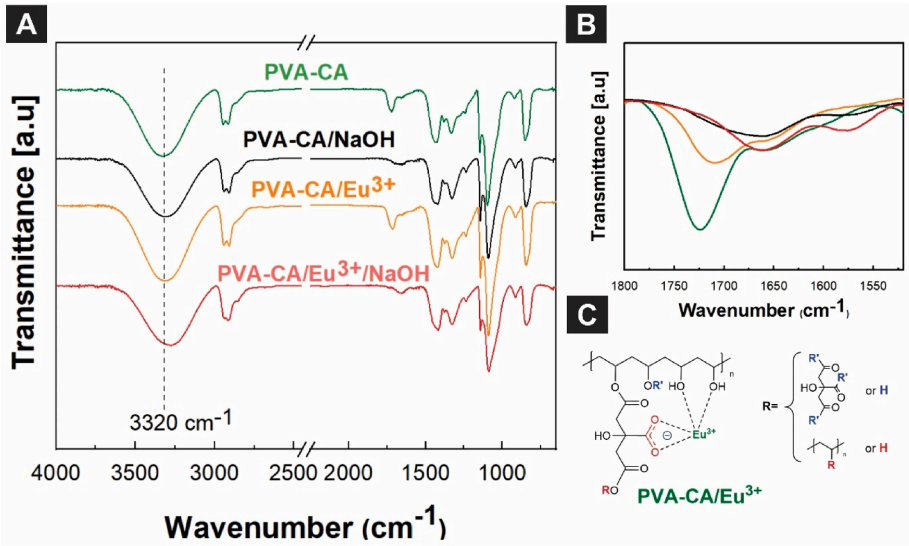

Fig. 2. A. FTIR spectra of PVA-CA, PVA-CA/NaOH, PVA-CA/Eu^{3+} and PVA-CA/Eu^{3+}/NaOH; **B**. close-up of spectra from 1800 to 1520 cm^{-1}; **C**. Coordination between PVA-CA and Eu^{3+} after basic treatment.

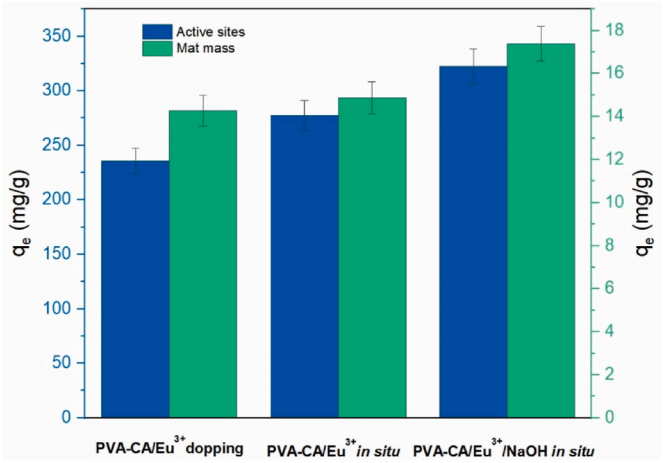

Fig. 3. Comparative study between doped and *"in situ"* europium incorporation and alkali treatment in mat mass and active sites.

system having a greater europium content (1 wt%) compared to the *"in situ"* incorporation system performed in this study (0.36 wt%). Finally, the material obtained by combining the "*in situ*" system followed by the alkaline treatment further increases the adsorption capacity of TC, due to an increase in the number of active sites, which promotes the formation of PVA-CA-Eu^{3+} increasing the formation of the PVA-CA/Eu^{3+}/NaOH/TC complexes.

3.3.2. Initial pH effect towards the TC adsorption

pH influences both the degree of ionization of the pollutants and the surface charge of the adsorbent, significantly affecting the adsorption process. Fig. 4 shows the pH effect on the adsorptive removal of TC using PVA-CA/Eu^{3+}/NaOH.

Since tetracycline is reported to have three different pKa values: 3.3, 7.7, and 9.7, which correspond to its cationic (TC^{+}), zwitterionic (TC$^{\pm}$), and anionic (TC^{-}) forms in acidic, neutral, and alkaline conditions (Fig. 4B and C), respectively we can indicate that:

A reduction in TC adsorption was observed at pH 5 due to electrostatic repulsion between positively charged TC species in the solution and Eu^{+3} immobilized in the mat (He et al., 2023; Zhao et al., 2023). As the pH increases from acidic to near neutral (pH 7–8), the charge of TC changes from positive to neutral or negative. Due to its high charge, Eu^{3+} exhibits a strong polarizing ability that generates negative charge density in TC, leading to increased adsorption capacity due to heightened electrostatic attraction. Therefore, the highest adsorption of TC can be attained under neutral conditions (Zhao et al., 2023).

Conversely, TC adsorption was reduced at pH values above 8. These results agree with Zhao et al. (2021), who attributed this behavior to the formation of europium hydroxide due to the competition for metal coordination sites between hydroxide groups and the oxygen ligands in the TC molecule. On the other hand, at pH above 7, repulsion forces are generated between the carboxylate groups generated in the material and the anionic TC^{-} species (Ocampo-Pérez et al., 2012).

3.3.3. Adsorption kinetic

The adsorption kinetics of tetracycline (TC) on PVA-CA/Eu^{3+}/NaOH were investigated over time intervals ranging from 1 to 1800 min, as shown in Fig. 5A and B. Both plots exhibit a similar trend: an initial rapid increase in adsorption during the first 90 min, attributed to the high availability of active sites. However, after 700 min, the adsorption rate decreased and gradually reached equilibrium at approximately 920 min. This behavior suggests that, as adsorption progresses, active sites become increasingly occupied, leading to gradual saturation and ultimately reaching the maximum adsorption capacity (Liao et al., 2022).

To elucidate the adsorption mechanism, PFO and PSO models were applied to describe the tetracycline adsorption by the PVA-CA/Eu^{3+}/NaOH system. As shown in Fig. 5C and D, the PSO model provided a higher concordance with an $R^2 = 0.99$, indicating that the TC adsorption process is predominantly governed by chemisorption (Choi et al., 2020). Similar findings were reported in the literature for various pollutant-adsorbent systems (Duman et al., 2019, 2020). The adsorption parameters derived from this model are $k_2 = (6.9 \pm 0.03) \times 10^{-4}$ min^{-1} and $q_e = 322.6 \pm 16$ mg/g, considering the active sites in the PVA-CA/Eu^{3+}/NaOH mat.

A comparison of the present results with those reported by Coin et al. (2024), reveals notable differences in the TC adsorption kinetics. That study demonstrated that PVA mats cross-linked and/or esterified with citric acid and doped with europium followed PFO kinetics and exhibited faster TC adsorption (60 min) compared to the PVA-CA/Eu^{3+}/NaOH matrix prepared via the *"in situ"* method. This suggests that, in the doping approach, TC was more rapidly physisorbed due to the higher availability of the adsorbent on the nanofiber surface. In contrast, for the "*in situ*" preparation method, the adsorption process required a longer period as the contaminant diffused into the nanofibers. This slower diffusion is driven by swelling, which promotes the formation of more stable and efficient complexes with the adsorbent, ultimately following PFO kinetics.

To gain a more complete understanding of the adsorption process undergone by the doped material, Fig. 6 presents a schematic

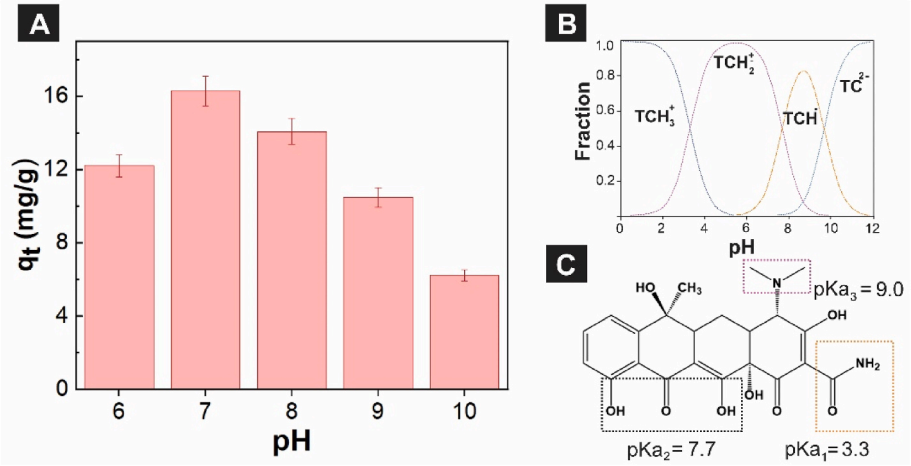

Fig. 4. A. Adsorption of TC on PVA-CA/Eu^{3+}/NaOH mats at different pH's; **B.** Effect of pH on the chemical speciation distribution of tetracycline; **C.** Molecular structure of TC ($pK_{a1} = 3.3$, $pK_{a2} = 7.7$, $pK_{a3} = 9.0$).

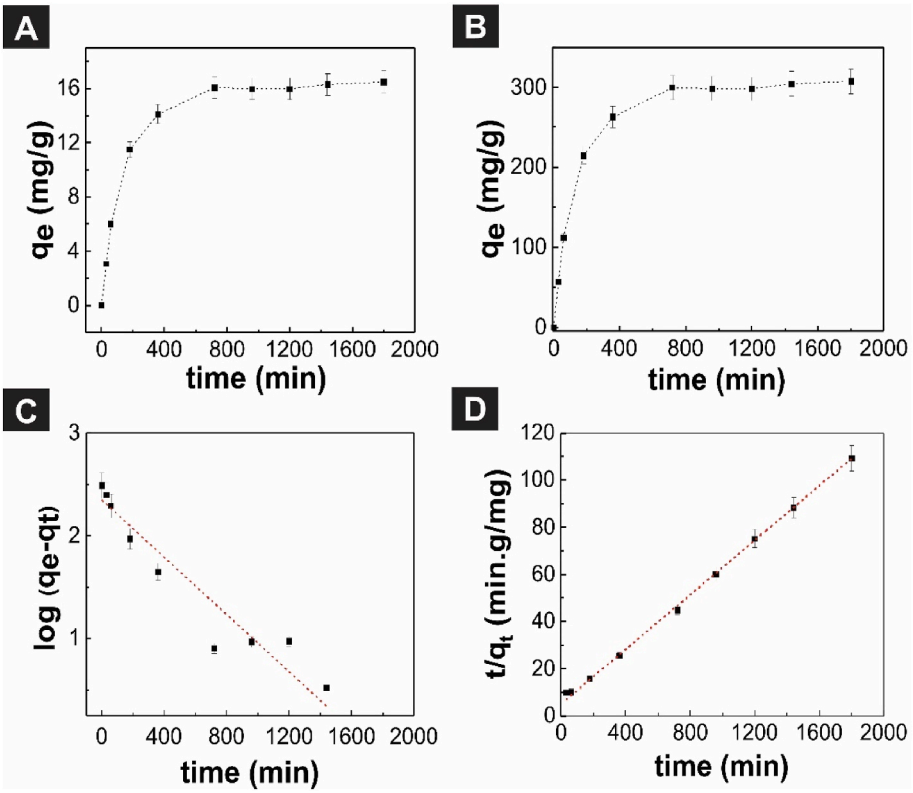

Fig. 5. **A.** Adsorption kinetics of TC on PVA-CA/Eu^{3+}/NaOH; **B.** Adsorption kinetics of TC normalized to the number of active sites in the PVA-CA/Eu^{3+}/NaOH mat; **C.** Plots of the PFO and PSO model adsorption at pH 7.

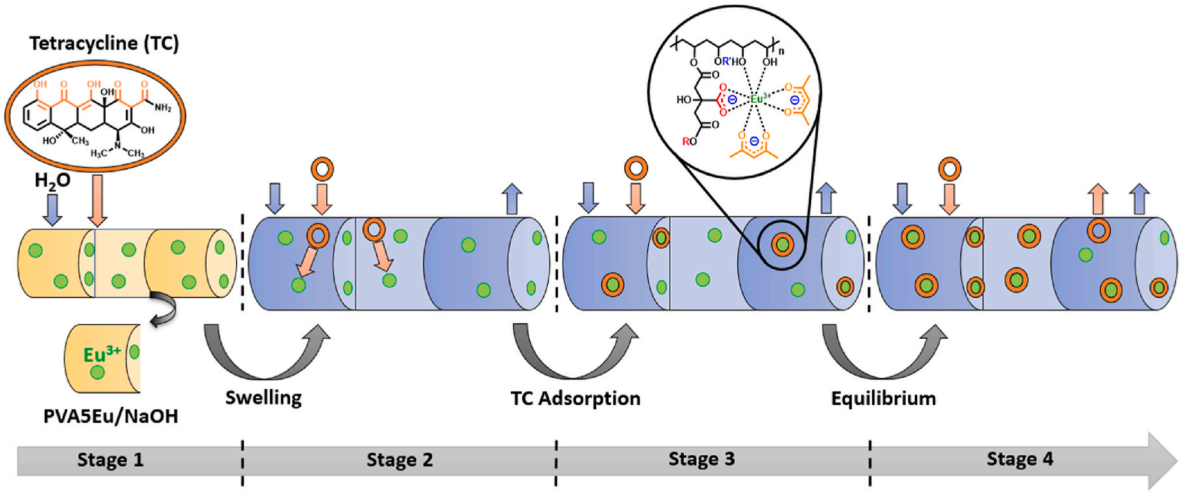

Fig. 6. Proposed TC adsorption mechanism in PVA-CA/Eu^{3+}/NaOH nanofibers.

representation of the proposed mechanism, illustrating the flow of water and TC. Initially, the mat undergoes swelling, the typical behavior of PVA mats when exposed to water (**Stage 1**) (Cimadoro and Goyanes, 2020). This swelling process facilitates the diffusion of the contaminant into the nanofibers (**Stage 2**), where interactions with the active sites of the adsorbent occur, promoting the formation of more efficient complexes (**Stage 3**) until equilibrium is reached (**Stage 4**). This mechanism provides insight into the differences in adsorption times compared to other approaches, such as doping, where adsorption predominantly occurs on the nanofiber surface.

3.3.4. *Adsorption isotherms for TC on PVA-CA/Eu^{3+}/NaOH*

To better understand the adsorption mechanism, the Langmuir, Freundlich and Temkin isotherm models were used to analyze the equilibrium adsorption characteristics of PVA-CA/Eu^{3+}/NaOH (Fig. 7).

In each case, the correlation coefficient (R^2) of the fitted curves was used as the criterion for selecting the best adsorption model. The TC isotherm was analyzed using the Langmuir, Freundlich, and Temkin models, as shown in Fig. 7. The Langmuir model provided the best fit with an R^2 value of 0.99, yielding a q_m of (23.5 ± 1.3) mg/g. The Freundlich model had an R^2 of 0.88 with $\mathbf{K_F}$ = (4.7 ± 0.2) mg/g, while the Temkin isotherm showed an R^2 of 0.94 and K_T = (0.0059 ± 0.0002) L/mg. These results strongly indicate monolayer adsorption of TC at

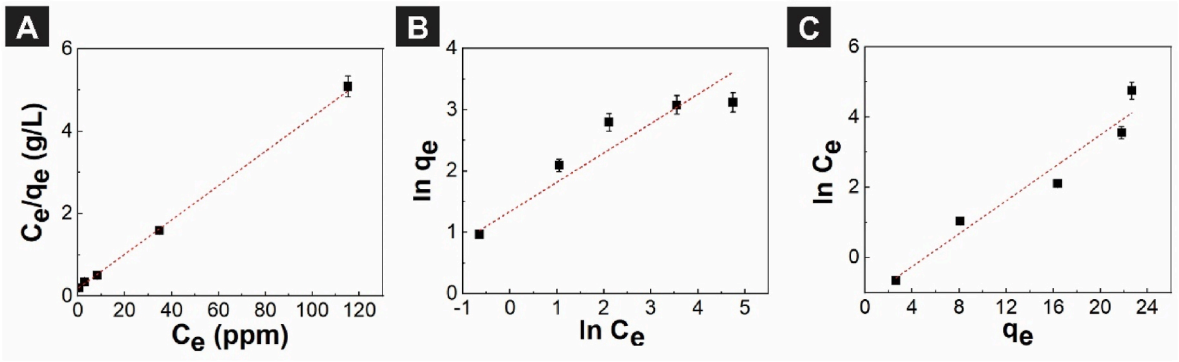

Fig. 7. Isotherm fitting curves of **A**. Langmuir; **B**. Freundlich and **C**. Temkin models.

specific, homogeneous sites on the adsorbent.

On the other hand, the results obtained in this work are comparable to those reported in different metals such as hematite (11.3 mg/g) (Zhu et al., 2020), magnetite (5.5 mg/g) (Zhu et al., 2020), Fe/Mn oxides loaded biochar and (14.2 mg/g) (Zhang et al., 2021). In the case of hybrid systems composed of magnetic zinc nanoparticles in a mixture of PVA/alginate/chitosan mat, maximum adsorption of 10.0 mg/g has been reported (Elkady et al., 2020). It is important to note that when comparing these results with a doped system (14.2 mg/g) (Coin et al., 2024), we note that the adsorption of the mat is superior, these results confirm what was previously observed in the adsorption kinetics tests where the homogeneous dispersion of europium in PVA-CA under alkaline treatment generates a potentiating effect on the removal of TC. In addition, the immobilization of europium within the PVA matrix prevents its release into the environment, preventing secondary contamination and providing a sustainable and safe solution for treating pharmaceutical wastewater treatment.

3.4. Reaction mechanism

The adsorption mechanism of PVA-CA/Eu^{3+}/NaOH for TC molecules was studied by monitoring changes in the chemical structure through ATR-FTIR analysis. As demonstrated in Fig. 8, a comparison of the spectra of the PVA-CA/Eu^{3+}/NaOH mat before and after tetracycline adsorption reveals significant changes in the bands within the 1650–1550 cm^{-1} region, attributed to the stretching vibrations of carboxylate (COO^{-}) groups. These changes suggest a strong interaction between the carboxylate functional groups in the mat and the TC molecules.

The findings in this study indicate that the europium ion (Eu^{3+}) plays a pivotal role in this adsorption mechanism by coordinating with functional groups present in the TC molecule, such as ketones, hydroxyls, and β-diketones. The β-diketone group acts as a bidentate ligand, forming chelate rings that stabilize the complex. This coordination is further enhanced at pH 7, where the TCH_2^+ and TCH^- species of TC predominate, which interact strongly with Eu^{3+}. While similar changes in carboxylate stretching bands have been reported in europium-doped MOF systems (Zhao et al., 2021), our study provides novel insights by highlighting the combined role of the PVA-CA matrix and the Eu^{3+}ions in the adsorption mechanism. This dual functionality facilitates the electrostatic attraction and stabilizes the adsorbed TC through chelation favored by electrostatic attraction at pH 7, as previously demonstrated by this group (Coin et al., 2024; Xie et al., 2024). The synergistic effect of the carboxylate functional groups and the europium ions is a unique feature of this material, enabling efficient adsorption and interaction with TC molecules.

3.5. Regenerative experiments

The reusability of the adsorbent capacity was evaluated by the following steps: first, the adsorbent was regenerated by desorbing the contaminant through acid treatment. The efficiency of two different acid solutions was evaluated. Secondly, the regenerated adsorbent was subjected to a new adsorption process. Steps 1 and 2 were then repeated

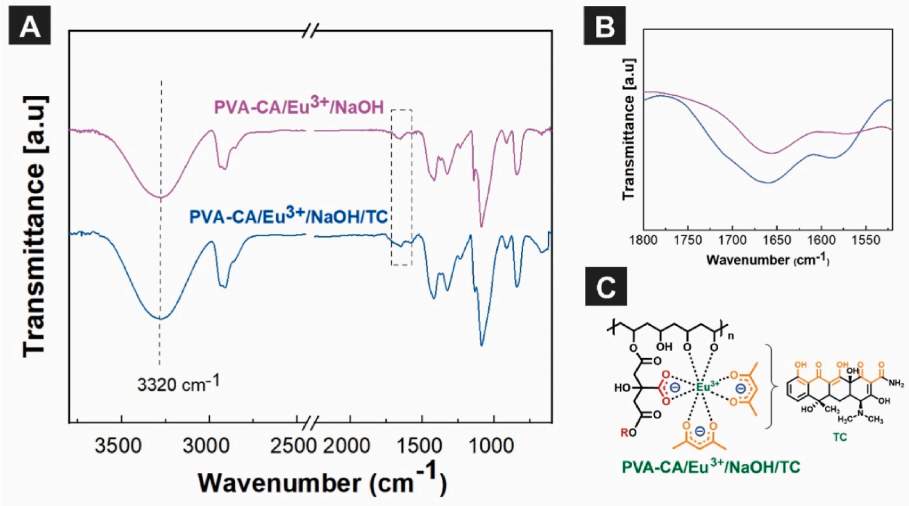

Fig. 8. A: Comparison of FTIR spectra of PVA-CA/Eu^{3+} before and after TC contact; **B**: close-up of spectra from 1800 cm^{-1} to 1500 cm^{-1}; **C**: Coordination of PVA-CA/Eu^{3+}/NaOH and TC.

four times. The results are shown in Fig. 9A. During the initial three cycles, the mat regenerated with HCl exhibited a consistently higher TC removal efficiency (above 80%) than the mat regenerated with CH_3COOH.

However, following the third cycle, both systems exhibited a decrease in adsorption efficiency, which can be attributed to the progressive depletion of active adsorption sites, compounded by incomplete desorption of TC during the regeneration process (Choi et al., 2020). Notably, the mats regenerated with CH_3COOH exhibited consistently lower efficiencies than those treated with HCl across all cycles. This phenomenon can be attributed to the potential formation of a Eu^{3+}-acetate complex during the regeneration process with acetic acid, which may hinder the availability of Eu^{3+} for coordination with TC molecules, thereby reducing the overall adsorption efficiency (Choi et al., 2020; Kataoka et al., 2022). On the contrary, it has been reported that Chloride complexes with Eu^{3+} are very weak and high chloride concentrations are needed to form such complexes (Jordan et al., 2022).

On the other hand, as HCl is a strong acid, the pH of a 1% solution is approximately 1. At this pH, the predominant TC species is TCH_3^+ (Fig. 4B). As discussed in section 3.3, the adsorbate-adsorbent interactions are favored at pH 7 while negligible at pH = 1. When using the weak acetic acid for regeneration, the pH of the solution decreases to 3. At this pH value, the dominant species is TCH_2^{+-}. Hence, some interaction of TC with the active sites in the mat can occur, resulting in incomplete desorption through the cycles. These results underscore the critical role of regeneration conditions in maintaining adsorption performance during successive cycles. Employing HCl as a regenerating agent has been shown to enhance desorption processes and preserve active sites, thereby ensuring enhanced reusability and TC removal efficiency. The decline in performance observed after repeated cycles underscores the necessity of further refined desorption protocols to maximize the lifetime and efficiency of the adsorbent (Fig. 9A and B).

3.6. Competitive effect

Fig. 10 shows interferents in TC adsorption in the presence of other drugs such as ibuprofen (Ibf), diclofenac (Dcl), trimethoprim (Trim) and chlorphen#iramine (Chlo).

Fig. 10 shows the reduction in TC adsorption in the presence of Ibf (12.3 mg/g) and Dcl (12.3 mg/g) relative to the adsorption observed in the absence of these drugs (16.4 mg/g). The smaller size of Ibf and Dcl and the carboxylate group in their chemical structure render them powerful ligands capable of coordinating with europium to form a complex. This, in turn, reduces in the number of active sites where TC can be coordinated (Kaup et al., 2017).

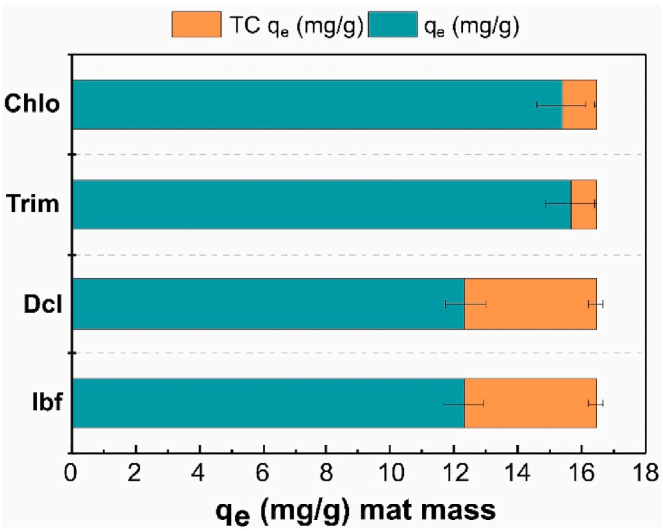

Fig. 10. Competitive effect Ibuprofen (Ibf), Diclofenac (Dcl), Trimethoprim (Trim), and Chlorpheniramine (Chlo) in the TC adsorption by PVA-CA/Eu^{3+}/NaOH.

The formation of complexes with europium using di-ketones is not significantly affected in the presence of neutral ligands due to the intrinsic nature of di-ketones. These molecules possess highly electronegative carbonyl groups that effectively donate electrons to the metal ion, forming strong and stable coordination bonds. Trim (15.7 mg/g) and Chlo (15.38 mg/g) are neutral ligands lacking electron-dense functional groups and cannot compete effectively with di-ketones in complex formation (Xu et al., 2015). This difference in coordination ability between TC and neutral ligands ensures that di-ketones continue to form preferential complexes with europium due to their higher affinity and metal ion stabilization capacity (de Oliveira et al., 2018; Echenique-Errandonea et al., 2017)

4. Conclusion

Incorporating the pollutant capturer during nanofiber mat fabrication "*in situ*" is a more effective approach than doping in terms of the adsorption capacity (q_e = 322.6 mg/g). The mat dopped with 1% Eu^{3+} and the mat prepared "*in situ*" with only 0.36% Eu^{3+} exhibit similar q_e values. Moreover, implementing alkaline treatment into the last material (mat produced via "*in situ*") increases its adsorption capacity by 16%. These results are attributed to the higher number of complexes formed

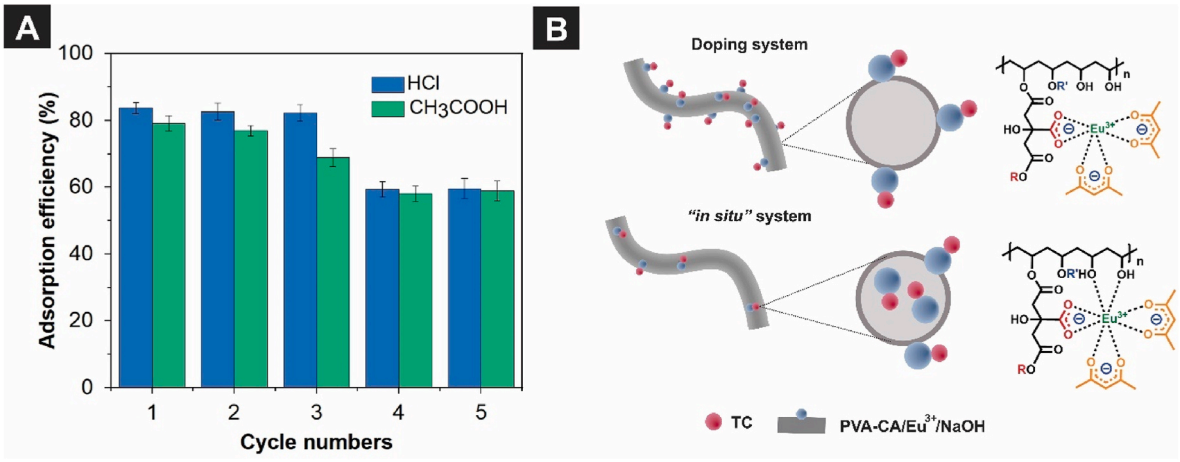

Fig. 9. A. Adsorption capacity studies of the PVA-CA/Eu^{3+}/NaOH mat for TC after five regenerations. **B:** Schematic of TC and the PVA-CA/Eu^{3+} complex with the addition of Eu^{3+} by doping or "*in situ*".

between Europium and diketone groups. The TC adsorption mechanism in the "*in situ*" Eu^{3+} mats follows the Langmuir isotherm model, indicating that TC is adsorbed in a monolayer on specific, uniform sites in the adsorbent. In addition, unlike doping, the "*in situ*" strategy allows the material to be reused at least 5 times with an efficiency of more than 80% during the first 3 reuse cycles and 60% during the next 2 reuse cycles. On the other hand, the presence of another antibiotic (Trim) or an antihistamine (Chlo) in the water did not significantly impact TC adsorption. However, the presence of Ibf and Dcl resulted in a notable decrease of approximately 25%. This can be attributed to the ability of carboxylate groups present in these drugs to form complexes with Europium, thus competing with the diketone groups in TC. All findings demonstrate the significant potential of this material as a sustainable solution for removing antibiotics in wastewater treatment.

CRediT authorship contribution statement

C.A. Rodríguez-Ramírez: Writing – review & editing, Writing – original draft, Methodology, Investigation, Data curation. **Francesco Coin:** Writing – review & editing, Writing – original draft, Methodology, Investigation, Formal analysis, Data curation. **Alicia Vergara-Rubio:** Writing – review & editing, Writing – original draft, Methodology, Investigation, Formal analysis, Data curation. **David Picón:** Writing – review & editing, Writing – original draft, Methodology, Investigation, Formal analysis, Data curation. **Silvina Cerveny:** Writing – review & editing, Writing – original draft, Supervision, Resources, Project administration. **Silvia Goyanes:** Writing – review & editing, Writing – original draft, Supervision, Resources, Project administration, Methodology, Investigation, Funding acquisition, Conceptualization.

Declaration of Competing Interest

The authors declare that they have no known competing financial interests or personal relationships that could have appeared to influence the work reported in this paper.

Acknowledgments

This research was supported by the National Agency for Scientific and Technological Promotion (ANPCyT: PICT 2019–04509, PICT 2021–01218), the University of Buenos Aires (UBACyT 2023, No 20020220200117BA and PDE_2_2024 No. EX-2023-02810510–UBA-DME#REC), the National Scientific and Technical Research Council (CONICET), bilateral agreement CSIC-CONICET (DD287) 29220230100166, PIP-CONICET 2022–2024 No 11220210100785CO, PID2023-146348NB-I00 funded by MCIN/AEI/10.13039/501100011033, IT1566-22 funded by the Basque Government, BILAT23076 funded by CSIC. Francesco Coin and Silvina Cerveny acknowledge the mobility program IMOVE CSIC.

Appendix A. Supplementary data

Supplementary data to this article can be found online at https://doi.org/10.1016/j.chemosphere.2025.144102.

Data availability

No data was used for the research described in the article.

References

Caneschi, A., Bardhi, A., Barbarossa, A., Zaghini, A., 2023. The use of antibiotics and antimicrobial resistance in veterinary medicine, a complex phenomenon: a narrative review. Antibiotics 12. https://doi.org/10.3390/antibiotics12030487.

Cherian, T., Ragavendran, C., Vijayan, S., Kurien, S., Peijnenburg, W.J.G.M., 2023. A review on the fate, human health and environmental impacts, as well as regulation of antibiotics used in aquaculture. Environ. Adv. 13, 100411. https://doi.org/10.1016/j.envadv.2023.100411.

Choi, Y.K., Choi, T.R., Gurav, R., Bhatia, S.K., Park, Y.L., Kim, H.J., Kan, E., Yang, Y.H., 2020. Adsorption behavior of tetracycline onto Spirulina sp. (microalgae)-derived biochars produced at different temperatures. Sci. Total Environ. 710, 136282. https://doi.org/10.1016/j.scitotenv.2019.136282.

Choudhury, R.R., Gohil, J.M., Dutta, K., 2021. Poly(vinyl alcohol)-based membranes for fuel cell and water treatment applications: a review on recent advancements. Polym. Adv. Technol. 32, 4175–4203. https://doi.org/10.1002/pat.5431.

Cimadoro, J., Goyanes, S., 2020. Reversible swelling as a strategy in the development of smart membranes from electrospun polyvinyl alcohol nanofiber mats. J. Polym. Sci. 58, 737–746. https://doi.org/10.1002/pol.20190156.

Cimadoro, J., Ribba, L., Ledesma, S., Goyanes, S., 2018a. Electrospun mats: from white to transparent with a drop. Macromol. Mater. Eng. 1800237, 1800237. https://doi.org/10.1002/mame.201800237.

Cimadoro, J., Ribba, L., Ledesma, S., Goyanes, S., 2018b. Electrospun mats: from white to transparent with a drop. Macromol. Mater. Eng. 303, 1–5. https://doi.org/10.1002/mame.201800237.

Coin, F., Rodríguez-Ramírez, C.A., Oyarbide, F.S., Picón, D., Goyanes, S., Cerveny, S., 2024. Efficient antibiotic removal from water using europium-doped poly(vinyl alcohol) nanofiber mats esterified with citric acid. J. Water Process Eng. 63. https://doi.org/10.1016/j.jwpe.2024.105447.

Cui, J., Li, F., Wang, Y., Zhang, Q., Ma, W., Huang, C., 2020. Electrospun nanofiber membranes for wastewater treatment applications. Sep. Purif. Technol. 250, 117116. https://doi.org/10.1016/j.seppur.2020.117116.

de Oliveira, T.C., de Lima, J.F., Colaço, M.V., Jesus, L.T., Freire, R.O., Marques, L.F., 2018. Synthesis, characterization and spectroscopic studies of binuclear lanthanide complexes containing the anti-inflammatory drug Ibuprofen and CH3-disubstituted bipyridine ligands: influence of methyl group position in the photoluminescence. J. Lumin. 194, 747–759. https://doi.org/10.1016/j.jlumin.2017.09.046.

Duman, O., Diker, C.Ö., Uğurlu, H., Tunç, S., 2022a. Highly hydrophobic and superoleophilic agar/PVA aerogels for selective removal of oily substances from water. Carbohydr. Polym. 286. https://doi.org/10.1016/j.carbpol.2022.119275.

Duman, O., Özcan, C., Gürkan Polat, T., Tunç, S., 2019. Carbon nanotube-based magnetic and non-magnetic adsorbents for the high-efficiency removal of diquat dibromide herbicide from water: OMWCNT, OMWCNT-Fe3O4 and OMWCNT-K-carrageenan-Fe3O4 nanocomposites. Environ. Pollut. 244, 723–732. https://doi.org/10.1016/j.envpol.2018.10.071.

Duman, O., Polat, T.G., Diker, C.Ö., Tunç, S., 2020. Agar/κ-carrageenan composite hydrogel adsorbent for the removal of Methylene Blue from water. Int. J. Biol. Macromol. 160, 823–835. https://doi.org/10.1016/j.ijbiomac.2020.05.191.

Duman, O., Polat, T.G., Tunç, S., 2022b. Development of poly(vinyl alcohol)/β-cyclodextrin/P(MVE-MA) composite nanofibers as effective and selective adsorbent and filtration material for the removal and separation of cationic dyes from water. J. Environ. Manage. 322, 116130. https://doi.org/10.1016/j.jenvman.2022.116130.

Duman, O., Uğurlu, H., Diker, C.Ö., Tunç, S., 2022c. Fabrication of highly hydrophobic or superhydrophobic electrospun PVA and agar/PVA membrane materials for efficient and selective oil/water separation. J. Environ. Chem. Eng. 10. https://doi.org/10.1016/j.jece.2022.107405.

Echenique-Errandonea, E., Oyarzabal, I., Cepeda, J., San Sebastian, E., Rodríguez-Diéguez, A., Seco, J.M., 2017. Photoluminescence and magnetic analysis of a family of lanthanide(III) complexes based on diclofenac. New J. Chem. 41, 5467–5475. https://doi.org/10.1039/c7nj00794a.

Elkady, M., Salama, E., Amer, W.A., Ebeid, E.Z.M., Ayad, M.M., Shokry, H., 2020. Novel eco-friendly electrospun nanomagnetic zinc oxide hybridized PVA/alginate/chitosan nanofibers for enhanced phenol decontamination. Environ. Sci. Pollut. Res. 27, 43077–43092. https://doi.org/10.1007/s11356-020-10247-8.

Estevez-Areco, S., Guz, L., Candal, R., Goyanes, S., 2022. Development of insoluble PVA electrospun nanofibers incorporating R-limonene or β-cyclodextrin/R-limonene inclusion complexes. J. Polym. Environ. 30, 2812–2823. https://doi.org/10.1007/s10924-022-02390-9.

Gorito, A.M., Ribeiro, A.R., Almeida, C.M.R., Silva, A.M.T., 2017. A review on the application of constructed wetlands for the removal of priority substances and contaminants of emerging concern listed in recently launched EU legislation. Environ. Pollut. 227, 428–443. https://doi.org/10.1016/j.envpol.2017.04.060.

Gothwal, R., Shashidhar, T., 2015. Antibiotic pollution in the environment: a review. Clean 43, 479–489. https://doi.org/10.1002/clen.201300989.

He, X., Liu, Y., Wang, Q., Wang, T., He, J., Peng, A., Qi, K., 2023. Facile fabrication of Eu - based metal – organic frameworks for highly efficient capture of tetracycline hydrochloride from aqueous solutions. Sci. Rep. 1–13. https://doi.org/10.1038/s41598-023-38425-x.

Jordan, N., Thoenen, T., Starke, S., Spahiu, K., Brendler, V., 2022. A critical review of the solution chemistry, solubility, and thermodynamics of europium: recent advances on the Eu3+ aqua ion and the Eu(III) aqueous complexes and solid phases with the sulphate, chloride, and phosphate inorganic ligands. Coord. Chem. Rev. 473, 214608. https://doi.org/10.1016/j.ccr.2022.214608.

Kataoka, T., Hashimoto, T., Samitsu, S., Liu, Z., Tagaya, M., 2022. Coordination state control of citric acid molecules on europium(III) ion-doped hydroxyapatite nanoparticles for highly efficient photoluminescence toward biomedical applications. ACS Appl. Nano Mater. 5, 2305–2315. https://doi.org/10.1021/acsanm.1c03999.

Kaup, G., Meiners, D., Kynast, U.H., 2017. Rare earth Ibuprofen complexes: highlighting a pharmaceutical. Opt. Mater. 63, 26–31. https://doi.org/10.1016/j.optmat.2016.08.040.

Kong, L., Wang, Y., Andrews, C.B., Zheng, C., 2022. One-step construction of hierarchical porous channels on electrospun MOF/polymer/graphene oxide composite nanofibers for effective arsenate removal from water. Chem. Eng. J. 435, 134830. https://doi.org/10.1016/j.cej.2022.134830.

Liang, L., Xi, F., Tan, W., Meng, X., Hu, B., Wang, X., 2021. Review of organic and inorganic pollutants removal by biochar and biochar-based composites. Biochar 3, 255–281. https://doi.org/10.1007/s42773-021-00101-6.

Liao, Q., Rong, H., Zhao, M., Luo, H., Chu, Z., Wang, R., 2022. Strong adsorption properties and mechanism of action with regard to tetracycline adsorption of double-network polyvinyl alcohol-copper alginate gel beads. J. Hazard Mater. 422, 126863. https://doi.org/10.1016/j.jhazmat.2021.126863.

Martínez-Sabando, J., Coin, F., Melillo, J.H., Goyanes, S., Cerveny, S., 2023a. A review of pectin-based material for applications in water treatment. Materials 16. https://doi.org/10.3390/ma16062207.

Martínez-Sabando, J., Coin, F., Raposo, J.C., Larrañaga, A., Melillo, J.H., Cerveny, S., 2023b. Dual crosslinking of low-methoxyl pectin by calcium and europium for the simultaneous removal of pharmaceuticals and divalent heavy metals. Chem. Eng. J. 475. https://doi.org/10.1016/j.cej.2023.146162.

Martins, J.P., Martín-Ramos, P., Coya, C., Ramos, M., Eusebio, M.E.S., Andrés, A. De, Álvarez, Á.L., Martín-gil, J., 2015. Highly luminescent pure-red-emitting fl uorinated β -diketonate europium (III) complex for full solution-processed OLEDs. J. Lumin. 159, 17–25. https://doi.org/10.1016/j.jlumin.2014.10.020.

Mosharaf, M.K., Gomes, R.L., Cook, S., Alam, M.S., Rasmusssen, A., 2024. Wastewater reuse and pharmaceutical pollution in agriculture: uptake, transport, accumulation and metabolism of pharmaceutical pollutants within plants. Chemosphere 364, 143055. https://doi.org/10.1016/j.chemosphere.2024.143055.

Nayl, A.A., Abd-Elhamid, A.I., Awwad, N.S., Abdelgawad, M.A., Wu, J., Mo, X., Gomha, S.M., Aly, A.A., Bräse, S., 2022. Review of the recent advances in electrospun nanofibers applications in water purification. Polymers 14. https://doi.org/10.3390/polym14081594.

Ocampo-Pérez, R., Rivera-Utrilla, J., Gómez-Pacheco, C., Sánchez-Polo, M., López-Peñalver, J.J., 2012. Kinetic study of tetracycline adsorption on sludge-derived adsorbents in aqueous phase. Chem. Eng. J. 213, 88–96. https://doi.org/10.1016/j.cej.2012.09.072.

Palacio, D.A., Leiton, L.M., Urbano, B.F., Rivas, B.L., 2020. Tetracycline removal by polyelectrolyte copolymers in conjunction with ultra fi ltration membranes through liquid-phase polymer-based retention. Environ. Res. 182, 109014. https://doi.org/10.1016/j.envres.2019.109014.

Picón, D., Torasso, N., Roberto, J., Baudrit, V., 2022. Bio-inspired membranes for adsorption of arsenic via immobilized L -Cysteine in highly hydrophilic electrospun nanofibers. Chem. Eng. Res. Des. 185, 108–118. https://doi.org/10.1016/j.cherd.2022.06.042.

Picon, D., Vergara-Rubio, A., Estevez-Areco, S., Cerveny, S., Goyanes, S., 2023. Adsorption of methylene blue and tetracycline by zeolites immobilized on a PBAT electrospun membrane. Molecules 28, 1–17. https://doi.org/10.3390/molecules28010081.

Qi, X., Wang, Z., Ma, S., Wu, L., Yang, S., Xu, J., 2014. Complexation behavior of poly (acrylic acid) and lanthanide ions. Polymer (Guildf). 55, 1183–1189. https://doi.org/10.1016/j.polymer.2014.01.051.

Rusu, A., Buta, E.L., 2021. The development of third-generation tetracycline antibiotics and new perspectives. Pharmaceutics 13. https://doi.org/10.3390/pharmaceutics13122085.

Santos, A.C., Vergara-Rubio, A., Mazocca, A.J., Goyanes, S., 2024. Flow dynamics through a high swelling nanofiber membrane processed at different relative humidities : a study on a FexOy/polyvinyl alcohol composite. Membranes 14. https://doi.org/10.3390/membranes14090189.

Shang, K.X., Jing-Sun, Hu, D.C., Yao, X.Q., Zhi, L.H., Si, C.D., Liu, J.C., 2018. Six ln (III) coordination polymers with a semirigid tetracarboxylic acid ligand: bifunctional luminescence sensing, NIR-luminescent emission, and magnetic properties. Cryst. Growth Des. 18, 2112–2120. https://doi.org/10.1021/acs.cgd.7b01565.

Sitab, A.A., Tujjohra, F., Rashid, T.U., Rahman, M.M., 2023. Thermally crosslinked electrospun nanofibrous mat from chrome-tanned solid wastes for cationic dye adsorption in wastewater treatment. Clean. Eng. Technol. 13, 100621. https://doi.org/10.1016/j.clet.2023.100621.

Torasso, N., González-Seligra, P., Trupp, F., Grondona, D., Goyanes, S., 2022. Turning a novel janus electrospun mat into an amphiphilic membrane with high aromatic hydrocarbon adsorption capacity. Colloids and Interfaces 6, 1–13. https://doi.org/10.3390/colloids6040066.

Torasso, N., Vergara-Rubio, A., Pereira, R., Martinez-Sabando, J., Baudrit, J.R.V., Cerveny, S., Goyanes, S., 2023. An in situ approach to entrap ultra-small iron oxide nanoparticles inside hydrophilic electrospun nanofibers with high arsenic adsorption. Chem. Eng. J. 454. https://doi.org/10.1016/j.cej.2022.140168.

Torasso, N., Vergara-Rubio, A., Rivas-Rojas, P., Huck-Iriart, C., Larrañaga, A., Fernández-Cirelli, A., Cerveny, S., Goyanes, S., 2021. Enhancing arsenic adsorption via excellent dispersion of iron oxide nanoparticles inside poly(vinyl alcohol) nanofibers. J. Environ. Chem. Eng. 9, 104664. https://doi.org/10.1016/j.jece.2020.104664.

Vergara-Rubio, A., Ribba, L., Picón, D., Candal, R., Goyanes, S., 2022. A highly E ffi cient nanostructured sorbent of sulfuric acid from ecofriendly electrospun poly(vinyl alcohol) mats. Ind. Enginnering Chem. Res. 61, 2091–2099. https://doi.org/10.1021/acs.iecr.1c03530.

Wang, M., Li, X., Hua, W., Shen, L., Yu, X., Wang, X., 2016. Electrospun poly(acrylic acid)/silica hydrogel nanofibers scaffold for highly efficient adsorption of lanthanide ions and its photoluminescence performance. ACS Appl. Mater. Interfaces 8, 23995–24007. https://doi.org/10.1021/acsami.6b08294.

Xie, H., Li, S., Zhang, Y., Xi, S., Zheng, H., Wang, H., Li, Y., Wei, T., 2024. Sensitive and selective detection of tetracycline using fluorescence-enhanced Eu(III)-functionalized silver nanoparticles with homocysteine. Chemosphere 364, 143278. https://doi.org/10.1016/j.chemosphere.2024.143278.

Xu, H., Sun, Q., An, Z., Wei, Y., Liu, X., 2015. Electroluminescence from europium(III) complexes. Coord. Chem. Rev. 293–294, 228–249. https://doi.org/10.1016/j.ccr.2015.02.018.

Yao, R., Li, Z., Huo, P., Gong, C., Li, J., Fan, C., Pu, S., 2022. A Eu3+-based high sensitivity ratiometric fluorescence sensor for determination of tetracycline combining bi-functional carbon dots by surface functionalization and heteroatom doping. Dye. Pigment. 201, 110190. https://doi.org/10.1016/j.dyepig.2022.110190.

Zhang, S., Shi, Q., Christodoulatos, C., Meng, X., 2019. Lead and cadmium adsorption by electrospun PVA/PAA nanofibers: batch, spectroscopic, and modeling study. Chemosphere 233, 405–413. https://doi.org/10.1016/j.chemosphere.2019.05.190.

Zhang, X., Li, Y., Wu, M., Pang, Y., Hao, Z., Hu, M., Qiu, R., 2021. Bioresource Technology Enhanced adsorption of tetracycline by an iron and manganese oxides loaded biochar : kinetics , mechanism and column adsorption. Bioresour. Technol. 320, 124264. https://doi.org/10.1016/j.biortech.2020.124264.

Zhao, N., Ma, Q., Wei, Y., Wang, S., Zhong, X., 2023. Co 3 O 4 anchored on sepiolite surface grooves for superior adsorption of tetracycline from wastewater. Sep. Purif. Technol. 323, 124367. https://doi.org/10.1016/j.seppur.2023.124367.

Zhao, Y., Wang, Q., Wang, H., Zhangsun, H., Sun, X., Bu, T., Liu, Y., Wang, W., Xu, Z., Wang, L., 2021. Europium-based metal-organic framework containing characteristic metal chains: a novel turn-on fluorescence sensor for simultaneous high-performance detection and removal of tetracycline. Sensors Actuators, B Chem. 334, 129610. https://doi.org/10.1016/j.snb.2021.129610.

Zhu, Y., Yang, Q., Lu, T., Qi, W., Zhang, H., Wang, M., Qi, Z., Chen, W., 2020. Ecotoxicology and Environmental Safety Effect of phosphate on the adsorption of antibiotics onto iron oxide minerals : comparison between tetracycline and ciprofloxacin. Ecotoxicol. Environ. Saf. 205, 111345. https://doi.org/10.1016/j.ecoenv.2020.111345.

Supplementary Material

Enhanced tetracycline removal through "*in situ*" Europium Incorporation in poly (vinyl alcohol) (PVA) electrospun mats: Advantages of this strategy in adsorption and reuse over doping.

C.A. Rodríguez-Ramírez[1,2], Francesco Coin[3,4], Alicia Vergara-Rubio[1,2], David Picón[5], Silvina Cerveny[3,6], Silvia Goyanes[1,2].

[1] Universidad de Buenos Aires, Facultad de Ciencias Exactas y Naturales, Departamento de Física, Laboratorio de Polímeros y Materiales Compuestos, Ciudad Autónoma de Buenos Aires, Argentina.

[2] CONICET - Universidad de Buenos Aires, Instituto de Física de Buenos Aires (IFIBA), Ciudad Universitaria (C1428EGA), Ciudad Autónoma de Buenos Aires, Argentina.

[3] Centro de Física de Materiales (CSIC, UPV/EHU)-Materials Physics Center (MPC), Paseo Manuel de Lardizabal 5, San Sebastián 20018, Spain

[4] Departamento Polímeros y Materiales Avanzados: Física, Química y Tecnología, University of the Basque Country (UPV/EHU), P. Manuel Lardizábal 3, 20018 San Sebastián, Spain.

[5] Instituto de Ciencias, Universidad Nacional de General Sarmiento (UNGS), J. M. Gutierrez 1150, B1613GSX, Los Polvorines, Prov. de Buenos Aires, Argentina.

[6] Donostia International Physics Center (DIPC), San Sebastian 20018, Spain.

*Corresponding authors: Silvia Goyanes (goyanes@df.uba.ar); Silvina Cerveny (silvina.cerveny@ehu.es)

Figure S1. EDS spectra. **A**. PVA-CA and **B**. PVA-CA/Eu^{3+} before alkaline treatment.

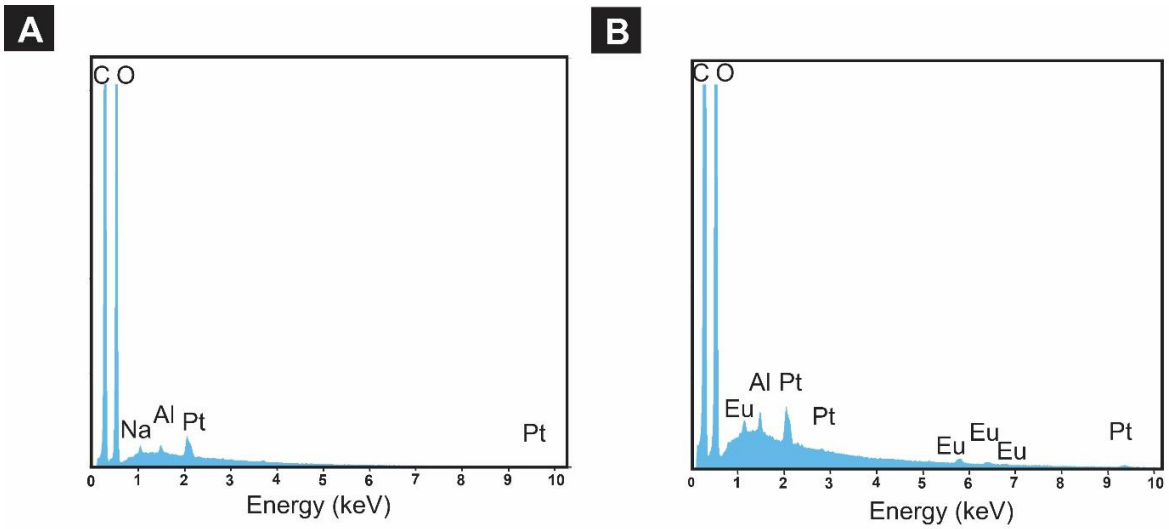

Figure S2. EDS spectra of PVA-CA/Eu^{3+}/NaOH after alkaline treatment.

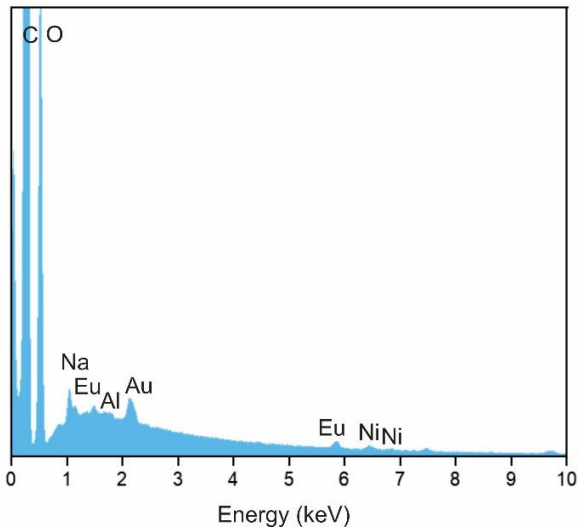

Table S1: Percentual atom composition in the different materials.

Material	% C	%O	%Eu	%Eu/%C
PVA-CA	48.98	50.50	-	-
PVA-CA/Eu^{3+}	48.45	50.29	0.15	0.003
PVA-CA/Eu^{3+}/NaOH	42.23	54.21	1.30	0.003

Carbohydrate Polymer Technologies and Applications 11 (2025) 100885

Contents lists available at ScienceDirect

Carbohydrate Polymer Technologies and Applications

journal homepage: www.sciencedirect.com/journal/carbohydrate-polymer-technologies-and-applications

Structural characterization of low methoxyl pectin-based adsorbents: the role of water on pectin structure

Francesco Coin [a], Aitor Larrañaga [b], Silvina Cerveny [a,c,*]

[a] Centro de Física de Materiales (CFM-MPC), CSIC-UPV/EHU, Paseo Manuel de Lardizabal 5, 20018 Donostia-San Sebastián, Spain
[b] SGIker, General Research Services, University of the Basque Country (UPV/EHU), (48080), Spain
[c] Donostia International Physics Center (DIPC), Paseo Manuel de Lardizabal 4, San Sebastián 20018, Spain

ARTICLE INFO

Keywords:
Pectin
Crosslink
Adsorption
Water treatment
Glass transition temperature

ABSTRACT

Heavy metal contamination risks global water resources, underscoring the need for sustainable remediation strategies. Pectin (PE) is a natural, water-soluble polymer that, when cross-linked with calcium ions (Ca^{2+}), becomes insoluble and a promising bio-adsorbent, providing active sites for the adsorption of heavy metals. This study introduces a new method to evaluate the glass transition temperature (T_g) of dry and hydrated films via physical aging. We also elucidate the structural evolution of neat PE cross-linked with different Ca^{2+} content and hydration levels (from 0 to 33 wt %) before and after zinc (Zn^{2+}) adsorption, using advanced techniques, including thermal gravimetric analysis (TGA), differential scanning calorimetry (DSC), infrared spectroscopy (FT-IR) and X-ray diffraction (XRD). Our findings show that water quickly hydrates calcium-binding sites, allowing for immediate Zn^{2+} capture with an adsorption capacity of 63.9 mg g^{-1} between pH 6 and 8. We also demonstrate the direct correlation between Ca^{2+} content, water-induced plasticization (lowering T_g), and adsorption performance, with a higher efficiency observed above T_g (317 K). Furthermore, our evaluation of PE film adsorption capacity for Zn^{2+} reveals a dual mechanism influenced by Ca^{2+} content: a quick ion exchange between Ca^{2+} and Zn^{2+} and the direct binding of Zn^{2+} to the pectin backbone.

1. Introduction

The contamination of drinking water by heavy metals is a growing global concern, posing a serious threat to public health and the environment (Mekonnen & Hoekstra, 2016; Shah et al., 2024; Yu & Gan, 2021). Heavy metals, antibiotics, and pesticides are frequently detected in water supplies (Carvalho & Santos, 2016; Cossu et al., 2024; Mitra et al., 2022). These contaminants primarily originate from industrial waste, agricultural runoff, and improper disposal of pharmaceuticals. This growing problem highlights the risks associated with heavy metal contamination and underscores the need for water quality monitoring and effective remediation strategies. In this regard, advanced treatment methods to remove contaminants are necessary to address these challenges. Various water cleaning methods have been explored recently, including chemical precipitation (Shah et al., 2024), electrodeposition (Mutalib & Jaafar, 2023), membrane filtration (Othman et al., 2022), photo-catalysis (Loeb et al., 2019) and adsorption (De Gisi et al., 2016). Adsorption has become the most popular and effective remediation technique due to its versatility and cost-effectiveness scalability In recent years, various new materials for water cleaning have been explored for heavy metals removal, such as activated carbon (Shah et al., 2024), clays (Sdiri et al., 2012), iron oxide nanoparticles (Torasso et al., 2023), and polyvinyl-alcohol composites (Picón et al., 2022; Coin et al., 2024).

Naturally occurring polysaccharides are biopolymers that have recently gained significant attention due to their potential as a sustainable alternative to synthetic polymers from petroleum resources (Nasrollahzadeh et al., 2021). They also meet growing consumer demands for environmentally friendly technologies and products. In particular, pectin is a natural hetero-polysaccharide in the cell walls of vegetables and fruits, especially citrus fruits and apples. It plays a crucial role in plant structure by providing rigidity and maintaining cell adhesion (Ciriminna et al., 2015). Pectin is widely used in the food industry and has gained attention in packaging and sanitation applications (Minzanova et al., 2015; Roy et al., 2023). Beyond these uses, their eco-friendly nature, renewability and biodegradability make it a promising material in various fields of material science (Jha & Mishra, 2024; Martínez-Sabando et al., 2023b; Namasivayam et al., 2024;

* Corresponding author.
E-mail address: silvina.cerveny@ehu.es (S. Cerveny).

https://doi.org/10.1016/j.carpta.2025.100885

Available online 6 June 2025

Ribeiro et al., 2025). However, its predominant water solubility poses challenges in specific applications. This limitation can be addressed by insolubilizing pectin through cross-linking with multiple agents, such as di- or trivalent cations such as calcium (Ca^{+2}) or europium (Eu^{+3}) (Martínez-Sabando et al., 2023b), among others.

The structure of neat pectin (i.e., not cross-linked) is based on a galacturonic acid (GalA) backbone, which includes homogalacturonan (HG), rhamnogalacturonan I (RG-I), and II (RG-II) (Voragen et al., 2009), whose characteristics are influenced by its origin, extraction method, and degree of esterification (DM). DM is the percentage of GalA residues esterified with methyl groups. Low methoxy pectin (LMP, <50 % esterified) tends to be more crystalline than high methoxy pectin (Braccini & Pérez, 2001; Luzio & Cameron, 2008; Ventura et al., 2013) (HMP, >50 % esterified), which exhibits a more amorphous structure (Axelos & Thibault, 1991; Oakenfull, 1991). Generally, LMP with high molecular weight and high GalA content has long HG regions between 6 and 20 units (Braccini & Pérez, 2001) and tends to form more ordered and linear domains interacting by H-bond (Willats et al., 2006). This linear arrangement facilitates the metal ion interactions (Stephen, 2006).

There are different methods for crosslinking pectin with cations (Secchi et al., 2014). The external crosslinking method (i.e., prepare a pectin film and then perform a crosslinking just by submerging the film in a calcium solution), also known as the diffusion setting method, enables free diffusion of Ca^{2+} into the solid pectin (Veronovski et al., 2014). In contrast, the internal method (i.e., preparing a pectin solution and mixing this solution with a calcium solution) relies on a pH-controlled slow release of Ca^{2+} into the pectin solution (Cao et al., 2020). These two approaches significantly affect the final properties of pectin. The external method is rapid, resulting in a higher concentration of Ca^{2+} on the surface. Conversely, the internal crosslinking process is more time-dependent, allowing the diffusion of Ca^{2+} ions internally to the material (Huynh et al., 2018). The ratio ($R = [Ca^{2+}]/[GalA]$) between the concentrations of Ca^{2+} ions adsorbed by pectin and the galacturonic acid content defines what type of structure will be induced by crosslinking (Gohil, 2011; Huynh et al., 2018). For $0.20 \leq R \leq 0.50$, cross-linked pectin will form "egg-box" dimers (i.e. parallel alignment of GalA chains with calcium ions at the center). In contrast, for $R > 0.50$, pectin will present multimers (i.e. lateral aggregation) (Cao et al., 2020). In both cases, crosslinking induces the amorphization of neat pectin, breaking the periodicity of the hydrogen bonds between pectin chains and enhancing its mechanical strength and thermal stability (Chaichi et al., 2019).

Among low-methoxyl pectins (LMPs), those having high molecular weight and long HG regions have linear and longer sequences of consecutive free carboxyl groups (Kontogiorgos, 2021). These features enhance their ability to form an "egg-box" structure, which is highly effective at trapping metal ions from aqueous solutions (Jakóbik-Kolon et al., 2017b). In addition, calcium cross-linked pectin is known for absorbing large amounts of water, facilitating the interaction between the active sites (i.e., the cross-linking metal ions) and metal ions in the aqueous solution. As a result, it exhibits excellent absorptive properties, especially when dealing with polluted water that contains heavy metals such as Zn^{+2}, Mg^{+2}, Ba^{+2}, or Ni^{+2} (Corda & Kini, 2020; Martínez-Sabando et al., 2023a).

Studying pectin at different cross-linking times is crucial for understanding how the structure and properties evolve, directly influencing its effectiveness in remediation applications. Cross-linking plays a key role in determining the density and arrangement of the pectin network, influencing properties such as swelling capacity and the availability of functional groups for binding contaminants. By analyzing samples at various stages of cross-linking, it is possible to identify the optimal conditions that enhance adsorption efficiency while maintaining structural integrity. In addition, understanding the remediation properties of an adsorbent requires a detailed analysis of how its physical properties change when it interacts with contaminated water. In the case of pectin, water absorption can induce significant structural alterations. For instance, during water absorption, the glass transition temperature (T_g) —a critical factor in determining the stability of amorphous materials— is expected to decrease due to plasticization, facilitating the uptake of heavy metals. However, obtaining reliable T_g values for dried and wet cross-linked pectin is challenging. This problem originates from the low heat capacity step (Δc_P) at T_g in cross-linked pectin and the overlap between the T_g temperature range and water evaporation (Gohil, 2011). In addition, structural changes such as matrix swelling or variation in the interlayer distance between two pectin chains, particularly within the "egg-box" structure, may influence adsorption. This emphasizes the need to investigate the physical properties of pectin when it interacts with contaminated water. While pectin shows excellent promise for heavy metal adsorption, detailed studies on the characterization of wet low-methoxyl pectin (LMP) in this context are still lacking in the literature.

In this work, we characterized low-methoxyl pectin (LMP), including its degree of methylation (DM), molecular weight, and monosaccharide composition. Using a combination of techniques (X-ray diffraction (XDR), differential scanning calorimetry (DSC), and Fourier transform infrared spectroscopy (FTIR)), we analyzed the structure and physical properties of pectin externally crosslinked with Ca^{2+}. Crosslinking was performed at different times (5, 15, and 40 min) to identify the optimal conditions that maximize heavy metal (Zn^{2+}) adsorption efficiency while preserving structural integrity. Additionally, for the sample crosslinked for 40 min, we examined how hydration (from dry pectin to 33 wt % water content) affects its glass transition temperature and structure. With increasing water content, we found that the interlayer distance (within the "egg-box" structure, formed by interactions between pectin chains) increases while the glass transition temperature decreases. Then, we elucidate the principles of adsorption, analyzing the structure after remediation of Zn^{2+}, and we propose a novel mechanism for water interaction, enhancing the understanding and application of pectin in environmental remediation and other advanced industrial uses. This approach provides valuable insights into the relationship between crosslinking time and material performance, enabling the development of tailored pectin-based adsorbents for effective heavy metal remediation.

2. Materials and methods

2.1. Materials

Citrus pectin powder (PE) with nominal values of 91 % of galacturonic acid (Gal) and 9.9 % DM was kindly supplied by Herbstreith & Fox. Sodium chloride (NaCl, product number S9625), Calcium chloride ($CaCl_2$, product number C1016), Zinc chloride ($ZnCl_2$, product number 208,086) and Sodium hydroxide (NaOH, product number S5881) were purchased from Sigma Aldrich; and nitric acid (HNO_3 65 % w/w, product number 7697–37–2) was purchased from Scharlab. NaOH and HNO_3 were used for the pH correction and milli Q water was used to prepare the solutions.

2.2. Characterizations of low-methoxyl pectin

2.2.1. Monosaccharides composition

The monosaccharide composition of pectin was determined using methanolysis, hydrolysis, and subsequent GC–MS analysis (Arnous & Meyer, 2008; Hua et al., 2015). 1.7 mg of pectin was subjected to methanolysis using 1 mL of 2 M HCl/MeOH at 80 °C for 16 h. The solvent was evaporated under reduced pressure, followed by hydrolyzed with 500 μL of 5 M trifluoroacetic acid (TFA) at 121 °C for 4 h. After adding 100 μg of inositol as an internal standard, TFA was evaporated under reduced pressure. Monosaccharides were derivatized into trimethylsilylated oxime derivatives by reacting with hydroxylamine chloride (98 % in 2.5 % pyridine) at 70 °C for 30 min, followed by bis-(trimethylsilyl)

trifluoroacetamide (BSTFA) at 80 °C for 10 min. Derivatized samples were analyzed using an Agilent 7980A-5975C GC–MS system with a DB-5HT column (30 $m \times 0.25$ mm ID × 0.1 μm) and helium as the carrier gas. The injector temperature was 275 °C, with a 100:1 split ratio. The heating rate was 2 K/min between 160 °C and 185 °C. Detection was performed in full-scan mode (m/z 40–550). Monosaccharides were identified by their retention times and quantified using peak areas relative to the internal standard. Data were analyzed using Agilent's OpenLab CDS Data Analysis 2.7 software.

2.2.2. Molecular weight

Seven diluted water solutions with different pectin concentrations have been prepared (0; 0,07; 0,09; 0.11; 0.13; 0.15; 0.175; 0.2) gL^{-1} and stirred for 24 h at 70 °C. To keep the ionic strength constant, a buffer of NaCl 0.1 M was used. A Micro-Ostwald capillary viscometer (type 517 10/l, Xylem Analytics Germany GmbH) and a detection device (Visco-Clock plus, Xylem Analytics Germany GmbH) were used. Each solution was measured seven times (and then averaged) at a thermalized temperature of 25 °C. Viscosity measurements were used to determine the molecular weight of pectin using the Huggins-Kramer plot (see S1 in SI). Density was measured using a densimeter (Anton Paar DMA 4500 M) at 25 °C.

2.3. Pectin film fabrication

A homogeneous solution was obtained by dissolving 3 g of PE in 100 mL of Milli Q water under stirring at 70 °C for one hour. The PE solution was then sonicated at 70 °C for 1 hour. Homogeneous and transparent PE films were obtained by dropping 10 mL of the PE solution into a 10 cm petri dish, and the solvent casted at room temperature overnight. The PE films were carefully removed and dried at 40 °C for 1 hour inside a vacuum oven. Since the adsorption of metal ions and water is influenced by sample size and weight, all samples were prepared with identical circular geometry (22 mm in diameter and 0.05 mm in thickness) and carefully weighted to minimize surface effects and ensure consistent experimental conditions.

2.4. Calcium crosslinking

PE films were crosslinked in batch conditions at room temperature using a dose of 1.25 g/L in 500 ppm of Ca^{2+} solution under constant shacking (125 rpm for 5, 15 and 40 min). After crosslinking, the films were washed five times (using the same dose of 1.25 g/L) with fresh deionized water for 1 hour to remove excess of calcium. As a result, three insoluble PE films crosslinked by Ca^{2+} (named PE-Ca5, PE-Ca15 and PE-Ca40) were obtained.

2.5. Pectin hydration

The PE films were dried under vacuum (10^{-2} mbar) at 40 °C for one week and carefully weighed before hydration. Sample hydration was performed in humidity-controlled environments inside desiccators where the specific relative humidity level (RH) was controlled using different saturated aqueous salt solutions. Samples at different hydration levels were obtained ranging from 0 to 33 wt % different RH and water uptake were explored (0, 11, 18, 25 and 33 wt %).

All samples were conditioned at 25 °C until equilibrium without observing any mass changes between two measurements within a time interval of 2 days (an approximate total of 2 weeks per hydration level). Mass measurements were carried out using Sartorius MSE225S analytical balance with a sensibility of 0.01 mg. The water uptake (c_w) was calculated using the formula

$$c_w = \frac{m_{wet} - m_{dry}}{m_{dry}} * 100 \quad (1)$$

where m_{dry} (g) is the dry mass and m_{wet} (g) is the mass after hydration.

2.4. Characterization techniques

2.4.1. Infrared spectroscopy (FT-IR) and degree of methyl-esterification (DM)

Infrared spectra were recorded in attenuated total reflectance mode (ATR) using Jasco FT-IR 6300 spectrometer (Japan) from 650 to 4000 cm^{-1} with a resolution of 4 cm^{-1} and 200 scans per spectrum. Five different FT-IR spectra were collected in different sample positions. After baseline correction, each set of measurements was normalized using the peak area of the glycosidic ring vibration of the poly-galacturonic acid chain (–C–O–C) at ~1140 cm^{-1} (see S2 in SI) (Synytsya et al., 2003). The DM of pectin powder was estimated by the area of methyl esterified carboxyl groups at ~1735 cm^{-1} ($Area_{1735}$) and the absorption peaks of carboxylate anions at ~1590 cm-1 ($Area_{1590}$) in the FT-IR spectrum (Chatjigakis et al., 1998)

$$DM\ (\%) = \frac{Area_{1730}}{Area_{1730} + A_{1590}} * 100 \quad (2)$$

2.4.2. Thermal gravimetric analysis (TGA)

Thermal gravimetric analysis Q500 from TA Instruments was employed to investigate the thermal stability and the water loss from 5 × 5 × 0.05 mm^3 PE-Ca samples under a constant N_2 flow of 25 mm^3/min. Samples were loaded immediately on the platinum pan to avoid possible hydration and water loss. We recorded the weight loss as a function of temperature for dried PE samples using a rate of 10 K/min.

2.4.3. X-Ray diffraction (XRD)

X-ray powder diffraction patterns were obtained using a Philips X'pert PRO automatic diffractometer. The diffractometer was operated at 40 kV and 40 mA in a theta-theta configuration, with a secondary monochromator and Cu-Kα radiation (λ = 1.5418 Å). A PIXcel solid state detector with an active length of 3.347° in 2θ was used. A variable divergence slit provided a constant 10 mm area of sample illumination. The data were analyzed using Fityk.

The lateral spacing (d, nm) was calculated applying the Braggs law:

$$n\lambda = 2d\sin\theta \quad (3)$$

where n is the diffraction order, λ [Å] is the X-ray wavelength, and θ is the Bragg angle (Ashcroft & Mermin, 1976).

2.4.4. Differential scanning calorimetry (DSC)

Standard DSC was performed with a TA Instruments DSC Q2000 with liquid nitrogen cooling, operating in a temperature range between 100 and 350 K. The chamber was purged with dry helium at a flow rate of 25 mL/min. The samples were prepared by pressing approximately 10 to 15 mg of pectin in a hermetic aluminum pan to avoid water losses. For annealing experiments, the cooling process involved rapid quenching (~20 K/min), while heating was carried out at 20 K/min. After cooling, the samples were heated to a specific annealing temperature (288 K) and held there for 4 h. After annealing, the samples were cooled to 110 K and reheated to 360 K for data recording. Measurements both before and after all aging cycles confirmed the absence of annealing-induced permanent changes in the properties of the samples.

2.4.5. Adsorption experiments

Adsorption kinetic experiments were performed in batches using a dose of 1 g/L under agitation at 125 rpm and (25 ± 1) °C. The pollutant concentration at different times ranging from 5 to 1440 min at a fixed initial concentration of 100 mg/L for zinc. Isotherm experiments were conducted at various initial zinc concentrations (1 to 100 mg/L) over a duration of 24 h. Inductively coupled plasma–atomic emission spectrometry (ICP-AES, Agilent 5100) was used to measure Ca^{2+} concentration during the crosslinking and washing cycles and both Zn^{2+}

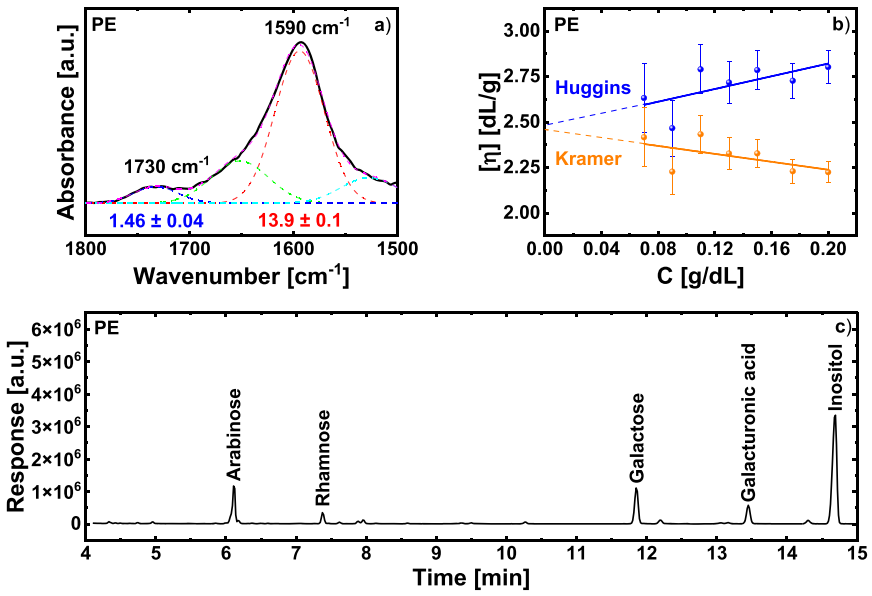

Fig. 1. (a) FT-IR carboxyl peak deconvolution for DM calculation. (b) Huggins and Kramer plot. The extrapolated [η] was = (2.5 ± 0.2) dL/g which correspond to (246.6 ± 21.8) cm^3/g. The M_w was determined using the Mark-Houking-Sakurada equation where $K = 0.023$ and $\alpha = 0.82$ (see S1 in SI). (c) GC–MS chromatogram of partially hydrolyzed pectin.

adsorption and Ca^{2+} desorption during the remediation stages. The amount of Ca^{2+} and Zn^{2+} was determined based on the difference between the initial and final concentrations in the solution (see S3 in SI).

The number of adsorbed ions were determined based on the difference between the initial and final concentrations in the solution. The equilibrium adsorption capacity ($q_{eq\ Ads}$; mg g^{-1}), the adsorption capacity at time t ($q_{t\ Ads}$; mg g^{-1}), the desorption capacity at time t ($q_{t\ Des}$; mg g^{-1}), the removal efficiency (R_{Eff} %) were calculated as follows:

$$q_{eq\ Ads} = \frac{C_0 - C_{eq\ Ads}}{d} \quad (4)$$

$$q_{t\ Ads} = \frac{C_0 - C_{t\ Ads}}{d} \quad (5)$$

$$q_{t\ Des} = \frac{C_{t\ Des}}{d} \quad (6)$$

$$R_{Eff}\% = \left(\frac{C_0 - C_{eq\ Ads}}{C_0}\right) \times 100\% \quad (7)$$

where C_0 is the initial concentration of a given crosslinking agent or pollutant (mg/L), $C_{eq\ Ads}$ is the equilibrium concentration (mg/L), $C_{t\ Ads}$ is the concentration at time t, d is the adsorbent dose (g/L). All adsorption experiments were done in triplicate.

3. Results and discussion

3.1. Characterization of neat pectin powder

Fig. 1a shows the Gaussian peak deconvolution in the carboxyl region for the estimation of the DM. The calculated DM was (9.5 ± 0.3) % in good agreement with the nominal value. Fig. 1b shows the Huggins and Kramer plot obtained for the viscosity. The extrapolated values of intrinsic viscosity ([η]) correspond to (246.6 ± 21.8) cm^3/g, which is in good agreement with previous studies on low DM % pectin (Qi et al., 2023). The estimated molecular weight (Mw) from this plot was (82,000 ± 9000) g mol^{-1}.

Fig. 1c shows the GC–MS chromatogram of the residual sugar content of the partially hydrolyzed pectin. From this, the residual sugar content of partially hydrolyzed pectin was quantified, revealing the low presence of arabinose (106.5 μg, 6.3 %), rhamnose (18.7 μg, 1.1 %), galactose (52.9 μg, 3.1 %), and galacturonic acid (41.7 μg, 2.5 %). The significant reduction in galacturonic acid from the nominal 91 % indicates partial hydrolysis of the pectin backbone. This partial hydrolysis likely targeted glycosidic bonds, releasing their associated monosaccharides. The low galacturonic acid content obtained (2.5 %), together with the high monosaccharides content (10.5 %), suggest a selective degradation of RG-I and RG-II (Sila et al., 2009). The high nominal galacturonic acid (91 %) reflects HG dominance, while the residual sugars highlight the low presence of RG-I and RG-II in the pectin structure. These findings agree with previous studies that showed partial hydrolysis preferentially targets hairy regions, reducing associated galacturonic acid (Yapo et al., 2007). Moreover, the high molecular weight and low DM of the pectin suggest a linear and extended homogalacturonan (HG) structure with consecutive free carboxyl groups. This arrangement is crucial to forming strong crosslinked "egg-box" networks.

3.2. Structure of dry pectin at different crosslinking times

LM pectin was crosslinked at different times (5, 15, and 40 min) to reach different calcium contents (see Section 3.3). The FT-IR spectra (Figs. 2a and b) show an intense band at ~3600–3000 cm^{-1}, indicating hydroxyl group stretching (OH). Bands in the 3000–2850 cm^{-1} range correspond to methyl group vibrations (CH_3). The band at ~1725 cm^{-1} is attributed to the $C = O$ ester stretching in non-ionic carboxyl groups (COOH, $COOCH_3$). Additionally, the bands at ~1400–1440 cm^{-1} and ~1585–1600 cm^{-1} represent the symmetric and asymmetric stretching vibrations of carboxylate anions (COO^-) (Balaria & Schiewer, 2008; Kozioł et al., 2022). After Ca^{2+} crosslinking, the carboxylate band (see Fig. 2b) shifts to higher wave numbers, indicating the interaction of divalent metal ions (Ca^{2+}) with the free ionic carboxyl group in the pectin chains. Specifically, the band at 1406 cm^{-1} for neat pectin depended on crosslinking time and gradually shifted to 1417 cm^{-1}, while the band at 1590 cm^{-1} slightly shifted to 1594 cm^{-1} after 40 min of crosslinking. This behavior means that the energy required for the molecular vibration associated with those bands has increased due to the coulombic interaction between Ca^{2+} ions and the ionized carboxyl group, which is responsible for the formation of "egg-box" structure, in agreement with Assifaoui et al. (Assifaoui et al., 2010).

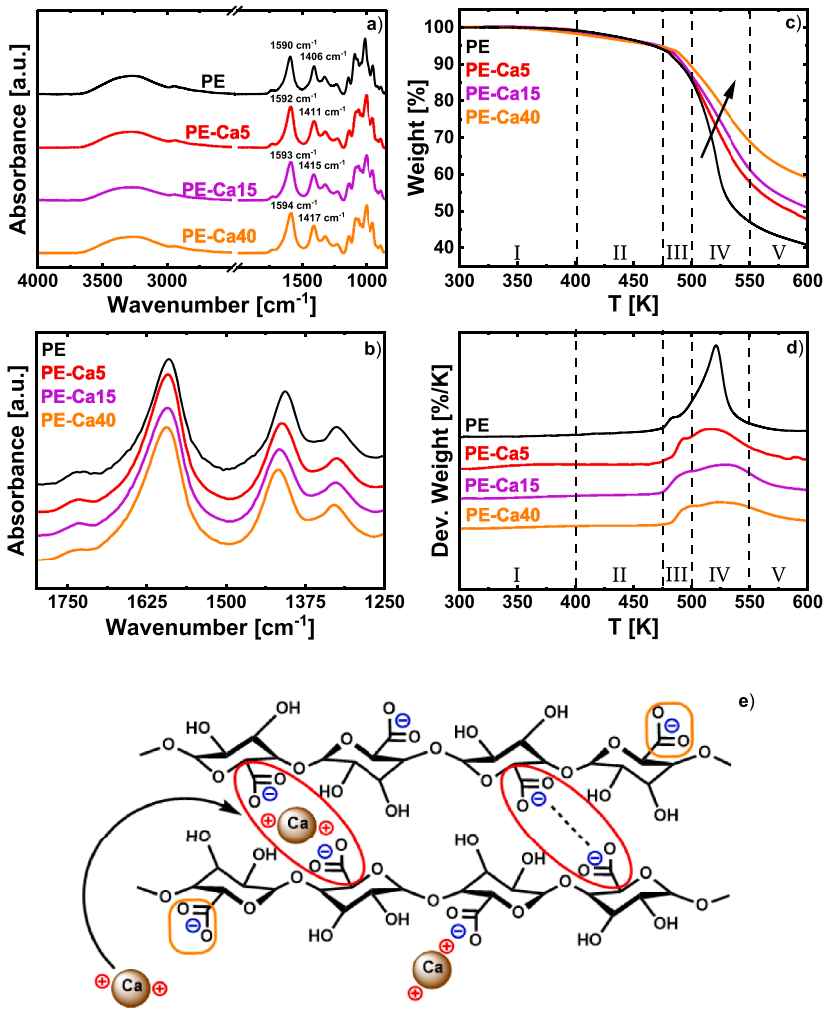

Fig. 2. (a) FT-IR spectra of PE films and (b) carboxylate bands shift of PE films. (d) Thermogravimetric scans and (d) derivative of weight loss as a function of temperature with heating rate of 10 K/min. (e) The cartoon depicts the "egg-box" structure. Orange square and red oval highlight the carboxyl group responsible for primary and secondary decarboxylation and carboxylate band shift of PE films, respectively.

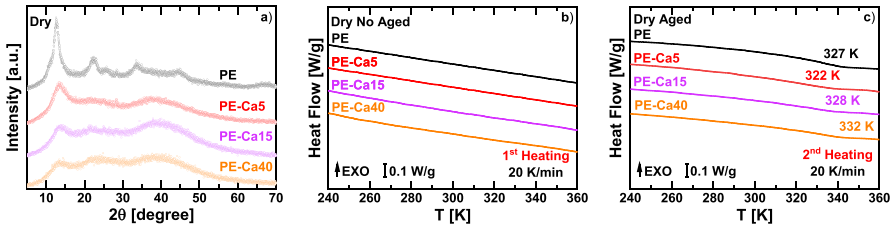

Fig. 3. (a) XRD pattern of dried neat pectin and crosslinked at different times (5, 15, and 40 min). Heat flow as a function of the temperature of dried pectin samples before (b) and after aging (c), where the glass transition temperature is revealed.

TGA measurements of dry pectin samples reveal different decomposition stages (Fig. 2c and d). Stage I (~400 K) shows slight weight loss due to strongly bound water evaporation. Above 400 K, PE decomposition begins in three stages, with Stage II involving the loss of weakly bonded volatile compounds like hydroxyl groups, showing no significant differences with varying Ca content (Kozioł et al., 2022). Above 475 K, decomposition depends on crosslinking, as crosslinked PE exhibits greater thermal stability with slower and reduced weight loss(Gohil, 2011). The derivative curve (Fig. 2d) highlights peaks in stages III and IV for neat PE, linked to primary and secondary decarboxylation, respectively, with primary decarboxylation arising from free carboxyl groups and secondary from groups interacting with divalent ions (illustrated in Fig. 3e) (Kozioł et al., 2022). In Stage V, successive mass loss results in pectin residue formation and pyrolysis at high temperatures (Kozioł et al., 2022).

Fig. 3a shows the XRD spectrum of the dry PE film crosslinked at different times. For neat PE (un-cross-linked, see Fig. 3a), intense and sharp Bragg peaks are observed at 2θ values of 12.6°, 22.6°, 33.8° and 45°. From the first and most intense diffraction peak, a *d*-spacing of 0.70 nm was obtained (Gohil, 2011; Li et al., 2007). This *d*-spacing represents the distance between two linear pectin chain segments interacting by H-bond (Gohil, 2011; Grant et al., 1973). While neat PE chains interact via H-bonds, the presence of Ca^{2+} ions introduces non-covalent Ca-b-ridges between two free carboxyl groups of two different PE chains,

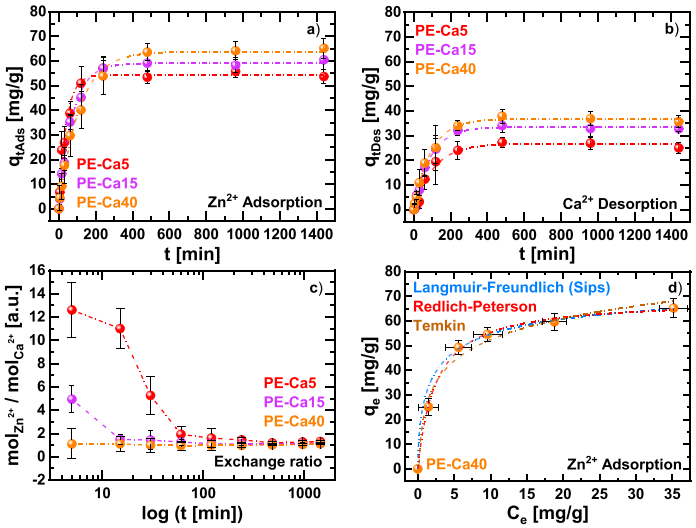

Fig. 4. (a) Zn^{2+} adsorption and (b) Ca^{2+} desorption kinetics at 25 °C of PE-Ca5, PE-Ca15, and PE-Ca40 at a dose of 1 g/L. The initial adsorbate concentration was 100 mg/L at pH 7. Dashed lines represent the fitting of the PFO model. (c) The exchange ratio as a function of time between the moles of adsorbed Zn^{2+} and desorbed Ca^{2+}. (d) Zn^{2+} adsorption isotherms of PE-Ca40 at a dose of 1 g/L at pH = 7. The cyan line indicates the nonlinear fitting obtained using the Sips model, the red line indicates the nonlinear fitting obtained using the R–P model and the brown indicates the nonlinear fitting obtained using Temkin model.

breaking the periodicity of the H-bond (Gohil, 2011), and forming "egg-box" dimers (Fang et al., 2008; Powell et al., 1982; Walkinshaw & Arnott, 1981). As a result, after Ca^{2+} crosslinking at different times, the observed diffraction peaks are broader than those neat PE films as previously observed (Martínez-Sabando et al., 2023b) and shift to higher 2θ values. From the most intense diffraction peak, the lateral spacing decreases to 0.66 nm, 0.65 nm and 0.63 nm, increasing the crosslinking time, indicating more packed crystals due to Ca^{2+} electronegativity. According to the "egg-box" model, this shrinking effect has also been previously reported for the dimerization of polymer chains through Ca^{2+} coordination (Walkinshaw & Arnott, 1981).

Finally, we analyze the glass transition temperature of the dry samples at different cross-linking times. As mentioned above, determining the glass transition temperature (T_g) of cross-linked pectin is challenging due to its nature as a complex polysaccharide, resulting in a very broad signal in a DSC experiment. Fig. 3b shows a DSC heating run (20 K/min) for neat and cross-linked pectin where the T_g is not readily observed as a flat signal is obtained. However, aging in a DSC experiment facilitates the observation of a T_g that was previously not visible due to enthalpy relaxation (Cangialosi, 2024). Before aging, the material may be in a non-equilibrated state, which can cause the transition to be broad or hidden. During aging (at a temperature below T_g), molecular rearrangements occur, thus reducing excess enthalpy. This produces a more defined step change in heat capacity (Δc_P), making T_g more apparent in the DSC scan.

Fig. 3c shows the heat flow after aging at 288 K for 4 h, where a clear step is observed. The glass transition of the neat pectin results in 327 K. Surprisingly, after 5 min of cross-linking, T_g decreases 5 degrees to 322 K. This is contrary to what is expected because, typically, T_g increases with cross-linking time as it restricts the molecular mobility (Marzocca et al., 1997). The structure of low methoxyl neat pectin consists of several hydrogen-bonded chains. During the cross-linking reaction, these hydrogen bonds are broken and replaced by calcium ions. Additionally, as observed in the X-ray diffraction patterns, the connected chains contract, increasing free volume and decreasing the glass transition temperature. After this first step of cross-linking, for 15 and 40 min, T_g increases with cross-linking time as expected.

3.3. Dependence of adsorption mechanisms of pectin with crosslinking time - structure after adsorption

This section evaluates the potential of PE-Ca^{2+} adsorbents, crosslinked at different times, for remediating heavy metals. ICP-AES experiments were conducted to measure the adsorbed Ca^{2+} ions after 5, 15, and 40 min of crosslinking, quantify Zn^{2+} uptake from aqueous solutions, and detect any Ca^{2+} release during Zn^{2+} remediation.

After cross-linking, five washing cycles were performed to extract any excess calcium not linked to pectin. After washing, the average adsorbed Ca^{2+} concentrations were 46.1 ± 4.2 mg/L (1.15 ± 0.10 mmol), 60.4 ± 1.1 mg/L (1.51 ± 0.03 mmol), and 67.5 ± 2.9 mg/L (1.69 ± 0.07 mmol) for 5, 15, and 40 min of crosslinking, respectively. Since the amount of GalA used for the Ca^{2+} crosslinking was 5.86 mmol (see S3 in SI), these values correspond to stoichiometric ratios (R) of 0.20, 0.26, and 0.29, consistent with the formation of "egg-box" dimers (Cao et al., 2020).

Fig. 4a shows the kinetic results of Zn^{2+} adsorption as a function of time for the three crosslinking times. All kinetics follow the pseudo-first-order (PFO) model (see Table 1), suggesting that electrostatic forces primarily drive the Zn^{2+} binding process (Jakóbik-Kolon et al., 2017a, 2017b). The results indicate that the sample crosslinked for 40 min

Table 1
ICP-AES results for Zn^{2+} adsorption and Ca^{2+} desorption kinetics using the Pseudo-First-Order (PFO) model for PE-Ca crosslinked at different times. The experiments were conducted at 25 °C with a dose of 1 g/L, an initial Zn^{2+} concentration (C_0) of 100 mg/L, and a pH of 7. The table includes the kinetic parameters: correlation coefficient (R^2), the kinetic constant (k_1 [min^{-1}]), the adsorption capacity (q_{eq}), and the removal efficiency (R_{Eff}).

Sample	R^2	Zn^{2+} adsorption				Ca^{2+} desorption			
		$k_{1\ ads}\ Zn^{2+}$ [min^{-1}]	$q_{t\ ads}\ Zn^{2+}$ [mg g^{-1}]	Zn^{2+}_{ads} [mmol]	$R_{eq\ Eff}$ [%]	$k_{1\ des}\ Ca^{2+}$ [min^{-1}]	$q_{t\ des}\ Ca^{2+}$ [mg g^{-1}]	Ca^{2+}_{des} [mmol]	Exchange ratio
PE-Ca5	0.98	0.025 ± 0.003	54.5 ± 1.4	0.83 ± 0.02	54.5 ± 1.4	0.009 ± 0.001	26.7 ± 0.9	0.67 ± 0.02	1.24 ± 0.05
PE-Ca15	0.99	0.0138 ± 0.0008	59.1 ± 0.9	0.90 ± 0.01	59.1 ± 0.9	0.0109 ± 0.0006	33.5 ± 0.5	0.84 ± 0.01	1.07 ± 0.02
PE-Ca40	0.99	0.0091 ± 0.0005	63.9 ± 1.2	0.98 ± 0.02	63.9 ± 1.2	0.0111 ± 0.0006	37.6 ± 0.6	0.94 ± 0.02	1.04 ± 0.03

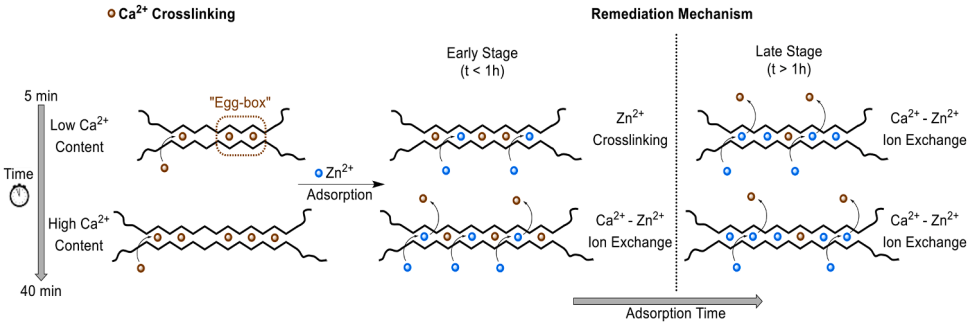

Fig. 5. Schematic illustration of how increasing crosslinking time (reflected by higher Ca^{2+} content) influences Zn^{2+} adsorption mechanisms. In samples with relatively low Ca^{2+} content (PE-Ca5 and PE-Ca15), both Zn^{2+} crosslinking (early stage) and Ca^{2+} - Zn^{2+} ion exchange (late stage) contribute to remediation. In contrast, when Ca^{2+} content is higher (PE-Ca40), ion exchange becomes the predominant removal mechanism.

(PE-Ca40) exhibited the highest adsorption capacity, attributed to the highest calcium ion content. However, PE-Ca40 showed slower Zn^{2+} adsorption kinetics due to its higher swelling capacity, requiring more time (see Fig. 5a). Notably, Zn^{2+} adsorption occurs rapidly, with PE-Ca40 achieving a removal efficiency of 17.8 ± 2.3 % within 30 min, increasing to 29.9 ± 1.4 % after 60 min. When the Zn^{2+} concentration in the solution was reduced to realistic pollutant levels (1 mg/L), the removal efficiency reached almost (100 ± 1) % in minutes.

To elucidate the Zn^{2+} remediation mechanism in PE-Ca adsorbents, we analyzed the kinetics of Ca^{2+} release (desorption) during Zn^{2+} remediation (Fig. 4b), i.e., we measured by ICP how many calcium ions appeared in the water solution during Zn remediation. This analysis revealed the degree of substitution of Ca^{2+} by Zn^{2+} over time.

The adsorbent cross-linked for 5 min (PE-Ca5), which started with 1.15 mmol of calcium, absorbed 0.83 mmol of zinc. However, only 0.67 mmol of calcium was released into the water. This result indicates that part of the remediation of Zn (0.67 mmol) is produced by exchanging positions with calcium, with an exchange ratio of 1.24 (0.83/0.67), like other studies have shown (Jakóbik-Kolon et al., 2017a, 2017b). However, some Zn ions (0.16 mmol = (0.83–0.67) mmol) do not interchange with Ca. The question is, therefore, how these Zn ions are being remediated. We propose a new mechanism in which these extra Zn ions continue crosslinking the pectin (see Fig. 5). Increasing the crosslinking time to 15 min (PE-Ca15), we find that approximately (0.90 ± 0.01) mmol of Zn^{2+} was adsorbed, with (0.84 ± 0.01) mmol of Ca^{2+} released, yielding an average exchange ratio of 1.07. Finally, for 40 min of crosslinking (PE-Ca40), (0.98 ± 0.04) mmol of Zn^{2+} was adsorbed and released (0.92 ± 0.04) mmol of Ca^{2+}, with an average exchange ratio closer to 1. Thus, increasing the crosslinking time (i.e. calcium content in the adsorbent), the exchange ratio decreases to 1. This is observed in Fig. 4c where the exchange ratio is plotted versus remediation times.

Fig. 4d shows the Zn^{2+} adsorption capacity of PE-Ca40 after 24 h as a function of the equilibrium Zn^{2+} concentration. The isotherm was fitted using both the Langmuir–Freundlich (Sips) (Sips, 1948), Redlich–Peterson (R–P) (Redlich & Peterson, 1959) and Temkin models. The sips model has the best statistics ($R^2_{adj} = 0.99$, $\chi^2 = 0.42$, $q_M = 77.9 \pm 9.7$ mg g^{-1}, $K_{LF} = 0.59 \pm 0.09$, $n = 0.7 \pm 0.2$) and considers a monolayer in which adsorption occurs at identical sites, with only one molecule able to be adsorbed at each location, suggesting that the adsorption is homogeneous and favorable. The R–P model also has a good statistic ($R^2_{adj} = 0.99$, $\chi^2 = 1.6$, $K_{RP} = 28.1 \pm 3.6$, $\alpha = 0.4 \pm 0.1$ L/mg, $\beta = 1.01 \pm 0.04$) and serves as an empirical hybrid of the Langmuir and Freundlich models, confirming that the adsorption is homogeneous and favorable. In contrast the Temkin model presumes that adsorption is a multi-layer process and is less statistically favorable ($R^2_{adj} = 0.97$, $\chi^2 = 11.1$, $A = 6.8 \pm 3.1$ L/mg, $b = 12.4 \pm 1.4$ J/mol) (Foo & Hameed, 2010; Wang & Guo, 2020).

To demonstrate that Zn ions continue to cross-link the pectin chains as a remediation mechanism, we measured the glass transition

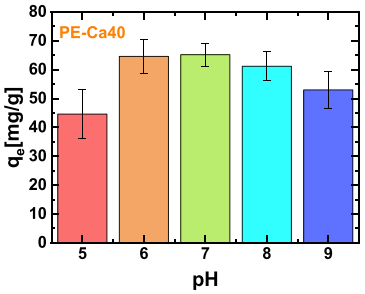

Fig. 6. Zn^{2+} adsorption at 25 °C of PE-Ca40 at a dose of 1 g/L. The initial adsorbate concentration was 100 mg/L at different pH levels.

temperature (T_g) of the absorbents before and after adsorption. The results revealed an increase in T_g for PE-Ca5 from 322 K to 328 K following Zn remediation. This indicates that the network post-remediation is more extensively cross-linked, approaching the T_g value of PE-Ca40 (see Fig. 5). This is also observed for pectin cross-linked for 15 min. The T_g of PE-Ca15 increases from 328 K to 331 K after remediation. However, no significant change in T_g was observed for PE-Ca40, as the primary mechanism involved is ion exchange (exchange ratio = 1) rather than additional cross-linking. Furthermore, after Zn^{2+} remediation, the sample PE-Ca40 displayed similar XRD patterns, TGA profiles, and FT-IR carboxylate peak wavenumbers to those of PE-Ca40 (see S4 in SI). This indicates that the structure is maintained even after substituting Ca^{2+} with Zn^{2+}, reinforcing that the ion exchange mechanism is the predominant process in PE-Ca40.

In conclusion, for LMP pectin-based adsorbents, both mechanisms - 1) Zn^{2+} crosslinking and 2) ion exchange- contribute to metal uptake after 5 and 15 min of Ca^{2+} crosslinking. In contrast, after 40 min of crosslinking, ion exchange becomes the predominant mechanism (Jakóbik-Kolon et al., 2017b; Minamisawa et al., 2005; Petrović et al., 2017). The distinction between these two processes can be visualized by plotting the exchange ratio over time (Fig. 4c). In the early stages (PE-Ca5 and PE-Ca15), the lower Ca^{2+} content allows Zn^{2+} ions to bind to unoccupied carboxyl preferentially (COO^-) groups, promoting additional crosslinking before engaging in ion exchange with Ca^{2+}. This behavior is attributed to the higher affinity of Zn^{2+} for carboxylate ligands, due to its smaller ionic radius, higher electronegativity, and involvement of d-orbitals in coordination. In contrast, PE-Ca40, with its more extensively crosslinked network, facilitates Zn^{2+} uptake predominantly through ion exchange. The strong interaction between transition metal ions like Zn^{2+} and pectin carboxyl groups is well-documented, with numerous studies highlighting their ability to form stable complexes with carboxylate ligands (Huynh et al., 2016; Ürüncüoğlu et al., 2021).

The pH dependence on the adsorption of the PE Ca40 was studied

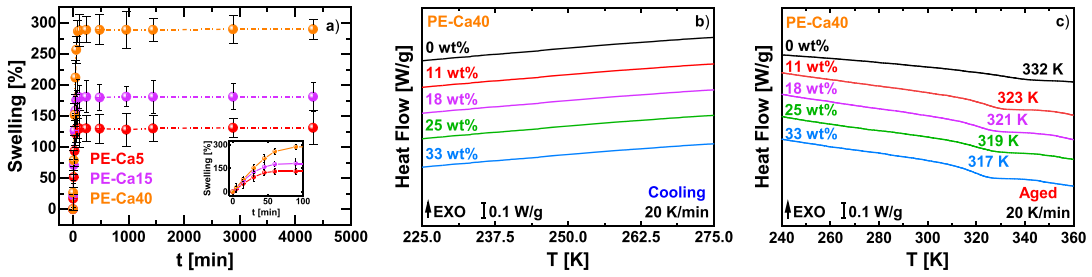

Fig. 7. (a) Swelling of PE-Ca crosslinked at different crosslinking time. The inset shows an enlargement of the graph for the first 100 min where plateau is reached. (b) Heat flow for hydrated PE-Ca40 during the cooling and (b) heating cycles at different water contents. Before the heating cycle, the sample was aged at 15 °C for 4 h.

after 24 hours (Fig. 6a). The adsorption capacity remained unaffected between pH 6 and 8. In contrast, it decreased at acidic pH due to the protonation of pectin carboxylates and at alkaline pH due to partial depolymerization of the pectin network.

Pectin is a promising and sustainable solution for heavy metal remediation at neutral pH due to its competitive adsorption properties, eco-friendliness, and abundance. Notably, our findings indicate that pectin offers rapid remediation kinetics and a high maximum adsorption capacity of 29.7 mg g^{-1} with a dose of 1 g/L after 1 hour. To illustrate these advantages, we can compare them with other recently proposed adsorbents. For instance, activated carbon from apple (Depci et al., 2012) achieved a maximum adsorption capacity of 7.8 mg g^{-1} under similar conditions (pH 5, 40 mg/L of Zn^{2+}, room temperature). However, it required a higher dose (4 g/L) for the same contact time (1 hour). Similarly, rice straw biochar (Park et al., 2017) reached 29.33 mg g^{-1} at same initial concentration (100 mg/L of Zn^{2+}), but at higher dose (2 g/L), and a longer contact time (5 h). Calcareous clay (Sdiri et al., 2012) achieved 13.32 mg g^{-1} with a comparable dose (1 g/L) and time (1 hour) but at a different pH (6) and lower initial concentration (20 mg/L). Chitosan–PVA nanofibers (Anitha et al., 2015) showed a significantly lower capacity (4.198 mg g^{-1}) even with a much higher dose (5 g/L) and a lower pH (5) and initial Zn^{2+} concentration (10 mg/L). Lastly, oxidized multi-walled carbon nanotubes (Ma et al., 2015) achieved a lower capacity (13.6 mg g^{-1}) in a 40 mg/L of Zn^{2+} at pH 5 requiring a significantly longer contact time of 60 h. These comparisons highlight pectin's potential for effective heavy metal removal. Finally, it is also important to note that pectin is reusable up to five adsorption-desorption cycles in acidic conditions. (Martínez-Sabando et al., 2023b).

3.4. The role of water on physical properties of pectin-based adsorbents

Water molecules facilitate the swelling and diffusion of contaminants in adsorbents, resulting in physical alterations that can influence the remediation process. Accordingly, we will examine how the physical properties of the adsorbent transform during hydration.

3.4.1. Water adsorption and the glass transition of hydrated pectin

Initially, we investigated how the crosslinking time influenced the swelling properties of the PE-Ca adsorbents. A high swelling capacity improves the movement of adsorbates into the active sites, thereby increasing the adsorption capacity. This characteristic is essential in water treatment, as pollutants must diffuse into the matrix to access the adsorption sites.

The PE-Ca5 and PE-Ca15 films reached the maximum water uptake equilibrium after 70 min, while the PE-Ca40 film required 90 min to reach equilibrium and showed a higher swelling capacity (Fig. 7a). The swelling capacity increases with increasing calcium content. During crosslinking, two carboxyl groups are attached to the Ca ion. Even though the availability of free COOH groups decreases with the increase in crosslinking time, the swelling capacity of pectin increases. This is because water can efficiently hydrate the "egg box" structure than the free COOH or hydroxyl groups, as observed in the XRD results (see below). Similar behavior has been previously reported in alginate crosslinked with varying amounts of Ca^{2+} (Remuñán-López & Bodmeier, 1997). Since PE-Ca40 demonstrated the highest adsorption capacity and swelling properties, we chose this material to investigate the structural changes induced by water in the pectin structure.

As mentioned above, determining the glass transition temperature (T_g) of wet and crosslinked pectin is challenging due to its nature as a complex polysaccharide. This results in a very broad T_g signal in a DSC experiment, making it difficult to determine. Here, we follow the same strategy for dried materials, i.e., we applied aging experiments at 288 K for 4 h. Fig. 7b and c show the calorimetric response of hydrated PE-Ca40 for different water contents (from dried to 33 wt %). No water crystallization is observed for water contents up to 33 wt % (see Fig. 6a), which indicates that, until this water content, all the water molecules are non-freezable bound water (Brunt, 1962; Hatakeyama et al., 1988; Iijima et al., 2000), as normally observed in aqueous solutions (Cerveny et al., 2007). On heating (Fig. 7b), after aging the sample at 288 K during 4 h, PE-Ca40 shows a glass transition (T_g), which progressively shifts to lower temperatures (from 332 K to 317 K) as the water content increases. This behavior is due to the well-known plasticization phenomenon produced by water and reported in other carbohydrates and most of hydrated polymers (Cerveny et al., 2005; Combarro Palacios et al., 2019; Einhorn-Stoll et al., 2012; Łukaszewska et al., 2024; Panchev et al., 2010; Roos, 1993). Due to plasticization, the viscosity and T_g decrease compared with the dry system. Furthermore, T_g is a characteristic property of the amorphous region of a polymer. Since T_g varies with hydration, the DSC measurements suggest that water primarily hydrates the amorphous portion of pectin. However, the semi-crystalline region (i.e. "egg-box" region), where remediation occurs, remains inaccessible by DSC.

The efficacy of an adsorbent for water remediation is affected by whether it is used below or above its glass transition temperature (T_g). Below T_g, the adsorbent remains in a glassy, rigid state, providing structural stability, well-defined pore sizes, and selective adsorption. This stability allows for more controlled adsorption because the functional groups (e.g., hydroxyl, carboxyl, etc.) remain in fixed positions, enhancing the selectivity toward target molecules. In addition, below T_g, the adsorbent has fixed pore sizes that allow only smaller molecules to enter while excluding larger ones. However, the diffusion rates of polluted water may be lower in this rigid state, potentially reducing adsorption efficiency. In contrast, when the adsorbent is used above T_g, it becomes rubbery, which increases molecular mobility and enhances diffusion. This can accelerate the adsorption rates because there is faster access to the functional groups used in the adsorption process. Still, excessive flexibility in this state might collapse the pore structure, resulting in decreased adsorption capacity, possible desorption of contaminants, or even degradation of the material.

Table 2
ICP results of Zn^{2+} adsorption and Ca^{2+} desorption by PE-Ca40 at different temperatures for 240 min, at a dose of 1 g/L, with Zn^{2+} initial concentration of 100 mg/L, at pH 7.

Sample	Zn^{2+} adsorption and Ca^{2+} desorption				
	T [°C]	q_{eq} Zn^{2+} [mmol]	Ca^{2+} released [mmol]	R_{Eff} [%]	Exchange ratio
PE-Ca40	40	0.97 ± 0.01	0.92 ± 0.09	63,4 ± 0,1	1.05 ± 0.09
PE-Ca40	50	1.02 ± 0.01	0.94 ± 0.05	66,7 ± 0,2	1.09 ± 0.06
PE-Ca40	60	1.09 ± 0.01	0.96 ± 0.05	71,45 ± 0,07	1.14 ± 0.06

Therefore, the optimal operating condition for an adsorbent depends on the specific adsorption mechanism and the properties of the material. Below T_g, stability is ensured for porous materials and rigid adsorbents, while slightly exceeding T_g may enhance performance in diffusion-limited systems, provided the adsorbent maintains its structural integrity.

We conducted zinc remediation experiments for 240 min at varying temperatures (40, 50, and 60 °C) to investigate the influence of the glass transition temperature (T_g) on the behavior of adsorption properties of pectin. The results demonstrate that Zn^{2+} adsorption is most effective at 60 °C, i.e., above the T_g of the adsorbent (see Table 2). PE-Ca40 transitions into a rubbery state at elevated temperatures, and the amount of adsorbed Zn^{2+} increases with temperature while maintaining an exchange ratio close to one. This indicates that the rubbery state of the adsorbent, induced by both adsorbed water and higher temperatures, and enhances the ion exchange process. The increased mobility of the polymer chains in the rubbery state likely facilitates better interaction between Zn^{2+} ions and the active sites, improving the overall adsorption efficiency. This behavior underscores the importance of temperature and material state in optimizing remediation.

3.4.2. *The role of water on the pectin structure*

As discussed earlier, the "egg-box" structure of pectin adsorbents (i.e. after crosslinking, the parallel alignment of HG chains with calcium ions at the center) plays a crucial role in the remediation mechanism. Therefore, in the following, we will discuss how this structure evolves during hydration.

Fig. 8a presents the XRD spectra of hydrated samples ranging from ~0 to 33 wt %. As is typical for amorphous polymers, hydrated pectin lacks long-range molecular order and exhibits no peaks characteristic of crystalline forms. Consequently, broad halos are observed at ~25° and ~40°. These amorphous halos exhibit different behaviors with changing hydration: for water contents below 18 wt %, only the relative intensity of the peaks varies, whereas, for water contents exceeding 18 wt %, the amorphous halos are significantly influenced by hydration. This behavior also agrees with the variation of the glass transition previously analyzed.

In addition to the amorphous halos, another peak is observed at low angles for all the hydration levels, which correspond to the *d*-spacing between two pectin changes. To determine the interlayer distance between two HG chains in the "egg-box" arrangement for each water content, we have restricted the 2θ values from 5° to 20° to shorten the measurement times and thus avoid sample dehydration. Fig. 8b shows these XRD spectra for all hydration levels. We observe how the peak, initially at 2θ =14°, is not modified by hydration until reaching 18 wt %. Above this value, the *d*-spacing systematically increases with hydration. This indicates that the lateral spacing rises from 0.63 nm to 0.89 nm as hydration increases (see inset in Fig. 8b and Table 3). This behavior indicates that water enters between the HG chains from the initial stages of hydration (above 11 wt %). As a result, the contaminated water immediately spontaneously interacts with the calcium ions within the "egg box" of pectin, enabling rapid remediation.

4. Conclusions

This work presented a quantitative function relationship for externally calcium-cross-linked, low methoxyl pectin (LMP) films. We clarified how crosslinking time, hydration, and temperature affect the ability to capture Zn^{2+} ions. The adsorption of Zn^{2+} onto cross-linked pectin films occurs through two main mechanisms: ion exchange between Ca^{2+} and $Zn^{2+}$and direct crosslinking of Zn^{2+} within the pectin network. In samples with lower Ca^{2+} content, Zn^{2+} contributes more significantly to crosslinking, while ion exchange dominates the process in highly cross-linked samples. Hydration significantly affects the structural properties of pectin, decreasing the glass transition temperature (T_g) from 332 to 317 K at 33 wt % of hydration. Additionally, the water sorption increases the interlayer distance from 0.63 to 0.89 nm within the "egg-box" configuration, facilitating better accessibility of metal ions to active adsorption sites. On the other hand, this rapid early swelling effect improves accessibility to adsorption sites and, together with water-induced plasticization, shifts the polymer into a rubbery state in which ion mobility is high. Adsorption tests confirm that Zn^{2+} removal rises when the operating temperature exceeds the hydrated T_g, achieving 71.45 % of extraction at pH 6–8. In this rubbery state, the material becomes more

Table 3
XRD parameters for hydrated PE-Ca40 at different water content.

Material	c_w [%]	2θ [degree]	d-spacing [nm]
PE-Ca40	0	14.02	0.63
PE-Ca40	11	14.02	0.63
PE-Ca40	18	12.39	0.72
PE-Ca40	25	11.46	0.78
PE-Ca40	33	10.28	0.89

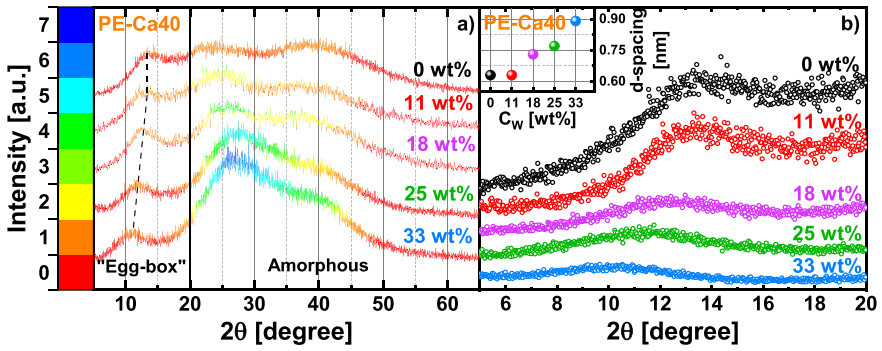

Fig. 8. (a) Multiple X-Ray scans while drying PE-Ca (color-scale indicates the intensity of each XRD pattern). (b) High XRD resolution measurements of PE-Ca at fixed water level. Inset: calculated D-spacing at fixed water level (the dashed line is just a guide for the eyes).

flexible, increasing ion mobility and facilitating the diffusion of metal ions within the polymer matrix. This behavior highlights the importance of understanding the relationship between temperature and adsorption performance. This study confirms that calcium-crosslinked pectin is a promising material for heavy metal removal from water. These findings demonstrate that performance is maximized when PE-Ca adsorbents operate above their hydrated T_g and during the initial stages of swelling. Simultaneously, the crosslinking protocol provides a molecular lever to balance capacity, rate, and selectivity. By optimizing hydration and Ca^{2+} loading, PE-Ca pectin emerges as a sustainable, biodegradable alternative to conventional heavy metal adsorbents. Moreover, the novel methodological framework presented here can be generalized to other polysaccharide networks and contaminant species in environmental remediation.

Finally, it is important to note that our analysis assumed homogeneous water distribution within the matrix, although localized variations in hydration could result in spatially distinct T_g values and inconsistent mechanical properties. The connection between T_g and adsorption efficiency, while compelling, remains inferential in the absence of direct molecular mobility data, such as diffusometry or spectroscopy. In particular, although crosslinked pectin in the rubbery state ($T > T_g$) demonstrated enhanced ion mobility and adsorption capacity, the study did not directly measure diffusion rates or identify rate-limiting steps at the molecular level.

CRediT authorship contribution statement

Francesco Coin: Writing – original draft, Investigation, Formal analysis, Data curation. **Aitor Larrañaga:** Investigation. **Silvina Cerveny:** Writing – review & editing, Writing – original draft, Supervision, Investigation, Funding acquisition, Formal analysis, Conceptualization.

Declaration of competing interest

The authors declare that they have no known competing financial interests or personal relationships that could have appeared to influence the work reported in this paper.

Acknowledgments

We acknowledge grant PID2023-146348NB-I00 funded by Ministerio de Ciencia, Innovación y Universidades/Agencia Estatal de Investigación (MCIN/AEI) and Department of Education of the Basque Government under grant PIBA_2024_1_0011. The authors thank for technical support provided by SGIker (UPV/EHU/ ERDF, EU).

Supplementary materials

Supplementary material associated with this article can be found, in the online version, at doi:10.1016/j.carpta.2025.100885.

Data availability

The data that support the findings of this study are available upon reasonable request.

References

Anitha, T., Senthil Kumar, P., & Sathish Kumar, K. (2015). Binding of Zn(II) ions to chitosan–PVA blend in aqueous environment: Adsorption kinetics and equilibrium studies. *Environmental Progress & Sustainable Energy, 34*(1), 15–22.

Arnous, A., & Meyer, A. S. (2008). Comparison of methods for compositional characterization of grape (Vitis vinifera L.) and apple (Malus domestica) skins. *Food and Bioproducts Processing, 86*(2), 79–86.

Ashcroft, N. W., & Mermin, N. D. (1976). *Solid state physics*. Holt: Rinehart and Winston.

Assifaoui, A., Loupiac, C., Chambin, O., & Cayot, P. (2010). Structure of calcium and zinc pectinate films investigated by FTIR spectroscopy. *Carbohydrate Research, 345*(7), 929–933.

Axelos, M. A. V., & Thibault, J. F. (1991). CHAPTER 6 - The Chemistry of low-methoxyl pectin gelation. In R. H. Walter (Ed.), *The chemistry and technology of pectin* (pp. 109–118). San Diego: Academic Press.

Balaria, A., & Schiewer, S. (2008). Assessment of biosorption mechanism for Pb binding by citrus pectin. *Separation and Purification Technology, 63*(3), 577–581.

Braccini, I., & Pérez, S. (2001). Molecular basis of Ca2+-induced gelation in alginates and Pectins: The egg-box model revisited. *Biomacromolecules, 2*(4), 1089–1096.

Brunt, N. A. (1962). The influence of swelling by water vapour on the mechanical properties of a polymer. *Kolloid-Zeitschrift und Zeitschrift für Polymere, 185*(2), 119–125.

Cangialosi, D. (2024). Physical aging and vitrification in polymers and other glasses: Complex behavior and size effects. *Journal of Polymer Science, 62*(9), 1952–1974.

Cao, L., Lu, W., Mata, A., Nishinari, K., & Fang, Y. (2020). Egg-box model-based gelation of alginate and pectin: A review. *Carbohydrate Polymers, 242*, Article 116389.

Carvalho, I. T., & Santos, L. (2016). Antibiotics in the aquatic environments: A review of the European scenario. *Environment International, 94*, 736–757.

Cerveny, S., Colmenero, J., & Alegria, A. (2007). Dielectric properties of water in amorphous mixtures of polymers and other glass forming materials. *Journal of Non-Crystalline Solids, 353*(47–51), 4523–4527.

Cerveny, S., Colmenero, J., & Alegría, A. (2005). Dielectric investigation of the low-temperature water dynamics in the Poly(vinyl methyl ether)/H2O system. *Macromolecules, 38*(16), 7056–7063.

Chaichi, M., Badii, F., Mohammadi, A., & Hashemi, M. (2019). Water resistance and mechanical properties of low methoxy-pectin nanocomposite film responses to interactions of Ca2+ ions and glycerol concentrations as crosslinking agents. *Food Chemistry, 293*, 429–437.

Chatjigakis, A. K., Pappas, C., Proxenia, N., Kalantzi, O., Rodis, P., & Polissiou, M. (1998). FT-IR spectroscopic determination of the degree of esterification of cell wall pectins from stored peaches and correlation to textural changes. *Carbohydrate Polymers, 37*(4), 395–408.

Ciriminna, R., Chavarría-Hernández, N., Inés Rodríguez Hernández, A., & Pagliaro, M. (2015). Pectin: A new perspective from the biorefinery standpoint. *Biofuels, Bioproducts and Biorefining, 9*(4), 368–377.

Coin, F., Rodríguez-Ramírez, C. A., Oyarbide, F. S., Picón, D., Goyanes, S., & Cerveny, S. (2024). Efficient antibiotic removal from water using europium-doped poly(vinyl alcohol) nanofiber mats esterified with citric acid. *Journal of Water Process Engineering, 63*, Article 105447.

Combarro Palacios, I., Olsson, C., Kamma-Lorger, C. S., Swenson, J., & Cerveny, S. (2019). Motions of water and solutes—Slaving versus plasticization phenomena. *The Journal Of Chemical Physics, 150*(12), Article 124902.

Corda, N., & Kini, M. S. (2020). Recent studies in adsorption of Pb(II), Zn(II) and Co(II) using conventional and modified materials:A review. *Separation Science and Technology, 55*(15), 2679–2698.

Cossu, L. O., De Aquino, S. F., Mota Filho, C. R., Smith, C. J., & Vignola, M. (2024). Review on pesticide contamination and drinking water treatment in brazil: The need for improved treatment methods. *ACS ES&T Water, 4*(9), 3629–3644.

De Gisi, S., Lofrano, G., Grassi, M., & Notarnicola, M. (2016). Characteristics and adsorption capacities of low-cost sorbents for wastewater treatment: A review. *Sustainable Materials and Technologies, 9*, 10–40.

Depci, T., Kul, A. R., & Önal, Y. (2012). Competitive adsorption of lead and zinc from aqueous solution on activated carbon prepared from Van apple pulp: Study in single- and multi-solute systems. *Chemical Engineering Journal, 200-202*, 224–236.

Einhorn-Stoll, U., Hatakeyama, H., & Hatakeyama, T. (2012). Influence of pectin modification on water binding properties. *Food Hydrocolloids, 27*(2), 494–502.

Fang, Y., Al-Assaf, S., Phillips, G. O., Nishinari, K., Funami, T., & Williams, P. A. (2008). Binding behavior of calcium to polyuronates: Comparison of pectin with alginate. *Carbohydrate Polymers, 72*(2), 334–341.

Foo, K. Y., & Hameed, B. H. (2010). Insights into the modeling of adsorption isotherm systems. *Chemical Engineering Journal, 156*(1), 2–10.

Gohil, R. M. (2011). Synergistic blends of natural polymers, pectin and sodium alginate. *Journal of Applied Polymer Science, 120*(4), 2324–2336.

Grant, G. T., Morris, E. R., Rees, D. A., Smith, P. J. C., & Thom, D. (1973). Biological interactions between polysaccharides and divalent cations: The egg-box model. *FEBS Letters, 32*(1), 195–198.

Hatakeyama, T., Nakamura, K., & Hatakeyama, H. (1988). Determination of bound water content in polymers by DTA, DSC and TG. *Thermochimica Acta, 123*, 153–161.

Hua, X., Wang, K., Yang, R., Kang, J., & Zhang, J. (2015). Rheological properties of natural low-methoxyl pectin extracted from sunflower head. *Food Hydrocolloids, 44*, 122–128.

Huynh, U. T. D., Chambin, O., du Poset, A. M., & Assifaoui, A. (2018). Insights into gelation kinetics and gel front migration in cation-induced polysaccharide hydrogels by viscoelastic and turbidity measurements: Effect of the nature of divalent cations. *Carbohydrate Polymers, 190*, 121–128.

Huynh, U. T. D., Lerbret, A., Neiers, F., Chambin, O., & Assifaoui, A. (2016). Binding of divalent cations to polygalacturonate: A mechanism driven by the hydration water. *The Journal of Physical Chemistry B, 120*(5), 1021–1032.

Iijima, M., Nakamura, K., Hatakeyama, T., & Hatakeyama, H. (2000). Phase transition of pectin with sorbed water. *Carbohydrate Polymers, 41*(1), 101–106.

Jakóbik-Kolon, A., Bok-Badura, J., Karoń, K., Mitko, K., & Milewski, A. (2017a). Hybrid pectin-based biosorbents for zinc ions removal. *Carbohydrate Polymers, 169*, 213–219.

Jakóbik-Kolon, A., Mitko, K., & Bok-Badura, J. (2017b). Zinc sorption studies on pectin-based biosorbents. *Materials, 10*(7), 844.

Jha, A., & Mishra, S. (2024). Exploring the potential of waste biomass-derived pectin and its functionalized derivatives for water treatment. *International Journal of Biological Macromolecules, 275*, Article 133613.

Kontogiorgos, V. (2021). *Pectin: Technological and physiological properties*. Springer Cham.
Kozioł, A., Środa-Pomianek, K., Górniak, A., Wikiera, A., Cyprych, K., & Malik, M. (2022). Structural determination of pectins by spectroscopy methods. *Coatings, 12*(4), 546.
Li, L., Fang, Y., Vreeker, R., Appelqvist, I., & Mendes, E. (2007). Reexamining the egg-box model in calcium−Alginate gels with x-ray diffraction. *Biomacromolecules, 8*(2), 464–468.
Loeb, S. K., Alvarez, P. J. J., Brame, J. A., Cates, E. L., Choi, W., Crittenden, J., … Kim, J.-H. (2019). The technology horizon for photocatalytic water treatment: Sunrise or sunset? *Environmental Science & Technology, 53*(6), 2937–2947.
Łukaszewska, I., Bukowczan, A., Raftopoulos, K. N., & Pielichowski, K. (2024). Examining the water–Polymer interactions in non-isocyanate polyurethane/polyhedral oligomeric silsesquioxane hybrid hydrogels. *Polymers, 16*(1), 57.
Luzio, G. A., & Cameron, R. G. (2008). Demethylation of a model homogalacturonan with the salt-independent pectin methylesterase from citrus: Part II. Structure–function analysis. *Carbohydrate Polymers, 71*(2), 300–309.
Ma, X., Yang, S.-T., Tang, H., Liu, Y., & Wang, H. (2015). Competitive adsorption of heavy metal ions on carbon nanotubes and the desorption in simulated biofluids. *Journal of Colloid and Interface Science, 448*, 347–355.
Martínez-Sabando, J., Coin, F., Melillo, J. H., Goyanes, S., & Cerveny, S. (2023a). A review of pectin-based material for applications in water treatment. *Materials, 16*(6), 2207.
Martínez-Sabando, J., Coin, F., Raposo, J. C., Larrañaga, A., Melillo, J. H., & Cerveny, S. (2023b). Dual crosslinking of low-methoxyl pectin by calcium and europium for the simultaneous removal of pharmaceuticals and divalent heavy metals. *Chemical Engineering Journal, 475*, Article 146162.
Marzocca, A. J., Cerveny, S., & Raimondo, R. B. (1997). Analysis of the variation of molecular parameters of NR during vulcanization in the frame of the conformational tube model. *Journal of Applied Polymer Science, 66*(6), 1085–1092.
Mekonnen, M. M., & Hoekstra, A. Y. (2016). Four billion people facing severe water scarcity. *Science Advances, 2*(2), Article e1500323.
Minamisawa, M., Minamisawa, H., Yoshida, S., & Takai, N. (2005). Characterization of adsorption gels prepared from plant biomaterials. *Green Chemistry, 7*(8), 595–601.
Minzanova, S. T., Mironov, V. F., Vyshtakalyuk, A. B., Tsepaeva, O. V., Mironova, L. G., Mindubaev, A. Z., & Milyukov, V. A. (2015). Complexation of pectin with macro- and microelements. Antianemic activity of Na, Fe and Na, Ca, Fe complexes. *Carbohydrate Polymers, 134*, 524–533.
Mitra, S., Chakraborty, A. J., Tareq, A. M., Emran, T. B., Nainu, F., Khusro, A., … Simal-Gandara, J. (2022). Impact of heavy metals on the environment and human health: Novel therapeutic insights to counter the toxicity. *Journal of King Saud University - Science, 34*(3), Article 101865.
Mutalib, A. A. A., & Jaafar, N. F. (2023). Electrogeneration of active photocatalysts for wastewater remediation: A review. *Environmental Chemistry Letters, 21*(2), 981–1003.
Namasivayam, S. K. R., Samrat, K., Arvind Bharani, R. S., Kavisri, M., John, F. K., & Meivelu, M. (2024). Pectin-nano zero valent iron nanocomposites for efficient heavy metal removal and bactericidal action against waterborne pathogens — Innovative green solution towards environmental sustainability. *International Journal of Biological Macromolecules, 277*, Article 133990.
Nasrollahzadeh, M., Sajjadi, M., Iravani, S., & Varma, R. S. (2021). Starch, cellulose, pectin, gum, alginate, chitin and chitosan derived (nano)materials for sustainable water treatment: A review. *Carbohydrate Polymers, 251*, Article 116986.
Oakenfull, D. G. (1991). CHAPTER 5 - The Chemistry of High-Methoxyl Pectins. In R. H. Walter (Ed.), *The chemistry and technology of pectin* (pp. 87–108). San Diego: Academic Press.
Othman, N. H., Alias, N. H., Fuzil, N. S., Marpani, F., Shahruddin, M. Z., Chew, C. M., … Ismail, A. F. (2022). A Review on the Use of Membrane Technology Systems in Developing Countries. *Membranes, 12*(1), 30.
Panchev, I. N., Slavov, A., Nikolova, K., & Kovacheva, D. (2010). On the water-sorption properties of pectin. *Food Hydrocolloids, 24*(8), 763–769.
Park, J.-H., Wang, J. J., Kim, S.-H., Cho, J.-S., Kang, S.-W., Delaune, R. D., … Seo, D.-C. (2017). Recycling of rice straw through pyrolysis and its adsorption behaviors for Cu and Zn ions in aqueous solution. *Colloids and Surfaces A: Physicochemical and Engineering Aspects, 533*, 330–337.
Petrović, M., Šoštarić, T., Stojanović, M., Petrović, J., Mihajlović, M., Ćosović, A., & Stanković, S. (2017). Mechanism of adsorption of Cu2+ and Zn2+ on the corn silk (Zea mays L.). *Ecological Engineering, 99*, 83–90.
Picón, D., Torasso, N., Baudrit, J. R. V., Cerveny, S., & Goyanes, S. (2022). Bio-inspired membranes for adsorption of arsenic via immobilized L-Cysteine in highly hydrophilic electrospun nanofibers. *Chemical Engineering Research and Design, 185*, 108–118.
Powell, D. A., Morris, E. R., Gidley, M. J., & Rees, D. A. (1982). Conformations and interactions of pectins: II. Influence of residue sequence on chain association in calcium pectate gels. *Journal of Molecular Biology, 155*(4), 517–531.
Qi, T., Ren, J., Li, X., An, Q., Zhang, N., Jia, X., & Wu, K. (2023). Structural characteristics and gel properties of pectin from citrus physiological premature fruit drop. *Carbohydrate Polymers, 309*, Article 120682.
Redlich, O., & Peterson, D. L. (1959). A Useful Adsorption Isotherm. *The Journal of Physical Chemistry, 63*(6), 1024. -1024.
Remuñán-López, C., & Bodmeier, R. (1997). Mechanical, water uptake and permeability properties of crosslinked chitosan glutamate and alginate films. *Journal of Controlled Release, 44*(2), 215–225.
Ribeiro, J. G., Raimondi, R. M., de Souza, A. G., dos Santos Rosa, D., & Paulino, A. T. (2025). An ecofriendly pectin-co-montmorillonite composite hydrogel for the separation of contaminant metal ions from water. *Journal of Water Process Engineering, 69*, Article 106629.
Roos, Y. (1993). Melting and glass transitions of low molecular weight carbohydrates. *Carbohydrate Research, 238*, 39–48.
Roy, S., Priyadarshi, R., Lopusiewicz, L., Biswas, D., Chandel, V., & Rhim, J. W. (2023). Recent progress in pectin extraction, characterization, and pectin-based films for active food packaging applications: A review. *International Journal of Biological Macromolecules*, 239.
Sdiri, A., Higashi, T., Chaabouni, R., & Jamoussi, F. (2012). Competitive removal of heavy metals from aqueous solutions by montmorillonitic and calcareous clays. *Water, Air, & Soil Pollution, 223*(3), 1191–1204.
Secchi, E., Munarin, F., Alaimo, M. D., Bosisio, S., Buzzaccaro, S., Ciccarella, G., … Piazza, R. (2014). External and internal gelation of pectin solutions: Microscopic dynamics versus macroscopic rheology. *Journal of Physics: Condensed Matter, 26*(46), Article 464106.
Shah, A., Zakharova, J., Batool, M., Coley, M. P., Arjunan, A., Hawkins, A. J., & Williams, C. (2024). Removal of cadmium and zinc from water using sewage sludge-derived biochar. *Sustainable Chemistry for the Environment, 6*, Article 100118.
Sila, D. N., Van Buggenhout, S., Duvetter, T., Fraeye, I., De Roeck, A., Van Loey, A., & Hendrickx, M. (2009). Pectins in Processed Fruits and Vegetables: Part II—Structure–Function Relationships. *Comprehensive Reviews in Food Science and Food Safety, 8*(2), 86–104.
Sips, R. (1948). On the Structure of a Catalyst Surface. *The Journal Of Chemical Physics, 16*(5), 490–495.
Stephen, A. M., & Phillips, G. O. (2006). *Food polysaccharides and their applications* (2nd ed.). CRC Press.
Synytsya, A., Čopíková, J., Matějka, P., & Machovič, V. (2003). Fourier transform Raman and infrared spectroscopy of pectins. *Carbohydrate Polymers, 54*(1), 97–106.
Torasso, N., Vergara-Rubio, A., Pereira, R., Martinez-Sabando, J., Baudrit, J. R. V., Cerveny, S., & Goyanes, S. (2023). An in situ approach to entrap ultra-small iron oxide nanoparticles inside hydrophilic electrospun nanofibers with high arsenic adsorption. *Chemical Engineering Journal, 454*, Article 140168.
Ürüncüoğlu, Ş., Alba, K., Morris, G. A., & Kontogiorgos, V. (2021). Influence of cations, pH and dispersed phases on pectin emulsification properties. *Current Research in Food Science, 4*, 398–404.
Ventura, I., Jammal, J., & Bianco-Peled, H. (2013). Insights into the nanostructure of low-methoxyl pectin–Calcium gels. *Carbohydrate Polymers, 97*(2), 650–658.
Veronovski, A., Tkalec, G., Knez, Ž., & Novak, Z. (2014). Characterisation of biodegradable pectin aerogels and their potential use as drug carriers. *Carbohydrate Polymers, 113*, 272–278.
Voragen, A. G. J., Coenen, G.-J., Verhoef, R. P., & Schols, H. A. (2009). Pectin, a versatile polysaccharide present in plant cell walls. *Structural Chemistry, 20*(2), 263–275.
Walkinshaw, M. D., & Arnott, S. (1981). Conformations and interactions of pectins: II. Models for junction zones in pectinic acid and calcium pectate gels. *Journal of Molecular Biology, 153*(4), 1075–1085.
Wang, J., & Guo, X. (2020). Adsorption kinetic models: Physical meanings, applications, and solving methods. *Journal of Hazardous Materials, 390*, Article 122156.
Willats, W. G. T., Knox, J. P., & Mikkelsen, J. D. (2006). Pectin: New insights into an old polymer are starting to gel. *Trends in Food Science & Technology, 17*(3), 97–104.
Yapo, B. M., Lerouge, P., Thibault, J.-F., & Ralet, M.-C. (2007). Pectins from citrus peel cell walls contain homogalacturonans homogenous with respect to molar mass, rhamnogalacturonan I and rhamnogalacturonan II. *Carbohydrate Polymers, 69*(3), 426–435.
Yu, L., & Gan, J. (2021). Mitigation of Eutrophication and Hypoxia through Oyster Aquaculture: An Ecosystem Model Evaluation off the Pearl River Estuary. *Environmental Science & Technology, 55*(8), 5506–5514.

Structural Characterization of Low Methoxyl Pectin-Based Adsorbents: The Role of Water on Pectin Structure

Francesco Coin[1], Aitor Larrañaga[3] and Silvina Cerveny[1,3*]

[1] *Centro de Física de Materiales (CFM-MPC), CSIC, UPV/EHU, Paseo Manuel de Lardizabal 5, 20018 Donostia-San Sebastián, Spain.*
[2] *SGIker, General Research Services, University of the Basque Country (UPV/EHU) (48080), Spain.*
[3] *Donostia International Physics Center (DIPC), Paseo Manuel de Lardizabal 4, San Sebastián 20018, Spain.*

Email: * silvina.cerveny@ehu.es

Keywords: pectin, crosslink, adsorption, water treatment, glass transition temperature

S1. Viscosity and Molecular weight

Measurements of viscosity were used to determine the molecular weight of the studied pectin trough Huggins-Kramer plot. In this method the kinematic viscosity η_k is given by

$$\eta_k = k \cdot (t_0 - t_n) = \left(\frac{\eta_d}{\rho}\right) \quad (1)$$

Where k is the capillary constant (k = 0.01116 mm^2/s^2), t_o and t_n is the efflux time of the sample solution in the capillary; η_d is the dynamic viscosity and ρ (g/cm^3) is the solution sample density. For diluted water solutions were ρ tends to 1 g/cm^3 and the solute concentration (C) tends to 0 g/L the $\eta_k \equiv \eta_d \equiv \eta$ and the total viscosity (η) of the solution can be written as:

$$\eta = \eta_1 + \eta_2 \quad (2)$$

Where η_1 and η_2 are the viscosities of the solvent and solute respectively. The specific viscosity η_{sp}, the relative viscosity η_{rel} and the intrinsic viscosity [η] where calculated following the equations:

$$\eta_{sp} = \frac{\eta_2}{\eta_1} = \frac{\eta - \eta_1}{\eta_1} = \eta_{rel} - 1 \quad (3)$$

$$\eta_{rel} = \frac{\eta}{\eta_1} \quad (4)$$

$$[\eta] = \lim_{C \to 0} \left(\frac{\eta_{sp}}{C}\right) \quad (5)$$

For a linear polymer in dilute solution, the value of [η] can be extrapolated as intercept from Huggins or Kramer equation:

$$\text{Huggins equation: } \frac{\eta_{sp}}{c} = [\eta]^2 \, K_H \, c + [\eta] \quad (6)$$

$$\text{Kramer equation: } \frac{\ln(\eta_r)}{c} = [\eta]^2 \, K_K \, c + [\eta] \quad (7)$$

The molecular weight (M_w) was determined using the Mark-Houking-Sakurada equation.

$$[\eta] = K \, M_w^{\alpha} \quad (8)$$

where K and α depends on the solvent and solute characteristics. We choose α = 0.82, which corresponds to a random coil polymer in good solvent, and K = 0.023 [1].

S2. FT-IR normalization

Figure S1 shows the FT-IR baseline correction and normalization considering the peak area of the glycosidic ring vibration of the poly-galacturonic acid chain (–C–O–C) at ~1140 cm^{-1} [2]

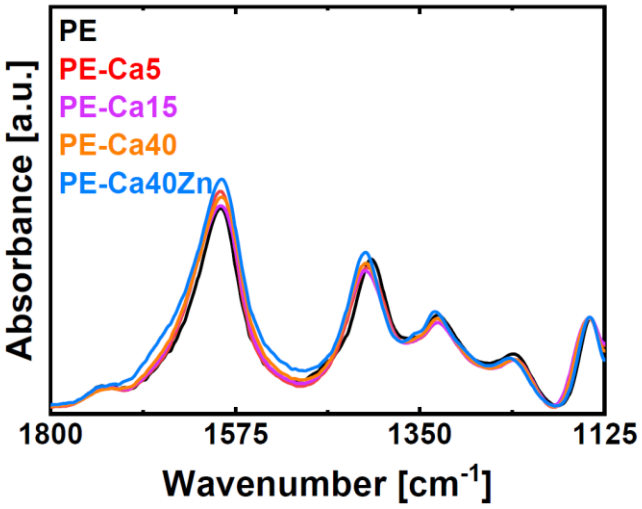

Figure S1. FT-IR baseline correction and normalization.

S3. Adsorption experiments

The number of adsorbed ions were determined based on the difference between the initial and final concentrations in the solution. The equilibrium adsorption capacity ($q_{eq\ Ads}$; mg/g), the adsorption capacity at time t ($q_{t\ Ads}$; mg/g), the desorption capacity at time t ($q_{t\ Des}$; mg/g), the removal efficiency (R_{Eff}%) and the stochiometric molar ratio (R) were calculated as follows:

$$q_{eq\ Ads} = \frac{C_0 - C_{eq\ Ads}}{d} \quad (9)$$

$$q_{t\ Ads} = \frac{C_0 - C_{t\ Ads}}{d} \quad (10)$$

$$q_{t\ Des} = \frac{C_{t\ Des}}{d} \quad (11)$$

$$R_{Eff}\% = \left(\frac{C_0 - C_{eq\ Ads}}{C_0}\right) \times 100\% \quad (12)$$

$$R = \frac{[Ca^{2+}]}{[GalA]} \quad (13)$$

where C_0 is the initial concentration of a given crosslinking agent or pollutant (mg/L), $C_{eq\ Ads}$ is the equilibrium concentration (mg/L), $C_{t\ Ads}$ is the concentration at time t, d is the adsorbent dose (g/L), [Ca^{2+}] is the amount of adsorbed calcium ions in the pectin matrix after the washing cycles and [GalA] is the amount of the galacturonic acid content (both expressed in mmol).

Given the molecular weight (Mw) of galacturonic acid (GalA) as 194 g/mol, along with the crosslinking dose (1.25 g/L), the GalA content (91%), and the degree of esterification (DM) of

9.9%, the corresponding amount of GalA used to crosslink the pectin samples is 5.86 mmol. The adsorption kinetics were fitted using the empirical pseudo-first-order (PFO; Eq. 10) kinetic model.

$$\text{PFO:} \quad q_t = q_e(1 - e^{-k_1 t}) \tag{14}$$

k_1 (min^{-1}) and is the characteristic time-related constants of the PFO model, indicating the adsorption speed at the beginning of the adsorption process [3].

The adsorption isotherms were fitted using the Langmuir–Freundlich (Sips), Redlich–Peterson (R–P) and Temkin models.

$$\text{Langmuir–Freundlich:} \quad q_{eq\ Ads}(C_{eq\ Ads}) = \frac{q_M K_{LF} {C_{eq}}^n}{1 + K_{LF} {C_{eq}}^n} \tag{15}$$

$$\text{Redlich–Peterson:} \quad q_{eq\ Ads}(C_{eq\ Ads}) = \frac{K_{RP} C_{eq}}{1 + \alpha C_{eq}^{\beta}} \tag{16}$$

$$\text{Temkin:} \ q_{eq\ Ads}(C_{eq\ Ads}) = \frac{RT}{b} \ln (A C_e) \tag{17}$$

where $q_{eq\ Ads}$ is the adsorption capacity; q_M (mg/g) is the maximum adsorption capacity; K_{LF} (L/mg) is the Langmuir–Freundlich constant; K_{RP} (L/mg), β, and α (mg/L) are R–P constants; and A L/g and b (J/mol) are the Temkin constants. n and β are a dimensionless parameter between 0 and 1, representing the heterogeneity factor. The closer the value to zero, the more heterogeneous the surface where the adsorbate interacts.

The exchange ratio helps to understand the ions exchange mechanism of the adsorbent material for specific ions. The exchange ratio is defined as:

$$Exchange\ ratio = \frac{Moles\ of\ adsorbed\ ion}{Moles\ of\ desorbed\ ion} \tag{18}$$

If the exchange ratio is equal to 1, it indicates a 1:1 molar exchange between the two ions. If the exchange ratio is mayor to 1, more of the adsorbed ion is taken up relative to the desorbed ion. However, If the exchange ratio is minor to 1, less of the adsorbed ion is taken up relative to the desorbed ion.

All adsorption experiments were done in triplicate, and the data were analyzed using one-way ANOVA on ranks with a 99% confidence level ($p < 0.01$). The results are reported as the mean values ± standard deviation.

S4. The effect of Zn^{2+} remediation on PE-Ca40 structure

Figure S2 compares PE-Ca40 before and after Zn^{2+} remediation (PE-Ca40Zn). After Zn^{2+} adsorption, the sample PE-Ca40Zn exhibited the same FT-IR wavenumbers for the carboxylate peak (Figure S2a-b), the TGA profiles of PE-Ca40 and PE-Ca40Zn were similar, with slight differences observed in Stage V. These differences are attributed to variations in pectin residue and pyrolysis behaviour at high temperatures (Figure S2c-d). Furthermore, the XRD patterns of both samples were nearly identical (Figure S2e), and the glass transition temperature (*Tg*) remained unaffected (Figure S2f), confirming that the structural integrity and thermal properties of the material were preserved after Zn^{2+} remediation. These results suggest that the "egg-box" structure is maintained even after the ion exchange process, highlighting the stability of the PE-Ca40 adsorbent.

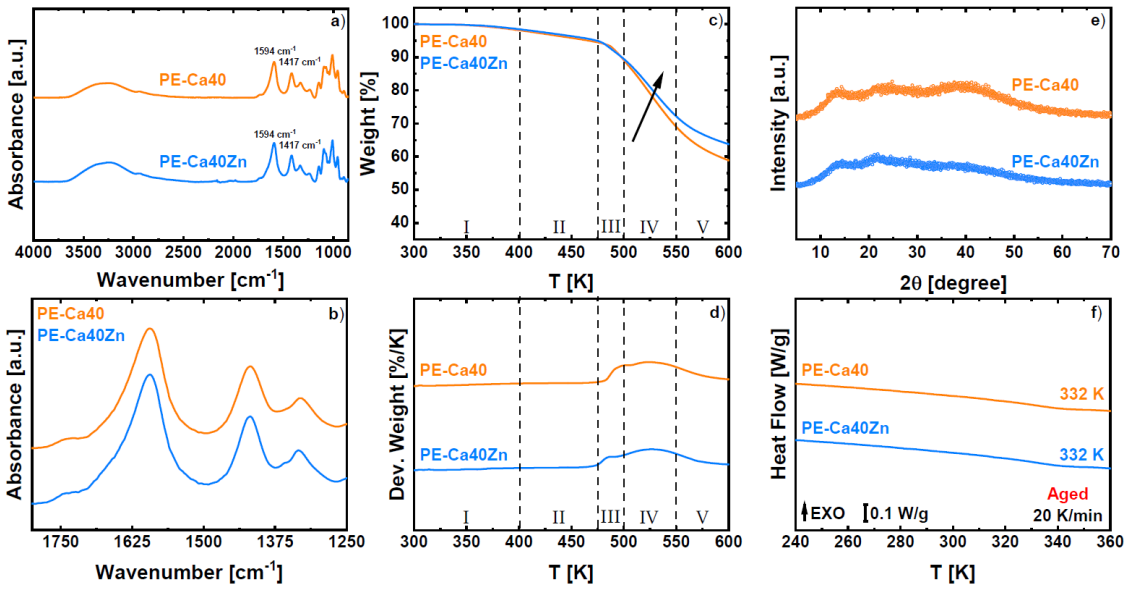

Figure S2. (a) FT-IR spectra of PE-Ca40 and PE-Ca40Zn films and (b) carboxylate bands shift. (d) Thermogravimetric scans and (d) derivative of weight loss as a function of temperature with heating rate of 10 K/min. (e) XRD pattern of dried. (f) Heat flow as a function of the temperature of dried pectin samples after aging

S5. Sample geometry and swelling

Figure S3 illustrates the sample circular geometry (22 mm in diameter and 0.05 mm in thickness) used for Ca^{2+} crosslinking, Zn^{2+} remediation, and swelling experiments. In their dry state, neat PE and PE crosslinked with Ca^{2+} at different time looks identical. However, after being submerged in water for 100 minutes, visual differences in water uptake capacity become evident, reflecting the varying swelling properties of the samples.

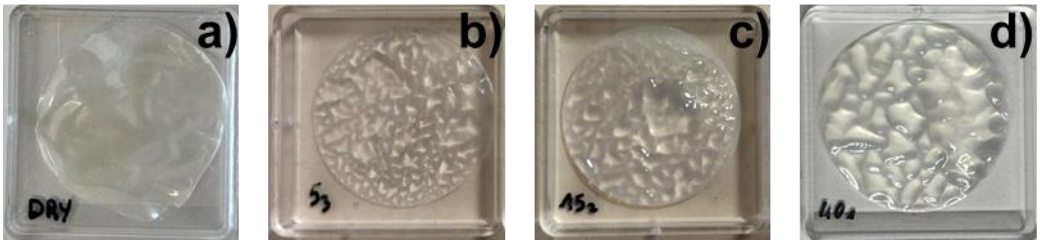

Figure S3. (a) Dry PE and PE-Ca samples geometry. (b) PE-Ca5, (c) PE-Ca15, (c) PE-Ca40 submerged in water for 100 minutes.

References

[1] T. Qi *et al.*, "Structural characteristics and gel properties of pectin from citrus physiological premature fruit drop," *Carbohydr. Polym.*, vol. 309, no. February, 2023, doi: 10.1016/j.carbpol.2023.120682.

[2] A. Synytsya, J. Čopíková, P. Matějka, and V. Machovič, "Fourier transform Raman and infrared spectroscopy of pectins," *Carbohydr. Polym.*, vol. 54, no. 1, pp. 97–106, 2003, doi: 10.1016/S0144-8617(03)00158-9.

[3] J. Wang and X. Guo, "Adsorption kinetic models: Physical meanings, applications, and solving methods," *J. Hazard. Mater.*, vol. 390, no. November 2019, 2020, doi: 10.1016/j.jhazmat.2020.122156.

The Journal of Chemical Physics ARTICLE pubs.aip.org/aip/jcp

The glass transition and the dynamics of water within pectin and metal–organic framework nanochannels

Cite as: J. Chem. Phys. 163, 164507 (2025); doi: 10.1063/5.0294531
Submitted: 4 August 2025 • Accepted: 7 October 2025 •
Published Online: 24 October 2025

Francesco Coin,[1] Valerio Di Lisio,[1,2] Daniele Cangialosi,[1,2] and Silvina Cerveny[1,2,a)]

AFFILIATIONS

[1] Centro de Física de Materiales (CSIC, UPV/EHU)-Material Physics Center (MPC), Paseo Manuel de Lardizabal 5, San Sebastian 20018, Spain
[2] Donostia International Physics Center (DIPC), Paseo Manuel de Lardizabal 4, San Sebastian 20018, Spain

[a)] **Author to whom correspondence should be addressed:** silvina.cerveny@ehu.es

ABSTRACT

The glass transition temperature (T_g) of water confined in nanoscale environments critically influences its dynamics and structure, thereby impacting the design of sustainable materials. Determining T_g in different confinement matrices remains challenging owing to variations in pore chemistry and geometry. Here, we investigated water confined within calcium-cross-linked pectin (PE–Ca) and metal–organic framework (Fe–BTC) nanochannels using differential scanning calorimetry, broadband dielectric spectroscopy, and FT-IR spectroscopy. We found that confined water exhibited a T_g between 170 and 200 K, with PE–Ca showing a higher T_g (193 K) than Fe–BTC (170 K), correlating with differences in the hydrogen bonding networks. Water in pectin forms a network similar to that of bulk water, whereas Fe–BTC confinement induces distorted structures with strong interfacial hydrogen bonds. These findings suggest that the T_g of bulk water is higher than that previously reported (~136 K) and highlight how confinement chemistry governs water dynamics, informing the development of eco-friendly materials and advancing our understanding of supercooled water.

I. INTRODUCTION

Water confined in nanoscale environments exhibits significantly different thermodynamic and dynamic properties than bulk water.[1,2] The freezing point is lowered, allowing water to exist in a supercooled liquid state at much lower temperatures. The glass transition temperature (T_g) indicates a transition from a liquid-like state to a glassy (amorphous solid) state as the temperature decreases. Studying T_g provides insights into the molecular mobility—the ability of molecules to move within a nanochannel—and the relaxation processes of water molecules inside confined nanochannels. This enhances our understanding of how confinement impacts the hydrogen bonding network and the overall structure of water, while also expanding our knowledge of bulk water in the no man's land temperature range[3] (150–235 K). This information is crucial for developing materials that facilitate efficient ion transport, enhance reaction selectivity, and lower energy consumption for applications such as water purification, energy storage, and eco-friendly catalysis, thereby supporting the advancement of more sustainable technologies.

The well-studied behavior of confined water in traditional nanochannels—such as MCM-41,[4–7] molecular sieves,[8,9] mineral clays,[10] graphene, or graphite oxide[11] (commonly referred to as "hard confinements")—contrasts with the relatively unexplored area of water[12] within sustainable materials, which encompasses biopolymers such as pectin, alginates, cellulose, lignin, and chitosan. For instance, pectin is very efficient in removing heavy metals from water by effectively utilizing ions and water confined within its nanochannels.[13,14] Unlike rigid, hard confinements, hydrophilic polymeric nanochannels, formed by cross-linked chains, are intrinsically flexible and responsive, capable of swelling or adapting to external stimuli.[15] These "soft" and dynamic environments provide a more adaptable platform for guiding water behavior, allowing targeted applications such as controlled delivery,[16] selective

transport,[17] or even catalysis,[13] highlighting the important role that nano-confinement plays in shaping water properties.[18] In addition, studies on glass transition in various types of nanochannels can provide insights into the broader issue of the glass transition of bulk water.

The issue of identifying the water glass transition has provoked ongoing debates in the literature. Differential scanning calorimetry on samples of low-density amorphous ice (LDA), high-density amorphous ice (HDA), and hyperquenched glassy water (HGW), all non-crystalline forms of water, shows weak endotherms identified as the onset of liquid-like behavior. T_g was determined at ~136 K for HGW,[19] ~126 K for LDA, and ~116 K for HDA,[20] corresponding to a slight increase in the heat capacity ($\Delta c_P \sim 1$ J/Kmol) and the onset of diffusive motion above these temperatures.[21] However, this T_g value has been debated by Velikov *et al.*,[22] who suggested that the step in heat capacity is a pre-peak typical of annealed hyper-quenched glasses, and the actual glass transition should occur at higher temperatures. On the same line, Giovambattista *et al.*,[23] using molecular dynamics simulations, showed that the commonly accepted value of $T_g \sim 136$ K corresponds to a weak "shadow transition," and, upon proper annealing, a much stronger calorimetric signal appears at a higher temperature, indicating that the actual glass transition of bulk water lies significantly above 136 K. Later, Lucas *et al.*[24] and Jia *et al.*[25] also agree with the same idea. Further evidence is available in the work of Chonde *et al.*[26] who investigates the glass transition in pure and doped amorphous solid water (ASW) using ultrafast microcalorimetry and found that pure ASW does not exhibit a detectable glass transition up to 205 K. Recently, Kimmel *et al.*[27] measured a nanoscale water film (at least 90% H_2O with D_2O) grown on a Pt(111) surface at 108 K, with thicknesses of up to ~100 nm, using infrared (IR) spectroscopy. They showed that the IR spectra change as these water films are annealed, and, therefore, the molecular motions should be composed of rotational and translational diffusion, bringing back to the idea that T_g of water should be close to 136 K. However, Shephard and Salzmann[28] studied the calorimetric response of LDA under isotopic substitution ($^{16}O \rightarrow {}^{18}O$ and $H_2O \rightarrow D_2O$), showing that the heat capacity at ~136 K was not affected by the substitution of ^{16}O to ^{18}O but shifted to D_2O. Therefore, this feature in the calorimetric response is due to the unfreezing of molecular rotational degrees of freedom and not translational motions of the oxygen atoms, although Loerting and collaborators[29] criticized this view. Finally, recently, we have reported the glass transition of water confined in nanochannels of MCM-41 and molecular sieves[9] and found that T_g occurs at temperatures between ~170 and 200 K, with the feature observed at lower temperatures being a shadow glass transition. From all this evidences, we concluded that the T_g of bulk water must be located at temperatures higher than 136 K.

In this study, we aimed to determine the glass transition temperature of water confined within pectin–calcium nanochannels at various hydration levels using annealing protocols employing differential scanning calorimetry. Furthermore, we complemented this soft confinement investigation with studies on the glass transition temperature and dynamics of water in an iron-based metal–organic framework [MOF, Fe–BTC (BTC: 1,3,5-benzenetricarboxylate)], which is a rigid semicrystalline material with a well-defined pore size compared to pectin [see Fig. 1(b)]. These results were compared with the dynamics of the same samples analyzed by dielectric spectroscopy. Both materials were also examined using ATR-FTIR spectroscopy to study the hydrogen-bonding structure at varying water content, demonstrating that the chemistry and geometry of the nanochannels significantly influence the structure of water. Our findings indicate that confined water has a T_g between 170 and

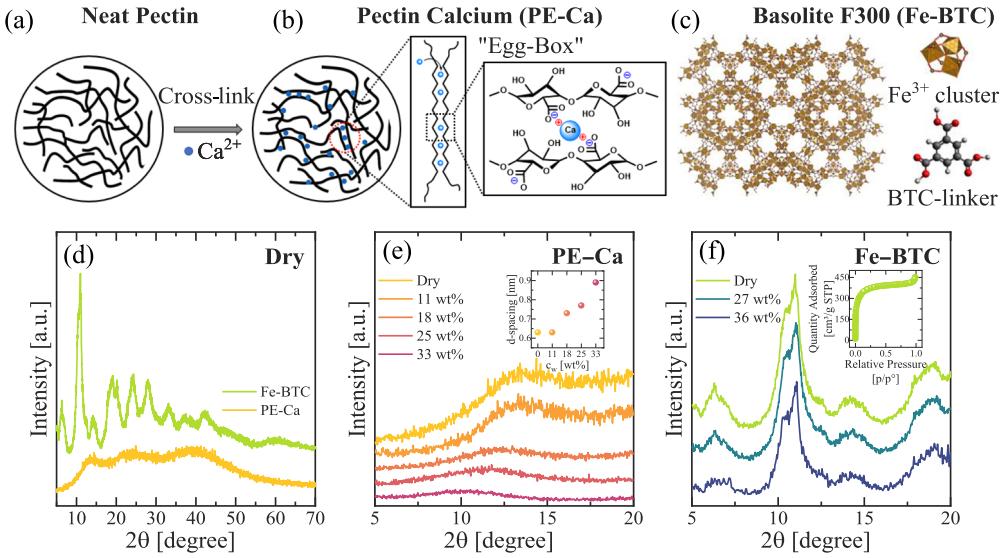

FIG. 1. Schematic representations of (a) neat pectin, (b) pectin cross-linked with calcium (PE–Ca), and (c) Basolite F300 (Fe–BTC) structures. (d) X-ray diffraction (XRD) patterns of dry PE–Ca and Fe–BTC. XRD patterns at different water contents for (e) PE–Ca and (f) Fe–BTC. The inset of panel (e) shows the calculated d-spacing at a fixed water level. The inset of panel (f) shows the Brunauer–Emmett–Teller (BET) analysis, indicating a pore diameter of 2.0 nm and a specific surface area of 1366 m^2/g for Fe–BTC.

200 K, depending on the type of confinement and the water structure within it. Regarding the dynamics, we demonstrated that confined water exhibits two distinct relaxations: the slower one, related to the calorimetric T_g (α- or structural relaxation), and the faster one, associated with the local motion of water molecules. Finally, we discuss the implications of these findings for bulk water.

II. EXPERIMENTAL

A. Materials

Low-methoxyl pectin (DM = 9.9%) was obtained from Herbstreith & Fox. Deuterium oxide (CAS 7789-20-0), metal–organic framework, Basolite F300 (Fe–BTC), and calcium chloride (CAS 7440-23-5) were purchased from Merck.

B. Sample preparation—hydration

After dissolving the pectin in water (3 g/100 ml) at 70 °C, 10 ml was cast into a 10 cm Petri dish. The cast film was first dried under a slow flow of air for 20 h and subsequently dried in a vacuum oven for 12 h. This method yields a compact, non-porous film, thereby preventing the large pore distribution typically found in xerogels or aerogels. The pectin films were cross-linked using calcium chloride ($CaCl_2$) by immersing them in a 500 mg/l solution for 40 min, resulting in pectin films cross-linked with calcium (PE–Ca).

For hydration, the PE–Ca films were dried under vacuum (10^{-3} mbar) at 40 °C for one week and carefully weighed before hydration. Fe–BTC was dried under high vacuum (10^{-4} mbar) at 200 °C for 1 h and weighed carefully before hydration.

Sample hydration was conducted in humidity-controlled environments at 25 °C, where the specific relative humidity (RH) was regulated using different saturated aqueous salt solutions over 4 weeks. The water content (c_w) was calculated as $c_w = [(m_{wet} - m_{dry})/m_{dry}] \times 100$, where m_{dry} (g) is the dry mass and m_{wet} (g) is the mass after hydration. The final water uptakes are c_w = ~0, 5, 11, 18, 25, 33, 39, and 49 wt. % for PE–Ca and ~0, 8, 27, 36, and 46 wt. % for Fe–BTC. Sample hydration with deuterium oxide (D_2O) has been performed in a glovebox to avoid water contamination. The final D_2O uptake was 52 wt. % for PE–Ca and 44 wt. % for Fe–BTC.

The adsorption isotherms of nitrogen at 77 K [see the inset of Fig. 1(f)] reveal a pore diameter of 2.0 nm and an area BET (Brunauer–Emmett–Teller method) of 1366 m^2/g for Fe–BTC.

C. Methods

Standard DSC was performed using a TA Instruments DSC Q2000 instrument with liquid nitrogen at cooling and heating rates of 20 K/min. The chamber was purged with dry helium at a flow rate of 25 ml/min. The samples were prepared by pressing ~10–15 mg of the sample in a hermetic aluminum pan to avoid water loss. Aging experiments were performed at different temperatures and times, cooled to 110 K, and heated at 20 K/min while recording specific heat data.

Using DSC step-response measurements, spontaneous fluctuations associated with α-relaxation have been characterized over two decades in time/frequency. The step-response measurement involves a series of cycles, each starting with a ΔT = 2 K up-jump at a heating rate β (15 K/min) and then maintaining an isotherm for a duration of t (120 s). The angular frequency can be expressed as

$$\omega_0 = \frac{2\pi}{t_P} = \frac{2\pi}{\frac{\Delta T}{\beta} + t}, \tag{1}$$

where the total period, t_P, includes the initial down-jump and duration of the isotherm.

By using the discrete fast Fourier transform relationship,

$$c_p^*(\omega) = c_P'(\omega) - ic_P''(\omega) = \frac{\sum_{t=0}^{t_P} HF(t)e^{-i\omega t}\Delta t}{\sum_{t=0}^{t_P} q_h(t)e^{-i\omega t}\Delta t}, \tag{2}$$

the frequency-dependent complex specific heat $c_p^*(\omega)$ was calculated for ω_0 and high-order harmonics ($\omega = k\omega_0$, where k = 1, 2, . . .), where $HF(t)$ and $q_h(t)$ are the instantaneous heat flow and heating rates, respectively.

Infrared spectra were recorded in the attenuated total reflectance (ATR) mode using a Jasco FT-IR 6300 spectrometer (Japan) from 4000 to 650 cm^{-1} with a resolution of 4 cm^{-1} and 200 scans per spectrum.

The complex dielectric permittivity $\varepsilon^*(\omega) = \varepsilon'(\omega) - i\varepsilon'(\omega)$ was measured in the frequency range of 10^{-1} to 10^6 Hz using a Novocontrol Alpha-A+ analyzer in the temperature range of 120–300 K every 5 K for Pe–Ca and 2 K for Fe–BTC. The samples were prepared as capacitors using gold-plated electrodes with a diameter of 20 mm (30 mm for Fe–BTC) and a thickness of 0.1 mm.

X-ray diffraction (XRD; Philips X'Pert Pro automatic diffractometer) was performed using Cu Kα radiation (λ = 1.5418 Å) with a secondary monochromator and a PIXcel solid-state detector. The voltage and current were set to 40 kV and 40 mA, respectively. The scans were performed with a step size of 0.026° in the 2θ range of 2°–70° at room temperature.

Adsorption isotherms were recorded at −196 °C using a Micromeritics ASAP 2420 instrument. Before sorption measurement, the sample was degassed at a pressure below 10^{-4} mbar and a temperature of 200 °C for 1 h using nitrogen gas. The BET area was determined using the Brunauer–Emmett–Teller (BET) method based on the adsorption data in the p/p_0 range of 0.05–0.20. The volume of the micropores (VMI) was evaluated using DFT (N_2 adsorption considering cylindrical pores).

III. RESULTS AND DISCUSSION

A. Structural aspects of PE-Ca and Fe–BTC during hydration

Pectin is a water-soluble polysaccharide composed of long chains of galacturonic acid units characterized by branching and methyl ester groups, which form a flexible polymeric network.[30] When pectin has a low methoxyl content, it can cross-link with divalent metal cations such as calcium, allowing it to become insoluble and exhibit a heterogeneous morphology. Cross-linking occurs through the interaction of calcium ions with the negatively charged carboxylate groups of pectin molecules, forming nanochannels [known as the "egg-box" structure;[31] see Fig. 1(b)]. Water in pectin not only interacts with the hydrophilic amorphous part (which is full of hydrophilic carboxyl groups) but also enters the nanochannels formed by ionic linkages between COOH groups on two different chains mediated by calcium. Meanwhile, Fe–BTC (Basolite F300) is an amorphous or poorly crystalline metal–organic framework composed of trivalent iron (Fe^{3+}) centers coordinated

to 1,3,5-benzene dicarboxylate (BTC) ligands. Unlike highly crystalline MOFs, such as MIL-100(Fe) and MIL-101(Fe), Fe–BTC lacks long-range order but retains a porous network of interconnected cages and channels.[32] The structure features iron-oxo clusters (typically Fe_3O units) bridged by carboxylate groups from BTC linkers, forming a three-dimensional coordination network. Despite its low crystallinity, Fe–BTC exhibits a high surface area and meso-porosity, with pore diameters typically ranging from 2 to 3 nm, making it suitable for confining water. Its disordered nature also allows for a broader distribution of pore environments compared with its crystalline counterparts. Figure 1 illustrates a schematic representation of the structure of neat pectin [Fig. 1(a), PE], pectin cross-linked with calcium [Fig. 1(b), PE–Ca], and MOF [Fig. 1(c), Fe–BTC].

To determine the role of water within the nano-pores of the PE–Ca and Fe–BTC, samples were carefully dried under vacuum and then hydrated (from the vapor phase) for 4 weeks to reach different water contents. Figure 1(d) shows the comparison of the x-ray diffraction (XRD) spectra of PE–Ca and Fe–BTC. PE–Ca exhibited broad, diffuse characteristics without sharp peaks, typical of an amorphous material that lacks long-range molecular order. In contrast, Fe–BTC exhibits better-defined diffraction peaks than pectin, although it displays the characteristics of a material with low crystalline order.

The XRD patterns of the hydrated samples (varying from $c_w \sim 0$ to $c_w = 39$ wt. % for PE–Ca and $c_w \sim 0$–46 wt. % for Fe–BTC) are shown in Figs. 1(e) and 1(f). To determine the interlayer distance

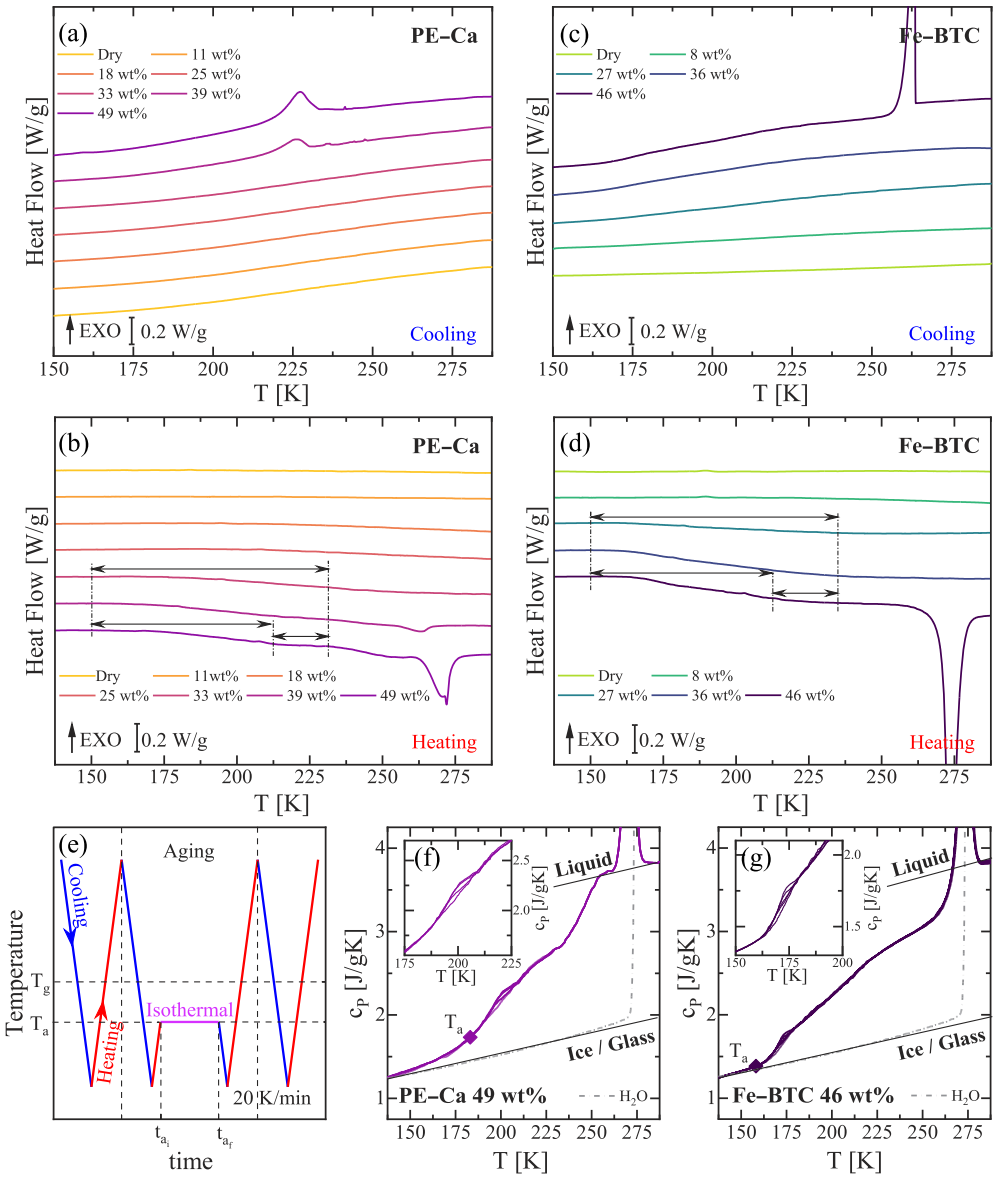

FIG. 2. Heat flow curves during cooling and heating at 20 K/min for (a) and (b) pectin cross-linked with calcium (PE–Ca) and (c) and (d) Fe–BTC, showing a broad step indicative of a thermal transition. (e) Schematic of the temperature protocols used for the aging experiments. Comparison between aged at different times and unaged samples for (f) PE–Ca (c_w = 49 wt. %, aged at 183 K for 2, 8, and 12 h) and (g) Fe–BTC (c_w = 46 wt. %, aged at 158 K for 10, 20, 60, and 120 min).

(d-spacing) between two pectin chains arranged in the "egg-box" configuration for each water content, we limited the 2θ values to a range of 5°–20° to reduce measurement duration and prevent sample dehydration. We note that the peak at 2θ = 14° remained unchanged by hydration up to c_w = 18 wt. %. Beyond this point, the d-spacing consistently grows with increased hydration from 0.63 to 0.89 nm for c_w = 33 wt. % [see the inset of Fig. 1(e)], as the two pectin chains separate more as the water content increases, as previously discussed.[14] In contrast, for Fe–BTC, no change in the position of the diffraction peaks was observed [see Fig. 1(f)], indicating that the pore structure remained unchanged as the water content increased.

B. The glass transition of confined water in PE–Ca and Fe–BTC

The heat flow during cooling at a rate of 20 K/min for water confined within the PE–Ca is shown in Fig. 2(a). At a low water content ($c_w \leq 33$ wt. %), water does not crystallize upon cooling, indicating its amorphous nature throughout the investigated temperature range. In contrast, a higher water content ($c_w \geq 39$ wt. %) resulted in partial crystallization, as evidenced by an exothermic peak. Upon heating [Fig. 2(b)], at water contents lower than $c_w \leq 18$ wt. %, the heat flow did not exhibit any observable transitions. However, increasing the water content ($c_w > 18$ wt. %) resulted in a broad step (~100 K for pectin with 33 wt. % water). This broad transition contrasts with the expected narrow temperature range (~10 K) for a glass transition of glass-forming materials. At even higher water contents, two separate steps can be observed [c_w = 49 wt. %, see arrows in Fig. 2(b)]. Note that when measuring over a broader temperature range[14] (from 150 to 350 K), we observe the glass transition temperature of pure pectin (332 K), which shifts to lower temperatures (from 332 to 317 K) as water content increases due to water-induced plasticization. Figure S1 of the supplementary material shows the heat flow and the heat capacity over a wide temperature range, where the two glass transitions (those corresponding to water and pectin plasticized by water) are observed. It is important to note that under these conditions, the molecular motions of pectin chains are essentially frozen at temperatures where the T_g of water is observed. In addition, note that water is mainly confined in the "egg-box" structure of pectin cross-linked with calcium, which corresponds to the crystal part of pectin.

To accurately determine the glass transition of confined water, aging experiments were conducted. The temperature protocols used in these experiments are shown in Fig. 2(e). The samples were rapidly cooled to 100 K (20 K/min) and then heated to a specific aging temperature (T_a), where they were held for a specified time (t_a) to allow the confined water molecules to relax toward lower energy states. Subsequently, the aged samples were cooled to 100 K and reheated at a heating rate of 20 K/min. The temperature interval over which an increase in enthalpy was detected corresponded to the glass transition temperature of the confined water[9] [see the inset of Fig. 2(c)].

Figure 2(f) shows the heat capacity of the water within the unaged and aged pectin (T_a = 183 K for 2, 8, and 12 h), which was calculated by subtracting the contributions of the excess bulk ice (in cases where crystallization was observed during the cooling cycle) and the dry contribution from the total heat capacity of the sample (see Fig. S2 of the supplementary material). A comparison of the results for the unaged and aged samples in Fig. 2(f) reveals that the broad step in the heat capacity, shown in Fig. 2(b), originates from two distinct thermal events. The lowest temperature thermal event is susceptible to aging and is, therefore, linked to the glass transition temperature. In contrast, the highest-temperature thermal event is unaffected by aging and thus cannot be associated with T_g.

The calorimetric response of water confined in Fe–BTC exhibited a behavior similar to that of pectin [see Figs. 2(c) and 2(d)]. Upon heating, no transition was observed for $c_w \leq 8$ wt. %; however, at higher water contents, one broad or two distinct steps were observed, similar to those observed for pectin. Figure 2(g) shows a comparison of aged (T_a = 158 K for 10, 20, 60, and 120 min) and unaged Fe–BTC, indicating that the lowest temperature thermal event is also related to the glass transition of confined water.

The high-temperature thermal event observed in both samples remains unaffected by aging, indicating that it is not a kinetic event associated with a glass transition, as was previously discussed for water confined in MCM-41 and molecular sieves.[9] This thermal event can be interpreted as related to the adsorption and desorption of water molecules on the inner surface of the pores, which is similar to that observed in polymers on an inorganic substrate.[33] The same phenomenon was observed for pectin and Fe–BTC, showing some universality for water under hydrophilic confinement. However, more studies are necessary beyond this work; hence, this high-temperature step will not be addressed further in this paper.

The broad range in which we observe a step in the specific heat and its heterogeneous nature prevents a clear assessment of the water T_g. Therefore, to determine the glass transition temperature from aged samples, we used a methodology previously applied to various systems with ill-defined T_g.[34] This approach is based on calculating the relaxed enthalpy accumulated during the aging process, which is typically obtained by integrating the heat capacity

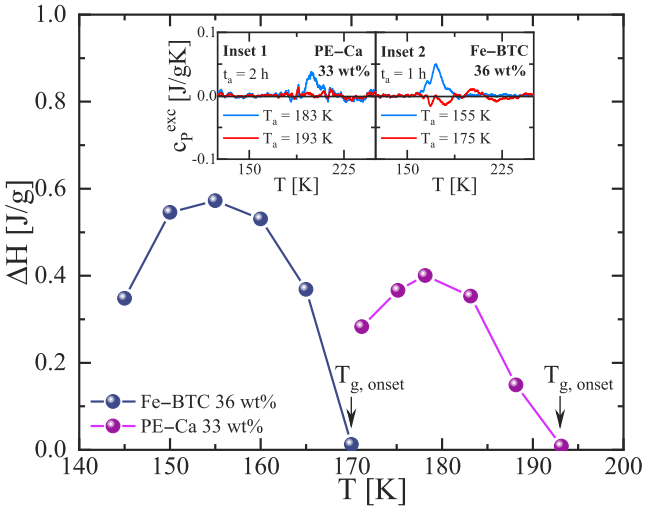

FIG. 3. Relaxed enthalpy as a function of aging temperature for PE–Ca (c_w = 33 wt. %, aged for 2 h) and Fe–BTC (c_w = 36 wt. %, aged for 1 h) samples. The linear extrapolation to ΔH = 0 indicates the glass transition temperature, defined as the onset on non-equilibrium effects. Insets: Excess specific heat capacity (c_P^{exc}) of the aged samples relative to the unaged reference, showing the endothermic overshoot characteristic of physical aging near the glass transition region.

difference between the aged and unaged (reference) samples during a DSC scan, as shown in the following equation:

$$\Delta H(T_a, t_a) = \int_{T \ll Tg}^{T \gg Tg} (c_{P,aged}(T) - c_{P,unaged}(T))\, dT, \quad (3)$$

where $c_{P,aged}(T)$ and $c_{P,unaged}(T)$ are the specific heats of an aged and the reference unaged samples, respectively.

The temperature at which enthalpy recovery effects appear offers insights into the glass transition, allowing for a more precise estimation of T_g. In particular, the temperature at which the relaxed enthalpy extrapolates to zero directly indicates the onset of T_g because above this point, the material is in thermodynamic equilibrium and aging results in no enthalpy change. Figure 3 shows the relaxed enthalpy as a function of the aging temperature after one hour of aging for PE–Ca (c_w = 33 and 39 wt. %) and Fe–BTC (c_w = 36 wt. %), where we can determine the onset of aging effects to determine T_g. We estimated T_g values of 193 K for water in PE–Ca (c_w = 33 wt. %) and 170 K for water in Fe–BTC (c_w = 36 wt. %).

C. Comparison of the hydrogen bonding structure of water confined in pectin and MOF with bulk water

ATR-FTIR spectroscopy enables the analysis of intermolecular interactions in confined water within pectin and MOF and allows comparison with bulk water to highlight the differences and similarities between the two types of water. Figures 4(a) and 4(b) show the vibrational spectra from 4000 to 650 cm^{-1} for bulk and confined water within pectin and MOF at different water contents, respectively. To isolate the contributions of the water OH stretching band, the difference spectra $\Delta Abs(c_w)$ were calculated by subtracting the weighted contribution of dry pectin and MOF, Abs(dry), from the hydrated spectra, $Abs(c_w)$, using the formula $\Delta Abs(c_w) = Abs(c_w) - Abs(dry) * (100\text{-}c_w)/100$ [see Figs. 4(c) and 4(d)]. Interestingly, the OH stretching band from water confined in pectin showed a maximum at 3350 cm^{-1} (with two additional shoulders at 3420 and 3570 cm^{-1}). In contrast, water in the MOF exhibits a distinctly different absorption spectrum, with a peak at 3450 cm^{-1} (featuring shoulders at 3240 and 3570 cm^{-1}, and an unusual broadening at lower wavenumbers, reaching down to 2800 cm^{-1}). To validate these differences, a similar hydration study was performed with deuterated water (D_2O) as an alternative method to separate the water absorption bands from those of the PE–Ca hydroxyl groups. Figure S3 of the supplementary material shows the ATR-FTIR spectra of D_2O-hydrated samples of PE–Ca at 52 wt. % and Fe–BTC at 44 wt. %. Consistent with the water O–H stretching reported in Figs. 4(c) and 4(d), the O–D stretching (located in the 2750–2000 cm^{-1} range) of confined D_2O exhibits the same spectral differences as its H_2O-hydrated counterpart. Moreover, an increase in the water content resulted in changes in the relative intensities of the four spectral features. The notable differences in the OH stretching spectral features, which are highly sensitive to the strength and geometry of the hydrogen bonds between water molecules, suggest that water confined in Fe–BTC and PE–Ca has distinct structures. This can be thoroughly analyzed through the spectral deconvolution of the OH stretching band of water.

Water molecules can form up to four hydrogen bonds, enabling the formation of various transient local structural configurations. Several models exist for the deconvolution of the OH stretching band,[35–37] the simplest of which considers different subpopulations of water molecules across multiple hydrogen-bonding environments, where an increase in the average degree of connectivity (from 0 to 4) correlates with a decrease in OH stretching absorption frequency (from 3750 to ~3000 cm^{-1}). It is important to note that although the water spectrum can be broken down into multiple components, interpreting these sub-bands physically remains a topic of ongoing debate. Some studies treat these components as separate populations of stable states,[35] while others see them as a statistical reflection of the overall hydrogen-bonding environment.[38] To analyze the hydration state of water confined in pectin and Fe–BTC, we successfully fitted the water OH stretching band for pure water and confined water in Fe–BTC (c_w = 49 wt. %) and PE–Ca (c_w = 46 wt. %), as shown in Figs. 4(e)–4(g), using three Gaussian and one Voigt functions, associated with water subpopulations with different levels of hydrogen bonding connectivity. It is important to note that, given the highly dynamic nature of the hydrogen-bonding network in liquid water, these components should not be interpreted as representing four discrete, thermodynamically stable species. Instead, our deconvolution provides a time-averaged statistical representation of the distribution of hydrogen-bond strengths within the system. Each component corresponds to a local-water structure or a specific subset of fluctuations along a continuum of hydrogen-bond strengths. The Gaussian component at 3550 ± 20 cm^{-1} is attributed to small water clusters exhibiting disturbed hydrogen bonding, resulting in fewer than 2 hydrogen bonds per molecule, often referred to as "multimer water."[39] The 3400 ± 20 and 3220 ± 20 cm^{-1} Gaussian's contributions are linked to the out-of-phase and in-phase OH stretching of tetrahedrally coordinated water molecules, known as "network water." A fourth Voigt component, positioned at 2995 ± 20 cm^{-1}, was added to account for the absorption at lower wavenumbers for bulk water and water confined in pectin and Fe–BTC. The latter, commonly observed in aqueous ionic solutions,[40,41] refers to water molecules that are strongly coordinated to anions or, more generally, to water molecules that interact intensely with their environment, hence called "strong HB water" and often associated with highly ordered, ice-like or tetrahedrally coordinated structures. The overall OH stretching band deconvolution across all hydration levels is shown in Fig. S4 of the supplementary material.

To compare the water characteristics in the PE–Ca and Fe–BTC environments directly, Figs. 4(h) and 4(i) show the relative concentrations of multimer, network, and strong HB water as a function of water content in the two systems. The relative concentrations were determined from the peak area of each water population (or the combined area of the 3400 and 3220 cm^{-1} peaks for network water), divided by the total area of the OH stretching band. The solid lines show the distribution of water subpopulations in bulk water (c_w = 100 wt. %), with 0.85 for network water, 0.11 for multimer water, and 0.04 for strong HB water. Reasonably, at lower hydrations, water confined in pectin exhibits an excess of multimeric water, as water molecules are likely trapped in small, isolated clusters. Increasing c_w above 25 wt. % confines the water confined in pectin [Fig. 4(h)], similar to bulk water, as water subpopulation concentrations approach those of pure water. In contrast, water confined in Fe–BTC showed markedly different behavior [Fig. 4(i)]. Across all hydration contents studied, a significant "strong HB

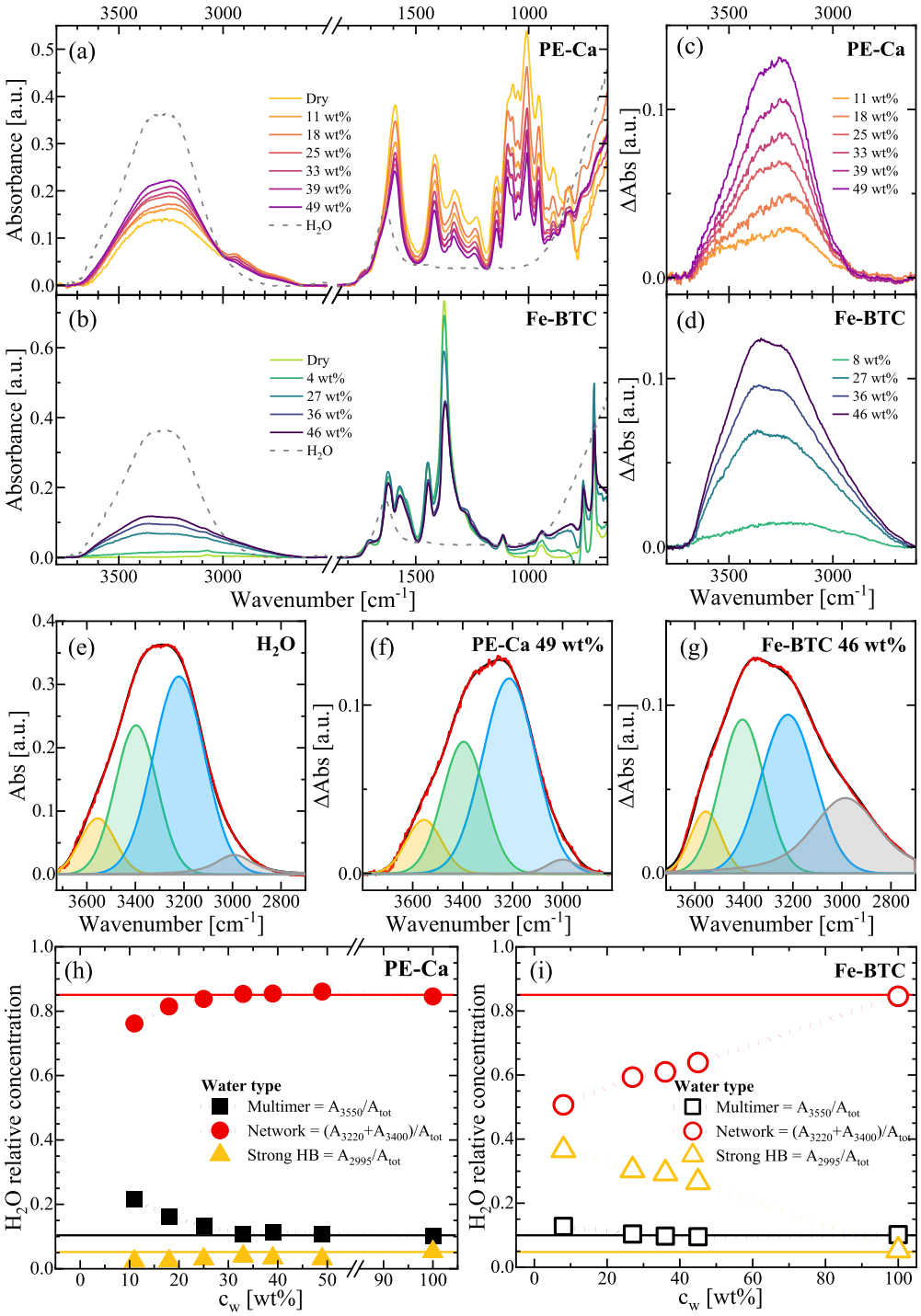

FIG. 4. ATR-FTIR spectra of water confined in (a) PE–Ca and (b) Fe–BTC at different water contents. The bulk water spectrum is represented by the dashed line. (c) and (d) The difference spectra of PE–Ca and Fe–BTC, respectively. (e)–(g) Deconvolution of the OH stretching band for bulk and confined water. The data analysis was performed using the Omnic software, and the spectra were baseline-corrected and fitted by a Gaussian function for the peaks centered at 3550, 3400, and 3220 cm^{-1}, and a Voigt function was used for the peak centered at ~3000 cm^{-1} (h) and (i).

water" population is observed, with a relative concentration between 0.35 and 0.25, reducing the "network" population in bulk water.

The difference between the water confined in pectin and the MOF can be attributed to the different geometric constraints imposed by the confining material and the interactions between the pore walls and water molecules. In a polysaccharide, such as calcium-cross-linked pectin, the presence of a permeable, hydrophilic environment made up of hydroxyl (–OH) and, in small amounts, carboxyl (–COOH) groups allows water to form clusters with an interconnected structure similar to that of pure water. In this case, the similarities between water and water and between water and environment (with hydroxyl and carboxyl groups) interactions do not significantly disrupt the formation of the water network. Meanwhile, strong confinement in the pores of the Fe–BTC framework causes a significant distortion of the water intermolecular network. This could be reasonably inferred by considering the high concentration of carboxylate anions (–COO–) in the organic linker, which form the building blocks of pore walls and can strongly coordinate with various shells of water molecules, similar to what occurs for anion solvation.[40,42,43] Indeed, Fe–BTC confined water is not comparable to bulk water, as the stronger water–environment interaction with pore walls disturbs the tetrahedral coordination typical of bulk water. In addition, it is important to note that the same phenomenological behavior observed in MOF occurs in MCM-41, a porous aluminosilicate (see Fig. S5 of the supplementary material). A peculiar correlation emerged when considering the glass transition temperatures of the confined water in these systems. The increase in strong interfacial hydrogen bonding between water and the environment seems to correlate with a decrease in the onset of the water glass transition from 193 K for PE–Ca to 170 K for Fe–BTC.

To determine whether the water subpopulation discrepancy between PE–Ca and Fe–BTC remained at low temperatures, where water glass transition occurred, ATR-FTIR spectra were collected for PE–Ca (c_w = 33 wt. %) and Fe–BTC (c_w = 36%) at temperatures as low as −100 °C, as shown in Fig. S6 of the supplementary material. Even though the vibrational spectra of water at −100 °C indicate an increased network character for both systems, a noticeable discrepancy still persists.

D. Dynamics of confined water in PE–Ca and Fe–BTC determined by dielectric spectroscopy and standard calorimetric measurements

Broadband dielectric spectroscopy (BDS) is a powerful technique for characterizing the dynamic behavior of water confined in various systems. Its broad frequency window enables the investigation of a wide spectrum of dynamic processes that occur on different timescales, from slow cooperative molecular rearrangements to fast local motions. BDS is particularly well suited for detecting slow molecular motions, such as the α-relaxation of water molecules under confinement, which can be challenging for other methods. However, high DC conductivity could mask this contribution, especially in water-containing samples, and it is necessary to employ a strategy (to study the electrical modulus or to use derivative analysis) that can reveal the α-relaxation. Therefore, we investigated the dynamics of water confined in PE–Ca and Fe–BTC when heated from 110 K to room temperature with varying water contents in the frequency range of 10^{-1} to 10^{6} Hz.

Figure 5(a) shows the imaginary part $\varepsilon''(\nu)$ of the complex permittivity of water confined in PE–Ca [the real part of the dielectric constant, $\varepsilon'(\nu)$, is shown in Fig. S7 of the supplementary material]. As is usual in confined supercooled water, one broad relaxation process (P2) is detected, appearing as a step-like feature in $\varepsilon'(\nu)$ or a peak in $\varepsilon''(\nu)$, which continuously shifts to higher frequencies with increasing temperature, as shown in Fig. 5(a) for PE–Ca [see the comparison of different water contents in Fig. 5(c), where this peak increases with water content; therefore, this relaxation is associated with the relaxation of water molecules]. PE–Ca samples exhibit extra relaxation (P1) at very low temperatures, as shown in Fig. 5(c) for low water contents, which was previously observed in several water-containing samples[44,45] and will not be discussed here. In addition, by analyzing the derivative of $\varepsilon'(\nu)$, we can see that another process (P3) emerges below the conductivity threshold (at ~220 K). Although we can identify this process, the exact identification of the relaxation time remains elusive [see Fig. 5(d), where the derivative analysis is shown in the open points]. To fit these data, we used three Cole–Cole functions (empirical equations to describe the dielectric data[46]) to consider these three dynamical processes,

$$\varepsilon^*(\omega) = \varepsilon_\infty + \frac{\varepsilon_S - \varepsilon_\infty}{\left[1 + (i\omega\tau)^\alpha\right]}, \tag{4}$$

where the correlation time τ is the relaxation time, α is the shape parameter, Δε is the relaxation strength, and ε_∞ and ε_S are the unrelaxed and relaxed dielectric constant values, respectively. The shape parameters of the main dielectric process (P2) are shown in the inset of Fig. 5(a). These values are almost independent of temperature up to 185 K, where α increases and Δε decreases slightly.

Figure 5(f) shows the relaxation map for the processes observed in Figs. 5(a) and 5(c) for PE–Ca (c_w = 33 wt. %), where two relaxations (processes 1 and 2) are visible. In addition, at open points, the relaxation times obtained from the DSC step response protocol are shown, where the relaxation times are obtained from the inflection point of the reversing specific heat, practically identical to the real part of the complex specific heat[47,48] (see Sec. I B). Figure 5(g) shows a comparison of relaxation times at different water contents; as the water content increases, the relaxation times become shorter, which is a common behavior of water in soft confinements.[49,50] When the water content reached c_w = 25 wt. %, the relaxation times became nearly independent of the water content, coinciding with a notable increase in the relaxation strength [see Fig. 5(h)].

The P2 dielectric process, consistent with several previous results on confined water,[51] reveals a change in the dynamics from an Arrhenius to a non-Arrhenius temperature dependence at T ~ 192 K. Below this temperature, the relaxation times follow the Arrhenius law [$\tau = \tau_0 \exp(E_a/k_BT)$] with an activation energy (E_a) of 0.49 eV. As noted earlier, the relaxation time associated with process 3 remains uncertain because it is not visible in the dielectric spectrum and is masked by the high conductivity. To address this, we also used the DSC step response protocol [see Figs. 5(d) and 5(e)] to determine a set of relaxation times for this process. These times are shown as open points in Fig. 5(f), and their extrapolation at t = 100 yields T_{100s} = 192 K, the same temperature at which the crossover occurs in process 2. This temperature corresponds to the T_g of confined water, as measured by DSC (see Fig. 3). Thus, this relaxation can be attributed to the α-relaxation of the water molecules confined within a rigid matrix.

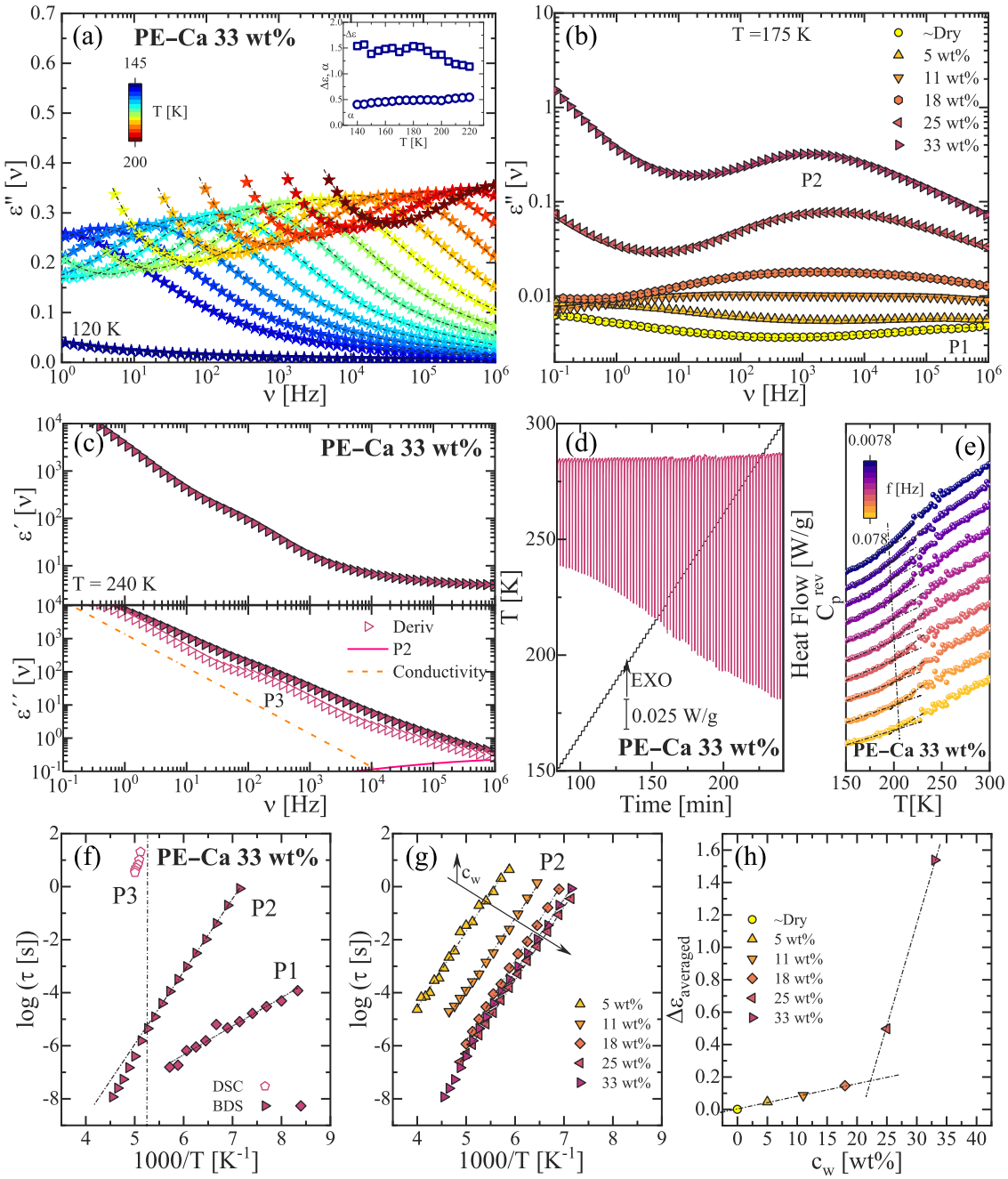

FIG. 5. (a) Dielectric loss $\varepsilon''(\omega)$ vs frequency of confined water in PE–Ca (c_w = 33 wt. %) at 120–200 K. The lines are the simultaneous fits of the real and imaginary parts using the fits described in the text. The insets show the Cole–Cole fit parameters [α, shape parameter (circles), and Δε, relaxation strength (squares)]. (b) Dielectric loss for different water contents for PE–Ca. For low water contents, an additional relaxation at very low temperatures and high frequencies is observed (P1). (c) Derivative analysis of $\varepsilon'(\omega)$ (open points) where process 3 is visible. (d) Step-response temperature program and heat flow as a function of time. (e) Reversing specific heat as a function of temperature for different frequencies. (f) Relaxation times for water confined in PE–Ca (c_w = 33 wt. %) with an interlayer distance of 0.89 nm, where the two dielectric processes (P1 and P2) are shown. Open points represent the times obtained from the DSC step response protocol. Black line: Arrhenius fit of P2 ($\tau = -17.90$, $E_a = 0.49$ eV). Dashed line: Arrhenius fit of P1 ($\tau = -12.8$, $E_a = 0.21$ eV). (g) Relaxation times as a function of the inverse of temperature in PE–Ca for different water contents (c_w). The Arrhenius fits are represented by solid lines. (h) Dependence of the average value of Δε on water content.

It is also important to note that P2 exhibits a universal behavior, as previously discussed by us and other authors.[51,52] Since process 2 is independent of the confinement type, meaning that it is universal for any studied confinement, this relaxation can be considered as the universal β-relaxation of confined water. In addition, this universal β-relaxation depends on pressure, which suggests that this process is of Johari–Goldstein type[53] (β_{JG}). This type of relaxation involves all atoms in a water molecule undergoing local (non-cooperative) and anisotropic motion, as observed in NMR studies[54] of water in MCM-41. In addition, it is well-known that the JG relaxation exhibits a kinetic crossover at T_g, as studied by Ngai and co-workers in glycerol,[55] providing further proof of our assignment.

The same analysis can be performed for the dielectric spectra of water confined in Fe–BTC, as shown in Fig. 6 [see Fig. S5 of the supplementary material for the real part of the dielectric constant, $\varepsilon'(\nu)$]. Process 2 exhibits a change in dynamics from Arrhenius to a non-Arrhenius temperature dependence at T ~ 167 K, below which it follows Arrhenius law with E_a = 0.49 eV. In addition, process 3, determined by the DSC step response protocol, is shown as open points. We observed that extrapolating the relaxation times of process 3 to 100 s resulted in a temperature of 166 K, similar to the T_g obtained by DSC (~170 K), and coincided with the temperature at which the crossover occurred in process 2.

E. The glass transition temperature of confined water and its relationship with bulk water

We performed a detailed study of the effect of nanoscale confinement on the glass transition behavior of water within pectin and a metal–organic framework using differential scanning calorimetry and dielectric spectroscopy. These results support our previous research on water confined in MCM-41 and molecular sieves,[9] offering new insights into how both confinement geometry (ranging from 0.7 to 2 nm pores) and water–matrix and water–water interactions together impact the dynamic properties of water, further extending our understanding beyond previous studies.

Infrared spectroscopy in the OH stretching region revealed distinct shifts in the population of specific hydrogen-bonding environments under confinement. At room temperature, the proportion of tetrahedrally coordinated water increases when water is confined within the pectin matrix. In contrast, for water in Fe–BTC (as well as in MCM-41), increasing the water content resulted in a less pronounced change in the proportion of tetrahedrally coordinated water. Unlike pectin, for water in Fe–BTC, the amount of tetrahedrally coordinated water does not reach the range of bulk water [see Figs. 4(h) and 4(i)]. This is also the case for water confined in MCM-41, where the tetrahedrally coordinated water does not seem to reach the values of bulk water (see Fig. S4 of the supplementary material). From this perspective, pectin or molecular sieves[9] (MS) previously

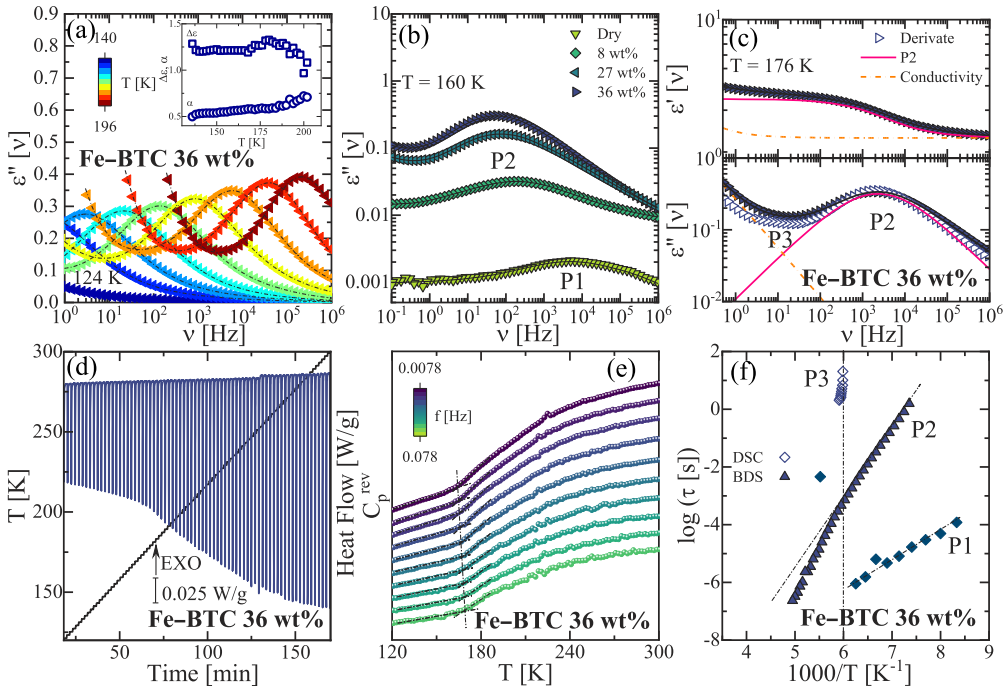

FIG. 6. (a) Dielectric loss $\varepsilon''(\omega)$ vs frequency of confined water in Fe–BTC (c_w = 36 wt. %) at 140–196 K. The lines are the simultaneous fits of the real and imaginary parts using the fits described in the text. The insets show the Cole–Cole fit parameters [α, shape parameter (circles), and Δε, relaxation strength (squares)]. (b) Dielectric loss for different water contents for Fe–BTC. For low water contents, an additional relaxation at very low temperatures and high frequencies is observed (P1). (c) Derivative analysis of $\varepsilon'(\omega)$ (open points) and the fitting performed (solid lines) for process 3. (d) Step-response temperature program and heat flow in a function of time. (e) Reversing specific heat as a function of temperature for different frequencies. (f) Relaxation times for water confined in Fe–BTC (c_w = 36 wt. %), where the two dielectric processes (P1 and P2) are shown. The open points represent the relaxation times (P3) obtained from the DSC step response protocol.

studied appear to be better models for examining the behavior of bulk water, even though MS and pectin are less organized than the pores found in MCM-41 or Fe–BTC.

Regarding the T_g values observed for confined water, we found a value of ~192 K for water confined in pectin, which matches the T_g observed for water in molecular sieves.[9] In contrast, the T_g value for water in Fe–BTC was ~166 K, which was consistent with that found in MCM-41.[9] Based on the infrared spectroscopy results, we suggest that the T_g of bulk water may be more similar to that of water in pectin or molecular sieves, that is, a value of ~200 K.

Nevertheless, this contrasts with previous studies, which reported a T_g for bulk water between 115 and 140 K, depending on the type of water analyzed.[56] In our case, for water confined in Pe–Ca or Fe–BTC, we did not observe any clear step in the heat capacity at these temperatures. However, we can gain insights into the thermal behavior in this low-temperature range by performing annealing experiments at these low temperatures. Figure 7(a) shows the results for water in Fe–BTC annealed at T = 113 K for 4 h. We observed an endothermic excess in the heat capacity, which was very small, compared to the excess observed after aging in the proximity of T_g. In addition, the former endothermic excess is less intense and quite broad, spanning ~19 K, compared with ~21 K for the excess related to T_g [see Fig. 7(b)]. The latter is better aligned with the T_g range typically observed in glass forming systems.

The presence of an excess in both low- and high-temperature annealing processes might initially suggest two distinct glass transitions for confined water: one around 130 K and another at 200 K. However, our observations align with a broader phenomenon observed in various confined systems, including water in molecular sieves and MCM-41,[9] polymers,[57,58] plastic crystals,[59] or metallic glasses.[60] In these materials, a similar thermal event with identical characteristics is consistently detected below the primary glass transition (T_g). This event is commonly referred to as the "low temperature endotherm," "sub-T_g peak," or "shadow glass transition."[61,62] Therefore, our findings indicate that confined water exhibits a single T_g ranging from 170 to 200 K, accompanied by a sub-T_g peak at 130 K.

Figure 8(a) shows the comparison of the dynamics of confined water in four different systems (pectin, Fe–BTC, MS, and MCM-41) with those observed in LDA and HDA[20] (star and cross points), where the filled points indicate the fast local relaxation of water and the open points represent the α-relaxation times obtained by the DSC step response protocol. The fast relaxation of water occurs similarly across all confinement systems. (In addition, note that the relaxation times of the fast water relaxation are equal to the relaxation times reported in several other previous studies[54,63–67] in the literature where the dynamics of confined water were studied.) However, the crossover temperature varies depending on the system, as previously discussed, and appears at the temperature at which DSC determines the glass transition of confined water. However, the α-relaxation of water, which is not well defined because of the

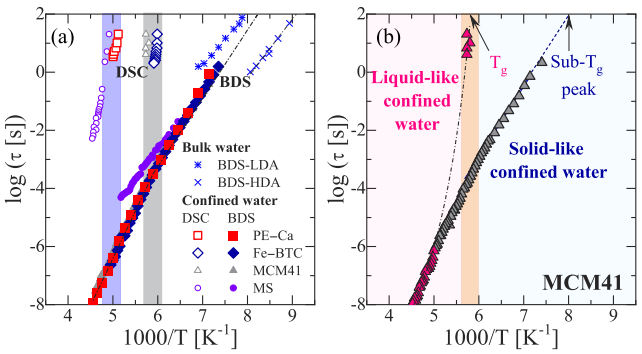

FIG. 8. (a) Relaxation times of water confined in PE–Ca, Fe–BTC, MS, and MCM-41. The fast relaxation of water is similar across all these confinement systems (shown with filled points). The α-relaxation time varies depending on the type of confinement and the interactions with the walls. Bulk LDA and HDA relaxation times are indicated by stars and crosses. (b) Schematic representation of the temperature dependence of the relaxation times of confined water. Points are based on the relaxation times of confined water in MCM-41-2.1 nm, obtained by BDS and DSC step response.

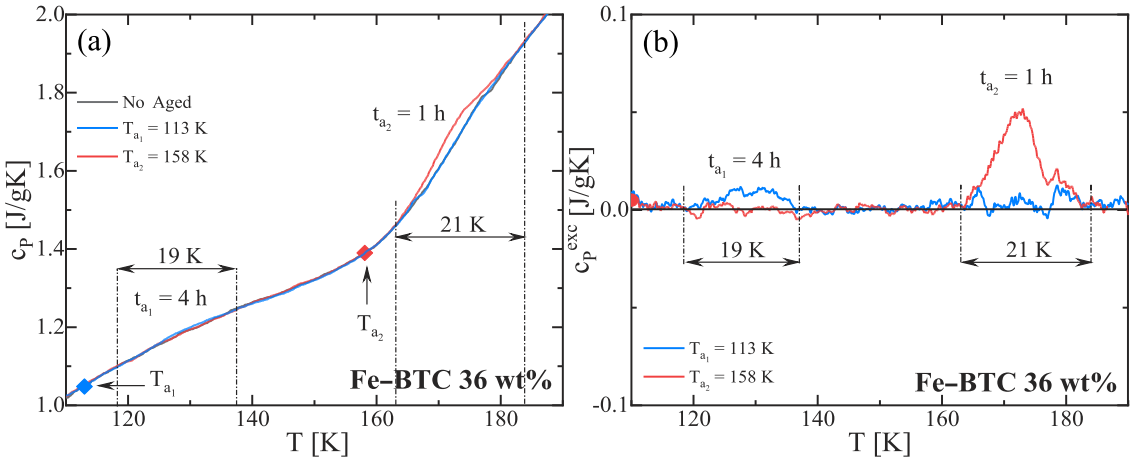

FIG. 7. (a) Heat capacity determined at 20 K/min (red curve, not annealed) of water confined in Fe–BTC, after annealing at T_a = 113 K (blue curve) and T_a = 158 K for 1 h. (b) Specific heat capacity (c_P^{exc}) of the aged samples in excess of the unaged reference.

high conductivity contribution in the dielectric measurement but confirmed by the DSC step response, depends on the interactions with the confinement walls. As discussed in our earlier paper, the similarity between the relaxation times of confined and bulk water indicates that relaxation in various forms of bulk water also reflects a (Johari–Goldstein) β-relaxation rather than an α-relaxation. We also indicate that this fast water relaxation shows characteristics that are not commonly observed in the (Johari–Goldstein) β-relaxation of other glasses, as discussed by Beilinson *et al.*[68] They indicate that low-temperature water dynamics involve quasi-isotropic reorientation rather than strongly restricted reorientation.

In Fig. 8(b), we show our expectations for the behavior of confined water in any system, with points indicating observations (specifically for water confined in MCM-41-2.1 nm) and lines representing the estimated times we have not yet been able to observe using our methods. In this plot, we expect the fast and slow processes of confined water (i.e., a JG-relaxation and an α-relaxation) to merge at a temperature above T_g, as discussed in previous publications[69] and in agreement with the previous work of Swenson[52,70] for bulk water and Vogel and collaborators[7] for confined water. In addition, this conclusion is similar to one reached by Lucas and collaborators[24] by examining the thermal behavior similarity between water and $Ge_2Sb_2Te_5$ (GST).

IV. CONCLUSION

This study successfully investigated the glass transition and dynamic behavior of water confined in two different matrices: a pectin-based biopolymer (PE–Ca) and a metal–organic framework (Fe–BTC). Our results show that the type of confinement significantly affects both the structure and dynamics of the water. Applying well-designed aging protocols in DSC experiments, we accurately measured the glass transition temperature, defined as the onset of aging effects. This was 193 K for water in PE–Ca and 170 K for water in Fe–BTC. In addition, more well-organized confinements, such as MCM-41 and MOF, exhibit a lower T_g, while less ordered systems, such as pectin or molecular sieves, have a higher T_g. Furthermore, ATR-FTIR spectroscopy analysis revealed that different confinement environments produced distinct hydrogen-bonding networks in confined water. In flexible PE–Ca nanochannels, water at high hydration levels forms a network similar to that of bulk water. Conversely, the rigid, carboxylate-rich pores of the Fe–BTC framework disrupted the intermolecular network of water, leading to the significant presence of "strong HB water." We found a clear link between the strong hydrogen bonding at the interface and lower T_g. Consistent with this, we observed that at the temperature where the JG relaxation of confined water extrapolates to 100 s, a sub-T_g peak appears, as observed in other glass-forming materials. These findings challenge earlier reports that suggested a much lower T_g for bulk water, leading us to conclude that the T_g of bulk water is probably higher than 136 K and closer to 200 K.

Our dielectric spectroscopy and DSC step-response measurements confirmed the presence of two distinct relaxation processes in the confined water. The slower process, which is the structural relaxation or α-relaxation, directly correlates with the glass transition temperature determined by DSC and the crossover in the relaxation times of the fast water relaxation. The α-relaxation of confined water, corresponding to the calorimetric T_g, is difficult to observe and is only detectable using the DSC step response protocol because conductivity prevents accurate measurement of the dielectric response.

Concerning bulk water, we found that the relaxation times of the confined water agreed with those of bulk water. Therefore, we suggest that both relaxations (in bulk and under confinement) must be attributed to the JG relaxation of confined water and bear no relation to the main α-relaxation. Regarding the exhibit of long-range translational diffusion observed by other authors in nanoscale water films[27] (10^{-22} m/s^2 at 125 K and 10^{-19} m/s^2 at 142 K), we infer that these low diffusion coefficients indicate that translational motions in this temperature range occur within a highly restricted glassy environment. This could be related to a molecular relaxation mechanism occurring deep in the glassy state,[71] which, owing to its translational nature, has the potential for glass equilibration rather than a typical glass transition in a strong liquid.

In conclusion, our work demonstrates that the physical and chemical properties of the confining material heavily influence the glass transition temperature and dynamic behavior of confined water. This study offers critical new insights into the properties of supercooled water, with significant implications for various applications, including sustainable materials and water purification.

SUPPLEMENTARY MATERIAL

The supplementary material includes figures showing the following: heat flow and heat capacity of hydrated pectin, heating scans of heat capacity for bulk water, dry PE–Ca and Fe–BTC, ATR-FTIR spectra of deuterated water confined in PE–Ca and Fe–BTC, ATR-FTIR spectra of water confined in PE–Ca, Fe–BTC, and MCM-41 at different water contents and the bulk water spectrum, water relative concentration for MCM-41 as a function of water content (c_w), comparison between the ATR-FTIR spectra collected for PE–Ca (c_w = 33 wt. %) and Fe–BTC (c_w = 36%) at 173 K and 295 K and contributions of the isolated water OH stretching band, difference spectra, the dielectric loss $\varepsilon''(\omega)$ vs frequency of confined water in PE–Ca (c_w = 5 and 33 wt. %) at 175 K.

ACKNOWLEDGMENTS

We acknowledge Grant No. PID2023-146348NB-I00 funded by Ministerio de Ciencia, Innovación y Universidades/Agencia Estatal de Investigación (MCIN/AEI), Department of Education of the Basque Government under Grant Nos. PIBA_2024_1_0011 and IT1566-22 funded by the Basque Government.

AUTHOR DECLARATIONS

Conflict of Interest

The authors have no conflicts to disclose.

Author Contributions

Francesco Coin: Data curation (equal); Formal analysis (equal); Investigation (equal); Writing – original draft (equal). **Valerio Di Lisio**: Data curation (equal); Investigation (equal); Resources (equal); Writing – original draft (equal). **Daniele Cangialosi**: Formal

analysis (equal); Investigation (equal); Writing – review & editing (equal). **Silvina Cerveny**: Conceptualization (lead); Investigation (lead); Project administration (lead); Resources (lead); Writing – original draft (lead); Writing – review & editing (lead).

DATA AVAILABILITY

The data that support the findings of this study are available within the article and its supplementary material.

REFERENCES

[1] M. C. Bellissent-Funel, A. Hassanali, M. Havenith, R. Henchman, P. Pohl, F. Sterpone, D. van der Spoel, Y. Xu, and A. E. Garcia, "Water determines the structure and dynamics of proteins," Chem. Rev. **116**(13), 7673–7697 (2016).

[2] N. Giovambattista, P. J. Rossky, and P. G. Debenedetti, "Effect of temperature on the structure and phase behavior of water confined by hydrophobic, hydrophilic, and heterogeneous surfaces," J. Phys. Chem. B **113**(42), 13723–13734 (2009).

[3] P. G. Debenedetti, "Supercooled and glassy water," J. Phys.: Condens. Matter **15**(45), R1669–R1726 (2003).

[4] J. Sjostrom, J. Swenson, R. Bergman, and S. Kittaka, "Investigating hydration dependence of dynamics of confined water: Monolayer, hydration water and Maxwell–Wagner processes," J. Chem. Phys. **128**(15), 154503 (2008).

[5] M. Weigler, M. Brodrecht, G. Buntkowsky, and M. Vogel, "Reorientation of deeply cooled water in mesoporous silica: NMR studies of the pore-size dependence," J. Phys. Chem. B **123**(9), 2123–2134 (2019).

[6] B. Malfait, A. Jani, J. B. Mietner, R. Lefort, P. Huber, M. Fröba, and D. Morineau, "Influence of pore surface chemistry on the rotational dynamics of nanoconfined water," J. Phys. Chem. C **125**(30), 16864–16874 (2021).

[7] E. Steinrücken, M. Weigler, V. Schiller, and M. Vogel, "Dynamical susceptibilities of confined water from room temperature to the glass transition," J. Phys. Chem. Lett. **14**(17), 4104–4112 (2023).

[8] H. Jansson and J. Swenson, "Dynamics of water in molecular sieves by dielectric spectroscopy," Eur. Phys. J. E: Soft Matter **12**, S51–S54 (2003).

[9] J. H. Melillo, D. Cangialosi, V. Di Lisio, E. Steinrücken, M. Vogel, and S. Cerveny, "Complexity of confined water vitrification and its glass transition temperature," Proc. Natl. Acad. Sci. U. S. A. **121**(41), e2407030121 (2024).

[10] R. Bergman and J. Swenson, "Dynamics of supercooled water in confined geometry," Nature **403**(6767), 283–286 (2000).

[11] S. Cerveny, F. Barroso-Bujans, Á. Alegría, and J. Colmenero, "Dynamics of water intercalated in graphite oxide," J. Phys. Chem. C **114**(6), 2604–2612 (2010).

[12] M. D. Ramírez-Alba, M. Romanini, M. M. Pérez-Madrigal, J. L. Tamarit, C. Alemán, and R. Macovez, "Protonic charge conduction and H2O-induced relaxations in hydrated sodium alginate and in calcium alginate hydrogels and xerogels," J. Chem. Phys. **163**(3), 034901 (2025).

[13] J. Martínez-Sabando, F. Coin, J. C. Raposo, A. Larrañaga, J. H. Melillo, and S. Cerveny, "Dual crosslinking of low-methoxyl pectin by calcium and europium for the simultaneous removal of pharmaceuticals and divalent heavy metals," Chem. Eng. J. **475**, 146162 (2023).

[14] F. Coin, A. Larrañaga, and S. Cerveny, "Structural characterization of low methoxyl pectin-based adsorbents: The role of water on pectin structure," Carbohydr. Polym. Technol. Appl. **11**, 100885 (2025).

[15] N. A. Peppas, Y. Huang, M. Torres-Lugo, J. H. Ward, and J. Zhang, "Physicochemical foundations and structural design of hydrogels in medicine and biology," Annu. Rev. Biomed. Eng. **2**, 9–29 (2000).

[16] H. Zhang, Y. Tian, J. Hou, X. Hou, G. Hou, R. Ou, H. Wang, and L. Jiang, "Bioinspired smart gate-location-controllable single nanochannels: Experiment and theoretical simulation," ACS Nano **9**(12), 12264–12273 (2015).

[17] P. Zuo, J. Ran, C. Ye, X. Li, T. Xu, and Z. Yang, "Advancing ion selective membranes with micropore ion channels in the interaction confinement regime," ACS Nano **18**(8), 6016–6027 (2024).

[18] J. Wang, X. Zhang, Z. Yu, Y. Gao, Q. Lu, C. Ma, K. Liu, Q. Yuan, and Y. Yang, "Fast water transport and ionic sieving in ultrathin stacked nanoporous 2D membranes," Natl. Sci. Rev. **12**(3), nwae482 (2025).

[19] G. P. Johari, A. Hallbrucker, and E. Mayer, "The glass–liquid transition of hyperquenched water," Nature **330**(6148), 552–553 (1987).

[20] K. Amann-Winkel, C. Gainaru, P. H. Handle, M. Seidl, H. Nelson, R. Böhmer, and T. Loerting, "Water's second glass transition," Proc. Natl. Acad. Sci. U. S. A. **110**(44), 17720–17725 (2013).

[21] F. Perakis, K. Amann-Winkel, F. Lehmkühler, M. Sprung, D. Mariedahl, J. A. Sellberg, H. Pathak, A. Späh, F. Cavalca, D. Schlesinger, A. Ricci, A. Jain, B. Massani, F. Aubree, C. J. Benmore, T. Loerting, G. Grübel, L. G. M. Pettersson, and A. Nilsson, "Diffusive dynamics during the high-to-low density transition in amorphous ice," Proc. Natl. Acad. Sci. U. S. A. **114**(31), 8193–8198 (2017).

[22] V. Velikov, S. Borick, and C. A. Angell, "The glass transition of water, based on hyperquenching experiments," Science **294**(5550), 2335–2338 (2001).

[23] N. Giovambattista, C. A. Angell, F. Sciortino, and H. E. Stanley, "Glass-transition temperature of water: A simulation study," Phys. Rev. Lett. **93**(4), 047801 (2004).

[24] P. Lucas, J. Pries, S. Wei, and M. Wuttig, "The glass transition of water, insight from phase change materials," J. Non-Cryst. Solids: X **14**, 100084 (2022).

[25] L. Jia, W. Shu-Ying, Z. Cai-Ping, X. Li-Juan, W. Dan, and S. Min-Hua, "Glass transition temperature of water: From simulations of diffusion and excess entropy," Chin. Phys. Lett. **24**(7), 2025 (2007).

[26] M. Chonde, M. Brindza, and V. Sadtchenko, "Glass transition in pure and doped amorphous solid water: An ultrafast microcalorimetry study," J. Chem. Phys. **125**(9), 094501 (2006).

[27] G. A. Kimmel, M. K. Dunlap, K. Gurdumov, R. S. Smith, L. Kringle, and B. D. Kay, "Translational diffusion in supercooled water at and near the glass transition temperature—136 K," J. Chem. Phys. **162**(24), 244505 (2025).

[28] J. J. Shephard and C. G. Salzmann, "Molecular reorientation dynamics govern the glass transitions of the amorphous ices," J. Phys. Chem. Lett. **7**(12), 2281–2285 (2016).

[29] V. Fuentes-Landete, L. J. Plaga, M. Keppler, R. Böhmer, and T. Loerting, "Nature of water's second glass transition elucidated by doping and isotope substitution experiments," Phys. Rev. X **9**(1), 011015 (2019).

[30] S. Roy, R. Priyadarshi, Ł. Łopusiewicz, D. Biswas, V. Chandel, and J. W. Rhim, "Recent progress in pectin extraction, characterization, and pectin-based films for active food packaging applications: A review," Int. J. Biol. Macromol. **239**, 124248 (2023).

[31] G. T. Grant, E. R. Morris, D. A. Rees, P. J. C. Smith, and D. Thom, "Biological interactions between polysaccharides and divalent cations: The egg-box model," FEBS Lett. **32**(1), 195–198 (1973).

[32] S. Dissegna, K. Epp, W. R. Heinz, G. Kieslich, and R. A. Fischer, "Defective metal-organic frameworks," Adv. Mater. **30**(37), 1704501 (2018).

[33] X. Monnier, S. Napolitano, and D. Cangialosi, "Direct observation of desorption of a melt of long polymer chains," Nat. Commun. **11**(1), 4354 (2020).

[34] J. Martín, N. Stingelin, and D. Cangialosi, "Direct calorimetric observation of the rigid amorphous fraction in a semiconducting polymer," J. Phys. Chem. Lett. **9**(5), 990–995 (2018).

[35] J.-B. Brubach, A. Mermet, A. Filabozzi, A. Gerschel, and P. Roy, "Signatures of the hydrogen bonding in the infrared bands of water," J. Chem. Phys. **122**(18), 184509 (2005).

[36] P. Wernet, D. Nordlund, U. Bergmann, M. Cavalleri, M. Odelius, H. Ogasawara, L. Å. Näslund, T. K. Hirsch, L. Ojamäe, P. Glatzel, L. G. M. Pettersson, and A. Nilsson, "The structure of the first coordination shell in liquid water," Science **304**(5673), 995–999 (2004).

[37] S. Le Caër, S. Pin, S. Esnouf, Q. Raffy, J. P. Renault, J. B. Brubach, G. Creff, and P. Roy, "A trapped water network in nanoporous material: The role of interfaces," Phys. Chem. Chem. Phys. **13**(39), 17658–17666 (2011).

[38] E. D. Donkor, A. Offei-Danso, A. Rodriguez, F. Sciortino, and A. Hassanali, "Beyond local structures in critical supercooled water through unsupervised learning," J. Phys. Chem. Lett. **15**(15), 3996–4005 (2024).

[39] M. Grossutti and J. R. Dutcher, "Correlation between chain architecture and hydration water structure in polysaccharides," Biomacromolecules **17**(3), 1198–1204 (2016).

[40] R. Li, Z. Jiang, F. Chen, H. Yang, and Y. Guan, "Hydrogen bonded structure of water and aqueous solutions of sodium halides: A Raman spectroscopic study," J. Mol. Struct. **707**(1–3), 83–88 (2004).

[41] M. Śmiechowski and J. Stangret, "Molecular picture of hydroxide anion hydration in aqueous solutions studied by FT-IR ATR spectroscopy," J. Mol. Struct. **834–836**, 239–248 (2007).
[42] E. Gojło, M. Śmiechowski, A. Panuszko, and J. Stangret, "Hydration of carboxylate anions: Infrared spectroscopy of aqueous solutions," J. Phys. Chem. B **113**(23), 8128–8136 (2009).
[43] N. Kitadai, T. Sawai, R. Tonoue, S. Nakashima, M. Katsura, and K. Fukushi, "Effects of ions on the OH stretching band of water as revealed by ATR-IR spectroscopy," J. Solution Chem. **43**(6), 1055–1077 (2014).
[44] G. Goracci, M. Monasterio, H. Jansson, and S. Cerveny, "Dynamics of nano-confined water in Portland cement - comparison with synthetic C-S-H gel and other silicate materials," Sci. Rep. **7**(1), 8258 (2017).
[45] S. Cerveny, I. Combarro-Palacios, and J. Swenson, "Evidence of coupling between the motions of water and peptides," J. Phys. Chem. Lett. **7**(20), 4093–4098 (2016).
[46] F. Kremer and A. Schönhals, *Broadband Dielectric Spectroscopy* (Springer, Berlin, 2003).
[47] X. Monnier and D. Cangialosi, "Thermodynamic ultrastability of a polymer glass confined at the micrometer length scale," Phys. Rev. Lett. **121**(13), 137801 (2018).
[48] X. Monnier, D. Cangialosi, B. Ruta, R. Busch, and I. Gallino, "Vitrification decoupling from α-relaxation in a metallic glass," Sci. Adv. **6**(17), eaay1454 (2020).
[49] S. Cerveny, A. Alegria, and J. Colmenero, "Universal features of water dynamics in solutions of hydrophilic polymers, biopolymers, and small glass-forming materials," Phys. Rev. E **77**, 031803 (2008).
[50] S. Cerveny, J. Colmenero, and Á. Alegría, "Dielectric properties of water in amorphous mixtures of polymers and other glass forming materials," J. Non-Cryst. Solids **353**(47–51), 4523–4527 (2007).
[51] S. Cerveny, F. Mallamace, J. Swenson, M. Vogel, and L. Xu, "Confined water as model of supercooled water," Chem. Rev. **116**(13), 7608–7625 (2016).
[52] J. Swenson, "Possible relations between supercooled and glassy confined water and amorphous bulk ice," Phys. Chem. Chem. Phys. **20**(48), 30095–30103 (2018).
[53] G. P. Johari and M. Goldstein, "Viscous liquids and the glass transition. II. Secondary relaxations in glasses of rigid molecules," J. Chem. Phys. **53**(6), 2372–2388 (1970).
[54] M. Sattig and M. Vogel, "Dynamic crossovers and stepwise solidification of confined water: A ^{2}H NMR study," J. Phys. Chem. Lett. **5**(1), 174–178 (2014).
[55] M. Paluch, C. M. Roland, S. Pawlus, J. Zioło, and K. L. Ngai, "Does the Arrhenius temperature dependence of the Johari-Goldstein relaxation persist above T_g?," Phys. Rev. Lett. **91**, 115701 (2003).
[56] K. Amann-Winkel, R. Böhmer, F. Fujara, C. Gainaru, B. Geil, and T. Loerting, "Colloquium: Water's controversial glass transitions," Rev. Mod. Phys. **88**(1), 011002 (2016).
[57] R. Androsch and C. Schick, "Hydrogen-bond density controlled sub-Tg annealing peaks in fast-scanning-chip calorimeter heating scans of non-crystallized aliphatic polyamides," Thermochim. Acta **748**, 179997 (2025).
[58] N. G. Perez-De Eulate and D. Cangialosi, "The very long-term physical aging of glassy polymers," Phys. Chem. Chem. Phys. **20**(18), 12356–12361 (2018).
[59] D. P. B. Aji and G. P. Johari, "Kinetic-freezing and unfreezing of local-region fluctuations in a glass structure observed by heat capacity hysteresis," J. Chem. Phys. **142**(21), 214501 (2015).
[60] L. Song, W. Xu, J. Huo, J.-Q. Wang, X. Wang, and R. Li, "Two-step relaxations in metallic glasses during isothermal annealing," Intermetallics **93**, 101–105 (2018).
[61] L. Hu and Y. Yue, "Secondary relaxation in metallic glass formers: Its correlation with the genuine Johari–Goldstein relaxation," J. Phys. Chem. C **113**(33), 15001–15006 (2009).
[62] Q. Yang, S.-X. Peng, Z. Wang, and H.-B. Yu, "Shadow glass transition as a thermodynamic signature of β relaxation in hyper-quenched metallic glasses," Natl. Sci. Rev. **7**(12), 1896–1905 (2020).
[63] M. R. Harpham, B. M. Ladanyi, N. E. Levinger, and K. W. Herwig, "Water motion in reverse micelles studied by quasielastic neutron scattering and molecular dynamics simulations," J. Chem. Phys. **121**(16), 7855–7868 (2004).
[64] N. Shinyashiki, W. Yamamoto, A. Yokoyama, T. Yoshinari, S. Yagihara, R. Kita, K. L. Ngai, and S. Capaccioli, "Glass transitions in aqueous solutions of protein (bovine serum albumin)," J. Phys. Chem. B **113**, 14448–14456 (2009).
[65] A. Panagopoulou, A. Kyritsis, R. Sabater i Serra, J. L. Gómez Ribelles, N. Shinyashiki, and P. Pissis, "Glass transition and dynamics in BSA–water mixtures over wide ranges of composition studied by thermal and dielectric techniques," Biochim. Biophys. Acta, Proteins Proteomics **1814**(12), 1984–1996 (2011).
[66] K. Sasaki, A. Panagopoulou, R. Kita, N. Shinyashiki, S. Yagihara, A. Kyritsis, and P. Pissis, "Dynamics of uncrystallized water, ice, and hydrated protein in partially crystallized Gelatin–Water mixtures studied by broadband dielectric spectroscopy," J. Phys. Chem. B **121**(1), 265–272 (2017).
[67] K. Sasaki, M. Takatsuka, N. Shinyashiki, and K. L. Ngai, "Relating the dynamics of hydrated poly(vinyl pyrrolidone) to the dynamics of highly asymmetric mixtures and polymer blends," J. Mol. Liq. **333**, 115907 (2021).
[68] Y. Beilinson, V. Schiller, J. Regentin, J. H. Melillo, A. Greenbaum, T. Antropova, S. Cerveny, M. Vogel, and Y. Feldman, "The nature of the low-temperature crossover of water in hard confinement," J. Phys. Chem. B **127**(22), 5128–5140 (2023).
[69] S. Cerveny, G. A. Schwartz, R. Bergman, and J. Swenson, "Glass transition and relaxation processes in supercooled water," Phys. Rev. Lett. **93**(24), 245702 (2004).
[70] J. Swenson and J. Teixeira, "The glass transition and relaxation behavior of bulk water and a possible relation to confined water," J. Chem. Phys. **132**, 014508 (2010).
[71] Z. Song, C. Rodríguez-Tinoco, A. Mathew, and S. Napolitano, "Fast equilibration mechanisms in disordered materials mediated by slow liquid dynamics," Sci. Adv. **8**(15), eabm7154 (2022).

Supplementary Material of

The glass transition and the dynamics of water within pectin and metal-organic framework nanochannels

Francesco Coin[1], Valerio Di Lisio[2], Daniele Cangialosi[1] and Silvina Cerveny[1*]

*corresponding author: silvina.cerveny@ehu.es

[1] *Centro de Física de Materiales (CSIC, UPV/EHU)-Materials Physics Center (MPC), Paseo Manuel de Lardizabal 5, San Sebastián 20018, Spain.*
[2] *Donostia International Physics Center (DIPC), Paseo Manuel de Lardizabal 4, San Sebastián 20018, Spain.*

1. Glass transition of pure and hydrated cross-linked pectin

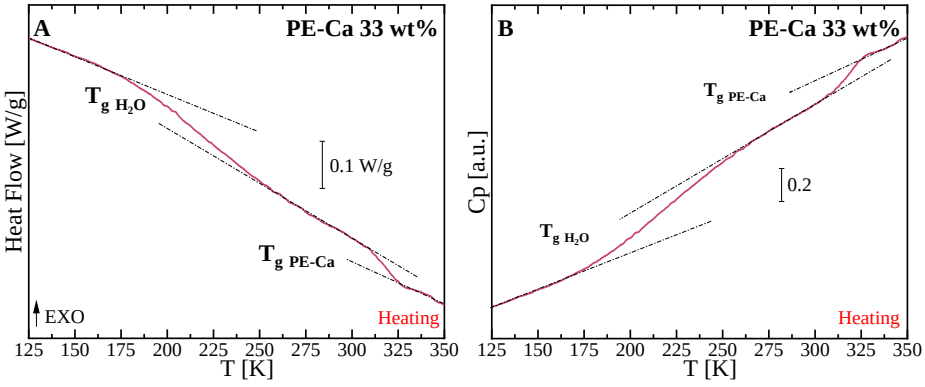

Figure S1. Heat flow (A) and heat capacity (B) during heating at 20 K/min of pectin cross-linked with calcium (PE-Ca) at 33 wt% hydration over a wide temperature range, showing the two glass transitions (those corresponding to water and pectin plasticized by water).

2. Calculation of the absolute value of heat capacity

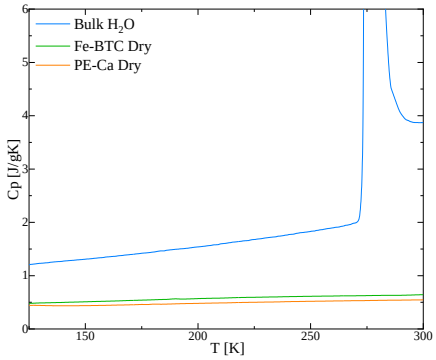

Figure S2. Heating scans of heat capacity for bulk water, dry PE-Ca, and Fe-BTC, respectively, in a function of the temperature. The heat capacity of the water confined within the pores was calculated by subtracting the contributions of excess bulk ice (when crystallization occurred during the cooling cycle) and the dry sample from the total heat capacity of the hydrated material using the formula $c_{P,H2O}[J/gK] = (c_{p,tot}[J/K] - m_{sample}[g]c_{p,sample}[J/gK] - m_{ice}[g]c_{p,ice}[J/gK])/m_{H2O}[g]$ where $c_{P,H2O}$ is the heat capacity of the water inside the pores, $c_{P,tot}$ is the heat capacity of the hydrated sample (PE-Ca or MOF), $c_{P,sample}$ is the heat capacity of the dried sample, $c_{P,ice}$ is the ice heat capacity per gram, and msample, m_{ice}, and m_{H2O} are the mass of PE-Ca or MOF, ice and water, respectively.

3. D_2O ATR-FTIR hydration study

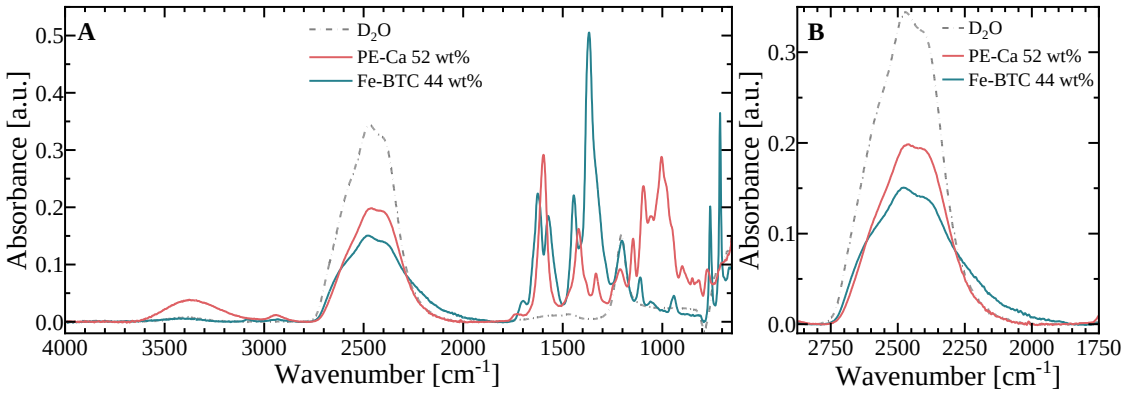

Figure S3. ATR-FTIR spectra of D_2O-hydrated PE-Ca at 52 wt% and Fe-BTC at 44 wt% compared with pure D_2O (dashed line) at room temperature (A). Magnification of OD stretching band (B).

4. OH stretching band deconvolution

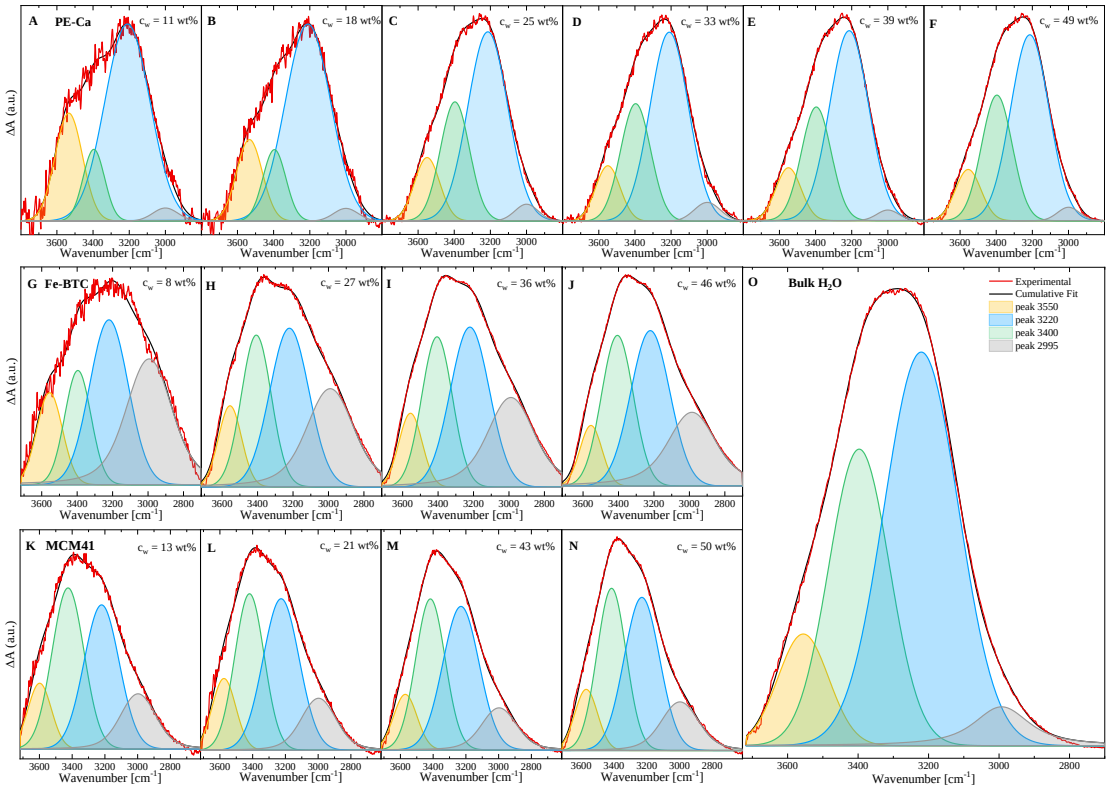

Figure S4. ATR-FTIR spectra of water confined in PE-Ca (A-F), Fe-BTC (G-J) and MCM41 (K-N) at different water contents and the bulk water spectrum (O). Deconvolution of the OH stretching band for bulk and confined water. The data analysis was performed using the Omnic software and the spectra were baseline-corrected, and fitted by a Gaussian function for the peaks centered at 3550, 3400 and 3220 cm^{-1} and a Voight function was used for the peak at centered ~3000 cm^{-1}.

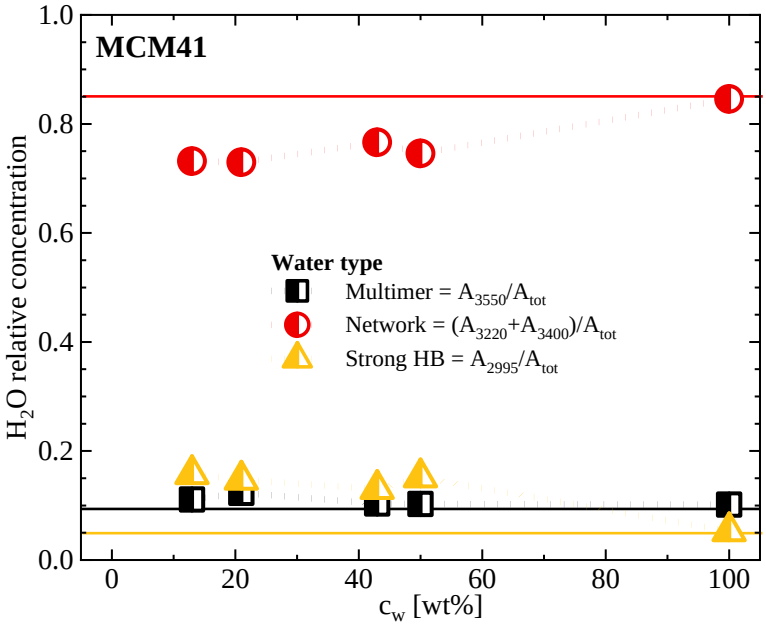

Figure S5. Water relative concentration for MCM41 as function of water content (c_w).

5. ATR-FTIR at low temperature

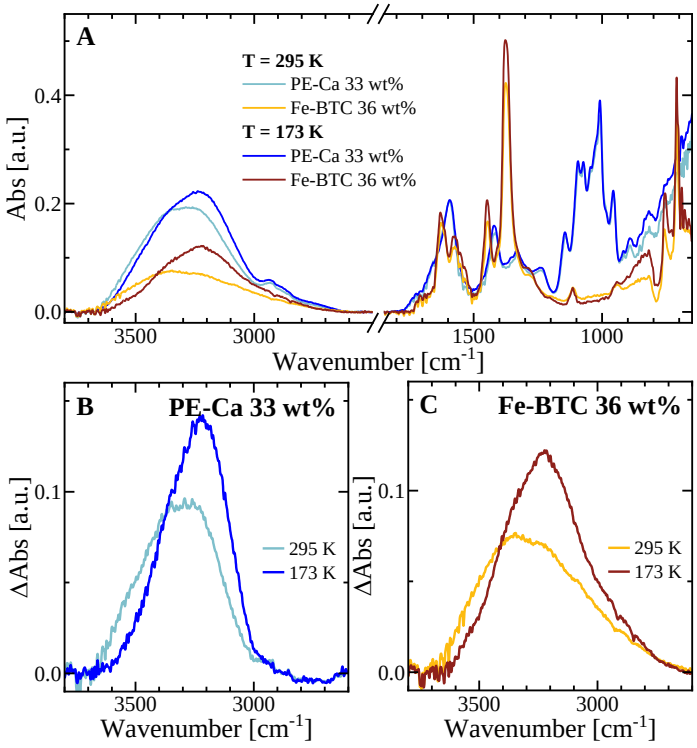

Figure S6. Comparison between the ATR-FTIR spectra collected for PE-Ca (c_w = 33 wt%) and Fe-BTC (c_w = 36%) at 173 K and at 295 K. (B-C) Contributions of the isolated water OH stretching band, difference spectra. ΔAbs(cw) were calculated by subtracting the weighted contribution of dry pectin and MOF, Abs(dry), from the hydrated spectra, Abs(cw), using the formula $\Delta Abs(c_w) = Abs(c_w) - Abs(dry)*(100-c_w)/100$.

6. Dynamics of confined water in PE-Ca and Fe-BTC determined by dielectric spectroscopy and standard calorimetric measurements

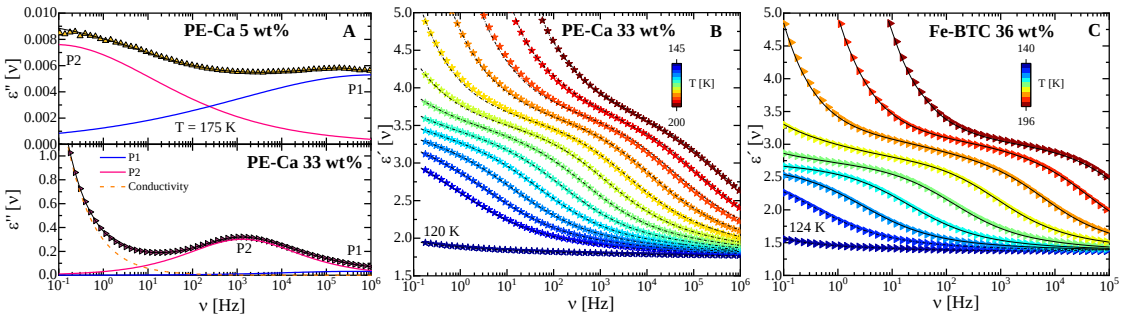

Figure S7. (A) Dielectric loss ε″(ω) versus frequency of confined water in PE-Ca (c_w = 5 wt% and 33 wt%) at 175 K. The lines are the simultaneous fits of the imaginary parts using Cole-Cole functions for process P1 and P2. Real part of the dielectric constant (ε') at different temperatures for (B) PE-Ca at 33wt% and (C) Fe-BTC at 36 wt%.

polymers

MDPI

Article

Bio-Based Pectin-Calcium Film and Foam Adsorbents with Immobilized Fe–BTC MOF for Water Contaminant Removal

Francesco Coin [1,*], Carolina Iacovone [1,2] and Silvina Cerveny [1,*]

[1] Centro de Física de Materiales (CSIC, UPV/EHU)—Materials Physics Center (MPC), Paseo Manuel de Lardizabal 5, 20018 San Sebastián, Spain; ciacovone001@ikasle.ehu.eus
[2] Donostia International Physics Center (DIPC), Paseo Manuel de Lardizabal 4, 20018 San Sebastián, Spain
* Correspondence: fcoin001@ikasle.ehu.eus (F.C.); silvina.cerveny@ehu.es (S.C.)

Abstract

Metal-organic frameworks (MOFs) offer high porosity for water remediation but face challenges in handling as powders. We address these limitations by physically immobilizing Fe–BTC MOF within calcium-crosslinked low-methoxyl pectin matrices (PE–Ca–MOF). Solvent-cast films and freeze-dried foams were fabricated using water-based and polyvinylpyrrolidone (PVP)-assisted Fe–BTC dispersions, preserving MOF and pectin structures confirmed by FT–IR. PVP improved Fe–BTC dispersion and reduced particle size, enhancing distribution and plasticizing the matrix proved by DSC. Incorporation of water-dispersed Fe–BTC increased the equilibrium adsorption capacity but reduced the initial adsorption rate, while the PVP-assisted foam further enhanced uptake in comparative batch tests through its more open porous structure. At pH 7, PE–Ca–5%MOF films showed high adsorption capacities and removal efficiencies for paraquat (35.5 mg/g, 70.6%) and tetracycline (14.5 mg/g, 46.8%), while maintaining Zn^{2+} uptake compared to calcium-pectin films without MOF. Adsorption followed pseudo-first-order kinetics and Langmuir isotherms. Green regeneration with acetic acid enabled >80% capacity retention over five adsorption–desorption cycles. Foam architectures increased porosity and active-site accessibility (SEM), improving performance even at lower MOF loadings. Overall, controlling MOF dispersion and composite morphology enables efficient, reusable, and environmentally friendly bio-based adsorbents for water purification.

Keywords: bio-based adsorbents; metal-organic framework (MOF); water purification; pectin-calcium films and foams; iron-based-MOF; adsorption

Academic Editor: Yan'an Gao

Received: 27 November 2025
Revised: 2 January 2026
Accepted: 5 January 2026
Published: 8 January 2026

1. Introduction

Nanotechnology has become a key tool for the next generation of water purification technologies. Various nanomaterials, such as nanofibers [1–3], nanoparticles [4], nanotubes [5], biochar [6], and/or mineral clays [7], have been explored for removing pollutants from water. Nanoparticles (NPs) are particularly effective due to their large surface area and high reactivity, enabling efficient pollutant capture [4]. Within the family of NPs, metal-organic frameworks (MOFs) have gained particular attention because of their adjustable porosity and versatile functionality, finding uses in fields such as catalysis, energy storage, drug delivery, gas separation, and, more recently, they have become highly promising adsorbents for environmental water cleanup [8].

In recent years, various MOF materials have been tested for water cleaning and pollutant removal. Examples include: Zr-based UiO-66 and its derivatives for antibiotics/dyes;

ZIF-type frameworks (ZIF-8/ZIF-67) for dyes, antibiotics and pesticides; Zr-MOF-808 for PFAS; Fe/Cr MIL-101 and MIL-53 families for dyes and oxyanions; and Ti-based MIL-125 for photocatalytic degradation of organics under UV/visible [9–12].

MOFs are crystalline porous materials composed of metal ions connected by organic linkers, which create a network with an extremely high porosity. Their ultra-high surface area and tunable surface chemistry enable the capture of a wide range of contaminants from aqueous systems [13]. However, in powder form, MOFs present several practical limitations for direct application in water treatment. Handling fine powder is challenging and can lead to fouling and secondary contamination of treated water, especially at high MOF concentrations. Additionally, if MOFs are not sufficiently water-stable, they may partially dissolve, releasing metal ions and organic linkers into the environment. These limitations have motivated researchers to immobilize MOFs within polymer matrices for improved handling and stability [12].

Despite growing interest in MOF–polymer composites for water treatment [13], three critical gaps limit their practical application and environmental sustainability. First, most studies employ synthetic, non-biodegradable polymers [14] that contradict green chemistry principles and contribute to plastic pollution. Second, the effect of MOF dispersion quality on composite performance is rarely investigated systematically; most studies use a single dispersion method without optimization or comparison, potentially leaving significant performance improvements unexplored. Third, the influence of composite morphology, particularly the comparison between two-dimensional films and three-dimensional porous structures (2D films vs. 3D foams), on adsorption kinetics and capacity remains poorly understood for bio-based matrices. Furthermore, while Fe–BTC (also known as Basolite F300) has demonstrated excellent adsorption capacity for various contaminants in powder form [15–20], its integration into sustainable bio-based matrices for multi-contaminant water purification has not been systematically explored.

Pectin, a polysaccharide present in plant cell walls, offers unique advantages and it is particularly promising: (1) abundant availability from citrus and apple processing waste, enabling waste valorization [21]; (2) excellent film-forming properties [22]; (3) tunable ionic crosslinking with Ca^{2+} ions, creating hydrogels with maintained macroscopic integrity [23]; (4) inherent adsorption capacity through carboxyl groups [24–26]; and (5)'biodegradability, ensuring minimal environmental impact at end-of-life [27]. Moreover, pectin has recently attracted growing interest also for fundamental studies of water mobility confined within nanochannels, which drive the mass transport to active adsorption sites in aqueous media [28,29]. Pectin has many hydroxyl and carboxyl functional groups, which can bind metal ions [23,30,31]. In particular, low-methoxyl pectin (LMP) can be cross-linked (for instance with Ca^{2+} ions) to form insoluble hydrogels composed of "egg-box" dimers, which are the active sites for binding metal ions [31]. Thus, calcium-crosslinked low-methoxyl pectin (PE–Ca) can provide a versatile platform for hosting MOF particles, thereby improving handling and preventing secondary contamination

Therefore, this study aims to develop sustainable PE–Ca–MOF composites using two distinct morphologies (solvent-cast films (2D) and freeze-dried foams (3D)) to investigate structure–performance relationships. We have systematically compared water-based and PVP-assisted MOF dispersion methods and their impact on particle size, distribution, and adsorption performance. We selected Fe–BTC for its availability, low cost, water stability [32], low toxicity [33], and strong affinity for target pharmaceuticals; Fe^{3+} sites and high internal surface area facilitate robust interactions with these molecules [15]. In addition, we have evaluated adsorption performance against three contaminant classes representing diverse physicochemical properties: heavy metals (Zn^{2+}), pesticides (paraquat), and antibiotics (tetracycline) and also assessed the adsorption properties of other pharmaceuticals

(Atenolol, Metformin, and Metoprolol). Moreover, we have assessed practical reusability and regeneration potential using bio-based acetic acid over multiple adsorption-desorption cycles. To elucidate structure–performance relationships through comprehensive characterization (DLS, FTIR, XRD, SEM, DSC) and adsorption modeling (kinetics and isotherms). This work bridges the gap between fundamental materials science and practical environmental applications, offering a sustainable alternative to synthetic polymer–MOF composites while providing mechanistic insights into dispersion.

2. Materials and Methods

2.1. Materials

Citrus pectin powder (PE) with nominal values of 91% of galacturonic acid (Gal) and methyl esterification degree (DM) of 9.9% was supplied by Herbstreith & Fox (Neuenbürg, Germany). Sodium chloride (NaCl, product number S9625), Calcium chloride ($CaCl_2$, product number C1016), Zinc chloride ($ZnCl_2$, product number 208086), Sodium hydroxide (NaOH, product number S5881), Atenolol (ATE, product number A7655), Metformin (MFT, product number 317240), Metoprolol (MET, product number PHR1076), Paraquat (PQ, product number 856177) and Tetracycline (TC, product number 87128) were purchased from Sigma Aldrich (Madrid, Spain). Nitric acid (HNO_3 65% *w*/*w*, product number 7697-37-2) was purchased from Scharlab (Barcelona, Spain). NaOH and HNO_3 were used to adjust the pH. Acetic acid (AA, glacial (99%)) was purchased from Fischer Chemical (Madrid, Spain) (product number UN2789) and used for the desorption experiments. Milli–Q water was used to prepare the solutions.

Contaminant Selection Rationale

Three model contaminants were selected to represent diverse physicochemical properties and environmental relevance: (1) Zinc (II) (Zn^{2+}) as a representative heavy metal commonly found in industrial effluents from electroplating, mining, and metallurgy [34], with ionic radius of 0.74 Å and +2 charge enabling ion exchange and coordination interactions; (2) Paraquat (1,1′–dimethyl–4,4′–bipyridinium dichloride, MW = 257.16 g/mol) as a widely used herbicide with high aquatic toxicity [35], existing as a di-cation (pKa >> 14) at neutral pH, enabling electrostatic interactions; and (3) Tetracycline ($C_{22}H_{24}N_2O_8$, MW = 444.43 g/mol) as a broad-spectrum antibiotic frequently detected in wastewater [36], existing as a zwitterion at pH 7 (pKa values: 3.3, 7.7, 9.5) with multiple functional groups enabling complexation, hydrogen bonding, and π–π interactions. This selection enables assessment of adsorbent versatility across different binding mechanisms and molecular sizes. In addition, also three more pharmaceuticals were tested: atenolol, metformin, and metoprolol.

2.2. MOF Dispersion Methods

Two dispersion methods were compared to optimize MOF particle size and distribution. In the water-based dispersed method, 1 wt%, 5 wt%, and 10 wt% of Fe–BTC (relative to the amount of pectin) were added to Milli-Q water (50 mL). In PVP-assisted dispersion method, 1% Fe–BTC was dispersed in 50 mL of a 2.5% (*w*/*v*) polyvinylpyrrolidone (PVP) aqueous solution, which served as a surfactant. In both methods, the solutions were continuously stirring and subjected to tip sonication for 30 min (10 s pulses at 35% amplitude) at 70 °C. The quality of dispersion was evaluated using dynamic light scattering (DLS), which revealed reduced particle aggregation in the PVP-assisted dispersion method (see Section 2.3).

2.3. Composite Preparation

2.3.1. Film Fabrication (Solvent Casting)

Pectin (PE) was dissolved in deionized water (3 g in 50 mL) under magnetic stirring at 70 °C for 1 h. The solution was then sonicated in a thermal bath at 70 °C for an additional hour to ensure complete PE dissolution.

The solution was kept at the same temperature and the MOF dispersion (water-based or PVP-assisted) was added dropwise under continuous stirring at 300 rpm and constant tip sonication for 30 min (10 s pulses at 35% amplitude) at 70 °C to achieve final MOF loadings of 1 wt%, 5 wt%, and 10 wt% relative to pectin dry weight.

The mixture was cast into Teflon Petri dishes (10 cm diameter) and dried at 23 °C and 70% relative humidity for 24 h and subsequently dried in a vacuum oven at 40 °C for 1 h. The films were immersed in a 500 ppm Ca^{2+} solution (1.25 g/L relative to PE weight) under constant shaking at 125 rpm for 40 min at room temperature to induce ionic crosslinking (external) [37]. To remove excess ions and unbound components, after crosslinking, the materials were washed five times with fresh deionized water (dose 1.25 g/L). The resulting films had a thickness of 0.10 ± 0.01 mm. Films were then dried in a vacuum oven at 40 °C for 1 h and then stored in sealed containers with silica gel desiccant until use.

Consequently, insoluble Ca^{2+}-crosslinked PE films with varying MOF concentrations were obtained and labeled as follows: PE–Ca (no MOF), PE–Ca–1%MOF, PE–Ca–5%MOF, PE–Ca–10%MOF (water-dispersion method), and PE–Ca–1%MOF–PVP (PVP-assisted dispersion method).

2.3.2. Foam Fabrication (Freeze-Drying)

Foam samples were prepared following the same protocol as films up to the casting step. The entire solution (50 mL) was poured into flat crystallization dish (15 cm diameter × 7 cm height) covering the entire surface, frozen with liquid nitrogen for 1 h to ensure complete ice crystal formation and then freeze-dried (Schneider Electric, Rueil-Malmaison, France) at −55 °C and <0.1 mbar for 24 h. The sublimation of ice crystals created an interconnected porous network. Foams were also crosslinked, dried and storage as previously explained in Section 2.3.1. As a result, an insoluble, Ca^{2+}-crosslinked PE foam containing 1 wt% of MOF (dispersed with PVP-assisted method) was obtained.

2.3.3. Samples Conditioning

All the fabricated materials were dried and stored under vacuum (10^{-2} mbar) at 40 °C for one week and carefully weighed before all structural and adsorption experiments.

2.4. Adsorption Experiments

All adsorption experiments were conducted at neutral pH (pH 7) using a temperature-controlled orbital shaker (23 ± 2 °C, 125 rpm, Ovan, Barcelona, Spain). Working at pH 7 is important because it is close to most natural water conditions, minimizing extreme acid/base effects and allowing us to evaluate the material's performance under realistic conditions. All conclusions about the mechanism discussed in this work refer exclusively to adsorption experiments carried out at neutral pH (pH 7); the pH-dependent behavior of the studied contaminants on these composites remains unknown on the basis of the present data and should be systematically investigated in future studies.

To minimize surface effects and maintain uniform experimental conditions, composite samples were cut into uniform pieces: 22 ± 1 mm in diameter and 0.10 ± 0.01 mm thick for films (approximately 5 mg) and cylinders of 10 ± 1 mm in diameter and 1.00 ± 0.01 mm thick (approximately 5 mg). Contaminant solutions were prepared fresh daily in deionized

water and pH-adjusted to 7.0 ± 0.1 using 0.1 M HNO_3 or NaOH. The composite dose was maintained at 1 g/L (adsorbent dry weight per liter of solution) for all experiments.

Adsorption data are reported as (mean value ± standard deviation), based on experiments carried out in triplicate. Model selection was based on R2 and reduced χ^2 values, the F-test, the Akaike (AIC), and Bayesian (BIC) information criteria (see Section S1 in the Supporting Material (SM) for details) [38–40]. Statistical differences were assessed using a one-way ANOVA on ranks with a 99% confidence level ($p < 0.01$).

2.4.1. Kinetic Experiments

Kinetic experiments were performed at an initial contaminant concentration of 10 mg/L (50 mg/L for Zn^{2+}), at pH 7 and at predetermined time intervals (5, 10, 15, 30, 60, 120, 240, 480, 960, and 1440 min).

The adsorption capacity at time t (q_t, mg/g) was calculated using:

$$q_t = \frac{C_0 - C_t}{d} \quad (1)$$

where C_0 is the initial concentration (mg/L), C_t is the concentration at time t (mg/L), d is the adsorbent dose (g/L).

2.4.2. Isotherms Experiments

Equilibrium isotherm experiments were conducted by varying the initial contaminant concentration (5, 10, 25, 50, and 75 mg/L) and a fixed contact time of 24 h. The equilibrium adsorption capacity (q_e, mg/g) was calculated using:

$$q_e = \frac{C_0 - C_{eq}}{d} \quad (2)$$

where C_0 and C_{eq} denote the initial and equilibrium concentrations (mg/L) of the crosslinking agent or pollutant, respectively.

The removal efficiency (R_{Eff}, %) was determined using the following expression:

$$R_{Eff}(\%) = \left(\frac{C_0 - C_{eq}}{C_0}\right) \times 100\% \quad (3)$$

2.4.3. Reusability Studies

Reusability was assessed over five consecutive adsorption–desorption cycles using paraquat and tetracycline as contaminant models. After each adsorption cycle (at pH 7, for 1 h), the adsorbent was recovered using 2% *v*/*v* acetic acid solution (at pH 2.3, for 1 h) to desorb the contaminant. Acetic acid was selected as a green regeneration agent due to its bio-based origin (fermentation), low cost, biodegradability, and ability to protonate carboxyl groups without damaging the pectin matrix or MOF structure [41]. Between cycles, samples were washed with water and dried to remove residual reagents. The desorption efficiency (R_{des}, %) was calculated as:

$$R_{des}(\%) = \frac{C_{Des}(n)}{C_0 - C_{eq}(n)} \times 100\% \quad (4)$$

For each cycle n, the initial concentration was C_0 (from the stock solution), the equilibrium concentration after adsorption was $C_{eq}(n)$ (from the treated solution), and the desorption concentration was $C_{Des}(n)$ (from the eluate). After desorption, the adsorbent was washed three times with deionized water, dried to remove residual reagents, and reused for the next cycle.

The retention rate was calculated to assess the stability and reusability of the materials, representing the percentage of adsorption capacity retained in each subsequent cycle compared to the first cycle. The retention rate compares the adsorption capacity in cycle (n) to that of the first cycle:

$$Retention\ rate_n(\%) = \frac{q_n}{q_1} \times\ 100\% \tag{5}$$

A high retention rate implies good structural stability and regeneration potential of the adsorbent [42].

2.4.4. Models

The adsorption kinetics were analyzed by fitting the data to empirical kinetic models, namely the pseudo-first-order (PFO) and pseudo-second-order (PSO) equations:

$$\text{PFO}: \ q_t = q_\text{e}\left(1 - \text{e}^{-k_1 t}\right) \tag{6}$$

$$\text{PSO}: \ q_t = \frac{q_\text{e}^2 k_2 t}{1 + q_\text{e} k_2 t} \tag{7}$$

q_e is the equilibrium adsorption capacity, k_1 and k_2 (min^{-1}) represent the characteristic time constants of the PFO and PSO models and describe the initial rate of the adsorption process [43].

The adsorption isotherm data were analyzed using the Langmuir (Equation (8)), Freundlich (Equation (9)) models [44]:

$$\text{Langmuir}: \ q_e(C_{eq}) = \frac{q_M K_L C_{eq}}{1 + K_L C_{eq}} \tag{8}$$

$$\text{Freundlich}: \ q_e\left(C_{eq}\right) = K_F C_e^{1/n} \tag{9}$$

In these models, q_e is the equilibrium adsorption capacity; q_M (mg/g) is the maximum adsorption capacity; K_L (L/mg), n and K_F ($\text{L}^{1/\text{n}}\text{mg}^{1-1/\text{n}}\text{g}^{-1}$) are the Langmuir and Freundlich constants, respectively.

The exchange ratio helps to understand the ion exchange mechanism of the adsorbent material for specific ions [45]. The exchange ratio is defined as:

$$Exchange\ ratio = \frac{Moles\ of\ adsorbed\ ion}{Moles\ of\ desorbed\ ion} \tag{10}$$

If the exchange ratio is equal to 1, it indicates a 1:1 molar exchange between the two ions. If the exchange ratio is greater than 1, more of the adsorbed ion is taken up relative to the desorbed ion. However, If the exchange ratio is less than 1, less of the adsorbed ion is taken up relative to the desorbed ion.

2.5. Characterization Techniques

The particle size of the dispersed Fe–BTC solutions was measured at 25 °C using a Zetasizer Nano ZS90 (Malvern Instruments Ltd., Worcestershire, UK). Measurements were performed in disposable quartz cuvettes using a backscatter detection angle of 173°. Reported values represent the average of three independent measurements.

The morphology and elemental composition of the pectin-based adsorbents were characterized by scanning electron microscopy (SEM; Quanta 250 ESEM, FEI, Eindhoven, The Netherlands) coupled with energy-dispersive X-ray (EDX) spectroscopy (silicon drift detector, EDAX, Tilburg, The Netherlands). The samples were fixed onto aluminum stubs using double-sided carbon tape, and the chamber pressure was adjusted to 80 Pa in low-

vacuum mode. Imaging was performed at an accelerating voltage of 10 kV and a beam current of 5 Pa, using a large-field detector to collect the electrons. Thermogravimetric analysis by TA Instruments (Q500) (New Castle, DE, USA) was employed to assess the water evaporation and thermal stability of PE–Ca samples ($5 \times 5 \times 0.05$ mm^3). Measurements were performed under continuous nitrogen flow of 25 mm^3/min. To prevent dehydration, the samples were placed on the pan as quickly as possible. The weight reduction was monitored as the temperature increased by 10 K/min for dried PE samples.

Differential scanning calorimetry (DSC) was carried out using a TA Instruments Q2000 equipped with liquid nitrogen cooling. Measurements were performed between 100 and 350 K, under a dry helium purge at 25 mL/min. Samples of approximately 10–15 mg were sealed in hermetic aluminum pans to limit water loss. For annealing experiments, samples were first rapidly cooled at ~20 K/min, then heated at the same rate. Once they reached 115 K, they were further heated to 288 K (annealing temperature) for 4 h. The samples were cooled back to 115 K and heated again to 370 K for a final heating scan. Comparative measurements before and after aging confirmed that no permanent changes occurred due to the annealing procedure.

X-ray powder diffraction (XRD) measurements were carried out on a Philips X'pert PRO automatic diffractometer (Philips, Almelo, The Netherlands) using Cu–Kα radiation (λ = 1.5418 Å) and a θ–θ configuration with a secondary monochromator. The instrument operated at 40 kV and 40 mA using a PIXcel solid-state detector (Philips, Almelo, The Netherlands) that provides an active length of 3.347° in 2θ. A variable divergence slit was employed to maintain a constant illuminated area of 10 mm on the sample surface.

Infrared spectra were collected in ATR mode using a Jasco FT–IR 6300 spectrometer (Jasco Global, Tokyo, Japan) over the range 4000–650 cm^{-1}, with a resolution of 4 cm^{-1} and 200 scans per spectrum. After baseline correction, the spectra were normalized to the area of the band at ~1140 cm^{-1}, assigned to the glycosidic (–C–O–C) vibration of the polygalacturonic acid backbone (see Section S2 in SM).

A Micromeritics ASAP 2420 instrument (Micromeritics Instrument Corporation, Norcross, GA, USA) was used to record the adsorption–desorption isotherms of nitrogen at −196 °C. Prior to nitrogen adsorption measurements, the samples were degassed under nitrogen at 200 °C for 1 h, reaching a pressure below 10^{-4} mbar The specific surface area was calculated using the Brunauer–Emmett–Teller (BET) equation in the relative pressure range p/p_0 of 0.05–0.20. Micropore volume (V_{MI}) was obtained from a DFT analysis assuming cylindrical pores. For comparison, N_2 isotherms at 77 K (see Section S3 in SM) for Fe–BTC indicate a pore diameter of 2.0 nm and a BET surface area of 1366 m^2/g. N_2 adsorption–desorption isotherms and BET surface area analysis were performed only on the Fe–BTC powder. No BET experiments were conducted on the pectin-based films and foams because the limited surface area would require milling of large sample volumes to reach the minimum mass required for reliable measurements, and the degassing temperatures used for N_2 sorption are not compatible with the thermal stability of the pectin matrix.

Equilibrium concentrations of calcium and zinc ions were quantified by inductively coupled plasma-atomic emission spectrometry (ICP-AES; Agilent 5100, Agilent Technologies, Santa Clara, CA, USA). The concentrations of the pharmaceutical compounds were determined by ultraviolet–visible (UV–Vis) spectroscopy (Agilent 8453A), using the absorption maxima at 260 nm for PQ and 356 nm for TC.

3. Results and Discussion

3.1. Characterization of MOF Dispersion

The particle size distribution of Fe–BTC dispersions (1 wt%) was characterized by dynamic light scattering (DLS) to evaluate the effectiveness of the two dispersion meth-

ods. Water-based dispersion yielded an average hydrodynamic diameter (Z-average) of (1171 ± 87) nm with a polydispersity index (PDI) of (0.52 ± 0.46), indicating substantial aggregation of MOF particles and moderate size distribution breadth. In contrast, PVP-assisted dispersion significantly reduced the average particle size to (793 ± 36) nm (32% reduction), demonstrating the effectiveness of PVP as a dispersing agent.

The particle size reduction with PVP can be attributed to steric stabilization mechanisms [46]. PVP macromolecules adsorb onto Fe–BTC particle surfaces through coordination between carbonyl groups of the pyrrolidone ring and exposed Fe^{3+} sites on the MOF surface [46]. The adsorbed PVP chains extend into the aqueous medium, creating a steric barrier that prevents particle–particle contact and subsequent aggregation through van der Waals forces [46]. The increased PDI in PVP-assisted dispersion (0.767 ± 0.139) suggests a broader distribution of particle sizes, likely due to variations in PVP adsorption density on different MOF crystal facets.

Despite the high PDI values (>0.4), which indicate polydisperse systems typical of MOF dispersions without extensive surface modification [47], the PVP-assisted method achieved significantly better dispersion quality.

3.2. Structural Characterization of PE–Ca–MOF Films Using the Water-Dispersed Method

Initially, the calcium content of all composites after crosslinking was determined to ensure the consistent formation of the "egg–box" structure [37] in pectin. It is important to note that, after crosslinking, the samples were washed five times to remove any excess calcium. Table 1 indicates that the Ca^{2+} content is similar across all samples (PE–Ca and PE with different MOF content (PE–MOF). Since all composites were prepared with the same amount of galacturonic acid (5.86 mmol), the resulting stoichiometric ratio, R = $[Ca^{2+}]/[GalA]$, is similar for all composites and meets the requirements of the "egg-box" structure formation [48]. Therefore, the addition of MOF does not interfere with the calcium crosslinking process, in agreement with the finding that pure MOF powder does not adsorb Ca^{2+} ions. Possible release of Fe–BTC particles was evaluated by ICP analysis of the crosslinking solutions and rinsing steps; in all cases the Fe^{3+} concentration was below the instrumental detection limit, indicating that no measurable amount of MOF was released to the liquid phase under the conditions employed.

Table 1. Calcium content (in mg/L and mmol) measured by ICP–AES and calculated stoichiometric ratio (R) for PE–Ca samples with various MOF contents after five washing cycles.

Material	Ca^{2+}_{ads} [mg/L]	Ca^{2+}_{ads} [mmol]	R
PE–Ca	67.5 ± 2.9 [a]	1.69 ± 0.07 [a]	0.29
PE–Ca–1%MOF	67.5 ± 1.6 [a]	1.68 ± 0.04 [a]	0.29
PE–Ca–5%MOF	68.6 ± 2.7 [a]	1.71 ± 0.07 [a]	0.29
PE–Ca–10%MOF	66.2 ± 3.1 [a]	1.65 ± 0.08 [a]	0.28

[a] Values with the same letters in the columns are not significantly different (errors arise from the experimental standard deviation of triplicate measurements).

Figure 1 shows the SEM images of PE–Ca–MOF composites with 1 wt% (a,b), 5 wt% (c,d), and 10 wt% (e,f) of water-dispersed MOF after washing cycles, captured at two magnifications. In the composites, increasing the MOF content results in the formation of larger MOF aggregates within the pectin matrix. EDX elemental mapping for PE–Ca–5%MOF (g–i) shows a uniform distribution of calcium (from the crosslinked matrix) and iron (from the MOF) across the composite surface.

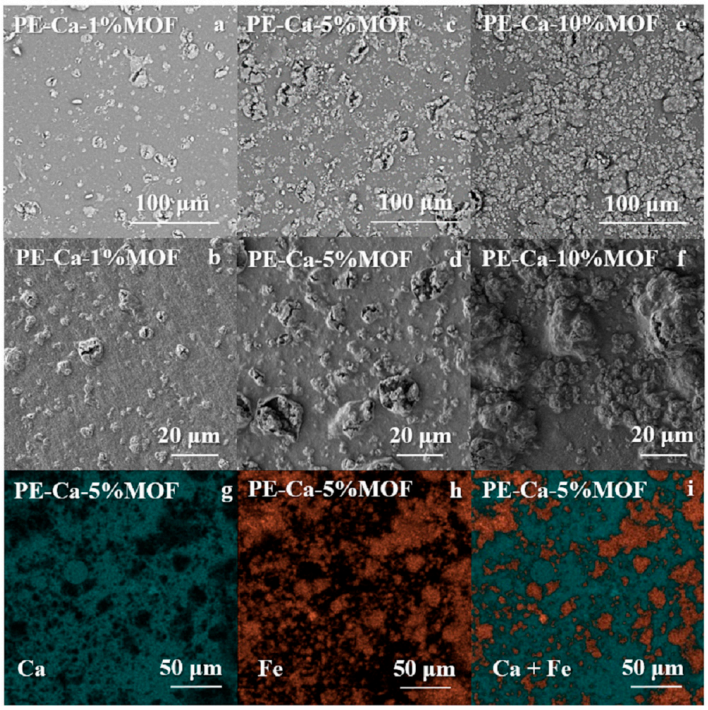

Figure 1. SEM images of (**a**,**b**) PE–Ca–1%MOF, (**c**,**d**) PE–Ca–5%MOF, (**e**,**f**) PE–Ca–10%MOF, and (**g**–**i**) EDAX mapping of PE–Ca–5%MOF.

TGA of PE–Ca and pure MOF (Fe–BTC) reveals distinct degradation patterns (Figure 2a). PE–Ca has four thermal degradation stages [31]: an initial mass loss due to water evaporation below ~400 K, followed by the release of volatile species between 400 and 475 K [24], the decarboxylation of free and calcium-bound carboxyl groups at 475–575 K, and a carbonaceous residue at higher temperatures [49]. In contrast, Fe–BTC exhibits three main events: water desorption (300–400 K), release of pending and unbounded small molecules (400–500 K), and framework collapse (550–600 K). When incorporated into pectin, Fe–BTC shifts to higher temperatures, with a new broad peak appearing around 615 K. This suggests that the pectin matrix stabilizes the MOF structure, thereby improving its thermal resistance. Figure 2b shows the heat flow versus temperature during the heating run at 20 K/min for Fe–BTC, PE–Ca, and pectin composites at different MOF content. As previously discussed, (see Section 2.5), to detect the glass transition of pectin, it is necessary to perform aging experiments (4 h at 288 K) [31]. For Fe–BTC, no glass transition is observed within the measured range. In contrast, the glass transition temperature of the composites grows from 332 K to 336 K with increasing MOF content, indicating increased rigidity and reduced polymer chain mobility, consistent with the observed rise in brittleness at higher MOF contents.

Figure 3a,b shows the infrared spectra of Fe–BTC, PE–Ca, and the composites. Fe–BTC exhibits characteristic vibrational bands associated with the benzene–1,3,5–tricarboxylate (BTC) linkers (~1350–1650 cm^{-1}) and Fe–oxo clusters (~680–780 cm^{-1}) [16]. Strong asymmetric and symmetric O–C–O stretching vibrations, observed between ~1350–1650 cm^{-1}, indicate deprotonated carboxylate groups coordinated to Fe^{3+} centers. Bands at around 1616 cm^{-1}, 1450 cm^{-1} are attributed to carboxylate C=O and aromatic C=C stretching, respectively [17]. A weak band near 1700–1705 cm^{-1} is linked to uncoordinated –COOH groups, while a broad band at ~3300 cm^{-1} corresponds to O–H stretching from residual adsorbed water. PE–Ca shows a broad and intense band for –OH stretching vibrations (3600–3000 cm^{-1}), and peaks around ~1725 cm^{-1} assigned to the C=O stretching of esterified or non-ionized carboxyl groups (–COOH, $–COOCH_3$). Symmetric and asymmetric COO^- stretching vibrations appear near ~1400–1440 cm^{-1} and ~1585–1600 cm^{-1}, respec-

tively [24–26]. The FT–IR spectra of the pectin composites exhibit features from both PE–Ca and Fe–BTC, indicating that the MOF is physically immobilized within the pectin matrix without framework collapse. The characteristic framework bands (~1350–1650 cm^{-1} and ~680–780 cm^{-1}) remain unchanged in the PE–Ca–MOF composites, showing that the phases are physically mixed with negligible interfacial interaction. The retention of these bands from each component suggests structural compatibility and confirms that no significant chemical reactions occurred during composite fabrication. The same conclusions were confirmed also from the XRD patterns of Fe–BTC, PE–Ca, and PE–Ca–5%MOF (see Section S4 in SM).

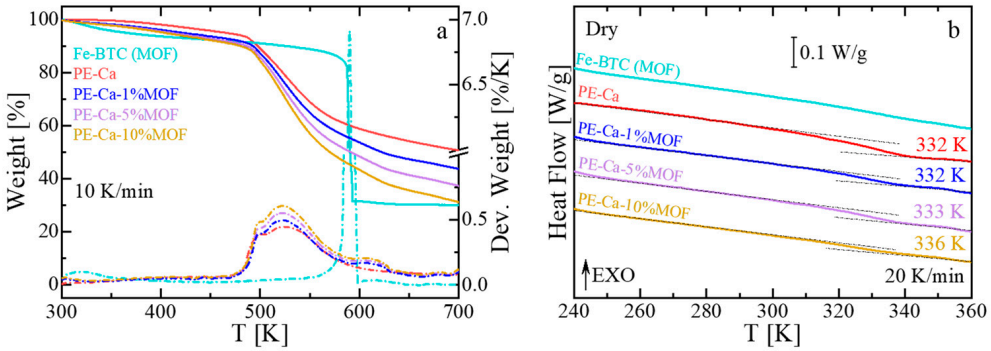

Figure 2. (**a**) Thermogravimetric analysis (TGA, solid line) and derivative weight loss (Deriv. weight, dashed lines) curves of PE–Ca, neat MOF (Fe–BTC), and PE–Ca–MOF water-dispersed composites, recorded at a heating rate of 10 K/min. (**b**) Heat flow as a function of temperature measured by differential scanning calorimetry (DSC) at a heating rate of 20 K/min for dried PE–Ca and PE–Ca–MOF composites after aging. A step change in heat flow indicates the glass transition temperature (T_g). Numbers on each curve indicated T_g, determined as the inflection point. The arrow EXO means that any exothermic event (releasing heat) is shown as an upward peak or curve.

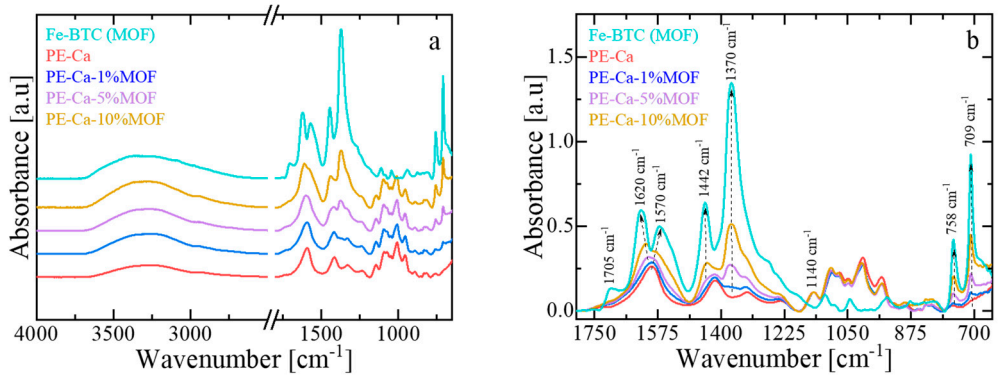

Figure 3. (**a**) FT–IR spectra of PE–Ca and PE–Ca–MOF composites containing water-dispersed Fe–BTC. (**b**) Detailed view of the PE and MOF carboxylate and MOF aromatic bands associated with the BTC linker. All spectra were normalized to the area of the glycosidic ring vibration (~1140 cm^{-1}, –C–O–C) of the polygalacturonic acid backbone. Dashed arrows serve as visual guides to highlight the main spectral changes resulting from the incorporation of Fe–BTC into the pectin matrix.

Figure 4 shows the effect of MOF amount on the swelling behavior of the composites; a higher swelling capacity facilitates the adsorbate diffusion into the matrix, increasing access to active sites and improving adsorption performance. While all composites reached swelling equilibrium within 90 min, increasing the amount of MOF led to reduced swelling, which also introduced brittleness. At 10 wt% of MOF, visible cracks appeared upon drying (see inset in Figure 4).

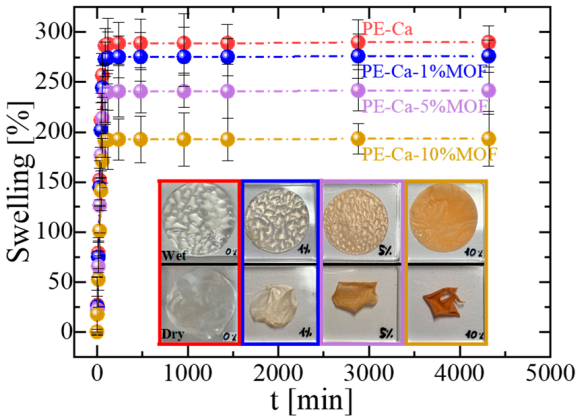

Figure 4. Swelling behavior of PE–Ca and PE–Ca–MOF composites containing water-dispersed Fe–BTC.

3.3. Influence of MOFs on the Adsorption of Heavy Metals

Pectin is widely recognized as an excellent adsorbent for heavy metals [50]. Our goal here was to determine if the composites containing MOFs retain this property by studying the adsorption of zinc ions (Zn^{2+}). To isolate the contributions of each component, we first conducted adsorption experiments using pure MOFs powder, confirming its inactivity to adsorb Zn^{2+} ions. After that, we have investigated whether the presence of immobilized MOF influences the Ca^{2+}/Zn^{2+} ion exchange within the PE matrix. Adsorption experiments with Zn^{2+} were conducted at an initial concentration of 50 mg/L, using a 1 g/L composite dose at pH 7 for 24 h for all adsorbents and compared with the reference PE–Ca (no MOF) (Table 2). As the MOF content increased, no significant differences in adsorption capacity were detected, confirming that the MOFs immobilization does not affect the adsorption properties of the PE–Ca.

Table 2. Zn^{2+} adsorption determined by ICP–AES using a composite dose of 1 g/L and a 50 mg/L of initial Zn^{2+} concentration for 24 h. The table reports the Zn^{2+} adsorption capacity ($q_{24\,h}$) and removal efficiency (R_{eff}) of PE–Ca–MOF composites.

Zn^{2+} Adsorption		
Material	**q_{24h} [mg/g]**	**R_{Eff} [%]**
PE–Ca	31.9 ± 1.9 [a]	63.9 ± 3.9 [a]
PE–Ca–1%MOF	31.8 ± 2.4 [a]	62.4 ± 4.7 [a]
PE–Ca–5%MOF	31.6 ± 2.1 [a]	62.1 ± 4.2 [a]
PE–Ca–10%MOF	32.5 ± 2.9 [a]	63.9 ± 5.6 [a]

[a] Values with the same letters in the columns are not significantly different (errors arise from the experimental standard deviation of triplicate measurements).

This finding is critical, as it allows us to conclude that any heavy metal adsorption detected in the PE–Ca–MOF composites is solely attributable to the pectin matrix. Kinetic analysis of zinc adsorption on PE–Ca and PE–Ca5%MOF, performed with an initial zinc concentration of 50 mg/L and a composite dose of 1 g/L at pH 7, is shown in Figure 5a. The kinetic data are well described by the pseudo-first-order (PFO) model, indicating that Zn^{2+} binding is mainly governed by electrostatic interactions [31,43], with fitting parameters detailed in Table 3. The addition of the MOF slows the adsorption rate, as indicated by the lower k_1 value in PE–Ca–5%MOF compared to PE–Ca. This decreased kinetic rate and longer time to reach equilibrium are likely a result of the reduced swelling of the composite (Figure 4). Furthermore, the q_{eq} value is consistent for both samples, indicating that the presence of Fe–BTC does not affect the adsorption of heavy metals on pectin.

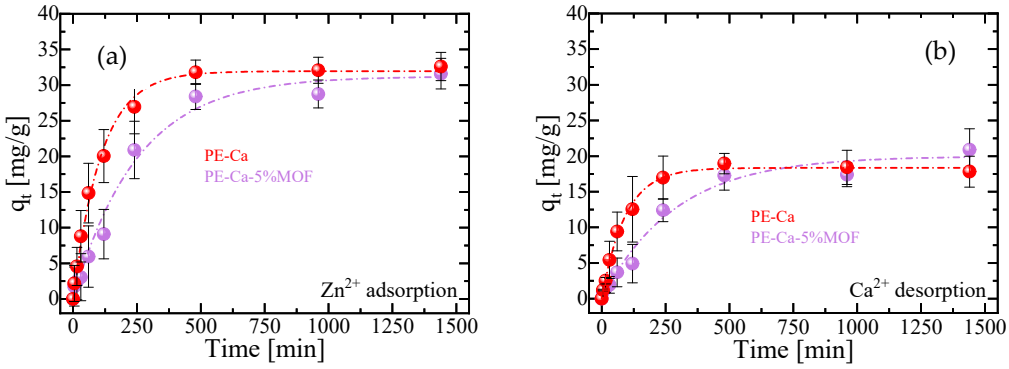

Figure 5. Kinetic profiles at pH = 7 of (**a**) adsorption of Zn^{2+} and (**b**) desorption of Ca^{2+} for PE–Ca and PE–Ca–5%MOF at 25 °C, using a composite dose of 1 g/L (C_0 = 50 mg/L). The fits to the PFO model are represented by dashed lines.

Table 3. Ca^{2+} desorption and Zn^{2+} adsorption kinetics of PE–Ca and PE–Ca–5%MOF films determined by ICP–AES, when experiments are performed at pH = 7, dose of 1 g/L, and an initial Zn^{2+} concentration (C_0) of 50 mg/L. Kinetic data were fitted using the PFO model. The table reports the correlation coefficient (R^2), the kinetic constant (k_1 [min^{-1}]), the equilibrium adsorption capacity (q_e), the removal efficiency (R_E), and the Ca^{2+}/Zn^{2+} exchange ratio.

		Zn^{2+} Adsorption				Ca^{2+} Desorption			
Material	**R^2**	**k_1 Zn^{2+} [min^{-1}]**	**q_e Zn^{2+} [mg/g]**	**Zn^{2+} [mmol]**	**R_{Eff} [%]**	**k_1 Ca^{2+} [min^{-1}]**	**q_e Ca^{2+} [mg/g]**	**Ca^{2+} [mmol]**	**Exchange Ratio**
PE–Ca	0.99	0.0091 ± 0.0005 [a]	31.9 ± 0.6 [a]	0.48 ± 0.01 [a]	63.8 ± 1.2 [a]	0.0109 ± 0.0006 [a]	18.4 ± 0.3 [a]	0.46 ± 0.01 [a]	1.04 ± 0.03 [a]
PE–Ca–5%MOF	0.99	0.0040 ± 0.0004 [b]	31.2 ± 1.2 [a]	0.48 ± 0.02 [a]	62.4 ± 2.4 [a]	0.0035 ± 0.0005 [b]	19.9 ± 0.9 [b]	0.49 ± 0.02 [a]	0.98 ± 0.06 [a]

[a,b] Values with the same letters in the columns are not significantly different (errors correspond to the uncertainties obtained from the model fits; $p > 0.01$).

To confirm the underlying adsorption mechanism, the kinetics of calcium desorption were simultaneously measured with the zinc uptake, as shown in Figure 5b. The Ca^{2+}/Zn^{2+} exchange ratio was close to 1 in all cases (see Table 3). This demonstrates that the adsorption mechanism remains an ion exchange process; however, the presence of the MOF in the composite noticeably slows the kinetics of this process, which is attributable to its reduced swelling capacity relative to the reference PE–Ca (Figure 4). Since Zn^{2+} is also able to crosslink low-methoxyl pectin, the Ca^{2+}-to-Zn^{2+} ion exchange during adsorption is expected to convert Ca–pectin junctions into Zn–pectin junctions rather than decrosslinking the network, consistent with the preserved macroscopic integrity of the films after Zn^{2+} uptake [31]. Finally, ICP measurements of the equilibrium solutions did not detect iron, confirming that the MOF particles are not released into the aqueous phase under these conditions.

In these composites, the degree of swelling decreases as the MOF content increases (Figure 4), consistent with the more rigid character of the network at higher Fe–BTC loadings, which increase T_g (Figure 2b). Adsorption then proceeds more slowly than swelling because, beyond simple water uptake, the contaminants must diffuse through the hydrated network, locate specific active sites, and interact with the corresponding functional groups, which requires at least partial disruption of their hydration shells. At short contact times, when swelling is still limited, the pores remain more constricted and partially hinder access of Zn^{2+} and other molecules to the internal adsorption sites, whereas once the material is fully swollen and the network is more open, the adsorption process is markedly enhanced. Under these conditions, adsorption equilibrium is reached after ap–proximately 6–8 h, reflecting the additional diffusive and interfacial steps involved compared with pure hydration.

3.4. Effect of MOFs Content on the Adsorption of Pharmaceuticals and Pesticides

To evaluate the potential of the composite material, we tested its adsorption capacity for a range of contaminants at pH 7. It is important to note that PE–Ca films (no MOF) can adsorb divalent and trivalent heavy metals as well as zwitterionic and mixed positively charged and neutral molecules, including atenolol (ATE), metformin (MTF), and metoprolol (MET) [51]. However, PE–Ca films are ineffective against tetracycline (TC) or paraquat (PQ), due to their poor compatibility with the pectin network. Consistent with previous reports [52], strongly positively charged molecules such as PQ can show negligible adsorption on PE–Ca, because the tightly bound hydration shell around the cationic adsorption sites makes dehydration and approach to the carboxylate sites energetically unfavorable; analogous behavior has been observed for other highly hydrated cationic species. In contrast, Fe–BTC MOF in powder form is highly effective in removing these contaminants (removal efficiency > 90%) (See Section S5 in SM) [18] because of its porous aromatic structure, which allows multiple non-covalent interactions, including electrostatic and π–π stacking attraction [13,18,19]. Figure 6a,b show the adsorption capacity and removal efficiency of ATE, MET, MFT, PQ, and TC at an initial concentration of 10 mg/L, using a 1 g/L composite dose at pH 7 for 24 h. As expected, the PE–Ca film showed no adsorption of PQ or TC after 24 h. However, the addition of Fe–BTC significantly improves the adsorption performance for all the contaminants (except for Zn, whose adsorption results are similar and independent of Fe–BTC content, as previously discussed in Section 3.2). While the best results are observed for the pectin filled with 10 wt% MOF, this sample has large aggregates and is very brittle, making it unsuitable for water remediation. Consequently, the sample with 5 wt% MOF content was selected for further studies on isotherms, kinetics, and reusability. In the adsorption experiments with organic contaminants, the supernatants were additionally monitored by UV–Vis spectroscopy, and no Fe–related bands or spectral shifts attributable to Fe–contaminant complexes were observed, further confirming that the Fe–BTC phase remained effectively immobilized within the pectin matrix during operation (see Section S6 in SM). The same conclusion was reached for the reusability tests after mild acidic regeneration over multiple cycles (Section 3.7).

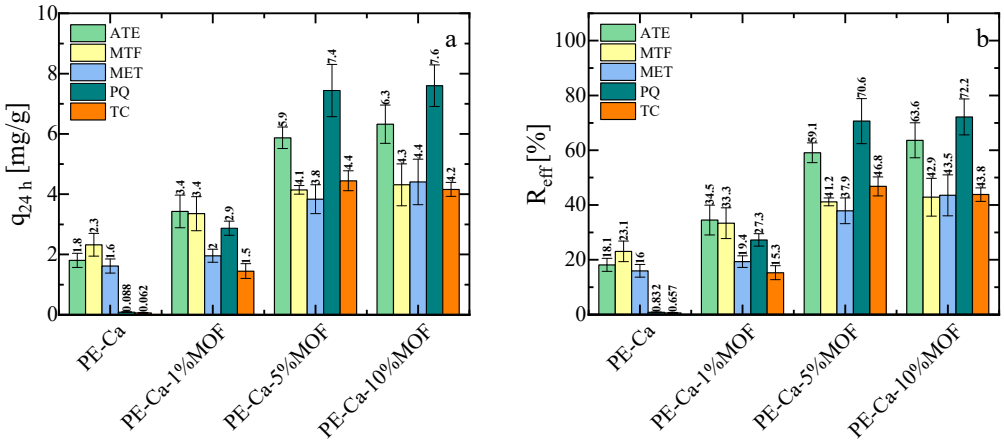

Figure 6. (**a**) Adsorption capacity and (**b**) removal efficiency of PE–Ca and PE–Ca composites with water-dispersed Fe–BTC after 24 h at an initial concentration of 10 mg/L, at a composite dose of 1 g/L and at pH 7.

3.5. Kinetics and Isotherms of Adsorption of Paraquat and Tetracycline on PE–Ca–5%MOF

Figure 7a,b show the adsorption isotherms and kinetics profiles for both contaminants. Although a total composite dose of 1 g/L was used, the calculated adsorption capacities were normalized by the mass of the active sites in the PE–Ca–5%MOF composite. This was possible because the PE–Ca matrix is not able to adsorb the PQ and TC (Figure 6). The

UV–Vis spectra of PQ and TC stock solutions, respectively, used for adsorption isotherms analysis (initial concentration of 5, 10, 25, 50 and 75 mg/L) are reported in the Section S5 in SM. The isotherms data (Figure 7a) were best described by the Langmuir model [44,53], which assumes that adsorption at identical sites with a monolayer coverage (only one molecule can be adsorbed at each active site); the fitting results for both models are reported in Table 4.

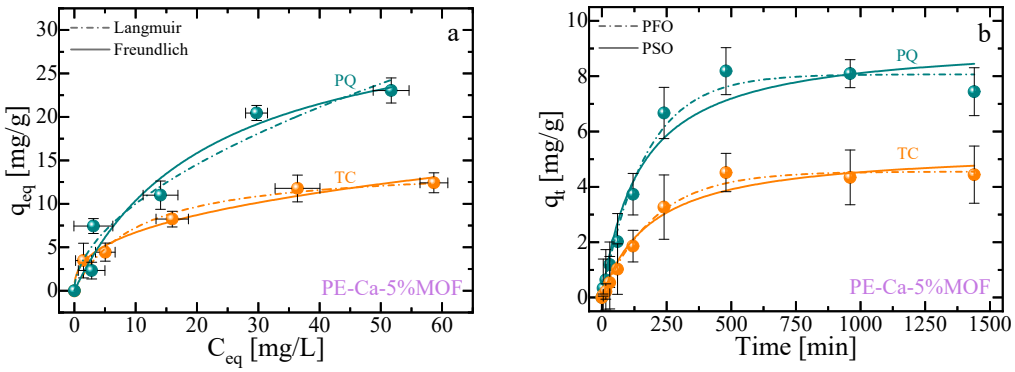

Figure 7. Adsorption isotherms (**a**) and adsorption kinetics (**b**) for paraquat (PQ) and tetracycline (TC) for PE–Ca–5%MOF at a composite dose of 1 g/L and pH 7. Isotherms performed at an initial concentration ranging from 5 to 75 mg/L and fitted using the Langmuir (dashed lines) and Freundlich (solid lines) models. Kinetics performed at an initial concentration of 10 mg/L and fitted using the PFO (dashed lines) and PSO (solid lines) models.

Table 4. Statistical adsorption isotherms fitting results for paraquat (PQ) and tetracycline (TC).

Adsorption Isotherms								
	Langmuir				Freundlich			
Pollutant	R^2	χ^2	q_m [mg/g]	K_L [L/mg]	R^2	χ^2	K_F [$L^{1/n}mg^{1-1/n}g^{-1}$]	$1/n$
PQ	0.95	4.8	33.5 ± 6.9 [a]	0.05 ± 0.02 [a]	0.91	6.8	2.9 ± 1.2 [a]	0.5 ± 0.1 [a]
TC	0.97	0.6	14.5 ± 1.3 [b]	0.10 ± 0.03 [a]	0.96	0.8	2.8 ± 0.5 [a]	0.37 ± 0.05 [a]

[a,b] Values with the same letters in the columns are not significantly different (errors correspond to the uncertainties obtained from the model fits; $p > 0.01$).

Figure 7b shows the adsorption kinetics of PQ and TC as a function of time (initial concentration of 10 mg/L, pH 7). Both contaminants are better fitted with a pseudo-first-order (PFO) kinetics model, indicating that Van der Waals interactions play a significant role in the adsorption mechanism. Notably, PQ was adsorbed more rapidly than TC, likely due to its structure allowing for more efficient π−π stacking interaction. The statistical fitting results for both the isotherms and kinetics studies are summarized in Tables 4 and 5, respectively.

Table 5. Statistical adsorption kinetics fitting results for paraquat (PQ) and tetracycline (TC).

Adsorption Kinetics								
	PFO				PSO			
Pollutant	R^2	χ^2	q_m [mg/g]	k_1 [min^{-1}]	R^2	χ^2	q_m [mg/g]	K_2 [min^{-1}]
PQ	0.99	0.2	8.1 ± 0.3 [a]	0.0059 ± 0.0006 [a]	0.96	0.5	9.3 ± 0.7 [a]	0.00073 ± 0.00023 [a]
TC	0.99	0.03	4.6 ± 0.1 [b]	0.0049 ± 0.0004 [a]	0.97	0.1	5.4 ± 0.4 [b]	0.00098 ± 0.00027 [a]

[a,b] Values with the same letters in the columns are not significantly different (errors correspond to the uncertainties obtained from the model fits; $p > 0.01$).

3.6. Interaction Mechanism

The interaction between the adsorbent and PQ/TC was investigated using Fourier transform infrared (FT-IR) spectroscopy. As shown in Figure 8a, Fe–BTC keeps its structural integrity after adsorption, as its characteristic vibrational bands of the BTC linker remain visible (carboxylate stretches (~1350–1650 cm^{-1}) and Fe–oxo bridge (~680–780 cm^{-1}). The presence of N–H and C–H shoulders in the 2800–3000 cm^{-1} region, together with a broadening of the O–H band near 3300 cm^{-1}, is consistent with the formation of hydrogen bonds between the contaminants and the material, and is more pronounced for TC due to its additional hydroxyl and amide groups [20]. Adsorption of both TC and PQ also leads to changes in the free C=O stretching band near ~1700 cm^{-1} (Figure 8b) and to slight shifts in the carboxylate region (1350–1650 cm^{-1}), suggesting partial deprotonation and coordination with unsaturated Fe^{3+} sites, forming Fe–OOC–TC/PQ linkages [17,54]. Subtle modifications in the ~680–780 cm^{-1} region are compatible with additional electrostatic and polar interactions between PQ or TC and Fe–oxo bridges (Figure 8c). Moreover, PQ and TC may interact through π–π stacking between their aromatic rings and the BTC linker [54], accompanied by band shifts and the appearance of a shoulder around 700 cm^{-1} that is compatible with the formation of π donor–acceptor complexes [17]. Overall, the observed shifts and broadenings of the Fe–BTC bands (Figure 8c) are consistent with effective adsorption of both contaminants through non-covalent interactions. Within this picture, TC appears to interact predominantly via coordination to Fe^{3+}, hydrogen bonding and π–π stacking [55], whereas PQ seems to interact mainly through π–π donor–acceptor interactions with the BTC linker together with weaker electrostatic contributions [17].

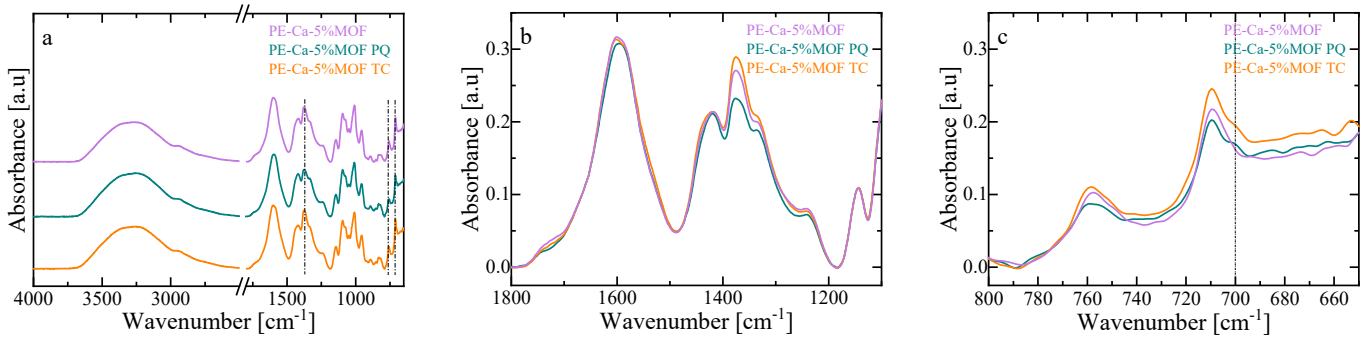

Figure 8. FT–IR spectra of Fe–BTC before and after adsorption of paraquat (PQ) and tetracycline (TC): (**a**) full spectral range, (**b**) carboxylate, and (**c**) aromatic regions (~750–1650 cm^{-1}). The black dashed line indicates the wavenumber 700 cm^{-1}.

3.7. Reusability of PE–Ca–5%MOF

Figure 9a,b show the results over five adsorption–desorption cycles for PE–Ca5%MOF with both pollutants, PQ and TC. The results indicate that the adsorbent can be reused after desorption with no significant decrease in performance, demonstrating its suitability for industrial uses. An acidic solvent was chosen as a desorption medium because this method is inexpensive, quick, and environmentally friendly.

The results showed that the composite performed significantly better for PQ compared to TC after the first adsorption–desorption cycle, indicating a stronger interaction between TC and the active sites of the composites. Conversely, PQ adsorption–desorption showed no significant changes during the cycles, confirming a weakly bound interaction that facilitates its release under acidic conditions. However, TC, likely due to its heavier and more complex structure and additional functional group interactions, is less desorbed under the same conditions.

As shown in Figure 9c, PQ retains (87.9 ± 4.3) % of its initial capacity, whereas TC declines to (81.1 ± 3.5) % by the fifth cycle, suggesting partial occupation of irreversible

sites after desorption. Overall, PE–Ca–5%MOF demonstrates better reusability for PQ than for TC under the tested conditions. The retention rate was defined as the ratio between the adsorption capacity in cycle n and that of the first cycle for the PE–Ca–5%MOF composite, with PE–Ca acting only as a structural blank (it shows negligible uptake and is not an active adsorbent for the studied contaminants), so that the reported values should be interpreted as apparent capacity retention under the specific adsorption–desorption protocol rather than as full proof of long-term regenerability. In addition, Fe-leaching data obtained by ICP and UV–Vis show no detectable iron release during adsorption–desorption, supporting the effective immobilization of the Fe–BTC phase in the pectin matrix under the conditions used.

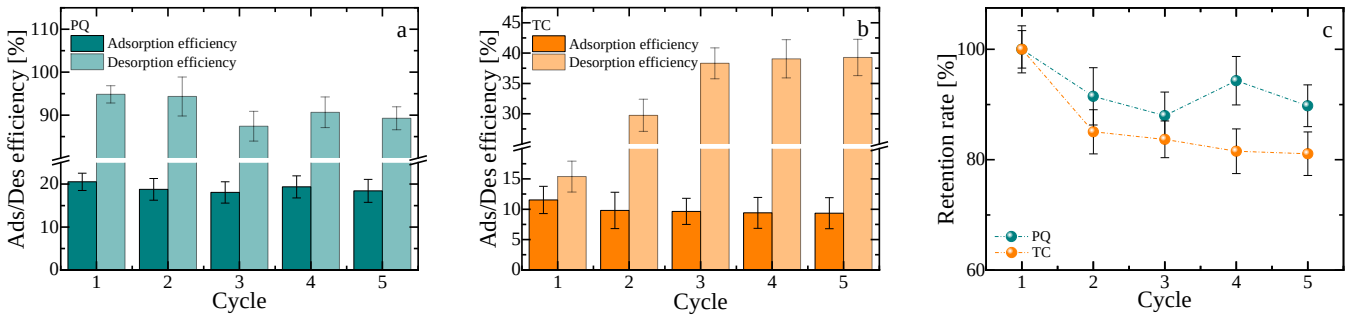

Figure 9. Adsorption–desorption efficiency of (**a**) paraquat (PQ) and (**b**) tetracycline (TC) over five consecutive cycles for PE–Ca–5%MOF. Reusability tests were performed with a fixed contact time of 1 h for both adsorption and desorption steps, using an initial adsorbate concentration of 10 mg/L, a composite dose of 1 g/L, and pH 7 for all cycles. (**c**) Retention rate of PQ and TC over the five reusability cycles.

3.8. Structural Characterization of PE–Ca–MOF Film and Foam Using the PVP–Dispersed Method

While incorporating MOFs into a pectin matrix significantly enhances the capacity of the adsorbent, the current approach results in poor dispersion of the MOF, as illustrated in Figure 1. This inadequate dispersion is problematic because it prevents the composite from realizing its full potential. When MOF particles agglomerate, their surface area for interaction decreases, thereby reducing the number of active sites necessary for adsorption. Consequently, enhancing dispersion is essential to boost adsorption performance. Several strategies can be employed to improve dispersion, such as surface modification of the MOF particles, using high-shear mixing during the composite fabrication, or enhancing MOF dispersion with surfactants that adsorb onto the surface of the particles and create a steric hindrance that prevents agglomeration [46]. Additionally, these approaches can help lower the MOF concentration, reducing the final cost of the adsorbent.

We explored two different strategies to improve the dispersion of MOF. In the first approach, we have used polyvinylpyrrolidone (PVP) as a surfactant, which prevents MOF from agglomerating (PE–Ca–1%MOF–PVP film) [46]. For the second strategy, apart from adding the PVP, the shape of the pectin matrix was modified by forming a highly porous structure (foam) through freeze-drying, which increased the surface area of the material, allowing for better exposure to contaminated water (PE–Ca–1%MOF–PVP foam). ICP–AES results indicate that neither the dispersion method nor the composite morphology significantly affects calcium adsorption during crosslinking or zinc adsorption during removal.

As shown in Figure 10, the structural characteristics of the samples containing a surfactant (PE–Ca–1%MOF–PVP film) and after freeze-drying (PE–Ca–1%MOF–PVP foam) were compared to the water-dispersed (PE–Ca–1%MOF) and pure dry PVP control samples. Infrared spectroscopy (Figure 10a) revealed no changes in the characteristic bands of either

the MOF or the pectin after adding PVP or forming the foam, indicating that the chemical structures of all components remain unchanged after improving the dispersion of Fe–BTC. The FT–IR spectra of the rinsed composites do not show the characteristic bands of PVP, indicating that PVP is largely removed during the washing steps, and that any direct contribution of PVP to the adsorption performance of the final composites is negligible.

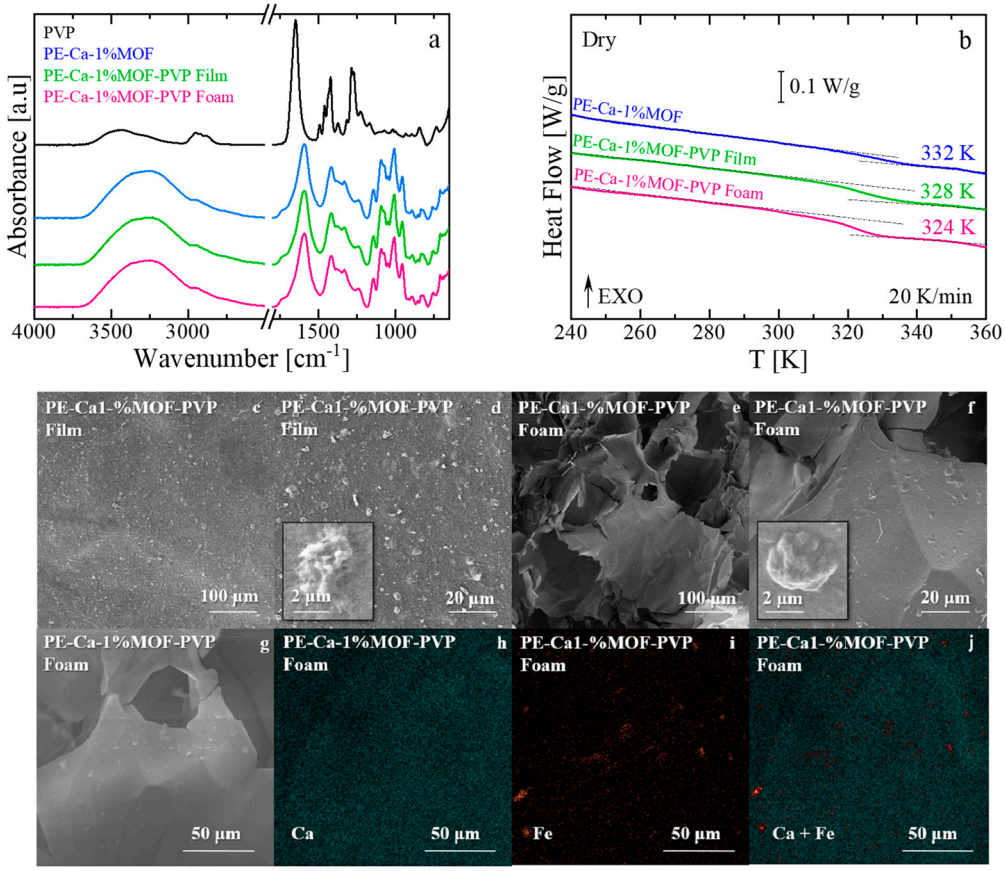

Figure 10. (**a**) Infrared spectra and (**b**) Heat flow versus temperature after thermal aging of PE–Ca–1%MOF (water-dispersed), PE–Ca–1%MOF–PVP film, and PE–Ca–1%MOF–PVP foam. The T_g is marked in the figure. The arrow EXO means that any exothermic event (releasing heat) is shown as an upward peak or curve. (**c**–**f**) SEM images of PVP–assisted 1 wt% MOF dispersion in film (**c**,**d**) and foam (**e**,**f**). (**g**–**j**) EDAX elemental mapping of calcium and iron for the corresponding foam samples.

DSC analysis nevertheless reveals a marked decrease in T_g for PE–Ca–1%MOF–PVP relative to the water dispersed PE–Ca–1%MOF control (Figure 10b), which we attribute to the transient porogen-like action of PVP during processing; when the PVP–MOF solution is mixed with the pectin prior to crosslinking and rinsing, (Section 2.2), PVP temporarily plasticizes the pectin network, improves MOF dispersion, and promotes the formation of pores and voids, thereby increasing the free volume. This effect is further amplified in the foam sample, which exhibits a larger T_g decrease due to the formation of pores and voids within its structure, thereby increasing the free volume between polymer chains [56,57]. After crosslinking and washing, the reduced T_g is thus attributed to this porogen-mediated increase in free volume rather than to the presence of PVP as a retained plasticizer in the final composite.

The structural difference between the sample made with the surfactant and those made in a foam shape is evident in the SEM images shown in Figure 10c–f. Compared to the film (Figure 10a,b), the foam architecture (Figure 10c,d) exhibits a significantly larger active area due to its high porosity. Furthermore, adding the surfactant creates a more homogeneous dispersion of the MOF solution (also confirmed by DLS measurements, see Section 3.1), in

line with better particle distribution in both architectures (film and foam) compared to the water-dispersed method used to make the film shown in Figure 1. The corresponding EDX maps (Figure 10g–j) further suggest this improvement by showing a more even distribution of calcium and iron throughout the pectin matrix, with smaller and thinner aggregates compared to the larger clusters seen in water-dispersed composites (Figure 1). The SEM and EDX images should be regarded as representative examples that point to an improvement in Fe–BTC dispersion in the PVP assisted samples, rather than as proof of a perfectly uniform distribution. These techniques provide local, mainly qualitative information and do not yield a full statistical mapping of particle positions. When considered together with the DLS data, however, they support an overall improvement in MOF dispersion in the presence of PVP.

The adsorption capacity and removal efficiency of the PVP-assisted film and foam containing 1 wt% of MOF were compared with those of the water-dispersed control sample (PE–Ca–1%MOF) for PQ (Figure 11a) and TC (Figure 11b), respectively. These experiments were conducted at an initial concentration of 10 mg/L, with a composite dose of 1 g/L, over 24 h at pH 7. The PVP-assisted film and foam, due to its better distribution of smaller MOF particles and porous structure with larger surface area, performed better than the water-dispersed samples (PE–Ca–1%MOF) (see Section S6 in SM for UV–Vis spectra for comparison of composites with 1 wt% and 5 wt% water dispersed MOF and PVP-dispersed films and foams with 1 wt% of MOF). Since TC is a larger and heavier molecule, the foam structure allows easier access to the MOF particles, resulting in higher adsorption performance. These findings demonstrate that using PVP as a dispersant agent enables the use of less MOF quantity in the composite improving the adsorption performance. The PVP-assisted foam shows the highest adsorption performance in comparative batch tests (Figure 11); however, detailed isotherm and kinetic analyses are still needed to fully validate the mechanistic interpretation established for the water-dispersed composites.

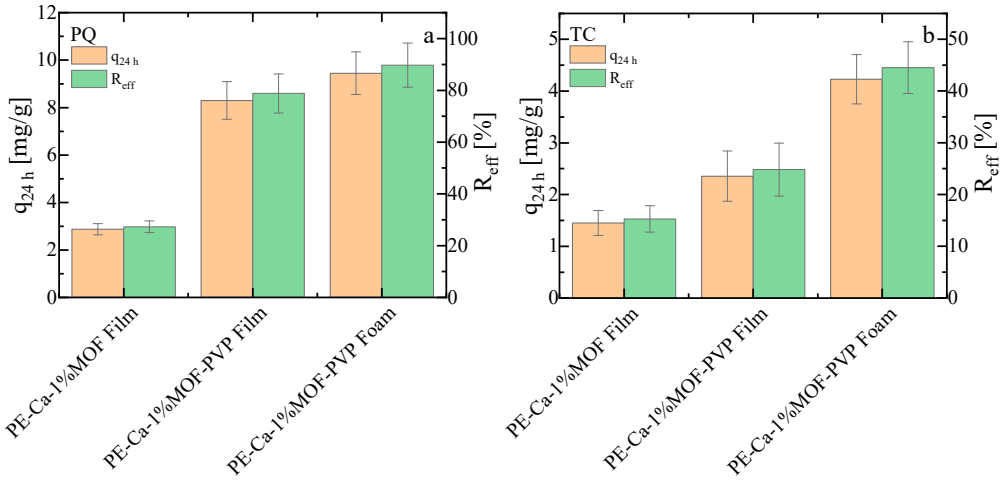

Figure 11. Adsorption capacity and removal efficiency of (**a**) paraquat (PQ) and (**b**) tetracycline (TC) for PE–Ca composites prepared with 1 wt% of MOF loading and dispersion methods (water or PVP-assisted, in film and foam geometries). Tests were conducted at an initial concentration of 10 mg/L, composite dose of 1 g/L, and contact time of 24 h at pH 7.

At realistic pollutant concentrations (1 mg/L of Zn^{2+}, PQ, and TC each), simultaneous treatment leads to essentially quantitative removal, reaching efficiencies of 100 ± 1% within a few minutes.

Because the present adsorbent is a pectin-supported MOF composite, while most of the literature capacities are reported for neat powders under different loadings, direct quantitative comparison of q per gram of material is not straightforward; therefore, we limit

our analysis to the raw experimental capacities per gram of composite and to a qualitative discussion of how these values relate to typical MOF powders.

4. Conclusions

This study successfully developed and characterized sustainable, bio-based adsorbents by integrating the metal-organic framework Fe–BTC MOF within a calcium-crosslinked pectin matrix, systematically demonstrating the critical roles of fabrication parameters in enhancing water purification performance. Optimal dispersion, achieved through a poly(vinylpyrrolidone) (PVP-assisted method), significantly reduced MOF particle aggregation, leading to a better distribution within the polymer and a notable improvement in overall adsorption capacity. Furthermore, the geometry of the materials was shown to be a key determinant of performance, with freeze-dried foams exhibiting superior porosity and faster adsorption kinetics compared to solvent-cast films. Freeze-dried foams exhibited higher porosity and higher adsorption capacity compared to solvent-cast films due to enhanced mass transfer through interconnected porous networks and improved accessibility of active sites.

The water-dispersed PE–Ca–MOF films exhibit higher equilibrium capacities than PE–Ca but a lower pseudo-first-order rate constant, in line with their reduced swelling and increased rigidity, which slows contaminant transport to the active sites. The PVP-assisted foam shows the highest uptake in comparative batch experiments, likely due to its open-cell structure and shorter diffusion paths; however, a complete kinetic analysis analogous to that performed for the water-dispersed films remains to be carried out to characterize its adsorption rates quantitatively.

This finding provides design principles for optimizing adsorbent geometry based on application requirements (e.g., batch vs. flow-through systems). The resultant pectin-MOF composite demonstrated versatile and effective removal of a range of water contaminants, including a heavy metal (Zn^{2+}), a pesticide (paraquat), and an antibiotic (tetracycline). This broad-spectrum efficiency is attributed to the complementary binding mechanisms resulting from the synergy between the pectin carboxyl groups and the coordination sites of the MOF. Analyses revealed that the adsorption process is best described by diffusion-controlled pseudo-first-order kinetics and fits the Langmuir isotherm model, confirming indicating favorable and largely homogeneous adsorption. Importantly, the composites exhibited good practical reusability, maintaining high capacity over multiple cycles when regenerated using a bio-based 2% v/v acetic acid solution, thus confirming their structural stability and viability for repeated environmental applications.

Finally, although the exact MOF loading in the final composites was not independently quantified by acid digestion, multiple independent observations support effective retention of the Fe–BTC phase within the pectin matrix: the absence of detectable Fe^{3+} in all aqueous phases (ICP), the co–localization of iron with MOF-containing regions in EDX mapping, and the systematic increase in adsorption capacity with nominal MOF loading. Consequently, all reported adsorption capacities are expressed per gram of composite material and do not depend on assumptions about the exact MOF content. All experiments were conducted at neutral pH (pH 7) using ultrapure water and single contaminants; the pH-dependent behavior of these contaminants and the effects of competing ions or natural organic matter typical of real-world water matrices remain to be investigated in future work.

Supplementary Materials: The following supporting information can be downloaded at: https://www.mdpi.com/article/10.3390/polym18020171/s1, Table S1: Statistical parameters for the PFO model fits in Figure 5 for Zn2+ adsorption and Ca2+ desorption; Table S2: Statistical parameters for the Langmuir and Freundlich isotherms fit in Figure 7 for PQ and TC adsorption; Table S3: Statistical parameters for the PFO and PSO kinetics fit in Figure 7 for PQ and TC adsorption; Table S4: Akaike Information

Criterion (AIC) and Bayesian Information Criterion (BIC) values for the isotherm and kinetics fits shown in Figure 7 for both PQ and TC contaminants. Lower AIC/BIC values indicate the preferred model; Table S5: Statistical parameters of the calibration curves used for quantification of paraquat (PQ) and tetracycline (TC); Figure S1: FT–IR baseline correction and normalization; Figure S2: N2 adsorption isotherms at −196 °C on commercial MOF Basolite F300® (Fe–BTC); Figure S3: XRD patterns of pure Fe–BTC, PE–Ca, and PE–Ca–5%MOF composite. The inset highlights the diffraction region between 5 ° and 20 °, showing the combined structural features of the MOF and the polymer matrix; Figure S4: Removal efficiency pure Fe–BTC (MOF) powder after 24 h at an initial concentration of 10 mg/L, at a composite dose of 1 g/L and at pH 7; Figure S5: UV–Vis spectra of (a) paraquat (PQ) and (b) tetracycline (TC) at initial concentrations ranging from 5 to 75 mg/L before (solid lines) and after 24 h of adsorption by PE–Ca–5%MOF (dashed lines) at a composite dose of 1 g/L and pH 7. Insets show the calibration curves constructed from the maximum absorbance values at 260 nm for PQ and 356 nm for TC; Figure S6: UV–Vis spectra of (a) paraquat (PQ) and (b) tetracycline (TC) at an initial concentration of 10 mg/L after 24 h of adsorption (composite dose: 1 g/L, pH 7) by PE–Ca composites containing 1 wt% and 5 wt% Fe–BTC (water-dispersed) and 1 wt% Fe–BTC (PVP-assisted) in film and foam geometries. Reference [58] is cited in Supplementary Materials.

Author Contributions: F.C. and C.I. investigation; F.C. validation, visualization, methodology, formal analysis, data curation, writing—original draft preparation; S.C. conceptualization, supervision, writing—review and editing, funding acquisition. All authors have read and agreed to the published version of the manuscript.

Funding: This research was funded by grant PID2023–146348NB–I00 funded by Ministerio de Ciencia, Innovación y Universidades/Agencia Estatal de Investigación (MCIN/AEI) and Department of Education of the Basque Government under grant PIBA_2024_1_0011 and IT-1820-26.

Institutional Review Board Statement: Not applicable.

Data Availability Statement: The original contributions presented in this study are included in the article/Supplementary Material. Further inquiries can be directed to the corresponding authors.

Acknowledgments: The authors thank for technical support provided by Aitor Larrañaga and Juan Carlos Raposo from SGIker (UPV/EHU/ERDF, EU). We thank Evgeni Modin for his assistance during the SEM/EDAX measurements and Herbstreith & Fox for kindly supplying pectin.

Conflicts of Interest: Author Francesco Coin, Carolina Iacovone and Silvina Cerveny statement: The company (Herbstreith & Fox), which was mentioned in the acknowledgments, had no role in the design of the study; in the collection, analyses, or interpretation of data; in the writing of the manuscript, and in the decision to publish the results.

References

1. Coin, F.; Rodríguez-Ramírez, C.A.; Oyarbide, F.S.; Picón, D.; Goyanes, S.; Cerveny, S. Efficient Antibiotic Removal from Water Using Europium-Doped Poly(Vinyl Alcohol) Nanofiber Mats Esterified with Citric Acid. *J. Water Process. Eng.* **2024**, *63*, 105447. [CrossRef]
2. Rodríguez-Ramírez, C.A.; Coin, F.; Vergara-Rubio, A.; Picón, D.; Cerveny, S.; Goyanes, S. Enhanced Tetracycline Removal through "in Situ" Europium Incorporation in Poly (Vinyl Alcohol) (PVA) Electrospun Mats: Advantages of This Strategy in Adsorption and Reuse over Doping. *Chemosphere* **2025**, *372*, 144102. [CrossRef] [PubMed]
3. Santos, A.C.; Coin, F.; Cerveny, S.; Marzocca, A.J.; Goyanes, S.N. Beyond the Surface Area: The Effect of Electrospinning versus Casting on Molecular Packing and Its Impact on the Production of Efficient PVA-Pectin-Fe Adsorbents. *Int. J. Biol. Macromol.* **2025**, *332*, 148565. [CrossRef] [PubMed]
4. T.C., P.; Sharma, S.K.; Kennedy, M. Nanoparticles in Household Level Water Treatment: An Overview. *Sep. Purif. Technol.* **2018**, *199*, 260–270. [CrossRef]
5. Das, R. *Carbon Nanotubes for Clean Water*; Springer: Berlin/Heidelberg, Germany, 2018; ISBN 3319956027.
6. Zeghioud, H.; Fryda, L.; Djelal, H.; Assadi, A.; Kane, A. A Comprehensive Review of Biochar in Removal of Organic Pollutants from Wastewater: Characterization, Toxicity, Activation/Functionalization and Influencing Treatment Factors. *J. Water Process. Eng.* **2022**, *47*, 102801. [CrossRef]
7. Vieira, Y.; Netto, M.S.; Lima, É.C.; Anastopoulos, I.; Oliveira, M.L.S.; Dotto, G.L. An Overview of Geological Originated Materials as a Trend for Adsorption in Wastewater Treatment. *Geosci. Front.* **2022**, *13*, 101150. [CrossRef]

8. Liu, X.; Shan, Y.; Zhang, S.; Kong, Q.; Pang, H. Application of Metal Organic Framework in Wastewater Treatment. *Green Energy Environ.* **2023**, *8*, 698–721. [CrossRef]
9. Singh, S.; Sivaram, N.; Nath, B.; Khan, N.A.; Singh, J.; Ramamurthy, P.C. Metal Organic Frameworks for Wastewater Treatment, Renewable Energy and Circular Economy Contributions. *NPJ Clean Water* **2024**, *7*, 124. [CrossRef]
10. Nazir, M.A.; Ullah, S.; Shahid, M.U.; Hossain, I.; Najam, T.; Ismail, M.A.; Rehman, A.U.; Karim, M.R.; Shah, S.S.A. Zeolitic Imidazolate Frameworks (ZIF-8 & ZIF-67): Synthesis and Application for Wastewater Treatment. *Sep. Purif. Technol.* **2025**, *356*, 129828. [CrossRef]
11. Liu, X.; Wang, X.; Kapteijn, F. Water and Metal-Organic Frameworks: From Interaction toward Utilization. *Chem. Rev.* **2020**, *120*, 8303–8377. [CrossRef]
12. El-Sewify, I.M.; Ma, S. Recent Development of Metal-Organic Frameworks for Water Purification. *Langmuir* **2024**, *40*, 5060–5076. [CrossRef] [PubMed]
13. Yang, F.; Du, M.; Yin, K.; Qiu, Z.; Zhao, J.; Liu, C.; Zhang, G.; Gao, Y.; Pang, H. Applications of Metal-Organic Frameworks in Water Treatment: A Review. *Small* **2022**, *18*, 2105715. [CrossRef]
14. Chu, H.; Wang, C.-C. Metal-Organic Frameworks Meet Synthetic Polymers for Water Decontamination: A Critical Review. *Chem. Eng. J.* **2023**, *476*, 146684. [CrossRef]
15. Fang, Y.; Yang, Z.; Li, H.; Liu, X. MIL-100(Fe) and Its Derivatives: From Synthesis to Application for Wastewater Decontamination. *Environ. Sci. Pollut. Res.* **2020**, *27*, 4703–4724. [CrossRef] [PubMed]
16. Santos, V.P.; Wezendonk, T.A.; Jaén, J.J.D.; Dugulan, A.I.; Nasalevich, M.A.; Islam, H.-U.; Chojecki, A.; Sartipi, S.; Sun, X.; Hakeem, A.A.; et al. Metal Organic Framework-Mediated Synthesis of Highly Active and Stable Fischer-Tropsch Catalysts. *Nat. Commun.* **2015**, *6*, 6451. [CrossRef]
17. Shizari, P.N.; Kamran-Pirzaman, A.; Kiadehi, A.D.; Abedini, H. Paraquat Herbicide Removal from Aqueous Medium Using ZIF-8 and Fe-BTC Adsorbents: A Comparative Study. *Sep. Purif. Technol.* **2025**, *363*, 132285. [CrossRef]
18. Azizi Vahed, T.; Naimi-Jamal, M.R.; Panahi, L. (Fe)MIL-100-Met@alginate: A Hybrid Polymer-MOF for Enhancement of Metformin's Bioavailability and PH-Controlled Release. *New J. Chem.* **2018**, *42*, 11137–11146. [CrossRef]
19. Rojas, S.; Navarro, J.A.R.; Horcajada, P. Metal-Organic Frameworks for the Removal of the Emerging Contaminant Atenolol under Real Conditions. *Dalton Trans.* **2021**, *50*, 2493–2500. [CrossRef]
20. Xiang, W.; Liao, Y.; Cui, J.; Fang, Y.; Jiao, B.; Su, X. Room-Temperature Synthesis of Fe/Cu-BTC for Effective Removal of Tetracycline Antibiotic from Aquatic Environments. *Inorg. Chem. Commun.* **2024**, *167*, 112728. [CrossRef]
21. Xiang, T.; Yang, R.; Li, L.; Lin, H.; Kai, G. Research Progress and Application of Pectin: A Review. *J. Food Sci.* **2024**, *89*, 6985–7007. [CrossRef]
22. Kontogiorgos, V. *Pectin: Technological and Physiological Properties*; Springer: Berlin/Heidelberg, Germany, 2020; ISBN 3030534219.
23. Martínez-Sabando, J.; Coin, F.; Melillo, J.H.; Goyanes, S.; Cerveny, S. A Review of Pectin-Based Material for Applications in Water Treatment. *Materials* **2023**, *16*, 2207. [CrossRef]
24. Kozioł, A.; Środa-Pomianek, K.; Górniak, A.; Wikiera, A.; Cyprych, K.; Malik, M. Structural Determination of Pectins by Spectroscopy Methods. *Coatings* **2022**, *12*, 546. [CrossRef]
25. Balaria, A.; Schiewer, S. Assessment of Biosorption Mechanism for Pb Binding by Citrus Pectin. *Sep. Purif. Technol.* **2008**, *63*, 577–581. [CrossRef]
26. Assifaoui, A.; Loupiac, C.; Chambin, O.; Cayot, P. Structure of Calcium and Zinc Pectinate Films Investigated by FTIR Spectroscopy. *Carbohydr. Res.* **2010**, *345*, 929–933. [CrossRef] [PubMed]
27. Jha, A.; Mishra, S. Exploring the Potential of Waste Biomass-Derived Pectin and Its Functionalized Derivatives for Water Treatment. *Int. J. Biol. Macromol.* **2024**, *275*, 133613. [CrossRef]
28. Coin, F.; Di Lisio, V.; Cangialosi, D.; Cerveny, S. The Glass Transition and the Dynamics of Water within Pectin and Metal-Organic Framework Nanochannels. *J. Chem. Phys.* **2025**, *163*, 164507. [CrossRef]
29. Ramírez-Alba, M.D.; Romanini, M.; Pérez-Madrigal, M.M.; Tamarit, J.L.; Alemán, C.; Macovez, R. Protonic Charge Conduction and H2O-Induced Relaxations in Hydrated Sodium Alginate and in Calcium Alginate Hydrogels and Xerogels. *J. Chem. Phys.* **2025**, *163*, 034901. [CrossRef]
30. Martínez-Sabando, J.; Coin, F.; Raposo, J.C.; Larrañaga, A.; Melillo, J.H.; Cerveny, S. Dual Crosslinking of Low-Methoxyl Pectin by Calcium and Europium for the Simultaneous Removal of Pharmaceuticals and Divalent Heavy Metals. *Chem. Eng. J.* **2023**, *475*, 146162. [CrossRef]
31. Coin, F.; Larrañaga, A.; Cerveny, S. Structural Characterization of Low Methoxyl Pectin-Based Adsorbents: The Role of Water on Pectin Structure. *Carbohydr. Polym. Technol. Appl.* **2025**, *11*, 100885. [CrossRef]
32. Zhu, R.; Cai, M.; Fu, T.; Yin, D.; Peng, H.; Liao, S.; Du, Y.; Kong, J.; Ni, J. Fe-Based Metal Organic Frameworks (Fe-MOFs) for Bio-Related Applications. *Pharmaceutics* **2023**, *15*, 1599. [CrossRef]
33. Chen, G.; Leng, X.; Luo, J.; You, L.; Qu, C.; Dong, X.; Huang, H.; Yin, X.; Ni, J. In Vitro Toxicity Study of a Porous Iron(III) Metal-Organic Framework. *Molecules* **2019**, *24*, 1211. [CrossRef]

34. Rajoria, S.; Vashishtha, M.; Sangal, V.K. Treatment of Electroplating Industry Wastewater: A Review on the Various Techniques. *Environ. Sci. Pollut. Res.* **2022**, *29*, 72196–72246. [CrossRef]
35. Donaher, S.E.; Van den Hurk, P. Ecotoxicology of the Herbicide Paraquat: Effects on Wildlife and Knowledge Gaps. *Ecotoxicology* **2023**, *32*, 1187–1199. [CrossRef] [PubMed]
36. Daghrir, R.; Drogui, P. Tetracycline Antibiotics in the Environment: A Review. *Env. Chem. Lett.* **2013**, *11*, 209–227. [CrossRef]
37. Cao, L.; Lu, W.; Mata, A.; Nishinari, K.; Fang, Y. Egg-Box Model-Based Gelation of Alginate and Pectin: A Review. *Carbohydr. Polym.* **2020**, *242*, 116389. [CrossRef]
38. Vareda, J.P. On Validity, Physical Meaning, Mechanism Insights and Regression of Adsorption Kinetic Models. *J. Mol. Liq.* **2023**, *376*, 121416. [CrossRef]
39. Cavanaugh, J.E.; Neath, A.A. The Akaike Information Criterion: Background, Derivation, Properties, Application, Interpretation, and Refinements. *WIREs Comput. Stat.* **2019**, *11*, e1460. [CrossRef]
40. Neath, A.A.; Cavanaugh, J.E. The Bayesian Information Criterion: Background, Derivation, and Applications. *Wiley Interdiscip. Rev. Comput. Stat.* **2012**, *4*, 199–203. [CrossRef]
41. Merli, G.; Becci, A.; Amato, A.; Beolchini, F. Acetic Acid Bioproduction: The Technological Innovation Change. *Sci. Total Environ.* **2021**, *798*, 149292. [CrossRef]
42. Chang, S.; Simeng, Y.; Henglong, T.; Shihao, F.; Zhu, L. Adsorption Properties and Interactions Analysis of Cyclodextrin-Based Polymer Networks towards Organic Dyes. *Carbohydr. Polym. Technol. Appl.* **2023**, *5*, 100317. [CrossRef]
43. Wang, J.; Guo, X. Adsorption Kinetic Models: Physical Meanings, Applications, and Solving Methods. *J. Hazard. Mater.* **2020**, *390*, 122156. [CrossRef] [PubMed]
44. Wang, J.; Guo, X. Adsorption Isotherm Models: Classification, Physical Meaning, Application and Solving Method. *Chemosphere* **2020**, *258*, 127279. [CrossRef]
45. SenGupta, A.K. *Ion Exchange in Environmental Processes: Fundamentals, Applications and Sustainable Technology*; John Wiley & Sons: Hoboken, NJ, USA, 2017; ISBN 1119157390.
46. Lu, G.; Li, S.; Guo, Z.; Farha, O.K.; Hauser, B.G.; Qi, X.; Wang, Y.; Wang, X.; Han, S.; Liu, X.; et al. Imparting Functionality to a Metal-Organic Framework Material by Controlled Nanoparticle Encapsulation. *Nat. Chem.* **2012**, *4*, 310–316. [CrossRef]
47. Li, C.; Liu, J.; Zhang, K.; Zhang, S.; Lee, Y.; Li, T. Coating the Right Polymer: Achieving Ideal Metal-Organic Framework Particle Dispersibility in Polymer Matrixes Using a Coordinative Crosslinking Surface Modification Method. *Angew. Chem. Int. Ed.* **2021**, *60*, 14138–14145. [CrossRef]
48. Assifaoui, A.; Lerbret, A.; Uyen, H.T.D.; Neiers, F.; Chambin, O.; Loupiac, C.; Cousin, F. Structural Behaviour Differences in Low Methoxy Pectin Solutions in the Presence of Divalent Cations (Ca^{2+} and Zn^{2+}): A Process Driven by the Binding Mechanism of the Cation with the Galacturonate Unit. *Soft Matter* **2015**, *11*, 551–560. [CrossRef]
49. Gohil, R.M. Synergistic Blends of Natural Polymers, Pectin and Sodium Alginate. *J. Appl. Polym. Sci.* **2011**, *120*, 2324–2336. [CrossRef]
50. Wang, R.; Liang, R.; Dai, T.; Chen, J.; Shuai, X.; Liu, C. Pectin-Based Adsorbents for Heavy Metal Ions: A Review. *Trends Food Sci. Technol.* **2019**, *91*, 319–329. [CrossRef]
51. Iacovone, C.; Coin, F.; Goyanes, S.; Cerveny, S. Calcium Crosslinking Modulates Structure and Pharmaceutical Removal of Pectin-Based Water Treatment Adsorbents. *SSRN* **2025**. [CrossRef]
52. Pappas, C.G.; Tzakos, A.G.; Gerothanassis, I.P. On the Hydration State of Amino Acids and Their Derivatives at Different Ionization States: A Comparative Multinuclear NMR and Crystallographic Investigation. *J. Amino Acids* **2012**, *2012*, 565404. [CrossRef]
53. Sips, R. On the Structure of a Catalyst Surface. *J. Chem. Phys.* **1948**, *16*, 490–495. [CrossRef]
54. Khezerlou, A.; Tavassoli, M.; Abedi-Firoozjah, R.; Alizadeh Sani, M.; Ehsani, A.; Varma, R.S. MOFs-Based Adsorbents for the Removal of Tetracycline from Water and Food Samples. *Sci. Rep.* **2025**, *15*, 502. [CrossRef]
55. Mirbagheri, N.S.; Heizmann, P.A.; Trouillet, V.; Büttner, J.; Fischer, A.; Vierrath, S. Adsorptive and Photo-Fenton Properties of Bimetallic MIL-100(Fe,Sn) and MIL-100(Fe,Ir) MOFs toward Removal of Tetracycline from Aqueous Solutions. *Mater. Adv.* **2024**, *5*, 5724–5737. [CrossRef]
56. Fox, T.G.; Loshaek, S. Influence of Molecular Weight and Degree of Crosslinking on the Specific Volume and Glass Temperature of Polymers. *J. Polym. Sci.* **1955**, *15*, 371–390. [CrossRef]
57. Tsivintzelis, I.; Panayiotou, C. Designing Issues in Polymer Foaming with Supercritical Fluids. *Macromol. Symp.* **2013**, *331–332*, 109–114. [CrossRef]
58. Synytsya, A.; Čopíková, J.; Matějka, P.; Machovič, V. Fourier Transform Raman and Infrared Spectroscopy of Pectins. *Carbohydr. Polym.* **2003**, *54*, 97–106. [CrossRef]

polymers

MDPI

Supplementary Materials

Bio–Based Pectin–Calcium Film and Foam Adsorbents with Immobilized Fe–BTC MOF for Water Contaminant Removal

Francesco Coin [1,*], Carolina Iacovone [1,2] and Silvina Cerveny [1,*]

[1] *Centro de Física de Materiales (CSIC, UPV/EHU)–Materials Physics Center (MPC), Paseo Manuel de Lardizabal 5, San Sebastián 20018, Spain*
[2] *Donostia International Physics Center (DIPC), Paseo Manuel de Lardizabal 4, San Sebastián 20018, Spain*
* Correspondence: fcoin001@ikasle.ehu.eus (F.C.); silvina.cerveny@ehu.es (S.C.)

Keywords: bio–based adsorbents; metal–organic framework (MOF); water purification; pectin–calcium films and foams; iron–based–MOF; adsorption

S1. Statistical Parameters and Model–Selection Criteria for Adsorption Isotherm and Kinetic Models

The following tables (Tables S1–S3) summarize the statistical descriptors used to evaluate the isotherm and kinetic adsorption data of paraquat (PQ) and tetracycline (TC). "Points number" indicates how many experimental measurements were included in the regression, while the "Degree of freedom" reflects the amount of independent information remaining after estimating the model parameters. The "Residual sum of squares (RSS)" quantifies the overall discrepancy between the experimental data and the model predictions, and the χ^2 value provides an additional goodness–of–fit metric. In both cases, lower values indicate a closer agreement with the experimental profile. The "t–Value" columns for q_e and k_1_report the statistical strength of each fitted parameter relative to its uncertainty, whereas "Prob>|t|" gives the associated two–sided p–values; small p–values indicate that q_e and k_1 are statistically significant and meaningfully contribute to describing the adsorption kinetics.

Table S1. Statistical parameters for the PFO model fits in Figure 5 for Zn^{2+} adsorption and Ca^{2+} desorption.

Zn^{2+} Adsorption								
Material	**χ^2**	**Points number**	**Degree of freedom**	**Residual sum of squares (RSS)**	**t–Value q_e**	**t–Value k_1**	**Prob>|t| q_e**	**Prob>|t| k_1**
PE–Ca	0.9	10	8	7.8	56	15.7	1.1×10^{-11}	2.6×10^{-7}
PE–Ca–5%MOF	2.4	10	8	19.4	26.6	8.8	4.2×10^{-9}	2.1×10^{-5}
Ca^{2+} Desorption								
Material	**χ^2**	**Points number**	**Degree of freedom**	**Residual sum of squares (RSS)**	**t–Value q_e**	**t–Value k_1**	**Prob>|t| q_e**	**Prob>|t| k_1**
PE–Ca	0.3	10	8	2.1	65.3	17.9	3.4×10^{-12}	9.8×10^{-8}
PE–Ca–5%MOF	1.4	10	8	11.1	20.9	7.2	2.8×10^{-8}	9.3×10^{-5}

Table S2. Statistical parameters for the Langmuir and Freundlich isotherms fit in Figure 7 for PQ and TC adsorption.

Langmuir Isotherm								
Material	**χ^2**	**Points number**	**Degree of freedom**	**Residual sum of squares (RSS)**	**t–Value q_M**	**t–Value K_L**	**Prob>|t| q_M**	**Prob>|t| K_L**
PQ	4.8	6	4	19.1	4.8	5.1	9×10^{-3}	9×10^{-3}
TC	0.6	6	4	3.4	10.9	3.2	4×10^{-4}	9×10^{-3}
Freundlich Isotherm								
Material	**χ^2**	**Points number**	**Degree of freedom**	**Residual sum of squares (RSS)**	**t–Value K_F**	**t–Value 1/n**	**Prob>|t| K_F**	**Prob>|t| 1/n**
PQ	6.9	6	4	20.6	2.5	4.8	8×10^{-3}	9×10^{-3}
TC	0.8	6	4	1.8	6.2	8.2	9×10^{-3}	4×10^{-3}

Table S3. Statistical parameters for the PFO and PSO kinetics fit in Figure 7 for PQ and TC adsorption.

PFO Kinetics								
Pollutant	**χ^2**	**Points number**	**Degree of freedom**	**Residual sum of squares (RSS)**	**t–Value q_e**	**t–Value k_1**	**Prob>|t| q_e**	**Prob>|t| k_1**
PQ	0.2	10	8	1.4	30.3	9.2	1.5×10^{-9}	1.5×10^{-5}
TC	0.03	10	8	0.3	35.7	11.3	4.1×10^{-10}	3.4×10^{-6}
PSO Kinetics								
Pollutant	**χ^2**	**Points number**	**Degree of freedom**	**Residual sum of squares (RSS)**	**t–Value q_e**	**t–Value k_2**	**Prob>|t| q_e**	**Prob>|t| k_2**
PQ	0.5	10	8	3.8	13.7	3.2	7.8×10^{-7}	9×10^{-3}
TC	0.1	10	8	0.8	15	3.6	3.7×10^{-7}	6×10^{-3}

The models used to fit the adsorption isotherms and kinetics were compared using R^2 and reduced χ^2 criteria. In addition, the models were evaluated based on the following criteria [1]:

– F–test;

– The Akaike Information criteria (AIC) [2];

– The Bayesian information criteria (BIC) [3].

Because the two candidate models for both the isotherm and kinetic datasets were fitted to the same data and had the same number of adjustable parameters, they had identical degrees of freedom; therefore, an F–test did not provide a meaningful basis for model discrimination and was inconclusive. Likewise, since the Langmuir and Freundlich isotherms and the PFO and PSO kinetic models were fitted using the same number of data points and parameters for both contaminants, the F–test remains inconclusive for these comparisons.

AIC and BIC are based on the likelihood function (Eq. 1 and Eq. 2 for AIC and BIC, respectively), and they are recognized as being able to measure the validity of non–linear models [1–3]. The lowest AIC or BIC value between the two compared models indicates the model that provides the best fit to the data..

$$AIC = 2p - 2\ln(L) \quad (3)$$

$$BIC = p\ln(n) - 2\ln(L) \quad (4)$$

where, n is the number of points in your data sample, p is the number of parameters estimated by the model, and L is the maximized value of the likelihood function of the model.

Table S4 reports the AIC and BIC values used to select the isotherm and kinetics model fits shown in Figure 7. In our case, the R^2, reduced χ^2, AIC, and BIC criteria all agree on the model that best fits the data. Among the isotherm models evaluated, the Langmuir equation provided the best fit for the adsorption of paraquat (PQ) and tetracycline (TC). The pseudo-first-order (PFO) model best described the kinetic data for both pollutants.

Table S4. Akaike Information Criterion (AIC) and Bayesian Information Criterion (BIC) values for the isotherm and kinetics fits shown in Figure 7 for both PQ and TC contaminants. Lower AIC/BIC values indicate the preferred model.

Isotherms							
Pollutant	**Model**	**Points number**	**Parameter number**	**F–test**	**AIC**	**BIC**	**Preferred model**
PQ	Langmuir	6	2	/	24.9	11.9	Langmuir
	Freundlich	6	2	/	37.1	12.3	
TC	Langmuir	6	2	/	14.5	–0.3	Langmuir
	Freundlich	6	2	/	24.9	1.9	
Kinetics							
Pollutant	**Model**	**Points number**	**Parameter number**	**F–test**	**AIC**	**BIC**	**Preferred model**
PQ	PFO	10	2	/	–7.1	–10.2	PFO
	PSO	10	2	/	–1.9	–4.9	
TC	PFO	10	2	/	–25.9	–28.9	PFO
	PSO	10	2	/	–14.9	–18.1	

S2. FT–IR normalization

Figure S1 shows the FT–IR baseline correction and normalization considering the peak area of the glycosidic ring vibration of the poly–galacturonic acid chain (–C–O–C) at ~1140 cm^{-1} [4].

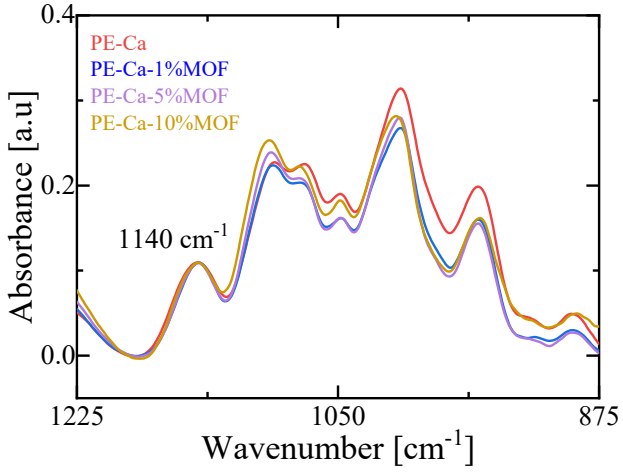

Figure S1. FT–IR baseline correction and normalization.

S3. Adsorption Isotherms of Nitrogen

Adsorption–desorption isotherms of nitrogen at −196 °C were recorded using the Micromeritics ASAP 2420 instrument. Before sorption measurement, the sample was degassed at a pressure below 10–4 mbar and 200 °C for 1 hour using nitrogen gas. The BET

area was determined using the Brunauer–Emmett–Teller (BET) method, based on adsorption data in the p/p_0 range of 0.05–0.20 (Figure S2). The volume of micropores (VMI) was evaluated using the DFT method (N_2 adsorption considering cylindrical pores). Adsorption isotherms of nitrogen at 77 K reveal a pore diameter of 2.0 nm (nm) and a BET area of 1366 m^2/g for Fe–BTC.

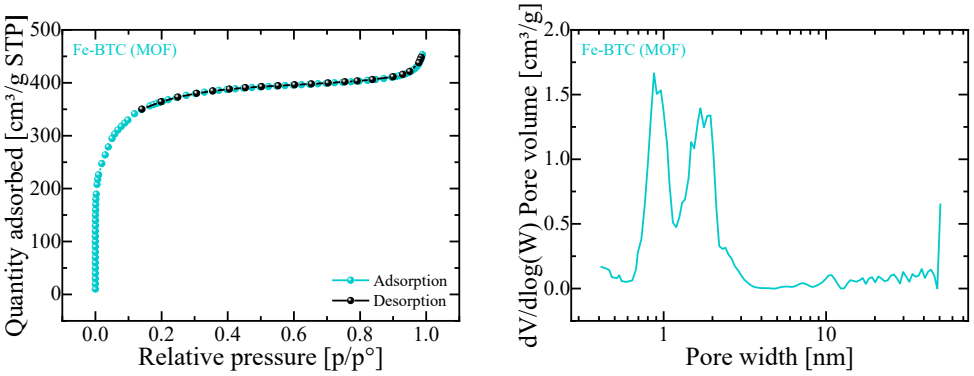

Figure S2. (a) N_2 adsorption isotherms at −196 °C on commercial MOF Basolite F300® (Fe–BTC). (b) BJH pore size distribution on commercial MOF Basolite F300® (Fe–BTC).

S4. X–Ray Diffraction

The PE–Ca film shows a broad amorphous peak at 14.02 °, which emerges after Ca^{2+} crosslinking [5],[6]. Fe–BTC exhibits sharper diffraction peaks, with an amorphous background, typical of Fe–BTC structures [7]. The PE–Ca–5%MOF pattern displays combined features of both components (Figure S3). Notably, a shoulder appears at 14.02 °, near the main Fe–BTC peak at 11.11 ° (inset on Figure S3), indicating successful incorporation of the MOF into the pectin matrix without structural disruption or chemical incompatibility

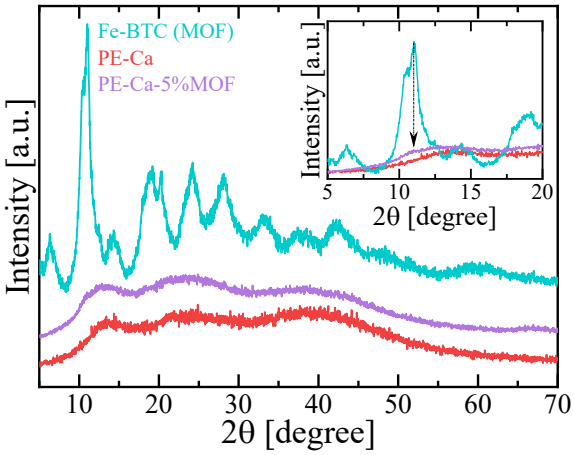

Figure S3. XRD patterns of pure Fe–BTC, PE–Ca, and PE–Ca–5%MOF composite. The inset highlights the diffraction region between 5 ° and 20 °, revealing the combined structural features of the MOF and the polymer matrix.

S5. Fe–BTC contaminants adsorption

Figure S4 show the removal efficiency of ATE, MET, MFT, PQ and TC at an initial concentration of 10 mg/L, using a 1 g/L dose at pH 7 for 24 hours for Fe–BTC.

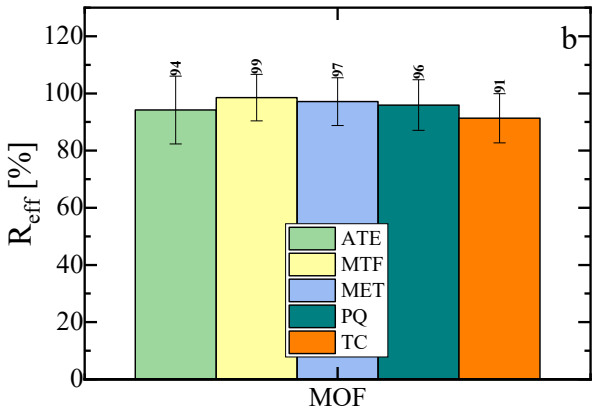

Figure S4. Removal efficiency pure Fe–BTC (MOF) powder after 24 h at an initial concentration of 10 mg/L, at a composite dose of 1 g/L and at pH 7.

S6. UV–Vis spectra

Figure S5 presents the UV–Vis spectra of PQ and TC solutions, used for adsorption isotherm analysis (initial concentrations of 5, 10, 25, 50, and 75 mg/L, with a composite dose of 1 g/L at pH 7). Solid lines represent the absorbance of the stock solutions, while dashed lines show the spectra after 24 hours of adsorption. The insets display the calibration curves (based on maximum absorbance at 260 nm for PQ and 356 nm for TC) used to calculate the residual concentrations.

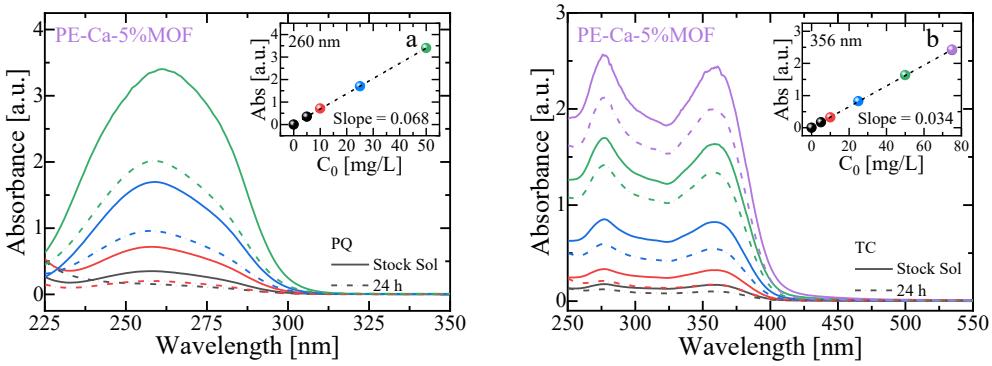

Figure S5. UV–Vis spectra of (a) paraquat (PQ) and (b) tetracycline (TC) at initial concentrations ranging from 5 to 75 mg/L before (solid lines) and after 24 h of adsorption by PE–Ca–5%MOF (dashed lines) at a composite dose of 1 g/L and pH 7. Insets show the calibration curves constructed within their respective linear ranges from the maximum absorbance values at 260 nm for PQ and 356 nm for TC.

The limits of detection (LOD) and quantification (LOQ) for paraquat (PQ) and tetracycline (TC) by UV–Vis were determined from the linear calibration curves (see Table S5 for statistical parameters) using the standard deviation–to–slope method. Calibration data (n = 10) were fitted by least–squares regression ($A = SC + b$), and the standard deviation of the response (σ) was estimated as the residual standard deviation of the regression, calculated from the residual sum of squares (RSS) as $\sigma = \sqrt{RSS/(n-2)}$. LOD and LOQ were then obtained as $LOD = 3.3\,\sigma/S$ and $LOQ = 10\,\sigma/S$, respectively, and are reported in the same concentration units as the calibration. Using this approach, PQ showed a LOD and LOQ of 0.492 mg/L and 1.49 mg/L, respectively while TC showed a LOD and LOQ of 0.840 mg/L and 2.55 mg/L, respectively. Both analytes exhibited a linear UV–Vis response

within the investigated calibration range, with PQ and TC showing linearity from the lowest calibration level up to 50 mg/L for PQ and 75 mg/L for TC, respectively. In Table S5 the "Intercept" corresponds to the predicted signal in the absence of analyte, while the "Slope" represents the method sensitivity, i.e., the change in signal per unit concentration; the reported ± values reflect the uncertainty of these fitted parameters. Finally, "LOD" (limit of detection) is the lowest concentration that can be reliably distinguished from the background, whereas "LOQ" (limit of quantification) is the lowest concentration that can be quantified with acceptable accuracy and precision, both reported in mg/L.

Table S5. Statistical parameters of the calibration curves used for quantification of paraquat (PQ) and tetracycline (TC).

Calibration Curves								
Pollutant	**n**	**χ^2**	**R^2**	**Intercept**	**Slope**	**Residual sum of squares (RSS)**	**LOD [mg/L]**	**LOQ [mg/L]**
PQ	10	0.99	0.99	0.01214 ± 0.0104	0.0677 ± 4.1×10^{-4}	8.1×10^{-4}	0.492	1.49
TC	10	0.99	0.99	0.00651 ± 0.00721	0.0343 ± 1.9×10^{-4}	6.1×10^{-4}	0.840	2.55

Figure S6 shows the comparison between the UV–Vis spectra of paraquat (PQ) and tetracycline (TC) solutions (10 mg/L, pH 7) after 24 h of contact with PE–Ca composites containing different MOF loadings and dispersion methods. For PQ (Figure S6a), both 1 wt% and 5 wt% water–dispersed composites significantly reduced the characteristic absorbance at 260 nm, with the PVP–assisted 1 wt% film reaching removal levels comparable to the 5 wt% water–dispersed film. The PVP–assisted foam exhibited the highest decrease in absorbance, indicating enhanced adsorption due to its increased porosity and improved MOF particle accessibility. For TC (Figure S6b), which absorbs maximally at 356 nm, adsorption was generally lower than for PQ due to its larger molecular size and reduced compatibility with the pectin network. Nevertheless, the PVP–assisted foam markedly improved removal compared to water–dispersed films, approaching the performance of the 5 wt% water–dispersed composite. These results highlight the importance of dispersion strategy and composite geometry in enhancing adsorption performance, especially for bulkier molecules such as TC.

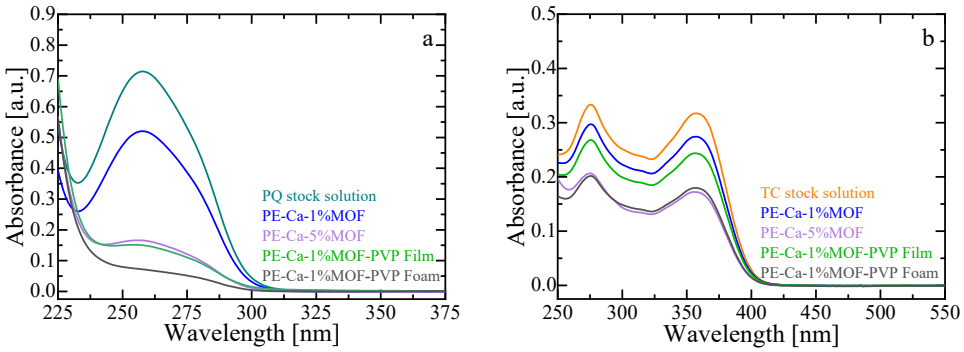

Figure S6. UV–Vis spectra of (a) paraquat (PQ) and (b) tetracycline (TC) at an initial concentration of 10 mg/L after 24 h of adsorption (composite dose: 1 g/L, pH 7) by PE–Ca composites containing 1 wt% and 5 wt% Fe–BTC (water–dispersed) and 1 wt% Fe–BTC (PVP–assisted) in film and foam geometries.

References

1. Vareda, J.P. On Validity, Physical Meaning, Mechanism Insights and Regression of Adsorption Kinetic Models. *J Mol Liq* 2023, *376*, 121416, doi:10.1016/j.molliq.2023.121416.
2. Cavanaugh, J.E.; Neath, A.A. The Akaike Information Criterion: Background, Derivation, Properties, Application, Interpretation, and Refinements. *Wiley Interdiscip Rev Comput Stat* 2019, *11*.
3. Neath, A.A.; Cavanaugh, J.E. The Bayesian Information Criterion: Background, Derivation, and Applications. *Wiley Interdiscip Rev Comput Stat* 2012, *4*, 199–203, doi:10.1002/wics.199.
4. Synytsya, A.; Čopíková, J.; Matějka, P.; Machovič, V. Fourier Transform Raman and Infrared Spectroscopy of Pectins. *Carbohydr Polym* 2003, *54*, 97–106, doi:10.1016/S0144–8617(03)00158–9.
5. Coin, F.; Larrañaga, A.; Cerveny, S. Structural Characterization of Low Methoxyl Pectin–Based Adsorbents: The Role of Water on Pectin Structure. *Carbohydrate Polymer Technologies and Applications* 2025, *11*, doi:10.1016/j.carpta.2025.100885.
6. Gohil, R.M. Synergistic Blends of Natural Polymers, Pectin and Sodium Alginate. *J Appl Polym Sci* 2011, *120*, 2324–2336, doi:10.1002/app.33422.
7. Chen, G.; Leng, X.; Luo, J.; You, L.; Qu, C.; Dong, X.; Huang, H.; Yin, X.; Ni, J. In Vitro Toxicity Study of a Porous Iron(III) Metal–Organic Framework. *Molecules* 2019, *24*, doi:10.3390/molecules24071211.